The Application of Bose-Einstein Condensates to Inertial Sensing

John Elias Debs

THE
AUSTRALIAN
NATIONAL
UNIVERSITY

A thesis submitted for the degree of
Doctor of Philosophy at
The Australian National University

February 2012

Typeset in Computer Modern by TEX and LATEX 2ε.

Declaration

To the best of my knowledge and except where acknowledged in the customary manner, the material presented in this thesis is original and has not been submitted in whole or part for a degree in any university. Where work has been performed in collaboration with others, I have acknowledged the contributions of all authors.

John Elias Debs
8 February 2012

For Mum, Dad, & especially Teta ...

Who was crazy enough to teach a kindergardener multiplication...

Acknowledgements

What I have achieved over the last four years would have been impossible were it not for the ubiquitous support given to me by so many people, past and present. First and foremost, to my supervisor Nick Robins. Without your never ending support, I would not be here today. You managed to reawaken a child in me who was all but lost; inquisitive, questioning, and demanding. I will always treasure your infectious enthusiasm, near impossible optimism, and even your puns. Most of all though, I will forever treasure your friendship. You have taught me as much about being a scientist, as you have about life. Thank you.

To my supervisor John Close, thank you for truly teaching me to be a better scientist, and for all the debating lessons. I will honestly always look back fondly at all our interactions, and greatly look forward to working with you and Nick into the future. To Cristina Figl, thanks for making me feel like one of the family, and for being so supportive, especially early on in my PhD.

By its nature, experimental physics is teamwork. I wouldn't be who I am today where it not for my wonderful fellow graduate students: Paul Altin, Daniel Döring, Rachel Poldy, and Gordon McDonald. It has been a privilege to work with you, and all of you have taught me to be a better scientist. Paul, thank you for always listening, and sharing the angst of being a senior PhD student with me. Daniel, thank you for all your patience and willingness to help me catch up. Rachel, I will always value your friendship, and thanks for sharing the struggles of starting a PhD with me. And Gordon, thanks for putting up with my stubbornness and your endless desire to always help. Thanks goes to Tom Barter for Gilligan's.

Special thanks goes to the theory group: Stuart Szigeti, Graham Dennis, Michael Hush, Mattias Johnsson, Robin Stevenson, Sarah Adlong, Brianna Hillman, Chris Bentley, and Joe Hope; who are always ready for an eye-opening discussion, be it about physics, life, the universe, or something slightly lower-brow. Thanks for teaching me at least half of the theoretical physics I know. Particular thanks goes to Stuart for the most exciting and interesting collaboration of my PhD, and to Graham for being more willing to help then anyone else I know. Also for turning me to the Mac.

To my mates both near and far. Thanks for providing me with the much needed release from the life of a PhD student. Particular thanks to Shaun New, who has ridden the PhD train with me through all its ups and downs. To the Radelaide gang, every time I see you, you all make me feel like I'd never left. Thank you. Noelia, your support really meant the world to me, and you will

always have a special place in my heart. I hope that life brings you everything you deserve and more. To the whole gang in Hannover at the Institute, thank you for making my time in Germany one of the most memorable in my life, especially Dennis Schlippert.

I came to Canberra and stumbled across probably the best share house in the city. To some amazing housemates over the years: Lauren, Shannon, Jess, Ali, Sophie, and Amy, thanks for giving me a place to call home and a great bunch friends. Canberra wouldn't have nearly been as awesome without you guys. Lauren, you get a special thanks for always injecting positivity into every situation, and sticking with me all this time. Also for teaching me to clean a toilet like a legend.

To those who helped me proofread my thesis: Nick, Paul, Stuart, John, and Gordon, I couldn't have done it without you. Especially Paul and Stuart, with your hawk-like eyes for grammar. A big thanks goes to ACQAO, and to Hans Bachor for directing such an amazing centre, which gave students like me such wonderful opportunities. To all the administrative staff, and the workshop at DQS, thanks for all the support. Particular thanks to Damien Hughes for all the entertaining chats, and for unheard of skill in solving bureaucratic problems. And to all the other people at DQS too numerous to mention, thanks for making it such a wonderful place to work.

Thanks to my wonderful high school teachers, who obviously saw something in me and did their best to nudge me onto the right track.

Last, but most certainly not least, to my family. Thank you for your unconditional love, and for supporting me through all the ups and downs. Mum, your belief in me is second to none. Dad, if it wasn't for all those Dick Smith's electronic kits, I probably wouldn't have been a physicist. Helen and Daniel, its been so great to see you guys grow up, and for us to grow from just siblings into friends. Most of all to Teta, you helped raise me like a spoiled son. Thank you for being a second mum and my first and most influential teacher. This Doctorate is for you.

Abstract

This thesis presents experimental and theoretical work investigating the application of Bose-condensed atomic sources to atom interferometer-based inertial sensors. In particular, we focus on gravity sensors, or *gravimeters*, which have applications in fundamental physics, Earth sciences, mineral exploration, and navigation. Using proof-of-principle experiments, and theoretical analyses, we show that Bose-condensed sources will be critical in the next generation of these devices.

We first investigate the the production of atomic sources and beamsplitters/mirrors. We design and implement a straightforward and passively stable laser system for driving Raman transitions between the hyperfine ground states of ^{87}Rb. This is used as an outcoupler for atom-lasers, and is compared to alternative methods such as radio frequency outcoupling. We find that our Raman outcoupler produces the highest brightness atom-lasers from a magnetically confined Bose-Einstein condensate (BEC). The same laser system can be reconfigured as an atomic beamsplitter, which we show operates at the atomic shot-noise limit using a BEC-based free-space Ramsey atom interferometer. Atom-lasers are also outcoupled from an optical trap, and we show that their divergence is Heisenberg-limited within experimental uncertainty.

Large momentum transfer (LMT) beamsplitters offer a clear path for improving the sensitivity to inertial forces. We design a laser system for Bragg diffracting atoms as an LMT technique, which we use for our beamsplitters and mirrors in a Mach-Zehnder gravimeter. We characterise the laser system's relative-phase noise, and highlight recent improvements. We are able to efficiently diffract atoms with up to $10\hbar k$ momentum transfer in a single coupling pulse. The same versatile laser system is also capable of driving Bloch oscillations as an LMT technique.

Using these tools, we construct the first Mach-Zehnder atomic gravimeter based on the interference of a BEC. We observe a high interference-fringe contrast, close to the theoretical limit for Bragg-based beamsplitters (see below). Using third-order Bragg diffraction, we increase our sensitivity to gravity to 1 part in 10^5. We also use Bloch oscillation-based LMT to increase our sensitivity, achieving a high fringe contrast compared with previous work. However, we find that the contrast decays rapidly when trying to further increase the interferometer space-time area. This is likely caused be systematic phase shifts not present for Bragg diffraction, and it would seem that Bragg diffraction is the preferable LMT technique.

Using a simple yet robust mean-field analysis, we estimate the atomic interaction induced phase-diffusion in a free-space interferometer such as a gravimeter. We find that, contrary to an often held view, atom-atom interactions do not limit the applicability of Bose-condensed sources to *free-space* atom interferometers for very reasonable experimental parameters.

We conclude by investigating the effect of momentum width in inertial sensors. Using a comprehensive theoretical model, we optimise the efficiency of Bragg mirror pulses, and find that there is a fundamental limit to the mirror efficiency set by the momentum width of the source (along the direction of diffraction). Thus, a narrow momentum width is required in order to improve the efficiency. When accounting for a limited coupling strength (by e.g. laser power), we find that efficiency is strongly reduced for increasing diffraction order, and can only be recovered by using a narrower momentum width source such as a BEC or atom-laser. This is supported by experimental results.

The effect of momentum width is also pronounced in the direction transverse to the beamsplitter laser. By comparing a BEC and an ultra-cold thermal source in our gravimeter, we find that the BEC gives superior fringe contrast in an otherwise identical setup. We use a simple model of wavefront errors to account for this, and highlight that narrower momentum widths can lead to further improvement in the contrast, and a reduction in systematic shifts. Furthermore, the Coriolis force results in additional systematic phase shifts, which depend on the transverse momentum width. Thus we again conclude that narrow Bose-condensed sources will help reduce these systematic shifts.

Contents

List of Figures

List of Acronyms

ALM atom-laser machine

AOM acousto-optic modulator

BEC Bose-Einstein condensate

CCD charge-coupled device

DDS direct digital synthesiser

DSO digital sampling oscilloscope

ECDL external cavity diode laser

EOM electro-optic modulator

FM frequency-modulation

FWHM full-width-half-maximum

GPE Gross-Pitaevskii equation

LIGO Laser Interferometer Gravitational Wave Observatory

LMT large momentum transfer

MOT magneto optical trap

ODE ordinary differential equation

OPD optical path difference

OPLL optical phase-locked loop

PBS polarising beamsplitter

PGC polarisation gradient cooling

PSD power spectral density

QUIC quadrupole-Ioffe configuration

RF radio-frequency

RMS root-mean-square

SI International System of Units (*French – Système international d'unités*)

SNR signal-to-noise ratio

TiSub titanium sublimation pump

UHV ultra-high vacuum

WEP weak equivalence principle

Clipart courtesy of Florida Center for Instructional Technology

Chapter 1

Introduction

From apples to atoms...

It is humbling to remember that it is over 250 years since Sir Isaac Newton, inspired by an apple falling from a tree in his orchard [1], made the mental leap to conjecture that the same force which caused this apple to fall also held the Moon to the Earth. This stimulated him to develop his Law of Gravitation, and led to the principle that all objects fall with the same acceleration irrespective of their mass, as observed by Galileo Galilei. Over 250 years ago, these scientists understood gravity as well as many people do today.

In reality, we still measure gravity by dropping a proverbial apple – a falling test mass whose trajectory we measure through space-time. Over two centuries have, however, led to a vast improvement in our *measurement precision*. With the development of the optical laser and atom interferometers over the last 50 years, we have far superior rulers, and far superior clocks with which to make such a measurement This thesis investigates the question of how using a Bose-Einstein condensate (BEC), the matter-wave analog of an optical laser, can allow for improved precision in an inertial sensor such as a gravimeter. In particular, BECs should enable us to use even more precise "rulers" to measure the trajectory of falling atoms, and reduce several systematic effects which compromise the accuracy of the measurement.

Mankind's most precise instruments are those that measure space and time. At the heart of these measurement devices is the phenomenon of wave interference. For example, the most precise rulers to date are optical interferometers, built for the detection of gravitational waves using very long baseline interferometers such as the Laser Interferometer Gravitational Wave Observatory (LIGO). This device measures distance with a sensitivity up to $\Delta L/L \sim 10^{-24}$ [2]. On the other hand, the most precise keeper of time is an atomic clock. With its ceaseless ringing, caesium is an oscillator that defines the International System

of Units (SI) second at the level of 1 part in 10^{16} [3, 4, 5]. Precise measurement of the caesium resonance at 9,192,631,770 Hz again relies on interference, in this case the interference of matter-waves in an *atom interferometer*.

1.1 Atom Interferometers as Inertial Sensors

By 1992, Kasevich and Chu had pioneered work on light-pulse atom interferometers [6, 7] which spawned a field of research that now provides (in some cases) the highest sensitivity measurements of inertial forces. Such measurements include that of gravitational acceleration [7, 8, 9, 10, 11], and the related field of gravity gradiometry [12, 13]; as well as rotations such as that of the Earth [14, 15, 16, 17]. Inertial sensitivity has in turn led to the precision measurement of fundamental constants, such as the fine-structure constant (α), through measurement of the photon-recoil energy [18, 19, 20], and Newton's gravitational constant (G), through measurement of a gravity gradient [13, 21]. In the case of α, recent improvements to the work of Cladé *et al.* provide a contribution to the CODATA value with a precision of 6.6×10^{-10} [20]. This is within a factor of two in precision of an independent measurement of the electron magnetic moment, which currently provides the highest precision measurement of α [22]. In this thesis, we focus on atom interferometers as gravity sensors (*gravimeters*), although most results apply equally to other inertially sensitive configurations for both fundamental and practical applications.

1.1.1 Applications of Gravity Measurements

Practical Applications

The measurement of gravity has widespread practical applications. Earth scientists use absolute as well as differential gravity measurements to peer beneath the surface of the Earth, gaining valuable information about density structure and changes to the geoid due to tectonic plate movement, magma flows, volcanic activity, and tidal forces. Recent work, which has a direct impact on Australian government policy, has monitored groundwater variation in the Murray-Darling basin using space-based gravity measurements from the GRACE (Gravity Recovery and Climate Experiement) satellite mission [23].

Resource industries also benefit from gravity measurement, since it allows mining companies to better identify mineral deposits. Mineral explorers will typically look for anomalous gravity gradients caused by high density deposits of

ore, and these measurements can readily be done over tens of kilometres allowing effective and efficient initial surveys. The measurement of anomalous gradients is also of interest to defence and security agencies.

Also worth noting is that the precise measurement of accelerations (including rotations) is also of interest for dead reckoning navigation. This again has applications in defence, but also for space travel and exploration, where minute uncertainty in orientation can lead to a very large uncertainty in the final destination.

Fundamental Applications

The measurement of gravity is also of great importance to fundamental physics. The weak equivalence principle (WEP) states that inertial and gravitational mass are identical, and therefore all bodies fall with the same acceleration regardless of their mass. However, the attempt to reconcile General Relativity with Quantum Mechanics often leads to small violations of the WEP due to the prediction of new interactions that violate the universality of free-fall [24]. The WEP has currently been tested to the 10^{-13} level [25, 26], with predicted violations at the 10^{-18} level [24]. Improved precision in atomic gravimeters could provide the sensitivity required for these tests. They also have the advantage of using identical test masses: individual atoms. Recent proposals aim to reach a sensitivity of 10^{-17} [27]. In somewhat related work, there have been proposals for building atom interferometers for detecting gravitational waves [28, 29]. Müller *et al.* have also recently highlighted that atomic gravimeters are equivalently a test of the gravitational red shift [30, 31, 32, 33], although this has been the subject of controversy [34] and rigorous debate over the last two years [35, 36, 37, 38].

The Watt Balance project is a proposal to redefine the kilogram, which is the only remaining SI unit based on an artefact. The idea is to balance a test mass' gravitational weight using an electric current. Coupled with a high precision measurement of the local gravitational force, this allows the kilogram to be defined in terms of electrical units [39]. The target precision is $< 10^{-8}$, which requires an identical or better precision in the gravity measurement. An atom interferometer is a primary candidate for this task [40].

1.1.2 Atomic Gravimeters

The basic operation of a light-pulse atom interferometer is in principle the same as that of an optical interferometer, with the roles of matter and light reversed.

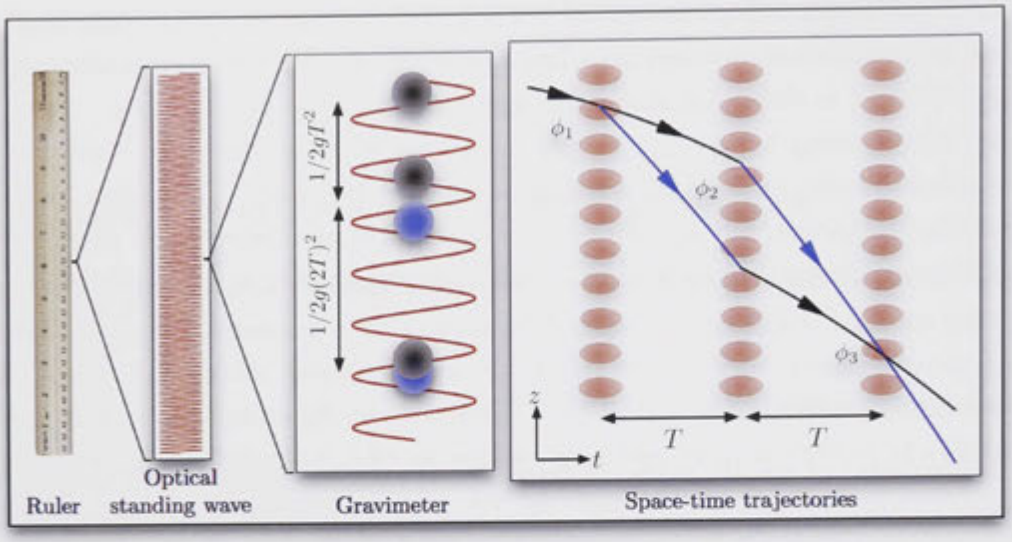

Figure 1.1: Basic operation of an atom interferometer, configured as a gravimeter. An atomic cloud falls freely under gravity through an optical standing wave, which forms an "optical ruler" with a precision proportional to its wavelength. Three pulses of the standing wave are applied, separated equally in time and with appropriate durations to beamsplit, reflect, and recombine the atomic wavepackets as shown in the space-time diagram on the right. The phase of the laser at each pulse is written onto the atomic state, encoding distance and time information onto the atomic state.

Laser pulses are used to beamsplit, reflect, and recombine atomic wavepackets using the absorption and emission of photons. This imparts momentum to the atoms, as shown in figure 1.1. In this example three pulses are applied, separated equally by time T and with appropriate durations $(\pi/2 - \pi - \pi/2)$ for a beamsplitter, mirror, and beamsplitter operation respectively, producing an analog Mach-Zehnder interferometer as shown to the right. At each pulse, the phase of the laser is transferred to the atomic state, encoding information about the atomic trajectories through the beam. In the configuration shown, the atomic trajectory is (ideally) due only to gravity and the initial conditions, and thus information about the gravitational acceleration is encoded in the atomic state. At the final beamsplitter of the interferometer, the phase information is converted to the probability of finding atoms in one of the two motional states, and the phase accumulated due to gravity (or equivalently any uniform acceleration) is:

$$\Phi = \phi_1 + 2\phi_2 + \phi_3 = -\mathbf{k}_e \cdot \mathbf{g}T^2 \tag{1.1}$$

where ϕ_i is the optical phase of the ith pulse, $\hbar\mathbf{k}_e$ is the momentum transferred

by the beamsplitter and is proportional to the laser wave vector, and $\mathbf{g}$ the acceleration due to gravity.

Because the laser beam is periodic in space and has a well defined phase, with an optical wavelength $\sim 500\,\text{nm}$, it effectively forms an "optical ruler" far more precise than an everyday ruler we might use to measure a falling apple. A shorter wavelength laser has finer "graduations" than a longer wavelength laser, and the higher the phase-stability of the laser, the more precisely defined are the graduations.

1.2 Bose-Einstein Condensates and Atom Interferometry

Key developments in the success of atom interferometers have been laser and evaporative cooling, which has made ultra-cold atomic sources readily available [41, 42, 43]. Cooling an atomic source narrows its momentum width and is analogous to spectrally purifying an optical source. Optical interferometers have generally benefited from the use of a spectrally pure source, and this was traditionally achieved by frequency filtering. However, with the advent of the optical laser, a high brightness and spectrally pure source of photons became readily available, which quietly revolutionised optical interferometry. Although white (or *thermal*) light typically has a higher flux, and white-light interferometers can in principle be as sensitive as laser interferometers, a laser is usually preferred for its practical advantages such as easier mode matching, greater flexibility of design, and a lower sensitivity to misalignment.

To date, the vast majority of atom interferometers have used cold, yet still thermal atomic sources – the direct analog of thermal light. Almost simultaneous with the development of modern atom interferometers was the observation of Bose-Einstein condensation in dilute atomic gases in 1995 [44, 45]. Predicted by Bose and Einstein as an outcome of seminal papers on the statistical mechanics of identical bosons [46, 47, 48], this statistical phase of (bosonic) particles occurs at a phase-space density higher than ~ 2.612 and results in a macroscopic occupation of the ground state in a given system. In this sense, a BEC is the matter-wave equivalent of the optical laser, which is a macroscopic photon population in a single optical mode. This motivated several groups to extract atoms from a trapped condensate, producing a beam of Bose-condensed atoms now known as an atom-laser [49, 50, 51, 52, 53, 54, 55]. The analogy with the optical laser even extends into the quantum regime, with Öttl *et al.* showing that atom-lasers have a second order correlation function equal to 1 [56], as is the case for an optical

laser.

Given the strong analogy between BECs and optical lasers, an important question to ask is:

Are BECs advantageous as a source for atom interferometers?

The goal of this thesis has been to take important steps in answering this question in the context of inertial sensors.

1.2.1 Atomic Interactions

To date, BECs have largely been neglected by the precision measurement and interferometry community. Perhaps one major hurdle early on was the added complexity required to produce a BEC. However, BECs are now an almost standard option in any atom optics laboratory. An often-cited argument against the use of a BEC is that atom-atom interactions lead to undesirable effects such as systematic shifts [57], reduced mode-matching due to spatial dynamics [58, 59, 60], and phase diffusion of the many-body wavefunction [61, 62]. This is in fact a major difference between optical lasers and BECs; photons do not interact in a linear medium. In relatively recent work however, we [63] as well as Jamison *et al.* [64] have independently shown that interactions can be negligibly small in free-space interferometers such as inertial sensors. Details of our estimate can be found in chapter 9. In any case, interactions also have the potential to produce squeezed states, which could be used to surpass the shot-noise limited sensitivity of atom interferometers. Multiple schemes have been proposed, and proof-of-principle experiments have produced squeezing [65, 66, 67, 68, 69, 70, 71, 72, 73, 74, 75]. In particular, Gross *et al.* have used squeezing to enhance the sensitivity of an atom interferometer [72]. Our group has investigated producing useful squeezing in large atom number ($\sim 10^6$) condensates, and this is discussed in detail in [59, 76].

1.2.2 Atom Flux

Another point of difference between thermal and condensed sources is atom flux. The best BEC sources [77] are still a factor of 25 lower in flux than the best ultracold thermal sources [10]. Although this is potentially a factor of 5 in shot-noise limited sensitivity, many inertial sensors (in particular gravimeters) are limited by technical noise and systematics [9]. Furthermore, if flux becomes a serious issue, then increasing it is likely a question of cost and engineering, as opposed

to a fundamental limitation.

1.2.3 Momentum Width

Perhaps the two most compelling reasons to pursue BEC sources are (a) that large momentum transfer (LMT) beamsplitting can be performed on a condensate with high efficiency (see our work [78]), and (b) BECs have an inherently low susceptibility to systematic effects. LMT beamsplitting involves using an atom-light interaction in which the effective wave vector [$\mathbf{k}_e$ in equation (1.1)] is increased. This increases the momentum transferred to the atoms, increasing the phase shift in direct proportion. LMT has already proven crucial in the latest generation atom interferometers, such as those for measuring α [20]. The proposed gravitational wave detectors require beamsplitters transferring at least 100, and up to 1000 photon recoils [28]. To date, the largest momentum transfer in an interferometer capable of making a phase measurement has been 24 photon recoils [79].

One example of an LMT atom-light interaction is Bragg diffraction [80, 81, 82, 83, 84, 85, 86], which is described in detail in chapter 8. In recent work, we have shown that there is a fundamental limit to the diffraction efficiency set by the momentum width of the atomic source; with a narrower momentum width resulting in higher efficiency [78]. This is in contrast to statements in [87] claiming efficiency limits are of a technical nature. Additionally, when considering the very realistic scenario of finite laser power, a narrow momentum width is again favourable, particularly for very large momentum transfer beamsplitters. This work is highlighted in chapter 9. BECs have momentum widths 5-10 times smaller than typical thermal sources, while atom lasers have up to 100 times narrower transverse momentum width (see chapter 5).

Wavefront Errors

From a practical perspective, there are several advantages to condensed sources for gravimeter-type configurations (including α measurements, and gradiometers). In particular, the transverse momentum relative to $\mathbf{k}_e$ can lead to systematic shifts and a reduction in the interference fringe contrast. For example, aberrations in the beamsplitter laser lead to trajectory-dependent phase shifts across a cloud [88, 89] (also see chapter 9). Hotter clouds have a larger spread in trajectories, which are typically averaged over during detection leading to a reduction in contrast and systematic shifts. In chapter 9 and reference [63], we

perform a direct comparison between a thermal and BEC source, showing significant improvement in contrast for a BEC in an otherwise identical system. Wavefront errors have long been known as a problem [8], and are a major source of uncertainty in some state-of-the-art devices [20, 88, 89]

Rotation and the Coriolis Force

Until this point we have discussed sensors designed to measure gravity. Another important class of sensor aims to measure rotations. Atom interferometer gyroscopes are operated with the atoms travelling perpendicular to the beamsplitter laser. Thus transverse momentum components in a gravimeter lead to systematic rotational phase shifts on Earth due to the Coriolis effect. Again, the size of this effect will increase with the momentum width of the atomic source, as well as any uncertainty in the initial velocity. More details are given in chapter 9. Suffice it to say here that the symmetry of the momentum distribution is also important. Bose-condensed sources are not only narrower in momentum, but because their state is defined by their trap, they are typically more symmetric than laser-cooled sources, and have more precisely determined initial conditions for free-fall.

The Coriolis force has yet another consequence. Rotation of the Earth rotates $\mathbf{k}_e$, which results in a small displacement between the two wavepackets at the final beamsplitter. This is analogous to a mode mismatch in an optical interferometer. Because the thermal de Broglie wavelength of the atoms characterises the wavepacket's spatial extent, colder sources are less susceptible to this effect, as recently pointed out in [90].

These effects are beginning to limit atom interferometers, and several groups are now either starting to use BEC [63, 87], or plan on doing so in the near future [91]. Combined with the aggressive proposals for future sensors, it is the argument of this thesis that Bose-condensed sources are a compelling alternative to thermal sources in the next generation inertial sensors based on atom interferometry. This thesis presents clear proof-of-principle interferometry experiments, as well as the development of the highest brightness atom lasers to date, and shot-noise limited atomic beamsplitters.

1.3 Publications

The following peer-reviewed publications have resulted from work within, as well as collaborative work undertaken during this thesis.

1. S. S. Szigeti, J. E. Debs, J. J. Hope, N. P. Robins, and J. D. Close. Why momentum width matters for atom interferometry with Bragg pulses. *New J. Phys.* **14**, 023009, 2012. http://stacks.iop.org/1367-2630/14/i=2/a=023009

2. J. E. Debs, P. A. Altin, T. H. Barter, D. Döring, G. R. Dennis, G. McDonald, R. P. Anderson, J. D. Close, and N. P. Robins. Cold-atom gravimetry with a Bose-Einstein condensate. *Phys. Rev. A* **84**, 033610, 2011. http://link.aps.org/doi/10.1103/PhysRevA.84.033610.

3. P. A. Altin, G. R. Dennis, G. D. McDonald, D. Döring, J. E. Debs, J. D. Close, C. M. Savage, and N. P. Robins. Collapse and three-body loss in a ^{85}Rb Bose-Einstein condensate. Phys. Rev. A **84**, 033632, 2011. http://link.aps.org/doi/10.1103/PhysRevA.84.033632

4. P. A. Altin, G. McDonald, D. Döring, J. E. Debs, T. H. Barter, J. D. Close, S. A. Haine, T. M. Hanna, R. P. Anderson, and N. P. Robins., Optically trapped atom interferometry using the clock transition of large ^{87}Rb Bose-Einstein condensates., *New J. Phys.* **13**, 065020 & 119401 (Addendum), 2011. http://stacks.iop.org/1367-2630/13/i=6/a=065020 & Addendum http://stacks.iop.org/1367-2630/13/i=11/a=119401.

5. J. E. Debs, D. Döring, P. A. Altin, C. Figl, J. Dugué, M. Jeppesen, J. T. Schultz, N. P. Robins, and J. D. Close. Experimental comparison of Raman and rf outcouplers for high-flux atom lasers. *Phys. Rev. A* **81**, 013618, 2010. http://dx.doi.org/10.1103/PhysRevA.81.013618

6. D. Döring, G. McDonald, J. E. Debs, C. Figl, P. A. Altin, H.-A. Bachor, N. P. Robins, and J. D. Close. Quantum-projection-noise-limited interferometry with coherent atoms in a Ramsey-type setup. *Phys. Rev. A* **81**, 043633, 2010. http://dx.doi.org/10.1103/PhysRevA.81.043633

7. P. A. Altin, N. P. Robins, D. Döring, J. E. Debs, R. Poldy, C. Figl, and J. D. Close. ^{85}Rb tunable-interaction Bose-Einstein condensate machine., *Rev. Sci. Instrum.* **81**, 063103, 2010. http://link.aip.org/link/?RSI/81/063103/1.

8. P. A. Altin, N. P. Robins, R. Poldy, J. E. Debs, D. Döring, C. Figl, and J. D. Close. Measurement of inelastic losses in a sample of ultracold ^{85}Rb. *Phys. Rev. A* **81**, 012713, 2010. http://dx.doi.org/10.1103/PhysRevA.81.012713

9. J. E. Debs, D. Döring, N. P. Robins, C. Figl, P. A. Altin, and J. D. Close. A two-state raman coupler for coherent atom optics. *Opt. Express* **17**, 2319, 2009. http://www.opticsexpress.org/abstract.cfm?URI=oe-17-4-2319.

10. D. Döring, J. E. Debs, N. P. Robins, C. Figl, P. A. Altin, and J. D. Close. Ramsey interferometry with an atom laser. *Opt. Express* **17**, 20661, 2009. http://www.opticsexpress.org/abstract.cfm?URI=oe-17-23-20661.

11. J. T. Schultz, S. Abend, D. Döring, J. E. Debs, P. A. Altin, J. D. White, N. P. Robins, and J. D. Close. Coherent 455 nm beam production in a cesium vapor. *Opt. Lett.* **34**, 2321, 2009. http://ol.osa.org/abstract.cfm?URI=ol-34-15-2321.

12. J. E. Debs, N. P. Robins, A. Lance, M. B. Kruger, and J. D. Close. Piezo-locking a diode laser with saturated absorption spectroscopy. *Appl. Opt.* **47**, 5163, 2008. http://ao.osa.org/abstract.cfm?URI=ao-47-28-5163.

1.4 Structure of this Thesis

The thesis is structured into three parts which generally follow on from one another. This is summarised by the flow diagram in figure 1.2.

Part I gives the necessary theoretical background on atom-light interactions and basic atom interferometer theory. A reader experienced in atom-light interactions and interferometry can safely skip part I, and simply use it as a reference. Part II covers our interferometric tools: atomic sources, beamsplitters, and mirrors, and Part III presents results from our BEC-based gravimeter, and discusses key advantages of Bose-condensed sources including an experimental comparison to a thermal source.

Chapter 2 describes a two-level atom in a classical light field. The treatment is slightly more comprehensive than common treatments, explicitly including the external motional states and highlighting the change in momentum of the atom due to absorption or emission of a photon; a crucial aspect of an atomic inertial sensor.

Chapter 3 then uses the two-level results to describe interferometry with two-level systems. In particular, Ramsey and Mach-Zehnder interferometers are discussed. The phase shift due to gravity is derived.

Chapter 4 describes the three-level atom, which allows for Raman (or multi-) photon transitions. These transitions are critical in enabling the coupling of long-

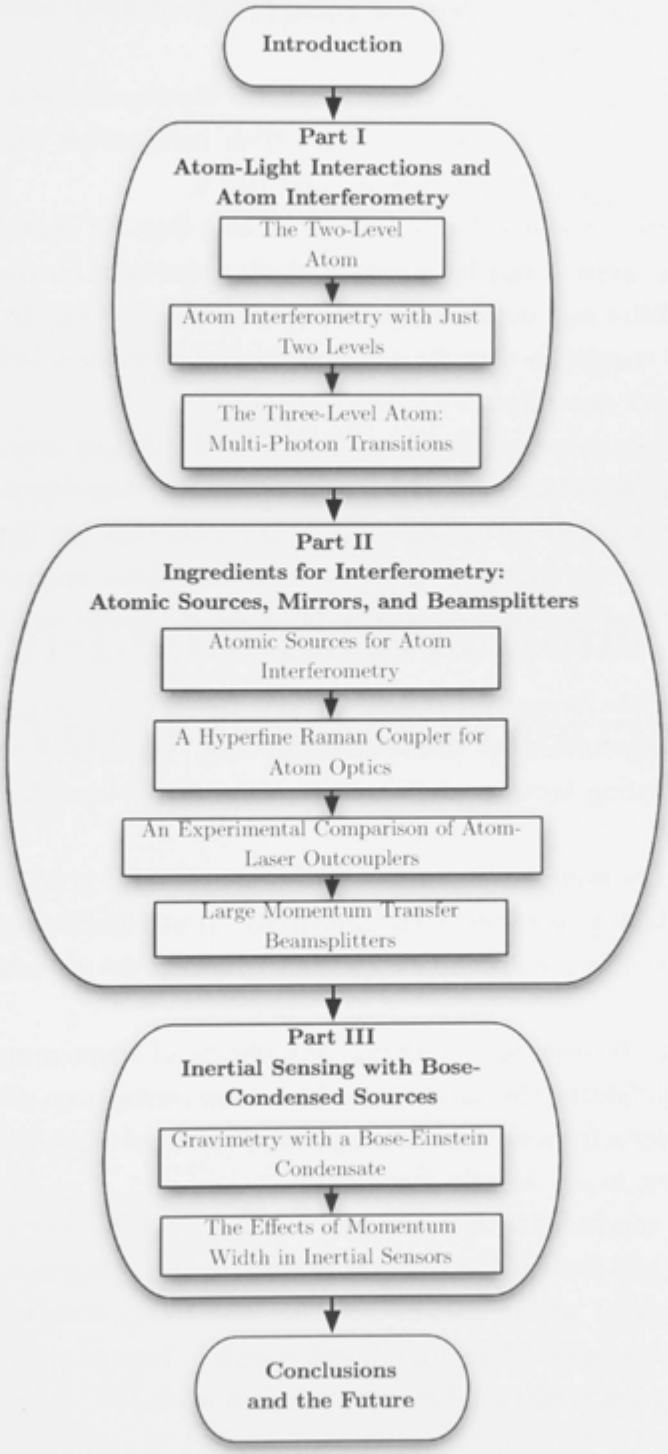

Figure 1.2: Thesis flow diagram.

lived states, and a significant momentum transfer, both of which are required for an inertially sensitive device.

Chapter 5 gives the theoretical background for Bose-condensed sources including atom-lasers, and in particular derives their momentum width. It also describes both of our apparatuses for producing BECs.

Chapter 6 describes a Raman laser-system for coupling the hyperfine ground states of ^{87}Rb. The system can be operated as an atom-laser outcoupler, or as an atomic beamsplitter and both configurations are characterised. In the case of beamsplitting, the coupler is used for a Ramsey interferometer which is able to reach the atomic shot-noise limit.

Chapter 7 presents a comprehensive comparison of different atom-laser outcouplers, including radio-frequency (RF) outcouplers for magnetically confined BECs and outcoupling from an optical trap. It is shown that our hyperfine Raman coupler produces the highest brightness atom-laser from magnetically confined samples, and that optical outcoupling produces a near Heisenberg-limited atom-laser beam.

Chapter 8 describes Bragg diffraction and our Bragg laser-system, which is used in our BEC gravimeter for LMT beamsplitting. Its noise characteristics are presented, including some recent improvements and proposals for further improvement.

Chapter 9 presents results from our proof-of-principle BEC gravimeter, which uses LMT beamsplitting to enhance the sensitivity. A straightforward model is used to estimate the effect of atomic interactions in such a device, which we find to be negligible.

Finally, chapter 10 discusses, in detail, the effects of momentum width in inertial sensors, highlighting the advantages of a narrow momentum width source. We also present results from an experimental comparison of a condensed source and a thermal source in our atomic gravimeter.

The thesis then concludes with a summary of the key results, and a discussion of future directions and possibilities. Also note that the thesis is generally written in the first-person plural '*we*' to keep in line with modern scientific writing style; highlighting the group-based nature of modern research. Except where explicitly stated otherwise, all material is the author's original work.

Part I

Atom-Light Interactions and Atom Interferometry

Chapter 2

The Two-Level Atom

The interaction of an ensemble of atoms with a laser beam lies at the heart of modern atomic physics and atom interferometry. Taking advantage of these interactions allows us to cool, heat, guide, trap, accelerate, probe, beamsplit, and reflect atoms. Fundamentally, atom-light interactions give us our deepest insight into atomic structure, resulting in a myriad of applications both within and external to atomic physics. In what follows, we provide a theoretical treatment of the interaction of monochromatic radiation with a two-level atom, which provides a foundation for describing many of the phenomena presented in this thesis.

2.1 A Two-Level Atom in a Classical Light Field

The two-level atom model is useful as it is often possible to approximate a multi-level atom as two-level for particular coupling configurations, and the simplest description of atom interferometry is that involving the interference of just two levels (see chapter 3). In chapter 7, we will discover that effective two-level atoms produce the highest flux atom lasers with clean beam profile, and finally when considering LMT beamsplitting in chapters 8 and 10, our goal will be to best reduce a multi-level system of momentum states to an effective two-level system.

Consider an atom in free space, with a centre-of-mass momentum $\mathbf{p}$,[1] and two electronic eigenstates. We label these states as $|e, \mathbf{p}_e\rangle$ and $|g, \mathbf{p}_g\rangle$ such that:[2]

$$\hat{H}_a|g, \mathbf{p}_g\rangle = \left(\frac{p_g^2}{2m} + \hbar\omega_g\right)|g, \mathbf{p}_g\rangle \tag{2.1}$$

and likewise for $|e, \mathbf{p}_e\rangle$, with eigenvalue $\frac{p_e^2}{2m} + \hbar\omega_e$. Choosing the zero of energy to be centred between ω_e and ω_g, we have $\omega_e = -\omega_g = \omega_0/2$. The internal energy

[1] $\mathbf{p}$ is assumed to be non-relativistic in all that follows.

[2] $|e, \mathbf{p}\rangle$ represents the direct product $|e\rangle \otimes |\mathbf{p}\rangle$, and likewise for $|g, \mathbf{p}\rangle$.

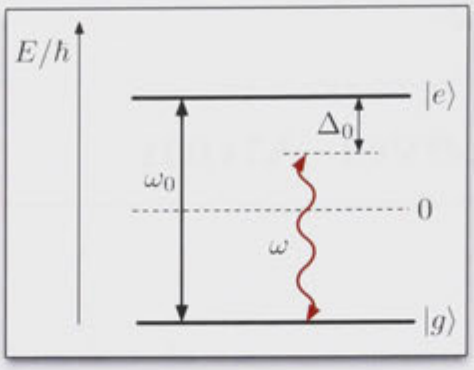

Figure 2.1: Electronic energy level diagram for a two-level atom.

level diagram of this atom is given in figure 2.1. The atomic Hamiltonian can be written as:

$$\hat{H}_a = \int_{-\infty}^{\infty} \left[\left(\frac{p^2}{2m} + \frac{\hbar\omega_0}{2} \right) |e,\mathbf{p}\rangle\langle e,\mathbf{p}| + \left(\frac{p^2}{2m} - \frac{\hbar\omega_0}{2} \right) |g,\mathbf{p}\rangle\langle g,\mathbf{p}| \right] \mathrm{d}^3\mathbf{p} \qquad (2.2)$$

Consider now the atom, with centre-of-mass position and momentum operators $\hat{\mathbf{r}}$ and $\hat{\mathbf{p}}$ respectively, interacting with a classical electromagnetic wave $\mathbf{E}(\mathbf{r}_L, t) = \mathbf{E}_0 \cos(\omega t - \mathbf{k}\cdot\mathbf{r}_L + \phi)$, where $\mathbf{E}_0$ is maximum field amplitude vector, $\mathbf{k}$ the wave vector, ω the angular frequency, and ϕ an arbitrary phase. Naturally, $[\hat{\mathbf{r}}, \hat{\mathbf{p}}] = i\hbar$. The electric field at the atom's position is then given by the operator $\mathbf{E}(\hat{\mathbf{r}}, t)$. Assuming an electric-dipole interaction, the Hamiltonian for this system is:

$$\begin{aligned}\hat{H} = \int_{-\infty}^{\infty} \Bigg[& \frac{p^2}{2m}(|e,\mathbf{p}\rangle\langle e,\mathbf{p}| + |g,\mathbf{p}\rangle\langle g,\mathbf{p}|) + \frac{\hbar\omega}{2}(|e,\mathbf{p}\rangle\langle e,\mathbf{p}| - |g,\mathbf{p}\rangle\langle g,\mathbf{p}|) \\ & + \frac{\hbar\Delta_0}{2}(|e,\mathbf{p}\rangle\langle e,\mathbf{p}| - |g,\mathbf{p}\rangle\langle g,\mathbf{p}|) \Bigg] \mathrm{d}^3\mathbf{p} + \hat{\mathbf{d}}\cdot\mathbf{E}(\hat{\mathbf{r}}, t)\end{aligned} \qquad (2.3)$$

where $\hat{\mathbf{d}} = e\hat{\mathbf{r}}_e$ is the electric-dipole moment operator[3] and $\Delta_0 = \omega_0 - \omega$, as shown in figure 2.1. We assume an atom with no permanent electric-dipole moment.[4]

[3]Here, e is the electronic charge, and should not be confused with the label in $|e,\mathbf{p}\rangle$. Furthermore, $\hat{\mathbf{r}}_e$ is the electron position operator, relative to the atomic nucleus and should not be confused with the centre-of-mass coordinate $\mathbf{r}$. The former acts on the space of $|e\rangle$, whereas the latter acts on the space of $|\mathbf{p}\rangle$.

[4]Although there are efforts to observe time reversal and parity symmetry violation through the measurement of a permanent electric-dipole moment (PEDM) in atoms such as ^{199}Hg [92, 93], these

This results in either even or odd parity electronic wavefunctions, and therefore, the diagonal matrix elements of the electric-dipole moment operator are zero. The dipole coupling term can therefore be written as:

$$\hat{\mathbf{d}} \cdot \mathbf{E}(\hat{\mathbf{r}}, t) = \int_{-\infty}^{\infty} \frac{\mathbf{d}_{eg} \cdot \mathbf{E}_0}{2} \left(e^{i(\omega t - \mathbf{k}\cdot\hat{\mathbf{r}} + \phi)} + c.c \right) \left(|e, \mathbf{p}\rangle\langle g, \mathbf{p}| + |g, \mathbf{p}\rangle\langle e, \mathbf{p}| \right) \mathrm{d}^3\mathbf{p}$$

$$= \int_{-\infty}^{\infty} \frac{\hbar\Omega}{2} \Big[e^{-i(\omega t + \phi)} (|e, \mathbf{p} + \hbar\mathbf{k}\rangle\langle g, \mathbf{p}| + |g, \mathbf{p} + \hbar\mathbf{k}\rangle\langle e, \mathbf{p}|) + e^{i(\omega t + \phi)} (|e, \mathbf{p} - \hbar\mathbf{k}\rangle\langle g, \mathbf{p}| + |g, \mathbf{p} - \hbar\mathbf{k}\rangle\langle e, \mathbf{p}|) \Big] \mathrm{d}^3\mathbf{p} \tag{2.4}$$

where in the last step, we recognise that $e^{i\mathbf{k}\cdot\hat{\mathbf{r}}}$ is the generator of translations in momentum space [94]. $\Omega = \frac{\mathbf{d}_{eg}\cdot\mathbf{E}_0}{\hbar}$ is defined as the Rabi frequency, with $\mathbf{d}_{eg} = \langle e|\hat{\mathbf{d}}|g\rangle$. We see that the electric-dipole interaction couples the electronic states $|e\rangle \leftrightarrow |g\rangle$, and momentum states $|\mathbf{p}\rangle \leftrightarrow |\mathbf{p} \pm \hbar\mathbf{k}\rangle$. It is perhaps obvious at this point that in coupling to a different momentum state, the resonance frequency will not be ω_0, but should also take into account the change in kinetic energy, suggesting that Δ_0 is an approximate detuning. This result will shortly be derived explicitly.

Consider now any general state of the system expanded in the electronic-momentum basis:

$$|\psi(t)\rangle = \int_{-\infty}^{\infty} c_e(\mathbf{p}, t)|e, \mathbf{p}\rangle + c_g(\mathbf{p}, t)|g, \mathbf{p}\rangle \, \mathrm{d}^3\mathbf{p} \tag{2.5}$$

with normalisation given by:

$$\int_{-\infty}^{\infty} |c_e(\mathbf{p}, t)|^2 + |c_g(\mathbf{p}, t)|^2 \, \mathrm{d}^3\mathbf{p} = 1 \tag{2.6}$$

Thus we can interpret $|c_g(\mathbf{p}, t)|^2$ and $|c_e(\mathbf{p}, t)|^2$ as the probability of finding an atom in the ground or excited state at momentum $\mathbf{p}$ and time t respectively.

efforts provide only an upper bound on the PEDM and the majority of elements are not known to possess an PEDM. Furthermore, the alkalis, which are the most common elements in cold-atom physics, have a single valence electron in a spherically symmetric s-state and therefore have no PEDM.

Our goal now is to solve the Schrödinger equation, $i\hbar\frac{d|\psi\rangle}{dt} = \hat{H}|\psi\rangle$, and obtain the amplitudes $c_g(\mathbf{p},t)$ and $c_e(\mathbf{p},t)$. In its current form, the Hamiltonian contains 'fast' terms evolving at $\omega \simeq \omega_0$ – typically a microwave or optical frequency for transitions between angular momentum states. It is convenient to make the unitary transformation $|\psi(t)\rangle \rightarrow e^{-i\hat{H}_0 t/\hbar}|\psi(t)\rangle_I$, with $\hat{H} = \hat{H}_0 + \hat{V}$, and $\hat{H}_0$ appropriately chosen to simplify the calculation by removing these fast terms.[5] Substituting this into the Schrödinger equation gives:

$$\begin{aligned} i\hbar\frac{d|\psi\rangle_I}{dt} &= e^{i\hat{H}_0 t/\hbar}\hat{V}e^{-i\hat{H}_0 t/\hbar}|\psi\rangle_I \\ &= \hat{V}_I|\psi\rangle_I \end{aligned} \tag{2.7}$$

Consider the choice:

$$\hat{H}_0 = \int_{-\infty}^{\infty} \frac{\hbar\omega}{2}(|e,\mathbf{p}\rangle\langle e,\mathbf{p}| - |g,\mathbf{p}\rangle\langle g,\mathbf{p}|)\,\mathrm{d}^3\mathbf{p} \tag{2.8}$$

Using this in the definition of $\hat{V}_I$, it is obvious that diagonal terms of $\hat{V}$ equal those of $\hat{V}_I$. However, the off-diagonal terms, as given by equation (2.4), do not. Consider just the *first exponential term* in (2.4):

$$\begin{aligned} &\int_{-\infty}^{\infty} e^{-i(\omega t+\phi)}e^{i\hat{H}_0 t/\hbar}(|e,\mathbf{p}+\hbar\mathbf{k}\rangle\langle g,\mathbf{p}| + |g,\mathbf{p}+\hbar\mathbf{k}\rangle\langle e,\mathbf{p}|)e^{-i\hat{H}_0 t/\hbar}\,\mathrm{d}^3\mathbf{p} \\ &= \int_{-\infty}^{\infty} \left(e^{-i\phi}|e,\mathbf{p}+\hbar\mathbf{k}\rangle\langle g,\mathbf{p}| + e^{i(\phi-2\omega t)}|g,\mathbf{p}+\hbar\mathbf{k}\rangle\langle e,\mathbf{p}|\right)\,\mathrm{d}^3\mathbf{p} \end{aligned} \tag{2.9}$$

Notice that although this eliminates the ω dependence in the first part of this term, the second part now has a 2ω dependence. We assume $\omega_0 - \omega \ll \omega_0 + \omega$, allowing us to neglect this term; it oscillates rapidly compared with the first term (and other terms in $\hat{V}_I$) and will average to zero when integrating the Schrödinger equation over a timescale associated with $\omega_0 - \omega$. This approximation is known as the "rotating-wave approximation" [95]. Using the rotating-wave approximation

[5] Unitary transformations preserve the norm of the state, and thus all probabilities. This particular transformation is often called the "Interaction Picture," whereas using the full Hamiltonian of equation (2.3) is called the "Schrödinger Picture."

on the *second exponential term* of equation (2.4) as well gives $\hat{V}_I$ as:

$$\hat{V}_I = \int_{-\infty}^{\infty} \Big[\frac{p'^2}{2m}(|e,\mathbf{p}'\rangle\langle e,\mathbf{p}'| + |g,\mathbf{p}'\rangle\langle g,\mathbf{p}'|) + \frac{\hbar\Delta_0}{2}(|e,\mathbf{p}'\rangle\langle e,\mathbf{p}'| - |g,\mathbf{p}'\rangle\langle g,\mathbf{p}'|) + \frac{\hbar\Omega}{2}\left(e^{-i\phi}|e,\mathbf{p}'+\hbar\mathbf{k}\rangle\langle g,\mathbf{p}'| + e^{i\phi}|g,\mathbf{p}'-\hbar\mathbf{k}\rangle\langle e,\mathbf{p}'|\right)\Big] \mathrm{d}^3\mathbf{p}' \tag{2.10}$$

where we have primed $\mathbf{p}$ to highlight it is only an integration variable. Inserting this into the Schrödinger equation (2.7), and projecting onto the state $|g,\mathbf{p}\rangle$ gives the equations of motion for the coefficient $c_g(\mathbf{p},t)$:

$$i\hbar\,\dot{c}_g(\mathbf{p},t) = \left(\frac{p^2}{2m} - \frac{\hbar\Delta_0}{2}\right) c_g(\mathbf{p},t) + \frac{\hbar\Omega}{2} c_e(\mathbf{p}+\hbar\mathbf{k},t)e^{i\phi} \tag{2.11}$$

As suggested by the Hamiltonian, at a given momentum eigenstate, the ground state couples to just a single momentum in the excited state. Thus, although the system contains an infinite number of momentum states, we see that every pair of states $|g,\mathbf{p}\rangle$ and $|e,\mathbf{p}+\hbar\mathbf{k}\rangle$ correspond to a two-level system. We therefore project equation (2.10) onto the state $|e,\mathbf{p}+\hbar\mathbf{k}\rangle$, giving the equation of motion for the coefficient $c_e(\mathbf{p}+\hbar\mathbf{k},t)$, and the second in a pair of coupled ordinary differential equations (ODEs) at each momentum $\mathbf{p}$:

$$i\hbar\,\dot{c}_e(\mathbf{p}+\hbar\mathbf{k},t) = \left(\frac{|\mathbf{p}+\hbar\mathbf{k}|^2}{2m} + \frac{\hbar\Delta_0}{2}\right) c_e(\mathbf{p}+\hbar\mathbf{k},t) + \frac{\hbar\Omega}{2} c_g(\mathbf{p},t)e^{-i\phi} \tag{2.12}$$

The equations of motion now closely resemble a more common treatment of the two-level atom that neglects the atomic momenta (see for example [96]). Although inclusion of the atomic momentum in the problem initially resulted in an infinite-dimensional space for determining $|\psi(t)\rangle$, this shows that the problem reduces to the more common treatment with just two levels, where we couple $c_g(\mathbf{p},t) \leftrightarrow c_e(\mathbf{p}+\hbar\mathbf{k},t)$. In other words, we need only solve these two coupled differential equations in order to construct the full state given any initial momentum distribution.

We proceed by defining:

$$\Delta(\mathbf{p}) = \Delta_0 + \frac{\mathbf{p}\cdot\mathbf{k}}{m} + \omega_r \tag{2.13}$$

where $\hbar\omega_r = \hbar^2k^2/2m$ is the kinetic energy of a single photon's momentum,

and ω_r is called the single-photon recoil frequency. Rearranging for Δ_0 and substituting this into equations (2.11) and (2.12) gives:

$$i\hbar\dot{c}_g(\mathbf{p},t) = \left(\frac{|\mathbf{p}+\frac{\hbar\mathbf{k}}{2}|^2}{2m} - \frac{\hbar\Delta(\mathbf{p})}{2}\right)c_g(\mathbf{p},t) + \frac{\hbar\Omega}{2}c_e(\mathbf{p}+\hbar\mathbf{k},t)e^{i\phi} \quad (2.14)$$

$$i\hbar\dot{c}_e(\mathbf{p}+\hbar\mathbf{k},t) = \left(\frac{|\mathbf{p}+\frac{\hbar\mathbf{k}}{2}|^2}{2m} + \frac{\hbar\Delta(\mathbf{p})}{2}\right)c_e(\mathbf{p},t) + \frac{\hbar\Omega}{2}c_g(\mathbf{p},t)e^{-i\phi} \quad (2.15)$$

The very first term in both equations is a constant energy offset, and can be removed with the unitary transformations $c_{e,g}(t) \rightarrow c_{e,g}(t)\exp\left[-i\left(\frac{|\mathbf{p}+\frac{\hbar\mathbf{k}}{2}|^2}{2m\hbar}\right)t\right]$.

To simplify the notation, we define $c_1(t) \equiv c_e(\mathbf{p}+\hbar\mathbf{k},t)$ and $c_2(t) \equiv c_g(\mathbf{p},t)$, and arrive at the compact form for the equations of motion:

$$\begin{pmatrix}\dot{c}_1(t)\\ \dot{c}_2(t)\end{pmatrix} = -\frac{i}{2}\begin{pmatrix}\Delta(\mathbf{p}) & \Omega e^{-i\phi}\\ \Omega e^{i\phi} & -\Delta(\mathbf{p})\end{pmatrix}\begin{pmatrix}c_1(t)\\ c_2(t)\end{pmatrix} \quad (2.16)$$

Notice that $\Delta(\mathbf{p})$ plays the same role as detuning in a treatment that neglects momentum. That is, the detuning from resonance is now momentum dependent, as was suggested following equation (2.4). Notice that $\Delta(\mathbf{p})-\Delta_0 = \frac{\mathbf{p}\cdot\mathbf{k}}{m}+\omega_r$, which is the sum of the Doppler shift and the recoil frequency. This agrees with our intuition that the resonant frequency should take into account the kinetic energy gained due to the photon's momentum. A corrected energy level diagram is given in figure 2.2, showing the momentum dependent detuning. Setting $\Delta(\mathbf{p}) = 0$ gives the resonant optical frequency $\omega_{res} = \omega_0 + \frac{\mathbf{p}\cdot\mathbf{k}}{m} + \omega_r$. Thus for an atom at rest, the resonant frequency is the sum of atomic level splitting ω_0, plus the recoil frequency. This is an often neglected feature of the two-level atom problem, and the derivation given here is suitable for treating ensembles of atoms with a range of momenta and therefore a spread of detunings. It also demonstrates the momentum change due to absorption (or emission) of a photon, a property that is crucial for atom optics, and atom interferometry.

In what follows, we suppress the the argument of Δ unless it is necessary for clarity. Solving the characteristic polynomial of the matrix in equation (2.16) gives the eigenvalues $\lambda_\pm = \pm\tilde{\Omega}$, where $\tilde{\Omega} = \sqrt{\Omega^2+\Delta^2}/2$ is the generalised Rabi

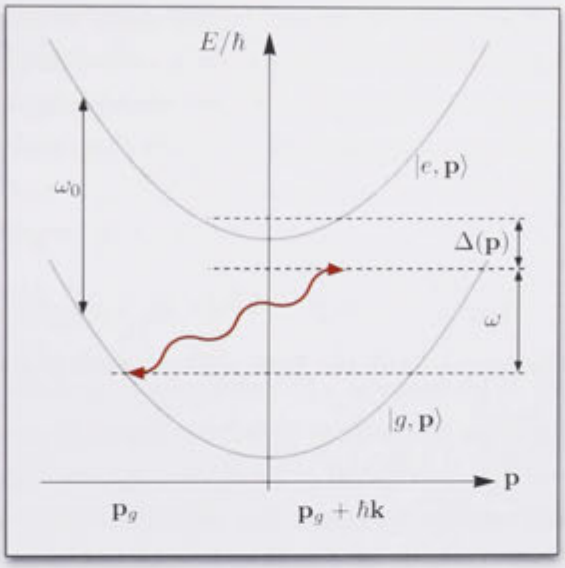

Figure 2.2: Energy level diagram, incorporating the centre-of-mass momentum and kinetic energy of the two-level atom. The detuning from resonance now takes into account the change in momentum during the absorption of a photon, and is therefore momentum dependent.

frequency. The corresponding eigenvectors are:

$$\begin{aligned} |\lambda_+\rangle &= \cos(\theta)|e, \mathbf{p} + \hbar\mathbf{k}\rangle + \sin(\theta)e^{i\phi}|g, \mathbf{p}\rangle \\ |\lambda_-\rangle &= -\sin(\theta)|e, \mathbf{p} + \hbar\mathbf{k}\rangle + \cos(\theta)e^{i\phi}|g, \mathbf{p}\rangle \end{aligned} \tag{2.17}$$

with

$$\begin{aligned} \cos(2\theta) &= \frac{\Delta}{\tilde{\Omega}} \\ \sin(2\theta) &= \frac{\Omega}{\tilde{\Omega}} \end{aligned}$$

These eigenstates are sometimes called 'dressed' atomic states (in contrast to 'bare'), and will be of critical importance when we discuss atom laser outcouplers in chapter 7 [95]. The dressed states have energies given by:

$$\hbar\lambda_\pm = \pm\hbar\frac{\sqrt{\Omega^2 + \Delta^2}}{2}. \tag{2.18}$$

Notice that on resonance, the energy is simply $\pm\hbar\Omega/2$, and increases as the detuning increases. In the absence of coupling ($\Omega = 0$), the atomic state energies are separated by $|\Delta|$ in the rotating frame, and are equal to the dressed state

energies. Thus $\hbar\lambda_\pm$ represents a shift in the energy eigenstates for the coupled system. This shift is known as the "AC Stark shift", also called the light shift. It is often most important when $|\Delta| \gg \Omega$, such that absorption is negligible – for example in the context of optical-dipole traps [97]. In this case, we can expand $\lambda_\pm$ to first order in Ω^2/Δ^2 giving:

$$\lambda_\pm \simeq \pm\left(\frac{\Delta}{2} + \frac{\Omega^2}{4\Delta}\right) \tag{2.19}$$

Therefore, in the large detuning limit the light shift on each of the atomic states is:

$$\pm\,\hbar\omega_{LS} = \pm\hbar\frac{\Omega^2}{4\Delta} \tag{2.20}$$

Using the eigenstates, we now construct the unitary matrix:

$$\hat{U} = \begin{pmatrix} \cos(\theta) & -\sin(\theta) \\ \sin(\theta)e^{i\phi} & \cos(\theta)e^{i\phi} \end{pmatrix} \tag{2.21}$$

which rotates the bare basis onto the eigenbasis (and back) using $|\lambda_j\rangle = \hat{U}|j, \mathbf{p}_j\rangle$, where j indexes the two dimensions of the 2×2 system [94]. Of course in the eigenbasis, the Schrödinger equation is diagonal:

$$\begin{pmatrix} \dot{c}_+(t) \\ \dot{c}_-(t) \end{pmatrix} = -\frac{i}{2}\begin{pmatrix} \tilde{\Omega} & 0 \\ 0 & -\tilde{\Omega} \end{pmatrix}\begin{pmatrix} c_+(t) \\ c_-(t) \end{pmatrix} \tag{2.22}$$

where $c_\pm(t) = \langle\lambda_\pm|\psi\rangle$. We assume the initial condition:

$$\begin{pmatrix} c_e(\mathbf{p}+\hbar\mathbf{k}, 0) \\ c_g(\mathbf{p}, 0) \end{pmatrix} = \begin{pmatrix} 0 \\ \psi(\mathbf{p}) \end{pmatrix} \tag{2.23}$$

where $|\psi(\mathbf{p})|^2$ is the initial momentum distribution of the state. Using this initial condition, the solutions for $c_\pm$ are:

$$\begin{pmatrix} c_+(t) \\ c_-(t) \end{pmatrix} = \begin{pmatrix} \psi(\mathbf{p})\sin(\theta)e^{-i\phi}e^{-i\frac{\tilde{\Omega}}{2}t} \\ \psi(\mathbf{p})\cos(\theta)e^{-i\phi}e^{i\frac{\tilde{\Omega}}{2}t} \end{pmatrix} \tag{2.24}$$

Transforming back to the bare basis using $\hat{U}$ gives the solutions for c_e and c_g:

$$\begin{pmatrix} c_e(\mathbf{p}+\hbar\mathbf{k}, t) \\ c_g(\mathbf{p}, t) \end{pmatrix} = \begin{pmatrix} -i\psi(\mathbf{p})\frac{\Omega}{\tilde{\Omega}}e^{-i\phi}\sin\left(\frac{\tilde{\Omega}}{2}t\right) \\ \psi(\mathbf{p})\left[\cos\left(\frac{\tilde{\Omega}}{2}t\right) + i\frac{\Delta}{\tilde{\Omega}}\sin\left(\frac{\tilde{\Omega}}{2}t\right)\right] \end{pmatrix} \tag{2.25}$$

Thus we have solved the Schrödinger equation for a two-level atom initially in the ground state and with an a momentum-space wavefunction $\psi(\mathbf{p})$. Notice that the excited state amplitude gains an additional phase of ϕ relative to the ground state. In other words, the laser phase is added onto the atomic phase. Although this phase is arbitrary at this point, it will be crucial when we consider atom interferometry in chapter 3. Consider now:

$$|c_e(\mathbf{p}+\hbar\mathbf{k},t)|^2 + |c_g(\mathbf{p},t)|^2 = |\psi(\mathbf{p})|^2 \tag{2.26}$$

which is time independent. This defines the normalisation for the two-level system, and furthermore, demonstrates that probability is distributed between the momentum states $|\mathbf{p}\rangle$ and $|\mathbf{p}+\hbar\mathbf{k}\rangle$ and is conserved. Often when dealing with the mean-field description of a BEC (see chapter 5), the normalisation as given in equation (2.6) is instead normalised to N, where N is the number of atoms in the condensate. Equation (2.26) then states that the fraction of atoms distributed between $\mathbf{p}$ and $\mathbf{p}+\hbar\mathbf{k}$ is conserved.

The *time-dependent* probabilities for the excited and ground state are:

$$P_e(t) = \frac{|c_e(\mathbf{p}+\hbar\mathbf{k},t)|^2}{|\psi(\mathbf{p})|^2} = \frac{\Omega^2}{\Omega^2+\Delta^2}\sin^2\left(\frac{\sqrt{\Omega^2+\Delta^2}}{2}t\right) \tag{2.27}$$

$$P_g(t) = \frac{|c_g(\mathbf{p},t)|^2}{|\psi(\mathbf{p})|^2} = \left[1 - \frac{\Omega^2}{\Omega^2+\Delta^2}\sin^2\left(\frac{\sqrt{\Omega^2+\Delta^2}}{2}t\right)\right] \tag{2.28}$$

respectively, which are identical in form to those commonly derived (again, see [96]), with the exception that Δ is momentum dependent. In this case, the system oscillates from $|\psi(\mathbf{p})|^2$ atoms in the ground state at momentum $\mathbf{p}$, to $|\psi(\mathbf{p})|^2$ atoms in the excited state at momentum $\mathbf{p}+\hbar\mathbf{k}$. These oscillations occur at the generalised Rabi frequency, $\tilde{\Omega}$ (which is also momentum dependent), and are named Rabi oscillations after Isidor Issac Rabi who received the 1944 Nobel Prize for first describing and measuring them with nuclear magnetic resonances in 1938 [98].

Figure 2.3 shows two examples of Rabi oscillations, plotting the probability for the excited and ground state as a function of $\tilde{\Omega}t$. One case assumes on resonant coupling at $\mathbf{p}$ (solid lines), and the other off-resonant (dashed lines). It is important to note that this off-resonant coupling can occur either at the same momentum $\mathbf{p}$, with a different electric field drive frequency ω', or at a

different momentum $\mathbf{p}'$, with the same drive frequency ω. When off resonantly coupled, the system oscillates at a higher frequency with a decreased amplitude. Considering the envelope function of P_e (or P_g), we see that when $\Delta = \pm\Omega$,

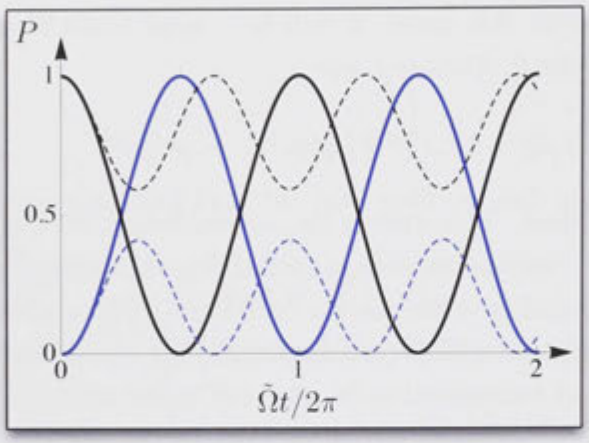

Figure 2.3: Rabi oscillations in a two-level system. Probability is plotted on the vertical axis, as a function of $\tilde{\Omega}t$ on the horizontal axis. Blue represents the ground state, and black the excited state. The solid curves represent coupling on resonance, i.e. $\Delta(\mathbf{p}) = 0$. Dashed curves represent off-resonant coupling with $\Delta(\mathbf{p}) = 1.2\Omega$.

$P_e = P_g = \frac{1}{2}$. Thus 2Ω defines the full-width-half-maximum (FWHM) for the resonance, assuming no spontaneous decay of the excited state. Thus, provided $\Delta \ll \Omega$, one can achieve probabilities close to 1, even off resonance – an important result when attempting to couple an entire cloud of atoms with some momentum distribution.

We conclude by constructing the general solution defined in (2.5) for our initial condition (2.23):

$$|\psi(t)\rangle = \int_{-\infty}^{\infty} -i\psi(\mathbf{p})\frac{\Omega}{\tilde{\Omega}}e^{-i\phi}\sin\left(\frac{\tilde{\Omega}}{2}t\right)|e, \mathbf{p}+\hbar\mathbf{k}\rangle + \psi(\mathbf{p})\left[\cos\left(\frac{\tilde{\Omega}}{2}t\right) + i\frac{\Delta}{\tilde{\Omega}}\sin\left(\frac{\tilde{\Omega}}{2}t\right)\right]|g, \mathbf{p}\rangle\, \mathrm{d}^3\mathbf{p} \tag{2.29}$$

$$= \int_{-\infty}^{\infty} \psi(\mathbf{p})\left(-ie^{-i\phi}\sqrt{P_e(t)}|e, \mathbf{p}+\hbar\mathbf{k}\rangle + \sqrt{P_g(t)}|g, \mathbf{p}\rangle\right)\mathrm{d}^3\mathbf{p} \tag{2.30}$$

Consider the term in the parentheses, which is weighted by the momentum space wavefunction. This has the form of the common two-level atom solution,

with the modification that the two states of the system not only represent electronic states of the atom, but also associate an external-momentum eigenstate with each electronic state. Having derived these results rigorously, and with the knowledge that absorption leads to a change in momentum by $\hbar\mathbf{k}$, an alternative and equivalent approach to the problem becomes clear for atoms in free space. We may first solve the strictly two-level system, accounting for the photon's momentum and an appropriate detuning, and then weight these solutions according to the momentum space wavefunction before integrating over all momenta to obtain the full solution. The probability of finding N_e atoms in the excited state at time t is then $N_e(t) = \int_{-\infty}^{\infty} |\psi(\mathbf{p})|^2 P_e(t)\,\mathrm{d}^3\mathbf{p}$, and similarly for N_g. This approach to including a momentum distribution will be used in chapter 10, when investigating the effects of a momentum width on the Bragg diffraction of a cloud of atoms.

Finally, it should be noted that this treatment neglects any irreversible processes such as spontaneous emission. Spontaneous emission can be derived from first principles with a quantisation of the electric field; see for example [99]. In this case, it arises from a coupling of the atomic states to the infinite number vacuum modes of the electric field, which gives a lifetime to the excited state of $1/\Gamma$, where Γ is the spontaneous emission rate or equivalently the natural linewidth. Thus coherent evolution only occurs over timescales much shorter than the excited state lifetime; i.e for $\Omega \gg \Gamma$, the solutions we have just derived provide an accurate description of the system.

As an example, the D_2 line of ^{87}Rb has $\Gamma \simeq 2\pi \times 6\,\mathrm{MHz}$ [100], and therefore coherent evolution only occurs over nanosecond timescales where $\Omega \gg \Gamma$. Because the inertial phase shift in an interferometer increases with the free evolution time T, such a transition is not particularly suitable for interferometry. On the other hand, for the transition between the the $F = 1$ and $F = 2$ hyperfine ground states of ^{87}Rb, the spontaneous emission rate from the "excited" $F = 2$ state is 16 orders of magnitude smaller due to a much weaker magnetic-dipole interaction and a smaller resonance frequency of $\sim 6.8\,\mathrm{GHz}$ (see appendix C in [96]). This is in fact why the $F = 2$ state is also called a ground state. Spontaneous emission is effectively completely negligible and very long coherent evolution can in principle be observed. As a result, the hyperfine ground states, which are common to all the alkali elements, have a very narrow linewidth making them ideal candidates for an atomic clock. Indeed, the second is currently defined through use of a transition between hyperfine ground states in ^{133}Cs [3].

The drawback to a microwave transition is that the momentum imparted in the absorption of a photon is negligible compared with that of an optical transition – around five orders of magnitude less, drastically reducing the inertial sensitivity. So although hyperfine transitions have long coherence times, they lack the necessary momentum transfer to result in high sensitivity inertial sensors. In chapter 4, we will see how the use of a two-photon (optical) coupling allows us to have sufficient momentum transfer, as well as long coherence times.

Chapter 3

Atom Interferometry with just Two Levels

We now discuss the application of atom-light interactions to atom interferometry. We will see that particular configurations of laser pulses enable us to build atom interferometers which are sensitive to the laser detuning, or the acceleration of the laser relative to the freely evolving atomic frame. In what follows, we assume a two-level system, which can represent any effective two-level atom (or system in general). In addition, we label the two coupled states as $|1\rangle$ and $|2\rangle$, with an implicit momentum label and momentum transfer. Likewise, any detuning term has an implicit momentum dependence.

3.1 Mirrors and Beam Splitters

An alternative method for describing the time evolution of a two-level system is with the unitary operator $\hat{U}(t)$:

$$|\psi(t)\rangle = \hat{U}(t)|\psi(0)\rangle \tag{3.1}$$

Using the two-level atom solutions from the last chapter, we may write $\hat{U}(t)$ in the $|1\rangle, |2\rangle$ basis:

$$\hat{U}(t) = \begin{pmatrix} \left[\cos\left(\frac{\tilde{\Omega}}{2}t\right) - i\frac{\Delta}{\tilde{\Omega}}\sin\left(\frac{\tilde{\Omega}}{2}t\right)\right] & -i\frac{\Omega}{\tilde{\Omega}}e^{-i\phi}\sin\left(\frac{\tilde{\Omega}}{2}t\right) \\ -i\frac{\Omega}{\tilde{\Omega}}e^{i\phi}\sin\left(\frac{\tilde{\Omega}}{2}t\right) & \left[\cos\left(\frac{\tilde{\Omega}}{2}t\right) + i\frac{\Delta}{\tilde{\Omega}}\sin\left(\frac{\tilde{\Omega}}{2}t\right)\right] \end{pmatrix} \tag{3.2}$$

Consider the two on-resonance cases $\Omega t_\pi = \pi$ and $\Omega t_{\pi/2} = \pi/2$. Assuming $|\psi(0)\rangle = |1\rangle$ this leads to:

$$\hat{U}(t_\pi)|1\rangle = -ie^{-i\phi}|2\rangle \tag{3.3}$$

$$\hat{U}(t_{\pi/2})|1\rangle = \frac{1}{\sqrt{2}}\left(|1\rangle - ie^{-i\phi}|2\rangle\right) \tag{3.4}$$

For t_π, called a π-pulse, there is a 100% transfer of population into state $|2\rangle$, and for $t_{\pi/2}$, called a $\pi/2$-pulse, there is a 50/50 superposition of states $|1\rangle$ and $|2\rangle$. Thus π-pulses and $\pi/2$-pulses represent atom optic mirrors and (50/50) beam-splitters respectively, in direct analogy with optics. By combining several of these pulses, one can build an atom interferometer in the same way mirrors and beam-splitters can be used to do so in optics. In the next sections, we investigate two important pulse sequences: the Ramsey pulse sequence, and the Mach-Zehnder pulse sequence.

3.2 The Ramsey Atom Interferometer

In 1949, Norman F. Ramsey developed a new method of spectroscopy, now known as the "Ramsey Method of Separated Oscillatory Fields" [101, 102]. This technique had a large role in the development of atomic clocks, and won him the Nobel Prize in 1989 [103]. In general, the Ramsey method involves applying two coupling pulses of radiation, separated in time. In between these pulses, the atomic state evolves coherently and freely. This results in a spectral resolution determined by the free evolution time rather than the pulse time of a single interaction.[1]

Consider applying two $\pi/2$-pulses separated by a time T, and with a finite detuning. Our $\pi/2$-pulse is defined by $\Omega\tau = \pi/2$. Each segment of this pulse sequence can be represented by the appropriate unitary operation. $U(\tau)$ is used for the interaction pulses, as defined in equation (3.2). For the free evolution, we have the simple matrix:[2]

$$\hat{U}_f(t) = \begin{pmatrix} e^{i\frac{\Delta}{2}t} & 0 \\ 0 & e^{-i\frac{\Delta}{2}t} \end{pmatrix} \tag{3.5}$$

Again assuming the atoms are initially in state $|1\rangle$, we determine the final state

[1] This would be the case in a Fourier limited system.

[2] Derived from the Schrödinger equation with $\Omega = 0$.

of the system by taking matrix products of each unitary operation:

$$|\psi(2\tau + T)\rangle = \hat{U}(\tau)\hat{U}_f(T)\hat{U}(\tau)|1\rangle \tag{3.6}$$

The result gives the probability for state $|2\rangle$, $P_2 = |c_2(2\tau + T)|^2$ as:

$$P_2 = \frac{\Omega^2}{2\tilde{\Omega}^4}\sin^2\left(\frac{\tilde{\Omega}\tau}{2}\right)\Big[2\Delta^2 + 2\tilde{\Omega}^2 + 2\Omega^2\left(\cos(\tilde{\Omega}\tau) + \cos(T\Delta + \Phi)\right) + (\tilde{\Omega} + \Delta)^2\cos(T\Delta + \Phi - \tilde{\Omega}\tau) + (\tilde{\Omega} - \Delta)^2\cos(T\Delta + \Phi + \tilde{\Omega}\tau)\Big] \tag{3.7}$$

where $\Phi = \phi_2 - \phi_1$ represents an overall phase difference between the driving field at the second and first $\pi/2$-pulses.[3] Notice that all but one cosine term contain the product $T\Delta$. Thus, in varying either the time between pulses or the detuning, the probability oscillates. These oscillations represent interference fringes know as Ramsey fringes, typically scanned via the detuning. These are plotted in figure 3.1 as a function of Δ for $\Omega = 12$ and $T = 1$ in arbitrary units. For $|\Delta| \ll \Omega$, the fringe period in Δ will be $\sim 2\pi/T$ as $\tilde{\Omega} \simeq \Omega$ in the cosine terms. In fact, it can be shown that:

$$P_2 \simeq \frac{1}{2}\left[1 + \cos\left(\Delta T + \Phi\right)\right] \text{ if } |\Delta| \ll \Omega \tag{3.8}$$

This is highlighted by the inset of figure 3.1, which shows just the central fringes. The period is ~ 1, and the fringe amplitude stays close to 1. Note that even with $\Omega = 12$ and $|\Delta| < 3$, which is not a particularly strong example of the limit, equation (3.8) still well approximates the fringes. Typical experimental numbers have Ω on the order of tens of kHz, and T on the order of 1 s. Thus Δ need only cover a range of a few Hz in order to scan several fringes, a range much less than Ω.

The scaling of the fringe period with $1/T$ has allowed unprecedented precision in spectroscopy. For example, with $T \sim 1$ s the central Ramsey fringe is less than one Hz wide, and mHz resolution of the resonant frequency is possible, giving a highly precise reference for locking the driving field frequency. It is this feature of Ramsey interferometry that aided development of ultra-precise atomic clocks

[3] Often this is zero in principle, although it can be used to scan fringes. It also importantly highlights a sensitivity to any phase noise of the driving field(s).

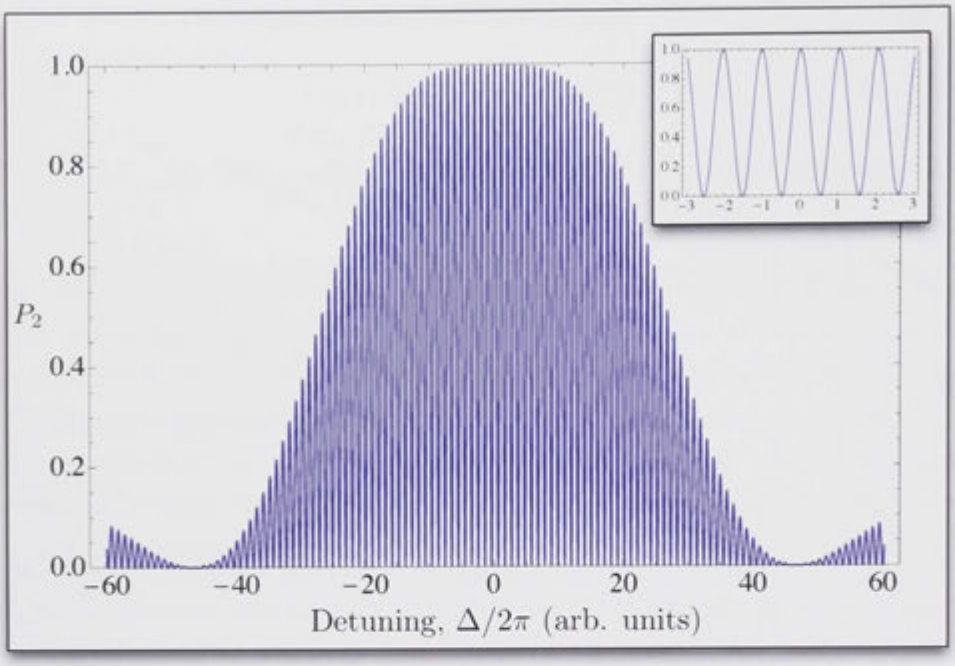

Figure 3.1: Ramsey fringes as a function of detuning for $\Omega = 12$ and $T = 1$ (arb. units). The inset shows the central fringes over the range $|\Delta| < 3$, and is well approximated by $P_2 = \frac{1}{2}[1 + \cos(\Delta T + \Phi)]$.

in the microwave domain, and inevitably the redefinition of the Second in terms of a Caesium hyperfine transition.

Finally, it is worth noting that the Ramsey method was initially developed as a spectroscopic technique for the measurement of nuclear magnetic moments. It evolved into a general spectroscopic technique, and can be understood as an interferometer in the sense that two phases are compared – the phase evolution of the atomic state, compared to the phase evolution of the driving field. In optics, this is analogous to a common-path polarisation interferometer, which can measure, for example, a birefringence (which delays the phase of one polarisation with respect to an orthogonal polarisation). Another similarity is to Young's double slit experiment, which compares the phase of two waves originating from two separated slits, at a screen some distance away. In this case, the slit separation is analogous to T, the slit width analogous to τ, and position on the screen[4] analogous to detuning. The fringes in figure 3.1 have a similar shape to the resultant interference pattern in optics, and in the perturbative limit, the equation describing Ramsey fringes is identical in form to that for the interference pattern

[4]I.e. the difference in the propagation distance from the two slits.

of the double slit experiment (see [96] for the perturbative calculation).

3.3 The Mach-Zehnder Atom Interferometer

The Mach-Zehnder interferometer in optics has the configuration given in figure 3.2. An input laser beam (red) propagating in mode $|1\rangle$ is split by a 50/50 beamsplitter into modes $|1\rangle$ and $|2\rangle$. These are then reflected by two mirrors before being recombined and interfered at a second beamsplitter. Scanning a relative phase shift between each arm ϕ (the wedge in the upper arm), results in interference fringes at both output ports in the number of detected photons, N_1 and N_2. Any additional phase shift can be measured as a shift in these fringes.

The mathematical description of beamsplitters and mirrors in optics is identical to that for two-level atoms as discussed in section 3.1. We may therefore construct an analogous Mach-Zehnder atom interferometer by utilising a three-pulse sequence in the order $\pi/2 - \pi - \pi/2$, where each pulse is separated by a time T. The two $\pi/2$-pulses are equivalent to the beamsplitters in figure 3.2, and the

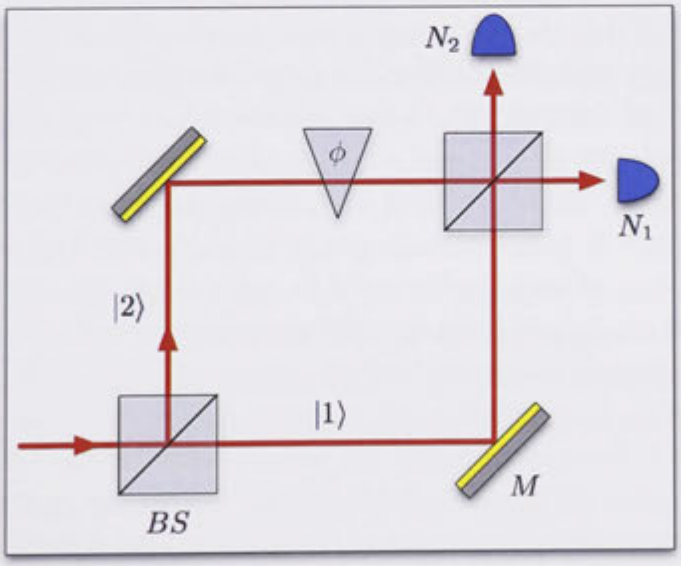

Figure 3.2: Mach-Zehnder optical interferometer. Two beamsplitters (BS) and two mirrors (M) are used to beamsplit, reflect, and then interfere an optical beam (red). $|1\rangle$ and $|2\rangle$ represent "vertical" and "horizontal" propagation modes of the light, in analogy with $|1\rangle$ and $|2\rangle$ for a two-level atomic system. The wedge represents some relative phase shift accumulated between the two arms of the interferometer. N_1 and N_2 represent the number of detected particles in each respective mode by two detectors (blue).

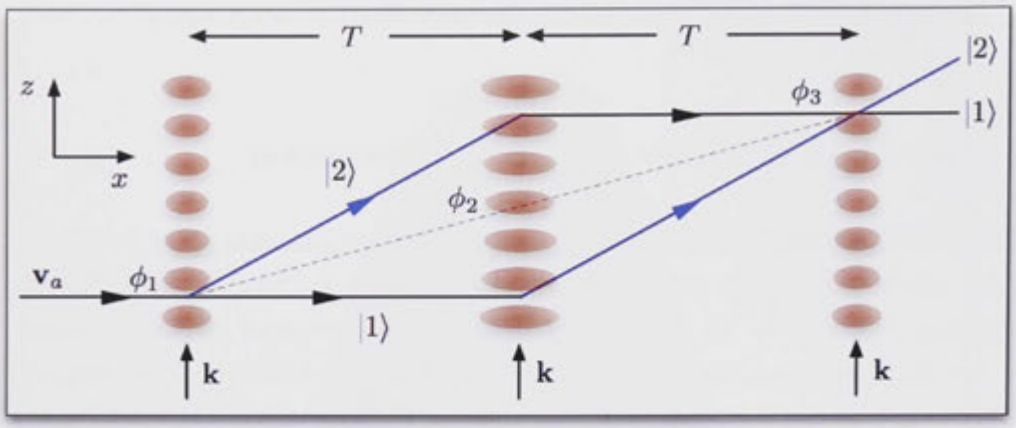

Figure 3.3: Mach-Zehnder atom interferometer for atoms incident with a constant mean velocity $\mathbf{v}_a$ in an inertial frame. $\mathbf{v}_a \cdot \mathbf{k} \neq 0$ in general, although $\mathbf{v}_a$ and $\mathbf{k}$ are perpendicular in this figure for the purpose of comparison with figure 3.2. The red ellipses represent the atom-light interaction regions, which are separated in time, and also space if $\mathbf{v}_a$ is not parallel to $\mathbf{k}$, as is the case for a gravimeter configuration. In general, each interaction pulse can have a different phase ϕ_i. The grey dashed line represents the centre-of-mass coordinate of the atomic state.

π-pulse equivalent to both mirrors as it simultaneously reflects both states.[5] This is shown schematically in figure 3.3 for atoms with a constant velocity $\mathbf{v}_a$ in an inertial frame. Recall that the two states of these interferometers are $|1\rangle \equiv |1, \mathbf{p}\rangle$ and $|2\rangle \equiv |2, \mathbf{p} + \hbar\mathbf{k}\rangle$; separated in momentum by $\hbar\mathbf{k}$. Thus there is a physical separation of the two arms of these atom interferometers.[6] Ramsey interferometers typically operate on microwave transitions, and thus the separation is negligible for reasonable values of T, due to the small magnitude of a microwave photon's momentum.[7] It is for this reason that almost perfect interference can still occur in the Ramsey sequence in the absence of a 'mirror'– the states are still extremely well overlapped at the second beamsplitter.

We may once again utilise unitary transformations to determine the action of a Mach-Zehnder pulse sequence on the state of the system:

$$|\psi(4\tau + 2T)\rangle = \hat{U}(\tau)\hat{U}_f(T)\hat{U}(2\tau)\hat{U}_f(T)\hat{U}(\tau)|1\rangle \tag{3.9}$$

[5] In the geometry of figure 3.2, both mirrors can be thought to 'act' simultaneously in the sense that the light beams arrive simultaneously from the first beamsplitter.

[6] In the current description, we are approximating the atoms by a momentum eigenstate, and thus a separation strictly exists only in momentum space; the states are plane waves in position space. However, we draw space trajectories in figure 3.3 to build the analogy with optics. In practice, atoms are best described by wavepackets, which have a finite momentum width and spatial extent. Therefore, given enough time, significant spatial separation occurs provided the momentum width is $< \hbar\mathbf{k}$.

[7] Equivalent to a velocity on the order of 10 nm/s for ^{87}Rb, compared with atomic cloud sizes on the order of hundreds of microns to several millimetres.

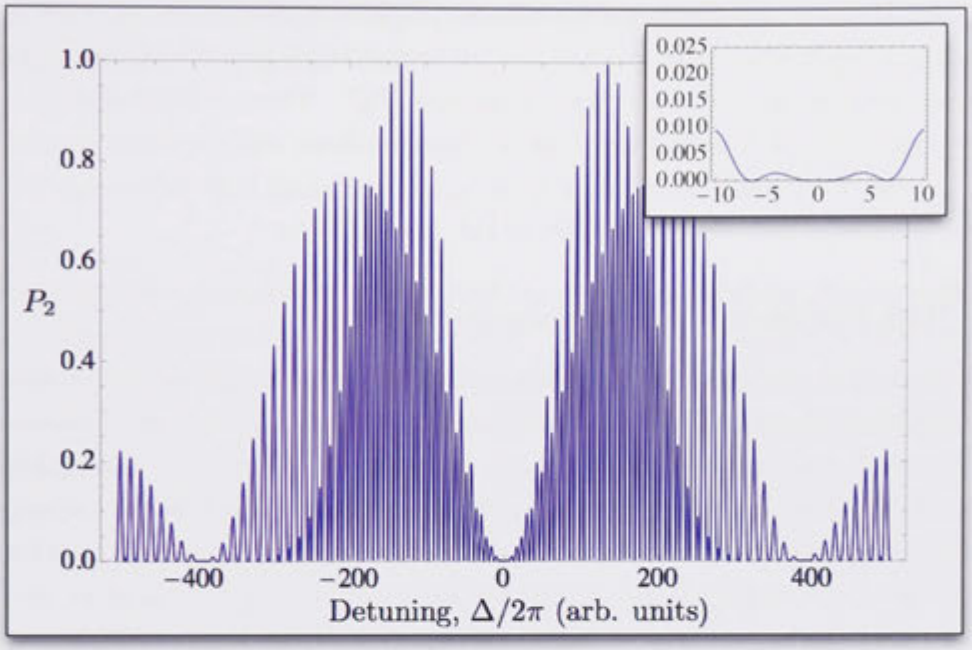

Figure 3.4: Mach-Zehnder interference fringes as a function of the pulse detuning for $\Omega = 100$ and $T = 0.5$ in arbitrary units. The inset shows the central region with $|\Delta| < 10$, demonstrating negligible sensitivity to the detuning in the limit that $|\Delta| \ll \Omega$.

where τ is again the $\pi/2$-pulse length, and each interaction pulse may have a different phase in general. As was the case for the Ramsey interferometer, an analytic expression for P_2 is readily derived. However, its complexity limits any insight gained by stating it explicitly, and we only plot the resulting fringes as a function of Δ in figure 3.4. In this case, $\Omega = 100$ and $T = 0.5$ in arbitrary units. Additionally, we assume that all three pulses have the same detuning and optical phase. An important difference between these fringes and Ramsey fringes is that for $|\Delta| \ll \Omega$, $P_2 \simeq 0$; apparent in the inset which plots the same fringes over the range $|\Delta| < 10$. We see that even for a modest ratio of $\Delta/\Omega = 0.1$, the population of the excited state is below 1%. Thus in the small detuning limit, a Mach-Zehnder atom interferometer is insensitive to the detuning of the driving pulses. Indeed, in this limit the expression describing the Mach-Zehnder fringes reduces to:

$$P_2 = \frac{1}{2}\left[1 - \cos\left(\phi_1 - 2\phi_2 + \phi_3\right)\right] \tag{3.10}$$

where ϕ_i is the relative phase of the ith coupling pulse. This obviously does not depend on the detuning. This can be explained by noting that any evolution between the first and second pulse due to a small detuning is reversed during the

second period of free evolution by the π-pulse. This reversal of the evolution is often called a 'spin-echo' [104], named in the context of a pseudo-spin description of two-level atoms and their evolution (see [95]). Thus, a Mach-Zehnder configuration is not well suited to frequency measurement and therefore atomic clocks. On the other hand, this immunity to small detunings is an advantage for inertially sensors, which are the subject of the next sections.

3.3.1 High Precision Mach-Zehnder Gravimeter

We now show that the phase shift of a Mach-Zehnder atom interferometer is sensitive to gravitational acceleration.[8] Consider an atom in a uniform gravitational field with acceleration $\mathbf{g} = -g\mathbf{z}$, and with $\mathbf{v}_a \times \mathbf{k} = 0$. In the lab frame (or equivalently the laser frame), the atoms undergo a constant acceleration leading to parabolic trajectories in the z coordinate. This is shown in figure 3.5. The solid grey parabola represents the centre-of-mass trajectory. Note that these are *space-time* trajectories, and atoms (ideal) move only in the z-direction (compare with figure 1.1 in the introduction). It is clear from the figure that the trajectories for the accelerated case will sample a different optical phase at each pulse with respect to the constant velocity case. This is simplest to analyse in the centre-of-

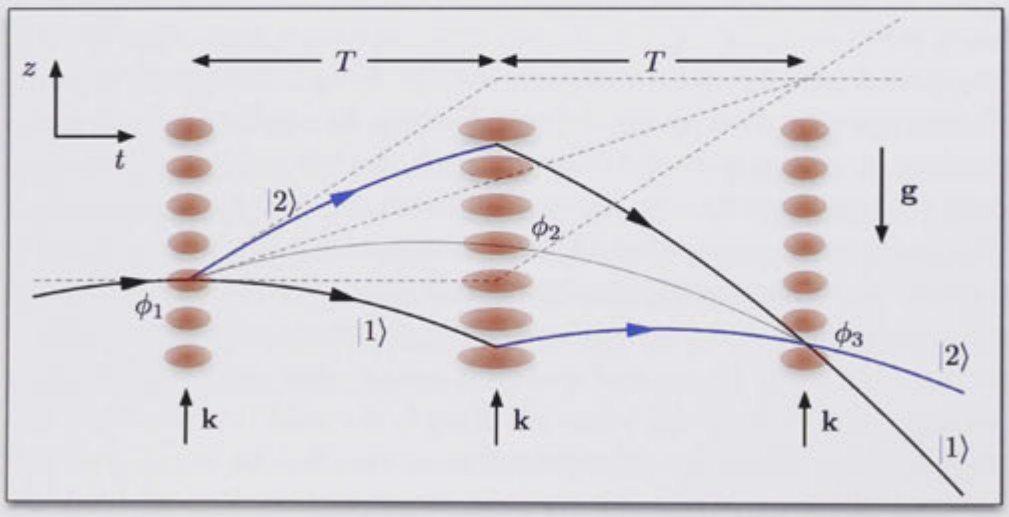

Figure 3.5: Mach-Zehnder atom interferometer in a uniform gravitational field $\mathbf{g} = -g\mathbf{z}$. The grey dashed lines are the unaccelerated trajectories from figure 3.3. Note this is a space-time diagram. An area is enclosed in space-time as $\mathbf{v}_a \times \mathbf{k} = 0$.

[8] Of course, a uniform acceleration cannot be distinguished from a gravitational field, and thus all that follows also applies to uniform acceleration of the apparatus with respect to the freely-falling atomic frame.

mass frame of the atomic state, which is accelerating at $\mathbf{g}$.[9] The (non-relativistic) transformation to this frame is given by:

$$\begin{aligned} t' &= t \\ z' &= z - \left(\frac{v_k}{2}t - \frac{1}{2}gt^2\right) \end{aligned} \tag{3.11}$$

where the primed coordinates are those of the accelerating frame, and $v_k = \hbar k/m$ is the velocity imparted by the beamsplitter. Note that the origin of coordinates of both frames coincide at the first $\pi/2$-pulse. In this frame, the lasers are seen to accelerate towards the atoms in the z-direction. Recall the definition of our coupling field:

$$\begin{aligned} &\mathbf{E}_0 \cos\left(\omega t - kz + \phi\right) \\ =&\mathbf{E}_0 \cos\left(\omega t - kz' + \phi - k_e\frac{v_k}{2}t + k_e\frac{1}{2}gt^2\right) \\ =&\mathbf{E}_0 \cos\left(\omega t - kz' + \phi'\right) \end{aligned} \tag{3.12}$$

where $\mathbf{k}\cdot\mathbf{r} = kz$ for the gravimeter configuration. In the accelerating frame, the electric field has the same form as that used in the derivation of the two-level atom, with the substitution $\phi \to \phi' = \phi - k\frac{v_k}{2}t + k\frac{1}{2}at^2$. This is important for two reasons. First, it implies that the laser frequency becomes:

$$\omega' = \omega - k\frac{v_k}{2} + kgt \tag{3.13}$$

The first additional term is a constant Doppler shift. The second term is a time-dependent Doppler shift – a frequency chirp. Therefore, assuming the laser is on-resonance at the first pulse ($t = 0$), it will strictly be off-resonant at the second and third pulses a time T and $2T$ later, respectively. Secondly, the phase ϕ' increases quadratically in time and therefore during a single pulse time $\sim \tau$, the optical phase added to the atomic phase will be time dependent. However, we will remain in the small detuning limit provided the time between pulses satisfies:

$$|kgT| \ll \Omega \tag{3.14}$$

[9] This frame is freely falling, and inertial in context of general relativity and the equivalence principle.

This additionally implies:

$$\begin{aligned} |kgT\tau| &\ll \Omega\tau \\ \therefore \quad \Delta\phi' &\ll \frac{\pi}{2} \end{aligned} \tag{3.15}$$

where $\Delta\phi'$ is the first-order change in ϕ' over the pulse time. Thus in the small detuning limit we can approximate the phase as constant during one pulse, and the detuning negligible. Equation (3.10) then still describes the interference fringes in the accelerating frame, with:

$$\begin{aligned} \phi_1' &= \phi_1 \\ \phi_2' &= \phi_2 - k\frac{v_k}{2}T + k\frac{1}{2}gT^2 \\ \phi_3' &= \phi_3 - kv_kT + 2kgT^2 \end{aligned} \tag{3.16}$$

and therefore the interferometric phase becomes:

$$\begin{aligned} \Phi_g &= \phi_1' - 2\phi_2' + \phi_3' \\ &= kgT^2 + \phi_1 - 2\phi_2 + \phi_3 \end{aligned} \tag{3.17}$$

for the configuration in figure 3.5. For the general case with $\mathbf{g}$ not parallel to $\mathbf{k}$:

$$\Phi_a = -\mathbf{k}\cdot\mathbf{g}T^2 + \phi_1 - 2\phi_2 + \phi_3 \tag{3.18}$$

Thus, through its sensitivity to the phase of the light, the interferometer is sensitive to acceleration parallel to $\mathbf{k}$. In particular, a small change in acceleration will be enhanced quadratically with increasing T. However, this benefit may seem limited at first glance, by virtue of equation (3.14), which places an upper limit on T. Indeed, if T is made too large then the second and third pulses will be far off-resonant. There is, however, a solution. As we are able to reliably control the laser frequency, we may attempt to balance the laser chirp seen in the accelerating frame, by imposing an opposing chirp α in the laboratory. This can be done in a way such that the additional laser phase is $\phi(t) = \alpha t^2/2$ and therefore:

$$\phi_1 - 2\phi_2 + \phi_3 = \alpha T^2$$

giving

$$\Phi_a = (\alpha - \mathbf{k}\cdot\mathbf{g})\,T^2 \tag{3.19}$$

In this way, sensitivity can be increased quadratically with T, and still satisfy equation (3.14). By scanning α, we can find the central interference fringe at $\Phi = 0$, giving $\alpha_0 = \mathbf{k} \cdot \mathbf{g}$. Precise knowledge of k and its alignment with respect to $\mathbf{g}$ gives a value for g.

As an example of the potential precision of an atomic gravimeter, consider equation (3.18) for a small change in gravity Δg:

$$\Delta\Phi = k\Delta g T^2 \tag{3.20}$$

and therefore

$$\Delta g = \frac{\Delta\Phi}{kT^2} \tag{3.21}$$

where we have assumed that $\mathbf{k} \cdot \mathbf{g} = -kg$. If we utilise a coupling on the ^{87}Rb D2 line, $k \sim 10^7\,\mathrm{m}^{-1}$. Assuming $T = 200\,\mathrm{ms}$, then:

$$\Delta g \simeq \times 2.5 \times 10^{-6} \Delta\Phi\,\mathrm{ms}^{-2} \tag{3.22}$$

Now $\Delta\Phi$ will typically be limited by technical noise and environmental factors such as mirror vibrations. However, as a fundamental limit we may consider the atomic shot-noise, or "projection noise," which gives $\Delta P_2 = P_2(1 - P_2)/\sqrt{N}$, where N is the total number of atoms detected at the interferometer output [105]. Assuming the interferometer has been biased midway up an interference fringe (i.e. $\Phi = \pi/2, P_2 = 0.5$), and combining this with a first order Taylor expansion of equation (3.10) gives:

$$\Delta\Phi = \frac{1}{\sqrt{N}} \tag{3.23}$$

Thus, for $N = 10^6$ atoms/s

$$\Delta g \simeq 2.5 \times 10^{-9}\,\mathrm{ms}^{-2}/\sqrt{\mathrm{Hz}}$$

or

$$\frac{\Delta g}{g} \simeq 2.5 \times 10^{-10}/\sqrt{\mathrm{Hz}} \tag{3.24}$$

This potential limit is beyond current state-of-the-art absolute gravimeters, such as falling corner cube devices ([106] and refs. therein). Indeed, the current state-of-the-art devices include an atom interferometer with $T = 400\,\mathrm{ms}$, and $N \sim 10^7$

atoms/s, resulting in a sensitivity of $1.1 \times 10^{-8}/\sqrt{\text{Hz}}$ [10]. Furthermore, the sensitivity can be enhance by using multi-photon transitions for LMT beamsplitters, which will be discussed in chapter 8.

3.3.2 Sensitivity to Rotations

In addition to sensitivity to linear acceleration, if the frame containing the lasers is rotating, there will be additional phase-shifts if $\mathbf{v}_a$ is not parallel to $\mathbf{k}$. This is the situation, for example, for an atom interferometer constructed in an Earth based laboratory as the lasers define a rotating frame due to the rotation of the Earth. In fact, if $\mathbf{v}_a \cdot k = 0$ then the interferometer will only be sensitive to rotation; an atomic gyroscope [14, 15, 16, 17]. We will not discuss gyroscopes in detail here, but will derive the first-order rotational phase-shift contribution.

We assume uniform rotation in what follows. The atoms once again represent an inertial frame, and are seen to follow curved trajectories in the rotating frame due to inertial forces that can be represented by the acceleration terms:[10]

$$\mathbf{a}_{\text{Cor}} = -2\boldsymbol{\Omega}_E \times \mathbf{v}_a \tag{3.25}$$

$$\mathbf{a}_{\text{Cen}} = -\boldsymbol{\Omega}_E \times (\boldsymbol{\Omega}_E \times \mathbf{r}) \tag{3.26}$$

where $\mathbf{a}_{\text{Cor}}$ and $\mathbf{a}_{\text{Cen}}$ are the Coriolis and centrifugal accelerations respectively [107]. $\boldsymbol{\Omega}_E$ is the Earth's local angular velocity, and $\mathbf{v}_a$ and $\mathbf{r}$ are the atomic velocity and position in the rotating frame. Thus, even if there is no acceleration in an inertial frame, the atoms seem to accelerate in the rotating frame. In what follows, we will only consider the first order, dominant contribution of these accelerations to the phase shift. Higher order corrections have been discussed in [108].

A typical interferometer evolution time of $T \sim 0.1 - 1\,\text{s}$ results in $|\boldsymbol{\Omega}_E|T \ll 1$, as $|\boldsymbol{\Omega}_E| \sim 7 \times 10^{-5}\,\text{rad/s}$. Thus the centrifugal contribution, which is second-order in $\boldsymbol{\Omega}_E T$, can be neglected. Furthermore, $\Omega_E T$ is the rotation angle of the wavevector, and thus $\mathbf{k} \cdot \mathbf{v}_a \simeq 0$ over the extent of the interferometer. The Coriolis acceleration can therefore be treated as a uniform acceleration in this limit. We use the result of equation (3.18) with equation (3.25), and calculate

[10] In the case of a non-uniformly rotating frame, an additional acceleration exists given by $\mathbf{a}_{\text{Eul}} = -\frac{d\boldsymbol{\Omega}_E}{dt} \times \mathbf{r}$. This is called the Euler acceleration.

the additional phase shift for uniform rotation:

$$\begin{aligned}\Phi_R &= -\mathbf{k}\cdot\mathbf{a}_{\mathrm{Cor}}T^2 + \phi_1 - 2\phi_2 + \phi_3 \\ &= 2\mathbf{k}\cdot(\boldsymbol{\Omega}\times\mathbf{v}_a)T^2 + \phi_1 - 2\phi_2 + \phi_3\end{aligned} \tag{3.27}$$

where we have dropped the subscript on the angular velocity as it can represent any local uniform rotation, provided $|\boldsymbol{\Omega}|T \ll 1$. The Coriolis shift has an impact even in atomic gravimeters, due to atomic trajectories with momentum components transverse to $\mathbf{k}$. This will be discussed in detail in chapter 10

Combining the phase shift for uniform acceleration with the phase shift for uniform rotation, the total inertial phase-shift of a Mach-Zehnder atom interferometer can be written as:

$$\Phi \simeq -\mathbf{k}_e\cdot(\mathbf{a} - 2\boldsymbol{\Omega}\times\mathbf{v}_a)T^2 + \phi_1 - 2\phi_2 + \phi_3 \tag{3.28}$$

where $\mathbf{a}$ is any uniform acceleration. We will assume $\mathbf{v}_a\cdot\mathbf{k} = 0$, and therefore $\boldsymbol{\Omega}\times\mathbf{v}_a = 0$ until chapter 10.

3.3.3 Additional Phase Shifts

It should also be noted that this entire derivation has only considered the phase shift arising from the atom-light interaction. In general, there are two more phase contributions. The first is the propagation phase, which arises from atomic state phase evolution during propagation in the interferometer. It was first described by Storey and Cohen-Tannoudji using Feynman path integrals to calculate the action over each classical trajectory using the Lagrangian [109]. The propagation phase is then:

$$\phi_{prop} = (S_{cl}^B - S_{cl}^A)/\hbar \tag{3.29}$$

where

$$S_{cl}^{A,B} = \int_{A,B}\mathcal{L}(z,\dot{z})dt \tag{3.30}$$

is the action for the classical trajectory in each interferometer arm A and B, and $\mathcal{L}$ the Lagrangian. Calculating ϕ_{prop} for a uniform gravitational field (i.e. neglecting gradients) gives $\phi_{prop} = 0$.

The second contribution is called the separation phase, and arises if the two

interferometer paths do not perfectly overlap at the final beamsplitter, leading to a spatial phase given by $\phi_{sep} = \bar{\mathbf{p}} \cdot \Delta\mathbf{z}/\hbar$, where $\bar{\mathbf{p}}$ is the average momentum of the two arms, and $\Delta\mathbf{z}$ is the separation of the two trajectories [108]. Again, for a uniform gravitational field, the paths will perfectly overlap with $\Delta\mathbf{z} = 0$ and therefore $\phi_{sep} = 0$. Thus for uniform acceleration, only the atom-light interaction contributed to the phase of the interferometer.

As a final note, the Ramsey and Mach-Zehnder interferometers discussed are the simplest interferometer configurations, and provide a firm introduction to atom interferometer theory. Other configurations exist, such as the Ramsey-Bordè interferometer (four successive $\pi/2$-pulses) [110], which is sensitive to the photon-recoil frequency [85]. This is a measure of the ratio h/m, and in turn, the fine-structure constant [18, 19, 20]. Other configurations have also implemented multi-path interference [111, 112], and a comprehensive review of atom interferometry can be found in reference [113].

Chapter 4

The Three-Level Atom: Raman Transitions

We have seen that two features are important for the sensitivity of light-pulse interferometers: long coherence times for long free evolution T, and a significant momentum transfer in the beamsplitting process. As mentioned at the end of chapter 2, spontaneous emission significantly reduced the coherence time for (large k) optical transitions, whereas long-lived microwave transitions have negligible momentum transfer.

In this chapter, we consider a three-level atom driven by two classical light fields. This forms the basis for the description of stimulated Raman transitions, which are two-photon transitions that can couple two long-lived grounds states, as well as transferring the momentum of two photons through an absorption /stimulated-emission process. They are the simplest multi-photon transitions, and are therefore a precursor to higher-order transitions such as those which describe Bragg diffraction. Bragg diffraction is used for LMT beamsplitting later in this thesis, and is discussed in chapter 8.

4.1 A Three-Level Atom in Two Classical Light Fields

Consider an atom with centre-of-mass momentum $\mathbf{p}$ and three electronic levels. These states are defined as in chapter 2: $|1,\mathbf{p}\rangle$, $|2,\mathbf{p}\rangle$, and $|e,\mathbf{p}\rangle$. The electronic level structure for this atom is given in figure 4.1(a). We use this to approximate the level structure of ^{87}Rb (and other alkalis) with $|1\rangle$ and $|2\rangle$ the hyperfine ground states, and $|e\rangle$ an excited state – for example one of the $5^2P_{3/2}$ hyperfine states [100]. We assume the atom is coupled to two electromagnetic fields $\mathbf{E}_{01}\cos(\omega_1 t - \mathbf{k}_1\cdot\hat{\mathbf{r}} + \phi_1)$ and $\mathbf{E}_{02}\cos(\omega_2 t - \mathbf{k}_2\cdot\hat{\mathbf{r}} + \phi_2)$ via an electric-dipole interaction. As we will see, in addition to coupling the ground states to the excited state via a

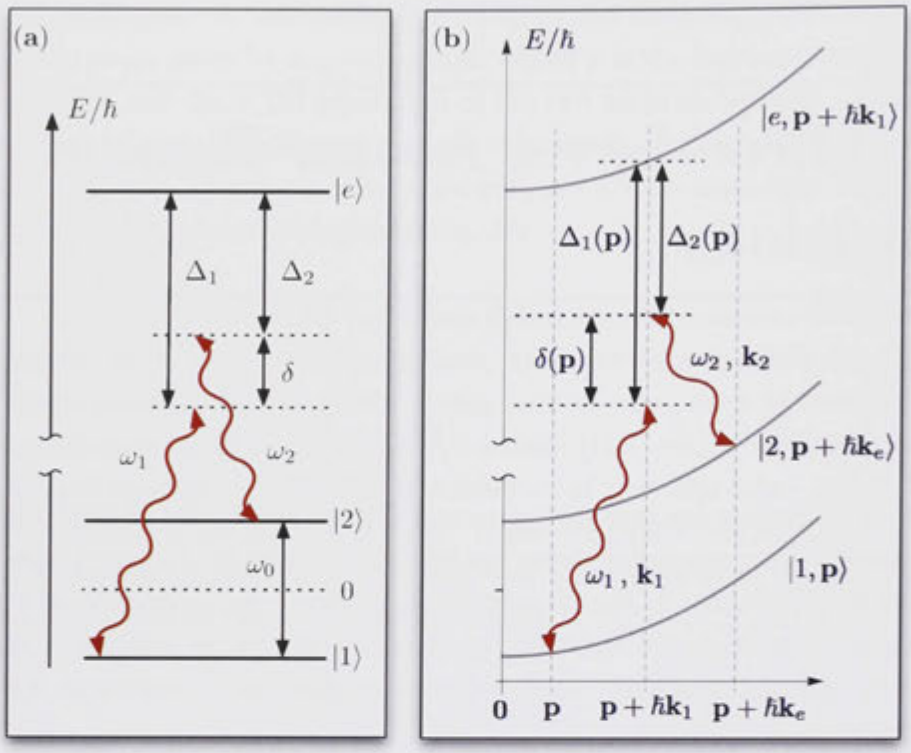

Figure 4.1: Three-level atom energy diagrams. (a) Electronic level structure, with two electromagnetic coupling fields of frequencies ω_1 and $\omega_2 \gg \omega_0$. This approximates the general level structure of an alkali element such as ^{87}Rb. Δ_1 and Δ_2 are the detunings from one-photon resonance with the excited state for states $|1\rangle$ and $|2\rangle$ respectively. δ is the detuning from two-photon resonance. One-photon coupling between $|1\rangle$ and $|2\rangle$ is neglected due to a very large detuning. (b) Energy level diagram including the centre-of-mass momentum of the atoms, similar to figure 2.2. In this case, Δ_1, Δ_2, and δ become momentum dependent as given in the main text. Based on the results of section 2.1, if we treat ω_1 as a photon absorption, and ω_2 a photon emission, then we couple momentum states $|\mathbf{p}\rangle \leftrightarrow |\mathbf{p} + \hbar\mathbf{k}_1\rangle \leftrightarrow |\mathbf{p} + \hbar\mathbf{k}_e\rangle$ with $\mathbf{k}_e = \mathbf{k}_1 - \mathbf{k}_2$.

one-photon coupling, these fields can drive a *two-photon* transition between the two ground states. We may neglect one-photon coupling between $|1\rangle$ and $|2\rangle$ as the driving fields are far off-resonance ($\omega_0 \ll \omega_1, \omega_2$).[1] We additionally assume that ω_1 only couples $|1\rangle$ to $|e\rangle$, and ω_2 only couples $|2\rangle$ to $|e\rangle$, with detunings Δ_1 and Δ_2 respectively.[2] The difference between these detunings is the two-photon detuning, $\delta = \Delta_1 - \Delta_2$. Generally, one chooses $\delta \ll \Delta_1, \Delta_2$.

[1] In addition, the ground hyperfine states of an alkali are only coupled via a magnetic dipole interaction, which is much weaker than an electric-dipole coupling.

[2] In principle, ω_1 also couples $|2\rangle$ to $|e\rangle$ with a modified detuning of $\Delta_1 - (\omega_1 - \omega_2)$. Similarly ω_2 couples $|1\rangle$ to $|e\rangle$. However, we neglect these couplings as they are far off resonant for the two-photon process, which is of primary interest here.

We now consider the centre-of-mass momentum of the atom. If we assume that ω_1 initally drives a photon absorption, and that ω_2 stimulates a photon emission, then based on the results for the two-level atom (section 2.1), we know that the absorption process will change the atomic momentum by $\hbar\mathbf{k}_1$, and the emission process will change the momentum by $-\hbar\mathbf{k}_2$. In other words, the coupled states of the system are: $|1,\mathbf{p}\rangle \leftrightarrow |2,\mathbf{p}+\hbar\mathbf{k}_1\rangle \leftrightarrow |e,\mathbf{p}+\hbar\mathbf{k}_e\rangle$, where $\mathbf{k}_e = \mathbf{k}_1 - \mathbf{k}_2$. This is summarised in figure 4.1(b). All detunings become momentum dependent as before. We use the result discussed at the end of section 2.1 and initially neglect the momentum distribution of the atomic state, first solving the simpler three-dimensional problem. The momentum distribution can then be accounted for at the end by weighting the solutions. Given this, we write the state of the atom in the combined momentum-electronic eigenbasis:

$$|\psi(t)\rangle = c_1(t)|1,\mathbf{p}\rangle + c_2(t)|2,\mathbf{p}+\hbar\mathbf{k}_e\rangle + c_e(t)|e,\mathbf{p}+\hbar\mathbf{k}_1\rangle \tag{4.1}$$

with normalisation given by:

$$\langle\psi(t)|\psi(t)\rangle = |c_1(t)|^2 + |c_2(t)|^2 + |c_e(t)|^2 = 1 \tag{4.2}$$

For simplicity, we drop the momentum labels from the kets, and simply associate each internal state with the corresponding momentum state. Again, utilising earlier results, the hamiltonian for the system can be written as:

$$\begin{aligned}\hat{H} = {} & E_1(\mathbf{p})|1\rangle\langle 1| + E_2(\mathbf{p})|2\rangle\langle 2| + E_e(\mathbf{p})|e\rangle\langle e| \\ & + \mathbf{d}_{1e}\cdot\mathbf{E}_{01}\cos(\omega_1 t+\phi_1)\Big[|1\rangle\langle e| + |e\rangle\langle 1|\Big] \\ & + \mathbf{d}_{2e}\cdot\mathbf{E}_{02}\cos(\omega_2 t+\phi_2)\Big[|2\rangle\langle e| + |e\rangle\langle 2|\Big]\end{aligned} \tag{4.3}$$

where $E_j(\mathbf{p})$ is the energy of the atom in the jth state, for an initial momentum $\mathbf{p}$, and $\mathbf{d}_{je} = \langle j|\hat{\mathbf{d}}|e\rangle$ the electric-dipole moment for the jth one-photon couplng. Note that the spatial term in each of the cosines is absent as it is accounted for by the momentum in the definition of the coupled states. Using figure 4.1, it can be shown that:

$$E_1(\mathbf{p}) = -\frac{\hbar\left[\Delta\omega + \delta(\mathbf{p})\right]}{2} + E_{kin} \tag{4.4}$$

$$E_2(\mathbf{p}) = \frac{\hbar\left[\Delta\omega + \delta(\mathbf{p})\right]}{2} + E_{kin} \tag{4.5}$$

$$E_e(\mathbf{p}) = \frac{\hbar\big(\Delta(\mathbf{p}) + \omega_1 + \omega_2\big)}{2} + E_{kin} \tag{4.6}$$

with

$$\Delta(\mathbf{p}) = \Delta_1(\mathbf{p}) + \Delta_2(\mathbf{p}) \ , \ \delta(\mathbf{p}) = \Delta_1(\mathbf{p}) - \Delta_2(\mathbf{p}) \ , \ \Delta\omega = \omega_1 - \omega_2 \tag{4.7}$$

and

$$E_{kin} = \frac{p^2}{2m} + \frac{\mathbf{k}_e \cdot \mathbf{p}}{2m} + \frac{\hbar\omega_r}{2} \tag{4.8}$$

Explicitly:

$$\Delta_1(\mathbf{p}) = \frac{\mathbf{k}_1 \cdot \mathbf{p}}{m} + \omega_r + \Delta_1 \tag{4.9}$$

$$\Delta_2(\mathbf{p}) = \frac{\mathbf{k}_2 \cdot \mathbf{p}}{m} + \omega_r - \omega_{2r} + \Delta_2 \tag{4.10}$$

where $\omega_{2r} = \hbar k_e^2/2m$ is the two-photon recoil frequency. Notice that E_{kin} is common to all states, and we may shift our zero of energy to remove it. Substituting the above into the Schrödinger equation, and choosing a frame rotating at $e^{-i\hat{H}_0 t/\hbar}$ with:

$$\hat{H}_0 = \frac{\hbar\Delta\omega}{2}\Big[|2\rangle\langle 2| - |1\rangle\langle 1|\Big] + \frac{\hbar(\omega_1 + \omega_2)}{2}|e\rangle\langle e| \tag{4.11}$$

gives the equations of motion for the state amplitudes:

$$\begin{pmatrix} \dot{c}_e(t) \\ \dot{c}_2(t) \\ \dot{c}_1(t) \end{pmatrix} = -\frac{i}{2}\begin{pmatrix} \Delta(\mathbf{p}) & \Omega_2 e^{-i\phi_2} & \Omega_1 e^{-i\phi_1} \\ \Omega_2 e^{i\phi_2} & \delta(\mathbf{p}) & 0 \\ \Omega_1 e^{i\phi_1} & 0 & -\delta(\mathbf{p}) \end{pmatrix}\begin{pmatrix} c_e(t) \\ c_2(t) \\ c_1(t) \end{pmatrix} \tag{4.12}$$

where we make the rotating-wave approximation once again, and $\Omega_1 = \mathbf{d}_{1e} \cdot \mathbf{E}_{01}/\hbar$ and $\Omega_2 = \mathbf{d}_{2e} \cdot \mathbf{E}_{02}/\hbar$, are the Rabi frequencies for the respective one-photon transitions. Consider the equation for $\dot{c}_e(t)$:

$$\dot{c}_e(t) = -\frac{i}{2}\left(\Delta(\mathbf{p})c_e(t) + \Omega_1 e^{-i\phi_1}c_1(t) + \Omega_2 e^{-i\phi_2}c_2(t)\right) \tag{4.13}$$

We are interested in the regime where the population in the excited state is negligible as we wish to avoid its relatively large spontaneous emission rate. This occurs in the limit that both $|\Delta_1(\mathbf{p})|$ and $|\Delta_2(\mathbf{p})| \gg \Omega_1, \Omega_2, |\delta(\mathbf{p})|$, for which

the excited state undergoes very small amplitude, high frequency oscillations $\sim \Delta(\mathbf{p})$. These average to zero over timescales associated with the evolution of the ground states, and we can neglect the excited state evolution by setting $\dot{c}_e(t) = 0$. Equation (4.13) then becomes:

$$c_e(t) = -\frac{\left(\Omega_1 e^{-i\phi_1} c_1(t) + \Omega_2 e^{-i\phi_2} c_2(t)\right)}{\Delta(\mathbf{p})} \tag{4.14}$$

This step is known as adiabatic elimination, as the excited state is assumed to adiabatically follow the ground states over the time scales of interest [114]. Another way of interpreting this limit is that the probability current flows smoothly between the ground states via the excited state. We substitute this result into equation (4.12) to give the reduced equations of motion:

$$\begin{pmatrix} \dot{c}_2(t) \\ \\ \dot{c}_1(t) \end{pmatrix} = -\frac{i}{2} \begin{pmatrix} \delta(\mathbf{p}) - \frac{\Omega_2^2}{\Delta(\mathbf{p})} & -\frac{\Omega_1\Omega_2}{\Delta(\mathbf{p})} e^{-i\Delta\phi} \\ \\ -\frac{\Omega_1\Omega_2}{\Delta(\mathbf{p})} e^{i\Delta\phi} & -\delta(\mathbf{p}) - \frac{\Omega_1^2}{\Delta(\mathbf{p})} \end{pmatrix} \begin{pmatrix} c_2(t) \\ \\ c_1(t) \end{pmatrix} \tag{4.15}$$

where $\Delta\phi = \phi_1 - \phi_2$. If we shift our zero of energy once more by adding $\frac{\Omega_1^2+\Omega_2^2}{2\Delta(\mathbf{p})}$ to both diagonal terms, we have:

$$\begin{pmatrix} \dot{c}_2(t) \\ \\ \dot{c}_1(t) \end{pmatrix} = -\frac{i}{2} \begin{pmatrix} \delta_e(\mathbf{p}) & \Omega_e e^{-i\Delta\phi} \\ \\ \Omega_e e^{i\Delta\phi} & -\delta_e(\mathbf{p}) \end{pmatrix} \begin{pmatrix} c_2(t) \\ \\ c_1(t) \end{pmatrix} \tag{4.16}$$

Notice that the reduced Schrödinger equation has exactly the same form as that for the two-level atom in (2.16). Thus, in the limit of large one-photon detunings, the three-level atom reduces to an effective two-level atom, with an effective detuning:

$$\begin{aligned} \delta_e(\mathbf{p}) &= \delta(\mathbf{p}) - \frac{\Omega_2^2 - \Omega_1^2}{4\Delta_a(\mathbf{p})} \\ &= \delta(\mathbf{p}) - \left(\omega_{LS}^{(2)} - \omega_{LS}^{(1)}\right) \end{aligned} \tag{4.17}$$

where we have used the light shifts derived for the two-level atom in equation (2.20), and the superscripts label each ground state. Additionally, we have made the substitution $\Delta(\mathbf{p}) = 2\Delta_a(\mathbf{p})$, with $\Delta_a(\mathbf{p})$ the average of the two one-photon detunings. Thus, the effective detuning is not simply the two-photon detuning, but includes a term proportional to the differential light shift of the ground states.

The effective Rabi frequency:

$$\Omega_e = -\frac{\Omega_1 \Omega_2}{2\Delta_a(\mathbf{p})} \tag{4.18}$$

now defines the coupling strength for the effective two-level system, and it is now the *relative* phase of the the two laser beams, $\Delta\phi$, that is added onto the atomic phase. Assuming an initial non-zero amplitude for one of the ground states, the three-level atom will undergo Rabi oscillations between the ground states at $\tilde{\Omega}_e = \sqrt{\Omega_e^2 + \delta_e(\mathbf{p})^2}$. These transitions are often named "Raman transitions."

It is interesting to consider two cases applied to a ^{87}Rb atom approximated by this three-level model. First note that an excited state of the D2 line in ^{87}Rb has a frequency of $\sim 384\,\mathrm{THz}$, whereas the hyperfine ground state separation is $\sim 6.83\,\mathrm{GHz}$ (see section 5.1). Thus, $|\mathbf{k}_1| \simeq |\mathbf{k}_2|$. Consider first the case of co-propagating laser beams, which implies that $\mathbf{k}_1 \simeq \mathbf{k}_2$. In this case, $\mathbf{k}_e \simeq 0$, and therefore the two ground states are coupled with negligible momentum transfer; the momentum of the absorbed photon is balanced by the recoil momentum due to the emitted photon (consider figure 4.1). This is reflected by the two-photon detuning:

$$\begin{aligned} \delta(\mathbf{p}) &= \frac{\mathbf{k}_e \cdot \mathbf{p}}{m} + \omega_{2r} + \delta \\ &\simeq \delta \end{aligned} \tag{4.19}$$

which shows that the two-photon resonance is independent of $\mathbf{p}$.[3] This configuration can be useful when attempting to couple internal states of an ensemble of atoms, equally across their momentum distribution. We use this configuration for our Ramsey interferometer in chapter 6.

The second case is that of counter-propagating laser beams, where $\mathbf{k}_1 \simeq -\mathbf{k}_2$. In this case $\mathbf{k}_e \simeq 2\mathbf{k}_1$, and therefore the two ground states are coupled with a momentum transfer of $2\hbar\mathbf{k}_1$. In other words, the momentum of the absorbed photon, and the recoil momentum due to the emitted photon add, as they are in

[3] The two-photon Rabi frequency is, however still weakly momentum dependent due to the one-photon detuning.

the same direction. Again this is reflected in the two-photon detuning:

$$\begin{aligned}\delta(\mathbf{p}) &= \frac{\mathbf{k}_e \cdot \mathbf{p}}{m} + \omega_{2r} + \delta \\ &= \frac{2\mathbf{k}_1 \cdot \mathbf{p}}{m} + 4\omega_r + \delta \end{aligned} \tag{4.20}$$

and the two-photon resonance becomes momentum dependent. This configuration is often called a "Doppler sensitive Raman transition." The two-photon detuning has the same form as that for the two-level atom [equation (2.13)], with twice the Doppler shift and four times the recoil frequency, as a result of two-photon momenta associated with the effective transition.

Both the above cases have applications in atom optics, including applications in velocimetry [115], atomic velocity selection [116], and optical memories [117]. The Doppler sensitive configuration is particularly useful in the context of atom interferometry, as it achieves our desired goal of coupling between long-lived ground states, but also transfers momentum on the order of that for an optical photon. As a result, Raman transitions are well suited to atom interferometer-based inertial sensors. Furthermore in Chapters 6 & 7 we will demonstrate the application of Doppler sensitive Raman transitions to producing high-flux atom lasers, and Doppler insensitive transitions to a free-space BEC Ramsey interferometer.

Part II

Ingredients for Interometry: Atomic Sources, Mirrors, and Beamsplitters

Chapter 5

Atomic Sources for Atom Interferometry

In this chapter, we give a background of the BEC and atom-lasers sources used in our atom interferometers. In particular, we focus on the momentum width of Bose-condensed sources using the mean-field description of a condensate. Momentum width will be shown to be of crucial importance in atom interferometers in chapter 10. We conclude with a description of our two different apparatus for producing BECs and atom-lasers.

5.1 ^{87}Rb and Transitions in a Multi-Level Atom

All of the work in this thesis uses ^{87}Rb, which is a single valence-electron alkali metal. As a result, it has a relatively simple, hydrogen-like level structure. Here, we summarise the main features necessary for this thesis. A comprehensive description of alkali atom level structure, and allowed transitions can be found in the text by C. Foot [96].

The level structure of ^{87}Rb is given in figure 5.1 for the fine structure line from $5^2S_{1/2} \rightarrow 5^2P_{3/2}$ at $\sim 780\,\text{nm}$, known as the "D_2 line" (D refers to "doublet"). A detailed summary of the rubidium D-line data has been written by D. Steck [100]. Each energy level represents the atomic state $|F, m_F\rangle$,[1] where F is the total atomic angular momentum (nuclear plus electronic) quantum number, and m_F the magnetic quantum number. Different F states are non-degenerate due to the hyperfine interaction between the nuclear and electron angular momenta. Different m_F states are also shown as non-degenerate, as occurs in a weak magnetic field due to the Zeeman effect [96].

[1] Unless explicitly stated otherwise, kets of the form $|F, m_F\rangle$ always refer to the internal atomic state.

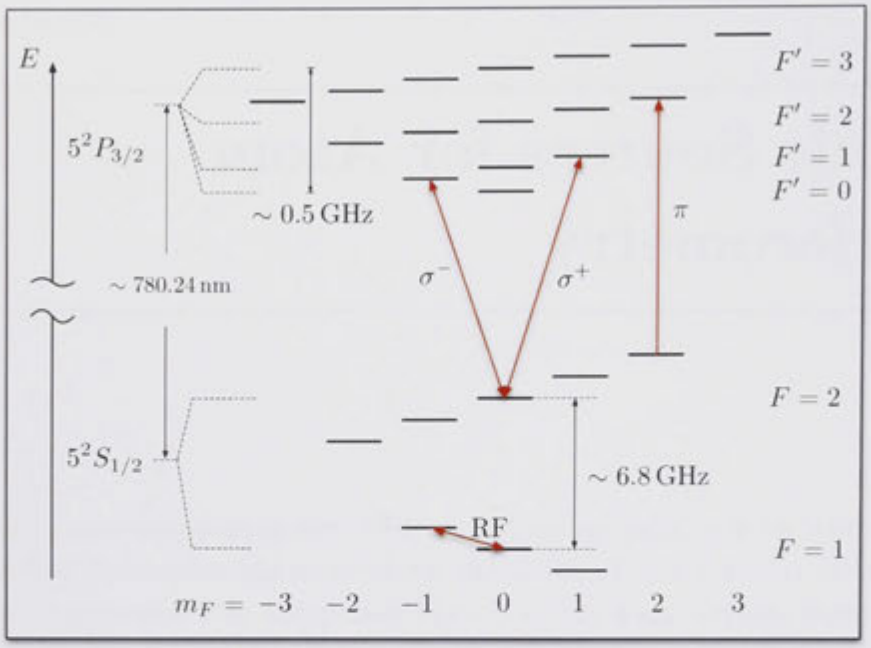

Figure 5.1: Hyperfine level structure of the ^{87}Rb D_2 line (not to scale). Different m_F states are shown as non-degenerate, as is the case in a weak magnetic field. Examples of allowed electric-dipole transitions are shown (σ^+, σ^-, π), which are important for laser-cooling, atomic detection, and Raman transitions. An example of an allowed RF magnetic-dipole transition is also shown, important for evaporative cooling, and atom-laser outcoupling.

In Part I, only two- and three-level atoms were considered. In practice, all atoms are multi-level, and can only be approximated as two- or three-level, when accounting for transition selection rules and (one-photon) detuning.

5.1.1 Electric Dipole Transition Selection Rules

In the case of electric dipole coupling, the coupling term $\mathbf{d}\cdot\mathbf{E}$ from equation (2.3) can be decomposed into three terms, which correspond to linearly independent basis-polarisations that couple different Zeeman states with $\Delta m_F = \pm 1$ or 0. These transitions are labelled σ^+, σ^- and π respectively. If we choose our quantisation axis parallel to the local magnetic field, then *in this case only*, σ^+, σ^- and π correspond to right circular, left circular, and linear polarisation respectively. For example, linearly polarised light propagating along the magnetic field is an equal superposition between σ^+ and σ^-; containing no π component. As such, it can only drive $\Delta m_F = \pm 1$ transitions. Linear light polarised along the local magnetic field is pure π polarisation. In addition, $\Delta F = \pm 1$ or 0, however, ΔF & $\Delta m_F \neq 0$ simultaneously due to conservation of angular momentum

(photons have $S = 1$).

In this thesis, electric dipole transitions are important for laser cooling and manipulation of ^{87}Rb (section 5.4.1), atom detection (section 5.4.2), dipole trapping (section 5.4.3), Raman transitions for beamsplitting and atom-laser outcoupling (chapter 6), and LMT beamsplitting (chapter 8).

5.1.2 Magnetic Dipole Transition Selection Rules

Magnetic dipole transitions are also possible, but are much weaker than electric dipole transitions due to their generally weaker coupling strength ($\boldsymbol{\mu}/c \ll \mathbf{d}$, where $\boldsymbol{\mu}$ is the magnetic dipole moment). However, in the case of the two hyperfine ground states, electric dipole transitions are forbidden by the $\Delta l = \pm 1$ selection rule, where l is the electron orbital angular momentum quantum number. Therefore only magnetic dipole transitions can occur between ground states, with the selection rules $\Delta F = \pm 1$ or 0, and $\Delta m_F = \pm 1$ or 0. Again, ΔF & $\Delta m_F \neq 0$ simultaneously. Such transitions are typically at RF frequencies (between Zeeman states within a given F state), or microwave frequencies (between Zeeman states in different F states).

In this thesis, magnetic dipole transitions are important for evaporative cooling (section 5.4) and atom-laser outcoupling (section 5.3.1 and chapter 7).

5.2 Bose-Einstein Condensates

The vast majority of interferometry work presented in this thesis has used Bose-condensed sources of atoms, based on the long term goal of answering the question if, and under which conditions, Bose-condensed sources are better choices for atom-interferometry. Since its first realisation in 1995 by the groups of Eric Cornell and Carl Wieman [44], and Wolfgang Ketterle [45], BEC has been studied extensively both experimentally and theoretically. An excellent experimental review by Ketterle *et al.* can can be found in [118], and an excellent theoretical review by Dalfovo *et al.* is given in [119].

5.2.1 Mean-Field Description of a Bose-Einstein Condensate

The celebrated mean-field description of a BEC, based on the Gross-Pitaevskii equation (GPE) [120, 121], provides an excellent theoretical description of the ground state of a condensate. In particular, it is useful for calculating the density

and momentum distributions of a condensate, as well as estimating the momentum width of a ballistically expanding BEC or weakly outcoupled atom-laser. In chapter 9 we will use a mean-field model, coupled with the quantum statistics from a many-body description [61], to estimate the effect of dephasing in an atomic gravimeter.

The phenomenon of BEC was first described by S. Bose in 1924 in his seminal paper on the statistics of photons [46]. A. Einstein extended Bose's work to massive particles in two more papers in 1924 and 1925 [46, 47, 48]. They predicted that below a certain critical temperature, a collection of N non-interacting bosons will begin to macroscopically occupy the ground energetic state of a given system. This phase transition occurs when the condition:

$$n\lambda_{th}^3 \simeq 2.612 \tag{5.1}$$

is met, where n is the particle density, and $\lambda_{th} = \sqrt{2\pi\hbar^2/mk_B\mathcal{T}}$ is the thermal deBroglie wavelength for particles of mass m at a temperature $\mathcal{T}$. k_B is Boltzmann's constant.

BEC is commonly produced in dilute atomic gases, confined in-trapping potentials which are well approximated by a harmonic potential:

$$V_{ext}(\mathbf{r}) = \frac{1}{2}m\left(\omega_x^2x^2 + \omega_y^2y^2 + \omega_z^2z^2\right) \tag{5.2}$$

where the trap is characterised by its trapping frequencies $(\omega_x, \omega_y, \omega_z)$ in the (x, y, z) directions respectively. Often, these traps are cylindrically symmetric about (say) the y-axis, with $\omega_x = \omega_z \equiv \omega_\rho$, producing a 'cigar' shaped trapping potential. The energy ground state of a single particle in a harmonic trap is that derived from the standard treatment of the quantum-mechanical harmonic oscillator:

$$\psi_0(\mathbf{r}) = \left(\frac{m\omega_{ho}}{\pi h}\right)^{3/4} e^{-\frac{m}{2\hbar}\left(\omega_x^2x^2+\omega_y^2y^2+\omega_z^2z^2\right)} \tag{5.3}$$

where $\omega_{ho} = (\omega_x\omega_y\omega_z)^{1/3}$ is the geometric mean of the trapping frequencies. In the absence of atomic interactions, the wavefuction of a BEC of N atoms is then related to the harmonic oscillator ground state via:

$$\phi(\mathbf{r}) = \sqrt{N}\psi_0(\mathbf{r}) \tag{5.4}$$

and $n(\mathbf{r}) = |\phi(\mathbf{r})|^2$ is the condensate density distribution. Notice that in the case of non-interacting particles, the condensate size is independent of N; char-

acterised by the harmonic oscillator length scale $a_{ho} = \left(\frac{\hbar}{m\omega_{ho}}\right)^{1/2}$. Likewise, the momentum-space wavefucntion, given by the Fourier transform of $\psi(\mathbf{r})$, has an N-independent width; governed only by the Heisenberg uncertainty relationship (i.e. $\sim a_{ho}^{-1}$). a_{ho} is typically on the order of $1\,\mu$m, giving momentum widths on the order of $0.1\hbar k$, with k the wavenumber for the ^{87}Rb D_2 line.

In order to take account of atomic interactions, one should in principle solve the Heisenberg equations of motion for the field operator $\hat{\Psi}(\mathbf{r}, t)$ using the many-body Hamiltonian of N interacting particles. However, the mean-field approximation, first formulated by Bogoliubov in 1945 [122], has provided an excellent description of Bose-condensed atomic samples. The key result is the celebrated Gross-Pitaevskii equation:

$$i\hbar\frac{\partial}{\partial t}\Phi(\mathbf{r}, t) = \left(-\frac{\hbar^2\nabla^2}{2m} + V_{ext}(\mathbf{r}) + U|\Phi(\mathbf{r}, t)|^2\right)\Phi(\mathbf{r}, t) \tag{5.5}$$

where U is the mean-field coupling constant, which approximates the the atomic interactions as low-energy binary collisions via the two-body potential $V_i(\mathbf{r}' - \mathbf{r}) = U\delta(\mathbf{r}' - \mathbf{r})$. Such collisions are assumed to be s-wave, which are spherically symmetric and characterised by the s-wave scattering length a with $U = 4\pi\hbar^2 a/m$. a can be thought of as the effective radius of a hard-sphere scattering potential.

This non-linear Schrödinger equation models a BEC as a single particle wavefunction normalised to N, with the atom-atom interactions treated as a potential term proportional to the BEC density $|\Phi|^2$. For $a > 0$, one can think of this as each atom in the condensate 'feeling' a mean repulsive potential due to every other atom. For all but very low atom numbers, $a < 0$ condensates are unstable and collapse [119], and we assume $a > 0$ for all that follows.

There are two critical assumptions in deriving the GPE: that $N \gg 1$, and that the s-wave scattering length is much less than the average particle separation, i.e. $\bar{n}a^3 \ll 1$, where $\bar{n}$ is the mean density.

The ground state for a given harmonic trap is a stationary solution, and can found by setting $\Phi(\mathbf{r}, t) = e^{-i\mu t/\hbar}\phi(\mathbf{r})$, where μ is the chemical potential. The GPE then becomes:

$$\mu\phi(\mathbf{r}) = \left(-\frac{\hbar^2\nabla^2}{2m} + V_{ext}(\mathbf{r}) + U|\phi(\mathbf{r})|^2\right)\phi(\mathbf{r}) \tag{5.6}$$

In general, equation (5.6) is readily solved numerically. However, the ratio of the

interaction to kinetic energy is given by Na/a_{ho},[2] and in the limit that $Na/a_{ho} \gg 1$ we may neglect the kinetic term, proportional to $\nabla^2\phi(\mathbf{r})$. Solving for the density, this gives:

$$\begin{aligned} n(\mathbf{r}) = |\phi_{TF}(\mathbf{r})|^2 &= \frac{1}{U}\left[\mu - V_{ext}(\mathbf{r})\right] \\ &= n_0\left(1 - \frac{x^2}{r_x^2} - \frac{y^2}{r_y^2} - \frac{z^2}{r_z^2}\right) \end{aligned} \tag{5.7}$$

This is known as the Thomas-Fermi approximation, with $n_0 = \mu/U$ the peak density and r_i the Thomas-Fermi radius in the ith direction. For the experiments in this thesis, we use ^{87}Rb condensates of typically $10^5 - 10^6$ atoms, and trapping frequencies on the order of $\omega_{ho} \sim 2\pi \times 50\,\mathrm{Hz}$. $a \sim 5 \times 10^{-9}\,\mathrm{m}$ for ^{87}Rb, and thus $Na/a_{ho} > 350$.

Equation (5.7) is an inverted parabola in each direction, as defined by $V_{ext}(\mathbf{r})$. When $V_{ext}(\mathbf{r}) = \mu$, the density goes to zero, giving the Thomas-Fermi radii for the condensate:

$$\begin{aligned} r_i &= \sqrt{\frac{2\mu}{m\omega_i^2}} \\ &= a_i\sqrt{\frac{2\mu}{\hbar\omega_i}} \end{aligned} \tag{5.8}$$

where a_i is the harmonic oscillator length in the i^{th} direction. Normalising the BEC wavefunction to N gives the value of the chemical potential as:

$$\mu = \frac{\hbar\omega_{ho}}{2}\left(\frac{15Na}{a_{ho}}\right)^{2/5} \tag{5.9}$$

For typical experimental parameters the Thomas-Fermi radii are on the order of $10\,\mu$m, larger than the harmonic oscillator length. In fact, as $Na/a_{ho} \gg 1$, and ω_{ho} is on the order of ω_i, then $r_i \gg a_i$. This can be intuitively understood through the mean-field repulsion, which pushes atoms further out into the wings of the density distribution compared with the non-interacting case. As a result, one expects that the momentum width of an interacting condensate *in-trap* will be *smaller* than that of a non-interacting bose gas due to simple Heisenberg arguments. This observation will be important when we come to discuss the divergence of atom-laser beams.

[2] This can be seen by converting equation (5.6) to dimensionless units using the harmonic oscillator energy and length scales

5.2.2 The Momentum Distribution of a Condensate

The narrow momentum distribution of a condensate is arguably its most attractive property for atom interferometry. The effects of momentum width are pronounced in the atom-light interaction for LMT beamsplitters, and a narrow momentum width can help reduce systematic effects; see chapter 10. Here we highlight the momentum distribution for trapped, and ballistically expanding BECs.

In-Trap

In order to calculate the in-trap momentum distribution of a BEC, we take the Fourier transform of the position-space wave-function. In the Thomas-Fermi limit, the momentum distribution is then:

$$\begin{aligned} n(\mathbf{p}) &= \left| \int e^{-i\mathbf{p}\cdot\mathbf{r}/\hbar} \phi_{TF}(\mathbf{r}) d^3\mathbf{r} \right|^2 \\ &= r_x r_y r_z \frac{15N}{16\hbar^3} \frac{J_2(\tilde{p})^2}{\tilde{p}^4} \end{aligned} \tag{5.10}$$

where $\tilde{p} = \frac{1}{\hbar}\sqrt{p_x^2 r_x^2 + p_y^2 r_y^2 + p_z^2 r_z^2}$ with $\mathbf{p} = (p_x, p_y, p_z)$, and J_2 is the second order Bessel function of the first kind. In general, the momentum width of this state should be calculated using the relation $(\Delta p_i)^2 = \langle \hat{p}_i^2 \rangle - \langle \hat{p}_i \rangle^2$ for the ith direction, where $\hat{p}_i$ is the momentum operator. However, $\langle \hat{p}_i^2 \rangle$ is divergent as a result of the sharp edges of the Thomas-Fermi density distribution [123]. In fact, the Bessel function is representative of this through its oscillatory behaviour with increasing $\tilde{p}$. A numerical calculation of the density distribution from the GPE does not have sharp edges, and consequently the momentum distribution simply decays with $\tilde{p}$.

We may estimate the momentum width from equation (5.10) by using a gaussian distribution [57], which well approximates the central lobe of $n(\mathbf{p})$ in each direction as shown in figure 5.2 for the i^{th} direction. The dashed curve is the gaussian, and both are normalised to 1 at $p_i = 0$ with arbitrary units. By equating the area under each curve, we obtain an estimate for the momentum width

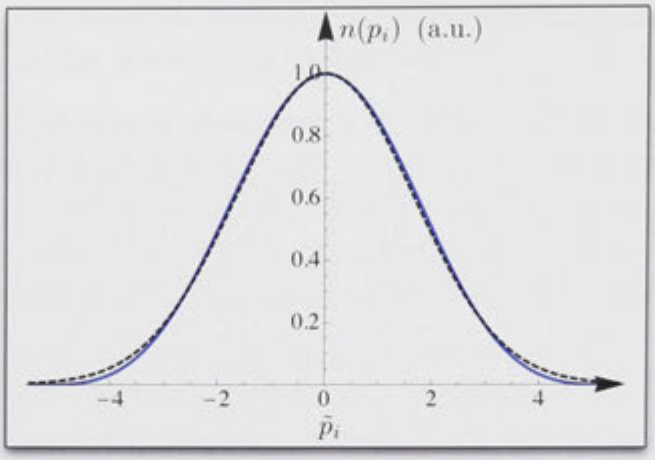

Figure 5.2: In-trap Thomas-Fermi momentum distribution along the i^{th}-direction (blue line), compared with a gaussian of width Δp_i (black dashed line). Both distributions are normalised to 1 at $p_x = 0$, with arbitrary units. Δp_x is estimated as the gaussian standard deviation which sets the areas under each curve equal.

from the gaussian standard deviation. For example, along the x-direction:

$$\begin{aligned} \Delta p_x &= \frac{2048\sqrt{2}}{315\pi^{3/2}} \frac{\hbar}{r_x} \\ &\simeq 1.65 \frac{\hbar}{r_x} \end{aligned} \tag{5.11}$$

with similar expressions for the y- and z-directions, replacing r_x with the corresponding Thomas-Fermi radius. Thus, the momentum width of a BEC in-trap is on the order of that dictated by the Heisenberg uncertainty principle, as intuition would suggest. As $r_i \sim 10\,\mu$m, typical in-trap momentum widths are $\Delta p_i \sim 0.01\hbar k$. This is around an order of magnitude smaller than the corresponding ground state of a non-interacting Bose-gas [equation (5.3)]. For an eye-opening comparison, a classical non-interacting gas with this momentum width corresponds to a Maxwell-Boltzmann distribution at a meagre temperature 40 pK for ^{87}Rb.

Ballistically Expanding Bose-Einstein Condensates

Although the momentum width of a BEC is very narrow in-trap, for the interferometers discussed in this thesis (and indeed most atom interferometry based inertial sensors) the atomic source must freely evolve in an inertial frame. For a BEC, this means releasing it from the trap, which is typically switched off sud-

denly. This results in a conversion of the interaction energy due to the mean-field into kinetic energy, driving expansion of the cloud and increasing its momentum width. In practice, it is straightforward to numerically integrate the GPE in order to determine the dynamic properties of the expanding cloud, including its momentum width. We may however gain some insight from an analytic treatment.

It can be shown that in the Thomas-Fermi limit, the parabolic profile of the condensate density is preserved, with a rescaling of the Thomas-Fermi radii in time [119]:

$$r_i(t) = b_i(t) r_i(0) \tag{5.12}$$

The dimensionless scaling parameters b_i obey the differential equations:

$$\frac{d^2 b_i}{dt^2} = \frac{\omega_i^2}{b_i b_x b_y b_z} \tag{5.13}$$

with $b_i(0) = 1$, and $\dot{b}_i(0) = 0$ for a sudden trap switch-off at $t = 0$. It can also be shown that the release energy of the condensate is related to the chemical potential and the scaling parameters by [119]:

$$E_{rel} = \frac{2\mu}{7}\left(\frac{1}{\prod_i b_i} + \frac{1}{2}\sum_i \frac{\dot{b}_i^2}{\omega_i^2}\right) = \frac{2\mu}{7} \tag{5.14}$$

where the second equality follows from conservation of energy ($\dot{E}_{rel} = 0$), as well as applying the initial conditions for b_i and $\dot{b}_i$. Equation (5.14) is nothing more than a sum of the interaction energy (1st term), and the kinetic energy (2nd term).

For simplicity, we now assume a spherical trap, and consider the asymptotic limit of E_{rel}. In this limit, the Thomas-Fermi radii grow to infinity, and thus the interaction energy term goes to zero. Note that a full numeric integration demonstrates that $\dot{b}$ has reached within 3% of is asymptotic value after $t = 4\omega_{ho}^{-1}$. In the asymptotic limit, equation (5.14) then becomes:

$$\dot{b} = \sqrt{\frac{2}{3}}\omega_{ho} \tag{5.15}$$

Thus, the radius of the BEC grows linearly in this limit and is considered to be

ballistically expanding at a velocity:

$$v = \dot{b}(t)r(0) = \sqrt{\frac{4\mu}{3m}} \tag{5.16}$$

or in terms of momentum,

$$p_{tof} = \sqrt{\frac{4m\mu}{3}} \tag{5.17}$$

This represents the momentum of the 'edge' of the cloud. We then use the root-mean-square (RMS) cloud radius $\bar{r} = r(0)/\sqrt{7}$ to give a measure of the ballistically expanded cloud's RMS momentum width:

$$\Delta p_{tof} = \sqrt{\frac{4m\mu}{21}} \tag{5.18}$$

As this estimate only derives from kinetic energy arguments, we must also include the effect of the initially non-zero momentum width in-trap. Combined in quadrature with result (5.11), the total momentum width for a ballistically expanding BEC can be estimated as:

$$\Delta p_{exp} \simeq \left(2.72\hbar^2\frac{m\omega_{ho}^2}{2\mu} + \frac{4m\mu}{21}\right)^{1/2} \tag{5.19}$$

In figure 5.3, we plot the momentum width of a BEC along the z-direction as a function of expansion time. The solid line represents a full numeric integration of the GPE for our experimental parameters of $N = 5 \times 10^4$ atoms and $(\omega_x, \omega_y, \omega_z) = (50, 57, 28)$ Hz. Data points are measured momentum widths using Bragg spectroscopy [57, 83] (also chapter 8 for our Bragg laser-system), with the inset giving an example Bragg spectrum. The vertical thickness of the data points represents the measurement uncertainty. Measured and theoretically calculated momentum widths are in excellent agreement, with $\Delta p_z \simeq 0.14\hbar k$.

Intriguingly, if we calculate Δp_z from equation (5.19) using the geometric mean of our experimental trapping frequencies for ω_{ho}, then we find agreement within 10% of the measured value. The discrepancy is likely due to the approximation of a spherical trap. Nevertheless, the analytic arguments given earlier can provide a robust estimate of the momentum width of a ballistically expanding BEC.

In general, very narrow momentum distributions are desirable for several reasons, which are discussed in detail in chapter 10. Suffice it to say that the atomic beamsplitters and mirrors involve momentum sensitive transitions, and

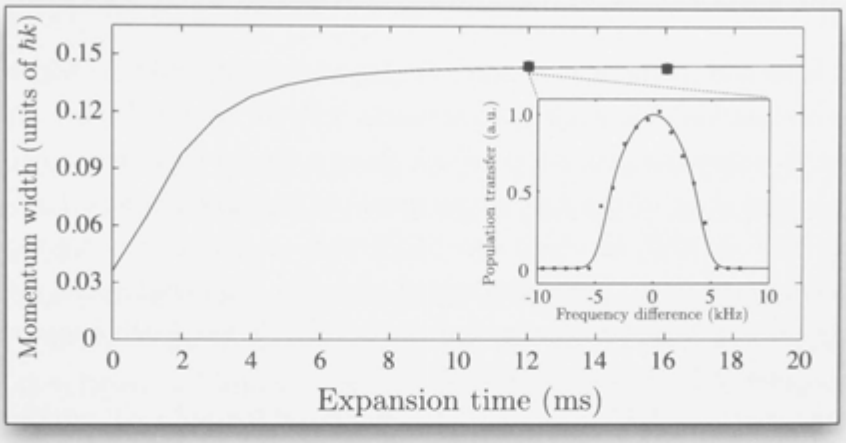

Figure 5.3: Momentum width along z (parallel to gravity) as a function of expansion time. Data points are measured values using Bragg spectroscopy. The inset is the Bragg spectroscopy data for the highlighted point. Solid lines are numeric solutions to the GPE with no free parameters.

thus a finite momentum width will play a role in determining the effectiveness of the atom-optical elements. It is worth noting that BECs can have momentum widths around an order of magnitude smaller than the coldest laser-cooled (thermal) atomic sources at around 150 nK [10]. Even so, work presented in [78] and in chapter 10 suggests sources even narrower than a condensate will be advantageous for LMT beamsplitters.

For the typical parameters above, Δp for an expanding cloud is the same order of magnitude as that of a non-interacting Bose-gas. Thus, while mean-field effects play a role in broadening the momentum width, switching them off completely in-trap (by using a Feshbach resonance, for example [124]), does not provide a large reduction in momentum width due to the reduction in cloud size (for a given trap). One possibility is to tune the interactions to zero at the time of release from the trap. This results in a momentum width equal to the in-trap width [equation (5.11)], which is smaller than the harmonic oscillator ground state momentum width [125]. Tuning to even larger interaction strength would increase the cloud size further, further reducing the momentum width for such a technique.

On the other hand, atom-lasers, both pulsed and continuous, can be made to approach the Heisenberg limit of the Thomas-Fermi momentum width [126]. Atom-lasers are the topic of the following section.

5.3 Atom Lasers

Often, BEC is touted as the matter-wave analog of the optical-laser, which is a macroscopic occupation of a single optical mode. Indeed, one of the key aspects of a BEC are its coherence properties, which share a strong similarity with that of the optical laser. One of the first experiments on interference with BEC was performed at MIT in 1997, in which two BECs were produced in a double-well trap, before being released. Once overlapped, the two condensates displayed a spatial interference pattern, in a similar fashion to Young's double slit experiment; demonstrating first-order spatial coherence [127].

In the same year, the MIT group also demonstrated RF-induced outcoupling of a magnetically trapped BEC. This produced pulses of coherent atomic clouds, which freely evolved under gravity – effectively producing the worlds first *pulsed* atom-laser [49]. Shortly after this, Esslinger *et al.* were able to extend the outcoupling process to produce the first *continuously* outcoupled beam of Bose-condensed atoms, strengthening the analogy with the optical-laser [51]. Furthermore, using single-atom counting statistics, it was latter shown by Esslinger's group that the second-order correlation function $g_2(\tau)$ of a continuous atom-laser was equal to 1, as is the case for the optical laser. This extended the analogy with the optical-laser to the quantum regime [56].

In this section, we review the properties of atom-lasers and the different outcouplers for producing them. In particular, we focus on transverse momentum width, in comparison to a ballistically expanding BEC. In chapter 7, we compare the atomic flux of atom-lasers produced using different outcoupling schemes.

5.3.1 Atom-Lasers from Magnetically Trapped BECs

BEC is often produced experimentally in a magnetic trap, which confines atoms by taking advantage of their magnetic moment. In the weak magnetic field of typical magnetic traps, the Zeeman splitting is much less than the hyperfine ground-state splitting, which allows one to approximate the Breit-Rabi formula [128] for the ^{87}Rb $5^2S_{1/2}$ ground states as:[3]

$$E_{F,m_F}(B) \simeq -\frac{\hbar\omega_{hf}}{8} + (-1)^F \left(\frac{\hbar\omega_{hf}}{2} + m_F g_F \mu_B B \right) \tag{5.20}$$

[3]The nuclear angular momentum number of ^{87}Rb is I = 3/2.

with g_F the total angular momentum gyromagnetic factor:

$$g_F \simeq \frac{g_s}{4} \tag{5.21}$$

where we have also used the fact that $g_I \ll g_s$.[4] $\hbar\omega_{hf}$ is the ground state hyperfine splitting, μ_B the Bohr magneton, and B the magnitude of an externally applied magnetic field.

Many current-coil configurations exist for producing magnetic fields with local minima. For the work in this thesis we use the quadrupole-Ioffe configuration (QUIC), developed in Münich [129] (see also section 5.4.2). The magnetic field magnitude about its minima can be well approximated by:

$$B(\mathbf{r}) = B_0 + \frac{B_x''(0)}{2}x^2 + \frac{B_y''(0)}{2}y^2 + \frac{B_z''(0)}{2}z^2 \tag{5.22}$$

where the we have considered only one dimension for simplicity and the origin is placed at the field minima B_0, also called the "bias field." Thus, the resultant harmonic potential has a trapping frequency in the ith direction proportional to the field curvature: $\omega_i^2 = m_F g_F \mu_B B_i''(0)/m$.

Combing (5.22) with (5.20), E_{F,m_F} has a local minima for negative m_F values for $F = 1$ and positive m_F values for $F = 2$. The energy splitting between adjacent m_F states is given by:

$$\Delta E_F(B) = (-1)^F \Delta m_F g_F \mu_B B(\mathbf{r}) \tag{5.23}$$

where $\Delta m_F = \pm 1$. ΔE_F is position dependent by virtue of equation (5.22), allowing us to selectively address different regions within a trapped cloud. This feature is critical for both RF-forced evaporative cooling, and atom-laser outcoupling in magnetically confined samples, which both rely on removing atoms from the trap by coupling them to the untrapped state ($m_F = 0$). More specifically, $g_F \mu_B / h \sim 0.7\,\mathrm{MHz/G}$, and thus Zeeman sublevels are split on the order of MHz for typical bias fields on the order of a few Gauss. Using RF [49] or Raman coupling [50], different m_F states can be coupled, and thus trapped atoms can be driven to either the untrapped state, or high-field seeking states that are ejected from the trap. In addition, Raman transitions between the hyperfine ground-states are also suitable for atom-laser production and produce superior beam quality and flux, as shown in this section and chapter 7 respectively.

[4] g_I is the nuclear gyromagnetic factor, and is smaller than the electron gyromagnetic factor g_s by the electron to proton mass ratio.

Atom-Laser Outcoupling

The basic operation of an atom-laser outcoupler for magnetically trapped condensates is a coupling between the trapped and untrapped m_F states. Under a weak perturbative coupling, atoms transferred to $m_F = 0$ will freely evolve under gravity and the mean-field potential, falling out of the magnetic trap and forming an atom-laser beam. As an example, consider the $|1, -1\rangle$ state of ^{87}Rb. Along the z-axis, the total potential for an atom is the sum of the Zeeman energy and gravitational potential, giving:

$$V_{1,-1}(z) = \frac{1}{2}m\omega_z^2 z^2 + mgz + \frac{\mu_B B_0}{2} + C \tag{5.24}$$

$$V_{1,0}(z) = mgz + C \tag{5.25}$$

for the trapped and untrapped m_F states respectively, with g the magnitude of acceleration due to gravity and C a constant. These potentials are given in figure 5.4, which is a schematic representation of atom-laser outcoupling. Note that the minimum of the trapping potential $V_{1,-1}$ is not centred at the field minimum ($z = 0$) but sags to $z_s = -g/\omega_z^2$ due to gravity.

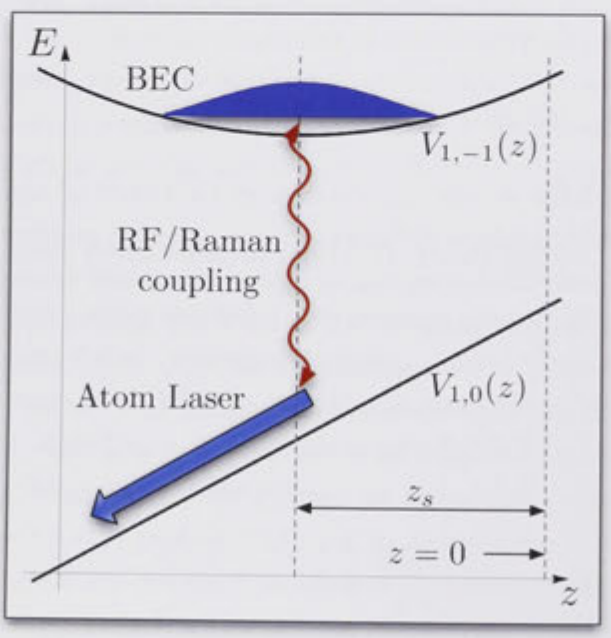

Figure 5.4: Schematic of atom-laser outcoupling from a magnetic trap. The condensate sags under gravity to $z_s = -g/\omega_z^2$, for which the local magnetic field environment then defines the RF or Raman resonance required to outcouple atoms from a particular region in the condensate.

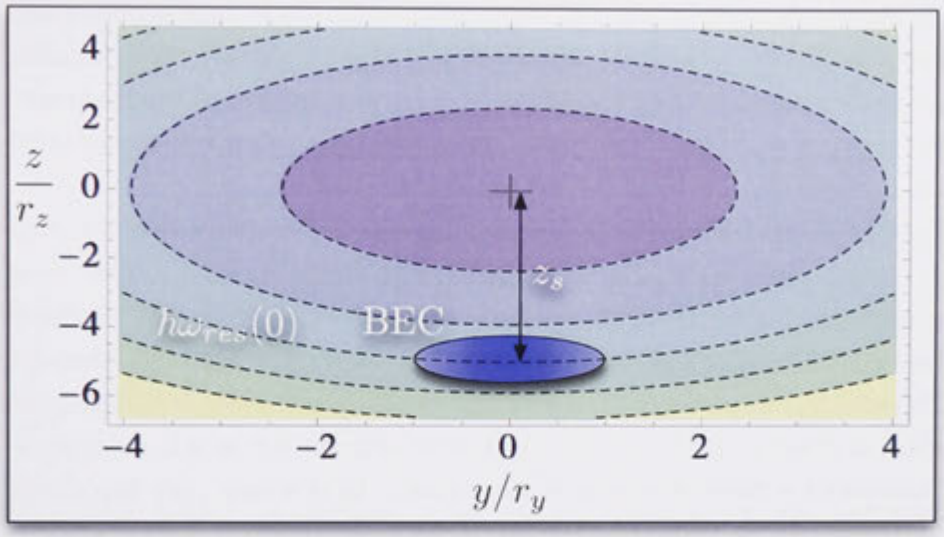

Figure 5.5: Cross-section of outcoupling-resonance surfaces in the yz-plane (dashed lines) in a harmonic magnetic trap. Energy increases from blue → green → yellow, with each contour representing an equal energy-step size. The BEC is represented by the blue ellipse, with accurate proportion to and position within the magnetic field. $\hbar\omega_{res}(0)$ labels the resonance surface which intersects the centre of the condensate. It is approximately planar within the condensate due to its sagging under gravity in the magnetic field.

The resonance at a particular position in the cloud is given by:

$$\begin{aligned} \hbar\omega_{res}(z) &= V_{1,-1}(z) - V_{1,0}(z) \\ &= \frac{1}{2}m\omega_z^2 z^2 + \hbar\omega_b \end{aligned} \tag{5.26}$$

where $\hbar\omega_b = \mu_B B_0/2$ and resonance at the centre of the condensate is given by $\omega_r(z_s)$. Of particular importance is the dependence of the resonance on the bias field. If the field-minimum is not stable in time, particularly over the duration of the outcoupling interaction, a continuous, uniform, and low-noise beam of atoms cannot be produced.

In three dimensions, the resonance condition corresponds to an energy surface defined by equation (5.26), and is thus an ellipsoid. Figure 5.5 shows resonance surfaces as lines in the yz-plane for $(\omega_\rho, \omega_y) = 2\pi \times (130, 13)$ Hz, which are typical values for the atom-laser experiments in this thesis. The BEC is represented by the blue ellipse, at its position and spatial extent within the magnetic field for the specified trapping frequencies. Because the BEC sags under gravity to $z = z_s$, an intersecting resonance surface is just a small fraction of the total ellipsoid, and is approximately planar in the xy-plane. Thus, in this regime and with

perturbatively weak outcoupling, the atom-laser originates from a narrow region centred on this plane.[5] Indeed, in the absence of gravity, or for much larger ω_z, this would not be the case, and the atom-laser is coupled from an ellipsoidal region within the condensate. This results in a highly divergent and multi spatial-mode beam; not particularly desirable for interferometry [130].

It should be noted that one of the results of coupling Zeeman states of a single hyperfine ground state is that the splitting between levels is equal to first order. Thus, population transferred to the untrapped state can be coupled to the anti-trapped state with non-negligible probability. The outcoupler system is therefore multi-level, adding complexity to the resultant beam. Multi-state outcouplers are investigated in detail in [131]. It is also possible to drive $\Delta F = \pm 1$, $\Delta m_F = \pm 1$ Raman transitions *between* hyperfine ground-states. In this case, only two atomic states are coupled due to two-photon selection rules. In chapter 6, we will describe our Raman laser system which can be used as a hyperfine-outcoupler, and in chapter 7, we will compare the output the different outcouplers: RF, Zeeman-Raman, and hyperfine-Raman.

Atom-Laser Momentum Width

In designing atom interferometers which utilise atom-lasers, a realistic configuration is with the beamsplitters perpendicular to the atom-laser beam. In this configuration, the transverse momentum width will play an important role (see chapter 10). The transverse momentum width (simply, "momentum width" from here on in this section) is related to the spatial-mode of the atom-laser, rather analogous to the relationship between the spatial mode of an optical laser-beam and its divergence. Indeed, without interactions the spatial-mode evolution is well described by Gaussian optics, diverging only due to the Heisenberg uncertainty principle. However, in the presence of interactions, the mean-field repulsion broadens and complicates the atom-laser's spatial mode. Detailed study of the spatial-mode of free space atom-lasers can be found in [52, 54, 126], as well as the thesis of M. Jeppesen [132]. Here, we give a simple semi-classical description of the atom laser momentum width, and derive an order of magnitude estimate.

Once coupled to the untrapped state, atoms evolve freely under gravity and the mean-field potential of the trapped atoms. Consider the yz-plane. Atoms will fall out of the condensate along z, and experience the mean-field repulsion

[5] What is meant by "weak" outcoupling here will be discussed in detail in chapter 7. For now, it is enough to consider the coupling as irreversible, such that atoms to not Rabi-flop back to the trapped state.

in all three directions. As we are interested in the transverse momentum width, we consider dynamics in the y-direction. Under the Thomas-Fermi approximation, the mean-field potential is an inverted parabola [see equation (5.5)] and the classical equation of motion along y is therefore:

$$m\frac{d^2y}{dt^2} = m\omega_y^2 y \tag{5.27}$$

which has the solution:

$$y(t) = y_0 \cosh(\omega_y t) \tag{5.28}$$

$$\therefore v_y(t) = \omega_y y_0 \sinh(\omega_y t) \tag{5.29}$$

where y_0 is the initial y-coordinate of the atom with respect to the centre of the condensate (i.e. $|y_0| \leq r_y$), and v_y is the classical velocity. An atom must fall a distance $d = r_z(1 - y_0^2/r_y^2)^{1/2} + z0$ to escape the condensate, with z_0 the initial z-cooridinate with respect to the condensate centre. Thus, the escape time due to gravity is given by:

$$t_e(y_0, z_0) = \frac{2}{g}\left[r_z(1 - y_0^2/r_y^2)^{1/2} + z0\right]^{1/2} \tag{5.30}$$

and the atom will have acquired a transverse velocity of $v_y(t_e)$. The contribution of the mean-field repulsion along z to t_e has been neglected as the gravitational force is an order of magnitude larger for typical experimental parameters. In the perturbative outcoupling regime, the resonance is Fourier limited – for example, 20 ms of outcoupling will have a width of $\Delta = \pm 2\pi \times 50\,\text{Hz}$. Combining this energy width with equations (5.22) and (5.23) gives an estimate of the upper and lower bounds $z_\pm$ of the coupling region within the condensate as:

$$\frac{1}{2}m\omega_z^2(z_s + z_\pm)^2 - \frac{1}{2}m\omega_z^2 z_s^2 = \mp\hbar\Delta \tag{5.31}$$

which assumes the coupling region is planar. Note that for $\Delta = 2\pi \times 50\,\text{Hz}$, the thickness of this region is $z_+ - z_- < 0.01 r_z$. The variance in v_y can then be found using the Thomas-Fermi wavefunction:

$$(\Delta v_y)^2 = \frac{1}{N_R}\int_R |\phi(\mathbf{r})|^2 v_y\left[t_e(y_0, z_0)\right]^2 dx_0 dy_0 dz_0 \tag{5.32}$$

where the integral is over the region volume R, and N_R is the number of atoms

in the coupling region. In general, this integral cannot be analytically solved. However, if we assume t_e is constant an analytic solution does exist and is given by:

$$(\Delta v_y)^2 = \frac{\mu r_x r_y^3 r_z}{210 U N_R} \left(\frac{12[z_+ - z_-]}{r_z} - \frac{4[z_+^3 - z_-^3]}{r_z^3} \right) \omega_y^2 \sinh^2(\omega_y t_e)$$
$$\simeq \frac{2\mu r_x r_y^3}{35 U N_R} (z_+ - z_-) \omega_y^2 \sinh^2(\omega_y t_e) \tag{5.33}$$

where the cubic terms in $z_\pm$ have been neglected as $z_\pm / r_z \ll 1$. For example, using the escape time from the centre of the condensate, $t_e = (2r_z/g)^{1/2}$, gives an upper bound on the momentum width, as it assumes all atoms interact with the mean-field for the maximum escape time. For our parameters, this upper bound is $\Delta p_y = m\Delta v_y \simeq 0.033\hbar k$. Numerical integration of equation (5.32) gives $\Delta p_y \simeq 0.024\hbar k$; almost 30% lower. The above results apply equally to the x-axis with the appropriate parameter substitutions. Using $\omega_x = 2\pi \times 130\,\text{Hz}$, numerical integration gives $\Delta p_x \simeq 0.27\hbar k$ in the tight-trapping transverse direction.

The above arguments show that an atom-laser has a momentum width substantially narrower than a ballistically expanding BEC, although still limited by mean-field effects. For example, in the y-direction, the Heisenberg limited in-trap momentum width is $\sim 0.002\hbar k$; an order of magnitude lower than the atom-laser momentum width. However, if Raman transitions are used, they can impart a momentum "kick" to the outcoupled atoms along gravity, leading to a reduction in t_e and therefore a reduction in the momentum width as the atoms interact with the mean-field for a shorter period of time. This was the focus of work by M. Jeppesen *et al.*, which rigorously showed that a Raman kick of $\sim 1.5\hbar k$ leads to a momentum width only a factor of 1.4 above the Heisenberg limit for their trap parameters [126, 132]. The above model estimates a momentum width of $\Delta p_y \simeq 0.011\hbar k$ and $\Delta p_x \simeq 0.11\hbar k$.

Atomic source	Momentum width
Laser cooled ^{133}Cs (150 nK) [10]	1 $\hbar k_{Cs}$
Ballistically Expanding BEC	0.1 $\hbar k$
Atom-laser	0.01 $\hbar k$

Table 5.1: Summary of atomic source momentum widths. Typical orders of magnitude are given. The laser cooled source is stated in units of the recoil momentum for the ^{133}Cs D_2 line.

Table 5.1 summarises the order of magnitude momentum width of typical and *current* atomic sources, including the coldest reported laser-cooled thermal source at $\sim 150\,\mathrm{nK}$ [10].

5.4 Experimental Production of Bose-Einstein Condesates

In general, the techniques for producing BEC are well documented and established, with excellent reviews given in [77, 133, 134]. While producing BEC remains a challenging feat, technology has advanced since its inception to the point that it has become a standard atomic source in many laboratories around the world. In this thesis, two existing BEC machines have been used for the experiments described. Over the last four years, the work in this thesis has made limited contributions to their construction. Here, we give only a brief description of each machine.

A generic scheme for cooling to BEC is summarised below:

1. Atoms are first captured and laser cooled in a 3D magneto optical trap (MOT). Often, the 3D MOT is loaded from a cold atomic beam such as that from a 2D MOT or a Zeeman slower. This allows the 3D MOT to be located in an ultra-high vacuum (UHV) region ($< 10^{-10}\,\mathrm{mbar}$), to minimise background collisions that limit the BEC trap lifetime. Cooling in a 3D MOT achieves Doppler limited temperatures, which is $\sim 145\,\mu\mathrm{K}$ for the D_2 line of $^{87}\mathrm{Rb}$ [100].

2. Sub-Doppler cooling techniques are applied to enable temperatures below the Doppler limit. This is typically polarisation gradient cooling (PGC) [135], which can achieve temperatures as low as $1\,\mu\mathrm{K}$. However, this is usually at the cost of density, and thus for BEC production 20-40 μK is more typical.

3. The ultra-cold cloud is then loaded into a trap, using either magnetic confinement (the Zeeman effect), or far off-resonant optical confinement which takes advantage of the AC Stark shift [97]. At this stage, often the cloud is compressed to boost the density at the cost of increased temperature.

4. The dense, compressed cloud is then evaporatively cooled to temperatures below the critical condensation temperature $\mathcal{T}_c$. In a magnetic trap, this is forced using RF induced spin flips, which selectively transfer more energetic

atoms into untrapped states. In an optical trap, the trap depth is reduced causing more energetic atoms to 'spill' out. In both cases, remaining atoms re-thermalise to a lower temperature.

5.4.1 Laser Cooling Systems

Laser cooling of atomic ensembles is a well established tool used in the first stages of cooling to condensation. For the purpose of this thesis we only summarise the laser systems used. For an excellent history of laser cooling, see [41, 42, 43]. In our labs, we source our cooling light from home-built grating-stabilised external cavity diode lasers (ECDLs), typically operated in the Littrow configuration [136]. These are driven by commercially developed diode laser controllers from MogLabs [137], which contain highly stable current and temperature controllers, as well as high-voltage piezo drivers and locking electronics. Lasers are locked using saturated absorption spectroscopy with Rubidium vapour cells, and different variations of the Pound-Drever-Hall frequency-modulation (FM) spectrocopy technique [138]. Often, we use Zeeman-modulation as our FM technique [139, 140], as this avoids modulating the laser, and potential broadening of the line width. Locked in this way, our home built ECDLs typically have line widths on the order of 100 kHz over timescales associated with an experimental cycle (10s of seconds). During the course of the work in this thesis, a simple and cost-effective locking technique was also developed based on introducing FM using a piezo-modulated mirror. This was the subject of a publication [141], which is provided in appendix A.

Where required (e.g. our 2D and 3D MOT lasers), we amplify our laser light using high-power tapered amplifiers (1.5-2.0 W) from m2kLaser [142]. Frequency shifting and shuttering is performed using a combination of acousto-optic modulators (AOMs) and electro-optic modulators (EOMs) as necessary. Light is then coupled into polarisation-maintaining single-mode optical fibres which clean the elliptical spatial mode, and isolate the laser system from the vacuum system optics (e.g. MOT and imaging). Typical optical power for each MOT is on the order 100 mW.

5.4.2 The Atom Laser BEC Machine

Originally built in 2006 by N. P Robins and C. Figl, the atom-laser machine (ALM) was designed to investigate the production of atom-lasers and their properties, with a major goal of producing a truly continuous atom-laser source. Im-

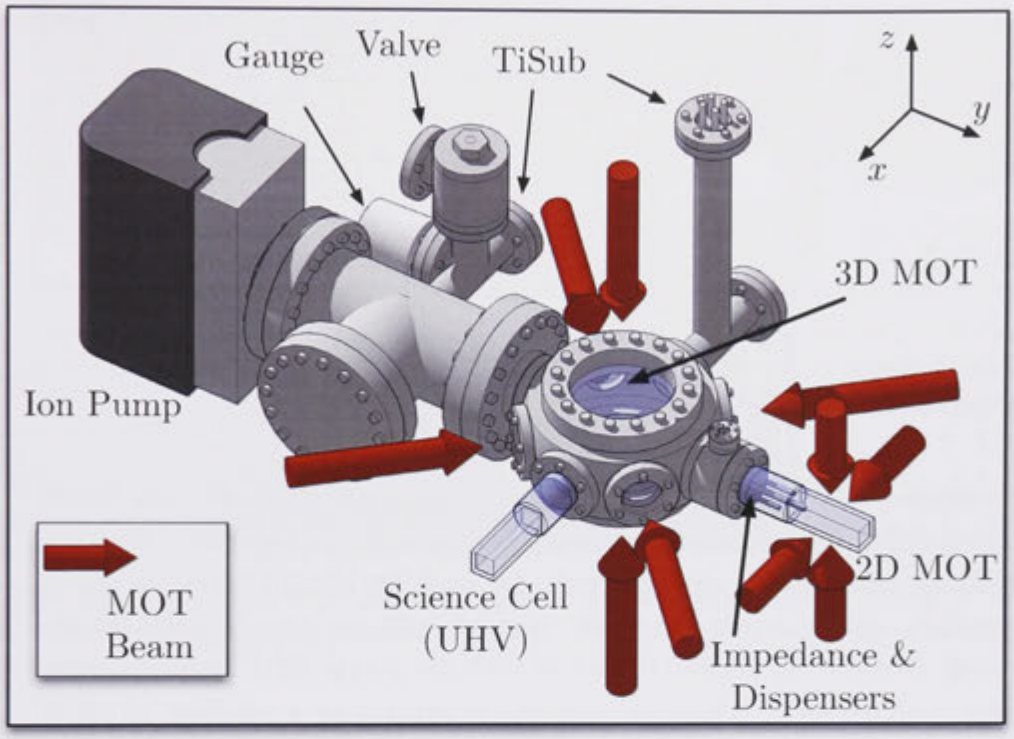

Figure 5.6: Simplified representation of the atom-laser machine vacuum system. A 2D MOT loads the 3D MOT through a pressure impedance. After laser-cooling and magnetic compression, the atomic ensemble is transported to the science cell where it is loaded into the magnetic trap for evaporation to BEC. Magnetic coils and their configurations are given in figure 5.7.

portant features of this system included a highly stable magnetic trap, in order to reliably address atoms in the BEC for outcoupling and pumping (see section 5.3), as well as separating the magnetic trap from the MOT region of the vacuum system; the intention being to simultaneously load MOTs while running a lasing condensate.

Figure 5.6 gives a simplified schematic of the ALM vacuum system. A key feature of the system are two quartz glass cells attached to a central main MOT chamber. The MOT chamber and adjoining science cell is operated at UHV ($\sim 10^{-11}$ mbar) in order to suppress background collisions, which limit the magnetic trap lifetime. Pumping is provided by a 40 L/s ion getter pump, and two titanium sublimation pumps (TiSubs), as shown. The second glass cell houses the 2D MOT and ^{87}Rb dispensers (Alvatech), and is isolated from the ultra-high vacuum region using a pressure impedance. The 2D MOT provides a flux of up to $\sim 10^{10}$ atoms/s for loading the 3D MOT using a push-beam (not shown).

The MOTs are constructed with the configurations given by the red arrows.

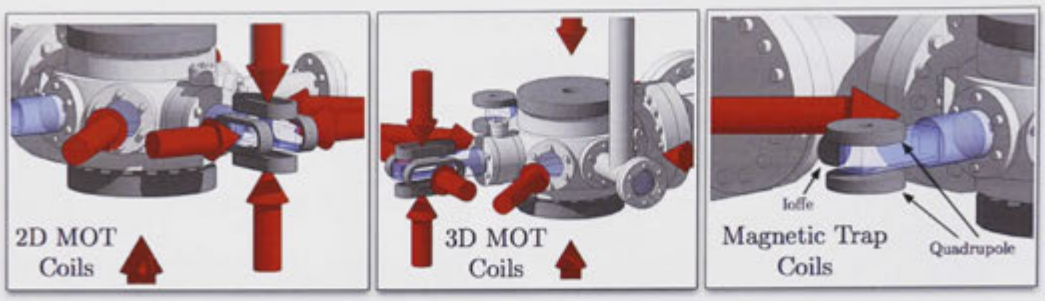

Figure 5.7: Atom-laser machine magnetic coils. 3D MOT coils are also used magnetic transport of the laser-cooled cloud to the magnetic trap. The magnetic trap coils are mounted on a chilled-water cooled aluminium block (see figure 5.8).

Counter-propagating beams are produced using retro-reflection, with the beams converging slightly to balance the intensity due to power loss on retro-reflection. Two-pairs of quadrupole 'racetrack' coils are used for the 2D MOT, as shown in figure 5.7. A single pair of circular current coils are used to generate the quadrupole field for the 3D MOT, coaxial with the z-axis MOT beams (gravity is in the $-z$-direction). These are capable of generating a gradient of up to 200 G/cm, and are also used for magnetic transport of laser-cooled atoms to the science cell (see cooling sequence below). Due to the large distance between them ($\sim$ 20 cm), the 3D MOT coils are required to carry up to 400 A of current. As a result, they are constructed from hollow copper tubing, which allows water to be pumped through the centre for cooling. The coils dissipate a peak power of $\sim$ 6 kW.

The magnetic trap is based on a simplfied Ioffe-Pritchard configuration known as a QUIC trap. It constitutes a set of quadrupole coils, with an orthogonal Ioffe coil as shown [129]. The trap is centred at the end of the science cell, with the Ioffe coil coaxial with the y-axis; defining the longitudinal axis of the cigar-shaped potential. Our trap is well approximated by a harmonic potential with trapping frequencies given by $(\omega_\rho, \omega_y) = 2\pi \times (130, 13)$ Hz for the $|1, -1\rangle$ state.

The experimental sequence for producing a BEC is as follows. The 2D MOT first loads more than 10^{10} atoms into the 3D MOT in less than 30 s. After loading, the MOT is magnetically compressed before applying a stage of PGC [135], which achieves temperatures of about 40 μK with little loss in atom number. At this stage, atoms are predominantly in the $F = 2$ ground state. By applying an optical pumping pulse of σ^- light, resonant with the $|F = 2\rangle \rightarrow |F' = 2\rangle$ transition, atoms are pumped into predominantly the $|1, -1\rangle$ state. The cloud is then caught in a magnetic quadrupole field with a gradient of 200 G/cm generated by the 3D

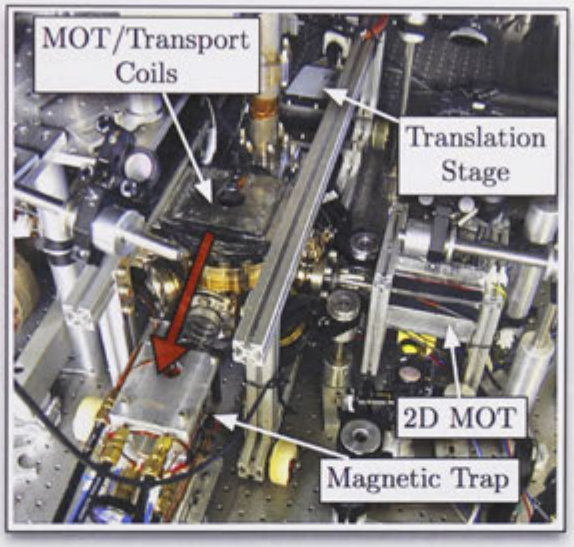

Figure 5.8: Photograph of the ALM, showing the magnetic trap, 2D and 3D MOTs, and the translation stage used for magnetic transport. The red arrow indicates the direction of translation.

MOT coils, which are switched on in under $10\,\mu$s. These coils are attached to a precision translation stage, oriented along the x-direction of figure 5.6, which allows precise transport of the cloud to the science cell and the magnetic trap. A photograph of the ALM is given in figure 5.8, showing the 2D and 3D MOTs, the translation stage and its direction of travel (red arrow), and the magnetic trap. After transporting the atoms over 20 cm, they are loaded into the harmonic trap, in which they are evaporatively cooled using a forced RF-evaporation ramp that selectively removes the most energetic atoms. This results in nearly pure Bose-condensed samples of up to 10^6 atoms, with no discernible thermal fraction.

The lifetime of the magnetic trap is ~ 40 s, which is ample time for the experiments in this thesis. Atoms are detected after release from the trap and during ballistic expansion using standard absorption imaging. Absorption imaging is well documented [118]. Briefly, we illuminate the atomic cloud using a $100\,\mu$s pulse of σ^+ radiation, resonant with the $|F = 2\rangle \rightarrow |F' = 3\rangle$ closed transition, and image them onto a charge-coupled device (CCD) camera using a single lens imaging system with a magnification of ~ 1.6. This image contains a shadow of the atomic cloud. A second pulse is applied after waiting 100 ms to give a background light intensity image. Using Beer's law, the logarithm of the ratio of these two images is then proportional to the column density $n(y, z) = \int n(\mathbf{r})dx$, where we image along the x-direction. In order to image atoms in $|F = 1\rangle$, we

apply a 100 μs pulse resonant with $|F = 1\rangle \rightarrow |F' = 2\rangle$, which repumps the atoms into $|F = 2\rangle$ prior to the first imaging pulse. A far more detailed analysis of our imaging system can be found in [143]. The total duty cycle of the machine is between 45 s and 60 s.

5.4.3 Dual-Species ^{87}Rb/^{85}Rb BEC Machine

Originally built by P. A. Altin and N. P. Robins, the dual-species Rubidium BEC machine was designed to produce condensates of ^{85}Rb in order to access a Feshbach resonance for tuning the atomic interactions via the scattering length [124]. In particular, a major goal was to revisit the so-called "Bosenova" experiments [144] and remedy a discrepancy between experimental and theoretical work [145]. This was recently accomplished by P. A. Altin *et al.* [146], with details being beyond the scope of this thesis. ^{85}Rb condensates are produced by sympathetically cooling with ^{87}Rb; thus a ^{87}Rb condensate is also produced, and it is with ^{87}Rb in this machine that the gravimetry experiments of chapter 9 were performed. This compact BEC machine has been extensively engineered, warrenting a detailed description of its design, operation, and performance in Review of Scientific Instruments [134]. Here, we only give a brief description of its operation for producing condensates of ^{87}Rb.

Figure 5.9 gives a simplified schematic of the vacuum system, including the major coil mount surrounding the science cell. The three smaller frames below show the different traps available for cooling to BEC. The vacuum system is relatively compact, and houses a high vacuum 2D MOT glass cell again isolated from the UHV region with a pressure impedance. The system is pumped with a combination of a 75 L/s ion getter pump and one TiSub. UHV pressure is on the order of 10^{-10} mbar.

The 2D MOT is essentially identical to that of the ALM, loading a 3D MOT with up to 10^{10} ^{87}Rb atoms in 5 s. The 3D MOT is located as shown in the figure, also setup in a slightly converging retro-reflection configuration. After loading, the cloud undergoes 20 ms of PGC before the repumping light is switched off for 1 ms, allowing the atoms to depump into the $F = 1$ ground state before all MOT light is switched off.

Atoms are then captured into the quadrupole field of the MOT coils and magnetically transported over 40 mm to the quadrupole field of the QUIC trap; oriented as shown in figure 5.9. This transport is aided by use of the rectangular transport coil, which is ramped up before ramping down (up) the MOT (QUIC)

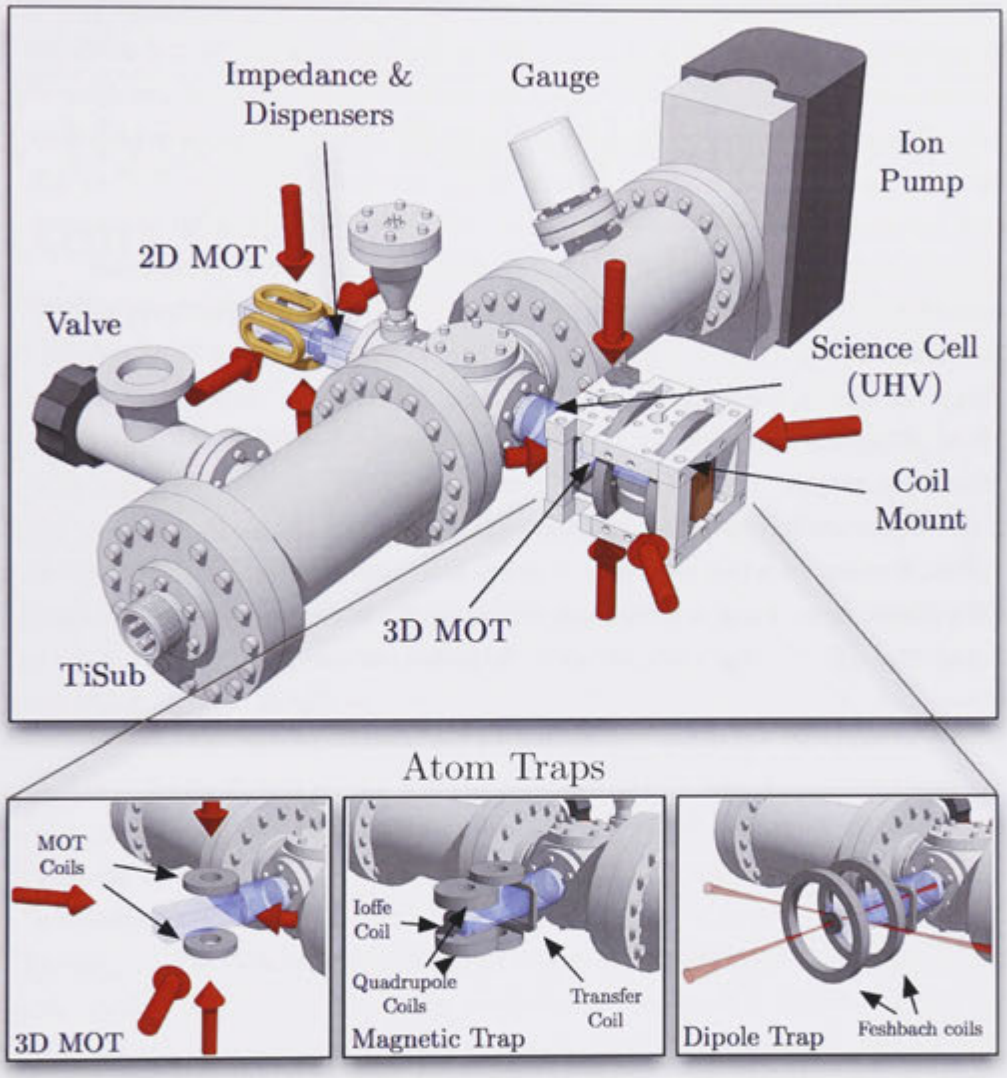

Figure 5.9: Simplified representation of the ^{87}Rb/^{85}Rb machine.

coils. The Ioffe coil is then ramped up converting the quadrupole trap field into the harmonic field of a QUIC trap, with trapping frequencies of $(\omega_\rho, \omega_y) = 2\pi \times (156, 16)\,\mathrm{Hz}$ for the $|1, -1\rangle$ state. There are in total 8 magnetic coils (not including coils for imaging, RF evaporation, etc.) surrounding the science cell in the coil mount, which is cooled by recirculated chilled water.

At this stage, there are on the order of 10^9 atoms at $200\,\mu\mathrm{K}$ in the QUIC trap, before RF forced evaporative cooling is applied over 15 s. In this way, pure ^{87}Rb condensate of 2×10^6 atoms can be produced. However, for the work in this thesis, we instead load the cloud into a dipole trap for the last stages of evaporation. The

dipole trap is necessary for producing ^{85}Rb condensates, which require application of an homogenous magnetic field to tune the scattering length. As the machine needs to be optimised for either the magnetic trap or dipole trap, at the time of the work in chapter 9, it was convenient to produce ^{87}Rb condensates in this way. Furthermore, operation in a dipole trap enables spin polarisation of the sample with ease by using Landau-Zener sweeps [147, 148, 149, 150]; useful for producing magnetically insensitive pure $|1,0\rangle$ condensates as a source for a gravimeter.

We produce a far off-resonant crossed dipole trap [97] using light from a 20 W Er-doped fibre laser at 1090 nm, which is split evenly on a polarising beamsplitter. Each beam passes through an $f = 100$ cm focal length lens. One"axial" beam is directed along the Ioffe coil axis, as shown in figure 5.9, with the lens place 98 cm from the atoms. The other beam crosses the axial beam at 75°, and also lies in the horizontal plane with the lens placed 106 cm from the atoms. RF evaporation is stopped when the cloud reaches a temperature of 10 μK, at which point the dipole beams are suddenly switched on to maximum power (9 W per beam) and the QUIC trap coils reduced to 50% current in order to aid with confinement along the axial beam. Evaporation in the dipole trap is initiated in this hybrid trap by reducing the power in the dipole beams, which reduces the trap depth. Towards the end of the evaporation cycle, the magnetic trap is completely switched off, leaving the atoms in the all-optical trap.

This scheme produces pure condensates of up to 10^6 ^{87}Rb atoms in 30-45 s, and a final harmonic potential with $(\omega_x, \omega_y, \omega_z) = 2\pi \times (57, 28, 50)$ Hz. Standard absorption imaging is used for detection, as described in section 5.4.2.

Chapter 6

A Hyperfine Raman Coupler for Atom Optics

Work in this chapter has been peer-reviewed and published in:

J. E. Debs, D. Döring, N. P. Robins, C. Figl, P. A. Altin, and J. D. Close. A two-state raman coupler for coherent atom optics. Opt. Express 17 p.2319 (2009). [55]

D. Döring, J. E. Debs, N. P. Robins, C. Figl, P. A. Altin, and J. D. Close. Ramsey interferometry with an atom laser. Opt. Express 17, p.20661 (2009). [151]

D. Döring, G. McDonald, J. E. Debs, C. Figl, P. A. Altin, H.-A. Bachor, N. P. Robins, and J. D. Close. Quantum-projection-noise-limited interferometry with coherent atoms in a ramsey-type setup. Phys. Rev. A 81, 043633 (2010). [105]

In part I, it was shown using a three-level atom model that Raman transitions are especially useful for inertial sensing with an atom interferometer, as was first realised and implemented by Kasevich and Chu [6, 7]. The advantages lies in their ability to couple long-lived internal atomic states, their ability to provide significant momentum transfer in the process, and their ability to label external motional states via internal atomic states. In addition, an interferometer utilising Raman-based beamsplitters is sensitive to only the the *phase difference* of the two driving fields, and therefore a relative phase-stability between two lasers is required – a task that is practically less formidable than stabilising the absolute phase of a single laser source.

In this chapter, we describe the development of a novel laser-system, designed to drive Raman transitions between the hyperfine ground states of ^{87}Rb. Much of the work in this chapter has been published in [55], and this laser system is an essential tool for the basis of two more publications on the first free-space Ramsey interferometer with a BEC [105, 151].

Although this "Raman-Coupler" can be used for any application of Raman transitions, the work presented in this thesis focuses on the following two applications:

- The production of atom-lasers comprised of atoms in a single internal atomic state, and with the highest attainable atomic flux.
- The beamsplitters and/or mirrors used in constructing free-space atom interferometers – an atomic 'ruler.'

We begin by discussing the design and construction of the Raman laser-system, and then characterise its use by coupling the hyperfine states of a magnetically confined ^{87}Rb Bose-Einstein condensate. This allows the production of an atom-laser beam, which will be investigated in more detail in chapter 7. The laser system was then refined for use as an atomic beamsplitter for the first BEC-based free-space Ramsey interferometer, and we highlight these results.

6.1 Basic Principles of the Raman Coupler Laser-System

The goal of our Raman coupler is to drive transitions between the $|F = 1, m_F\rangle$ and $|F = 2, m'_F\rangle$ hyperfine ground states of ^{87}Rb, where F and m_F are the total and and projected angular momentum quantum numbers respectively. $\Delta m_F = m'_F - m_F = \pm 1, 0$ for large one-photon detuning due to conservation of angular momentum [152]. An example of such a transition is given in figure 6.1 for $\Delta m_F = 1$.[1] This particular transition can be used to derive an $m_F = 0$ atom laser from a magnetically confined BEC in the $|1, -1\rangle$ state.

Several critical features must be demanded when designing the Raman-Laser system:

1. We require two lasers fields, with a tuneable frequency difference (on the order of 6.83 GHz for ^{87}Rb), to allow control of the two-photon detuning, δ in figure 6.1.

[1] Note that the external momentum of the atoms is implicitly included in this level diagram.

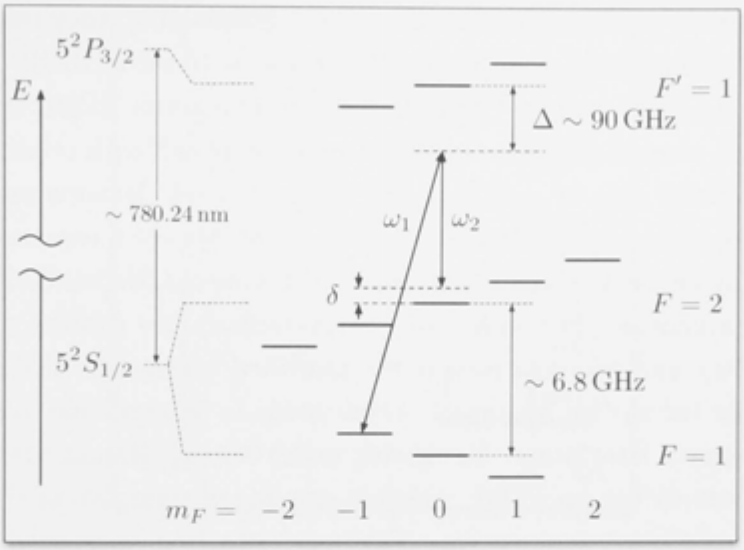

Figure 6.1: Simplified energy level diagram for Raman transitions on the D_2 line of ^{87}Rb, with both hyperfine and zeeman splitting shown. An example $\Delta m_F = 1$ Raman transition is shown, which we would use for outcoupling an atom laser from a BEC in the $|F = 1, m_F = -1\rangle$ ground state. A complete energy level diagram for the D_2 line ^{87}Rb can be found in [100].

2. A stable relative phase between the two lasers – particularly important for interferometers.

3. Intensity control and timing for pulse shaping.

4. Clean and simple spatial modes (e.g. Gaussian), ideally identical for each laser beam.

Point 3. is readily achieved by using an AOM, driven by a frequency synthesiser and pulse generator. Point 4 is also readily achieved by using an identical optical fibre for each beam, or better yet, coupling both beams into the same fibre with orthogonal polarisations.

Points 1. and 2. demand the phase-locking of two laser fields with a tuneable frequency difference. Phase-locking of two (for example) ECDLs has been previously achieved using the optical phase-locked loop (OPLL) technique [153, 154]. Briefly, this technique requires superimposing a small pick-off from the two lasers onto a fast photo-detector and measuring a microwave beat signal, which is then mixed down using a stable microwave reference, generating a phase-sensitive error signal. One laser is used as the master, and detuned (and ideally frequency locked) from resonance by Δ. The error signal is then fed back to the other (slave) laser with sufficiently high bandwidth, narrowing the relative line width between

the two lasers. While OPLLs offer flexibility and controllability, they require fast microwave electronics and high bandwidth feedback ($\sim 10\,\mathrm{MHz}$ [155]).

Another approach is to source two frequencies from a *single* ECDL by using a frequency shifting element; doing so ensures a common phase, with relative-phase fluctuations governed only by details of the chosen optical elements and setup, rather than the quality of an electronic phase-lock. AOMs are a commonly used frequency shifting element, and are available in the several-GHz band. However, at microwave frequencies, they suffer from excruciatingly low shifting efficiency ($< 3\%$ at $3.4\,\mathrm{GHz}$), and poor rejection of the unshifted frequency. This makes it difficult to isolate the shifted frequency, which needs to be amplified in order to recover the necessary laser power for driving power-hungry Raman transitions. Instead, we choose to use an EOM, which is capable of modulating the phase of the laser at microwave frequencies. This generates frequency sidebands at multiples of the modulation frequency, which can be chosen to be an integer fraction of the hyperfine splitting in ^{87}Rb.

We now give a theoretical description of phase-modulated light interacting with a three-level atom. Consider the phase-modulated electric field, written in complex notation:[2]

$$\mathbf{E}_{PM}(t) = \mathbf{E_0} e^{i\left(\omega_c t + \frac{\phi}{2}\cos[\omega_m t]\right)} \tag{6.1}$$

where ω_c is the frequency of the of the unmodulated ECDL, called the carrier frequency, ω_m is the EOM modulation frequency, and ϕ is the modulation depth. Using the relation:

$$e^{i\frac{\phi}{2}\cos[\omega_m t]} = \sum_{n=-\infty}^{\infty} i^n J_n(\phi/2) e^{in\omega_m t} \tag{6.2}$$

where J_n is the n^{th} order Bessel function of the first kind, we can write the modulated electric field as a sum of the carrier field, and sidebands at $\pm n\omega_m$ relative to the carrier frequency:

$$\mathbf{E}_{PM}(t) = \mathbf{E}_0 \sum_{n=-\infty}^{\infty} i^n J_n(\phi/2) e^{i[(\omega_c + n\omega_m)t]} \tag{6.3}$$

It is now apparent that $J_n(\phi/2)$ is the amplitude of the n^{th} order sideband (with the 0^{th} order "sideband" being the carrier). Figure 6.2 plots the first six Bessel functions over the range $0 \leq \phi \leq \pi$; a typically obtainable range using an EOM. Furthermore, each sideband has a well defined phase relative to every other

[2] At a given point in space.

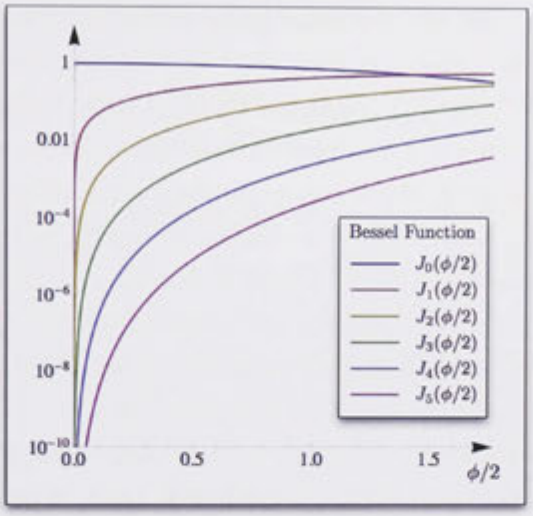

Figure 6.2: Bessel functions of the first kind, J_n, plotted on a logarithmic scale as a function of the modulation depth for $0 \leq n \leq 5$. For a typically feasible EOM modulation depth of $\phi = \pi$, the Bessel functions, and therefore the sideband amplitude, rapidly decreases with n.

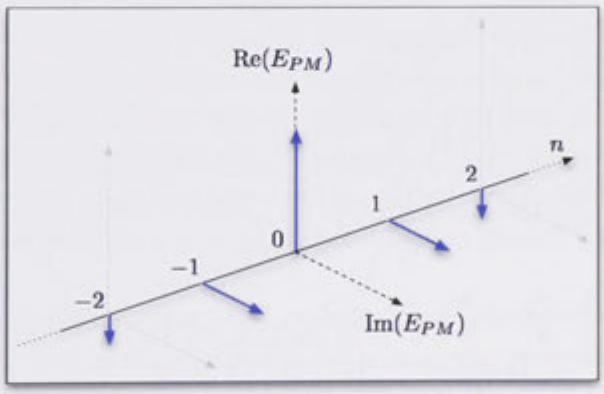

Figure 6.3: Phasor diagram for a phase-modulated electric field. Complex phasors for each sideband evolve in a plane perpendicular to the frequency axis indexed by n.

sideband and the carrier. This can be summarised using the 3-dimensional phasor diagram given in figure 6.3. Each sideband is represented along the frequency axis (labelled by n) by a phasor in an orthogonal complex plane. These are shown in blue for $t = 0$ and $|n| \leq 2$. All phasors then rotate around the frequency axis in time, at their respective sideband frequency. In the rotating frame of the carrier, the nth sideband rotates at $n\omega_m$.

Now, assuming that ω_0 is the resonant frequency of the desired ^{87}Rb hyperfine transition, then provided $k\omega_m = \omega_0$ with k a non-zero integer, there will exist pairs of sidebands in the phase-modulated beam, which satisfy the Raman

resonance condition. I.e. the nth sideband pairs with the $(n+k)$th sideband to satisfy resonance. At first glance, it may then be tempting to attempt driving Raman transitions directly with a phase-modulated laser beam. Indeed, each resonant frequency pair couples a two-photon transition. However, the contribution from all pairs destructively interferes to produce zero net coupling, provided $\omega_m \gg \Omega_0^2/\Delta$ and $\Delta \gg \omega_m$, where $\Omega_0 = \mathbf{d} \cdot \mathbf{E}_0/\hbar$, as defined in chapter 4.[3]

To see this, consider the result from chapter 4 that the effective Rabi frequency is given by $\Omega_e = -\frac{\Omega_1 \Omega_2^*}{2\Delta}$, where Ω_1 and Ω_2 now characterise the effective coupling between states $|1\rangle$ and $|e\rangle$, and $|2\rangle$ and $|e\rangle$ respectively; and we have included the complex conjugate for generality [consider the phase factors in equation (4.16)]. Thus, in the case of phase-modulated light, each resonant pair will contribute to the effective Rabi frequency. By considering all such pairs, it can be shown that:

$$\Omega_1 = \Omega_0 \sum_{n=-\infty}^{\infty} i^n J_n(\phi/2) e^{in\omega_m t} \tag{6.4}$$

$$\Omega_2 = \Omega_0 \sum_{n=-\infty}^{\infty} i^n J_n(\phi/2) e^{i(n+k)\omega_m t} \tag{6.5}$$

where we have used ω_c and ω_{-k} to define an appropriate rotating frame (i.e. $\omega_c \equiv \omega_1$ and $\omega_{-k} \equiv \omega_2$ in figure 4.1). As a result, the rotating wave approximation only eliminates time dependence for the carrier term, and the $-k$ sideband term in Ω_1 and Ω_2 respectively. Taking the product of these, the effective Rabi frequency is then:

$$\Omega_e = -\frac{\Omega_0^2}{2\Delta} \sum_{n=-\infty}^{\infty} \sum_{m=-\infty}^{\infty} i^{n-m} J_n(\phi/2) J_m(\phi/2) e^{i(m-n-k)\omega_m t} \tag{6.6}$$

In using the result $\Omega_e = -\frac{\Omega_1 \Omega_2^*}{2\Delta}$, we are assuming that $\Delta \gg \omega_m$ so that adiabatic elimination of the excited state applies for all resonant sideband pairs. More specifically, for $n = 4$, the sideband amplitude is already three orders of magnitude lower than the carrier over reasonable modulation depths, as can be seen in figure 6.2. Thus, practically speaking, Δ greater than a few times ω_m is sufficient. Now, only for terms with $m = n + k$ do the products in equation (6.6) represent resonant pairs of sidebands. Terms with $m \neq n + k$ are detuned off (two-photon) resonance by $(m - n - k)\omega_m$, the magnitude of which is always $\geq \omega_m$. Thus, we may restrict the sum to $m = n + k$ provided $\omega_m \gg \frac{\Omega_0^2}{\Delta}$, as stipulated earlier. As an example, typical values for experimental parameters give $\Omega_0^2/\Delta \sim$10-100 kHz,

[3] We assume the dipole moment for each one-photon coupling is equal for simplicity. This is not so in general.

whereas $\omega_m \sim 0.1\text{-}1\,\text{GHz}$. Thus, we may write:

$$\Omega_e = -i^{-k}\frac{\Omega_0^2}{2\Delta}\sum_{n=-\infty}^{\infty} J_n(\phi/2)J_{n+k}(\phi/2) \tag{6.7}$$

This specific sum of Bessel functions is zero, which can be seen in the following way. Consider the function $S(x) = \sum_{n=-\infty}^{\infty} J_n(x)J_{n+k}(x)$, and its derivative:

$$S'(x) = \sum_{n=-\infty}^{\infty} J_n'(x)J_{n+k}(x) + J_n(x)J_{n+k}'(x) \tag{6.8}$$

Using the relation $J_n'(x) = \frac{1}{2}[J_{n-1}(x) - J_{n+1}(x)]$, and relabelling the sum gives $S'(x) = 0$ for all x and k. A further property of Bessel functions is $J_n(0) = 0$ for all $n \neq 0$. Thus, $S(x) = 0$ for all x and k. We have tested this result extensively, and were unable to drive Raman transitions in stationary ^{87}Rb clouds using pure phase-modulated light over a large range of one-photon detunings (1-30 GHz), and several modulation frequencies (k = 1-3).[4]

Thus, the task at hand is to modify the phase-modulated light in a way so prevent total destructive interference of the different terms. As we shall see, this effectively amounts to (at least partly) converting phase-modulation to either polarisation- or amplitude-modulation, both of which can drive Raman transitions. For the work in this thesis, we choose two distinct methods for each application:

- For atom-laser outcoupling, and performing the comparison of outcouplers in chapter 7, we combine a phase-modulated beam, and an unmodulated (carrier) beam from the same ECDL with orthogonal polarisations. As a result, rather than the electric fields interfering to produce amplitude-modulation, there is a modulation of the plane of polarisation at the resonance frequency.

- For use as a beamsplitter in a Ramsey interferometer, we combine an unmodulated carrier beam with the phase-modulated beam with the same polarisation. This constitutes an optical interferometer with the EOM in one of the interferometer arms, and results in amplitude-modulation.

Both of these cases are considered in the next sections, including a more detailed description of polarisation- and amplitude-modulation.

[4] See section 6.3.1 for a discussion of how a moving cloud can break the symmetry of equation (6.7) due to the Doppler shift.

6.2 The Raman Laser System as an Outcoupler

We now discuss application of the Raman laser system as an atom-laser outcoupler. The requirements for atom-laser outcoupling are different to those for Ramsey interferometry, and as a result the laser systems are slightly different for each. For example, for outcoupling from a magnetic trap, we are interested in changing the m_F state of the atoms, as well as transferring momentum during the transition to help reduce divergence and maximise flux (discussed in detail in chapter 7). Furthermore, the requirements on the relative-phase stability of the Raman beams is somewhat relaxed, as the goal is to provide a weak coupling between trapped and untrapped atomic states, and the phase of the outcoupled beam is less important when considering applications in interferometry. On the contrary, for beamsplitting, relative-phase stability will limit the sensitivity of any atom interferometer, and at best should be stable at or below the atomic projection-noise limit.

6.2.1 Laser Setup

Production of the two Raman laser beams for use as an atom laser outcoupler is schematically represented in figure 6.4. Laser light is sourced from a home-built grating-stabilised ECDL, red-detuned by $\Delta \simeq 90$ GHz from one-photon resonance in order to suppress spontaneous emission to the level required to prevent heating of the BEC. The light is first sent through an AOM in a double-pass configuration to allow for intensity control, and fast shuttering on the order of 100 ns, before being split equally at a polarising beamsplitter. One is left unmodulated and coupled into a polarisation maintaining optical fibre. The other beam is phase-modulated using a fibre-coupled lithium niobate phase-modulator (EO-Space PM-0K5-10-PFA-PFA-780-UL). These modulators have the advantage of low power requirement, with a half-wave voltage[5] of $\sim 3\,\mathrm{V}$ into $50\,\Omega$, require no alignment other than standard optical fibre coupling, and have a typical insertion loss of about 50%. We drive the phase-modulator at $\omega_m = \omega_0/2 \simeq 3.415\,\mathrm{GHz}$ using a Rhode & Schwarz SMR-20 microwave frequency-generator. The sidebands in the modulated beam can be monitored using a commercial confocal fabry-perot cavity (Thor Labs SA210-5B) with a free spectral range of 10 GHz. At $\omega_m = 3.415\,\mathrm{GHz}$, we measure 20% of the total output power in each of the second order sidebands, with the carrier suppressed to less than 5%. The remaining power is distributed among the first and higher order sidebands, which are

[5] Half-wave voltage is that required for a modulation depth of $\phi = \pi$.

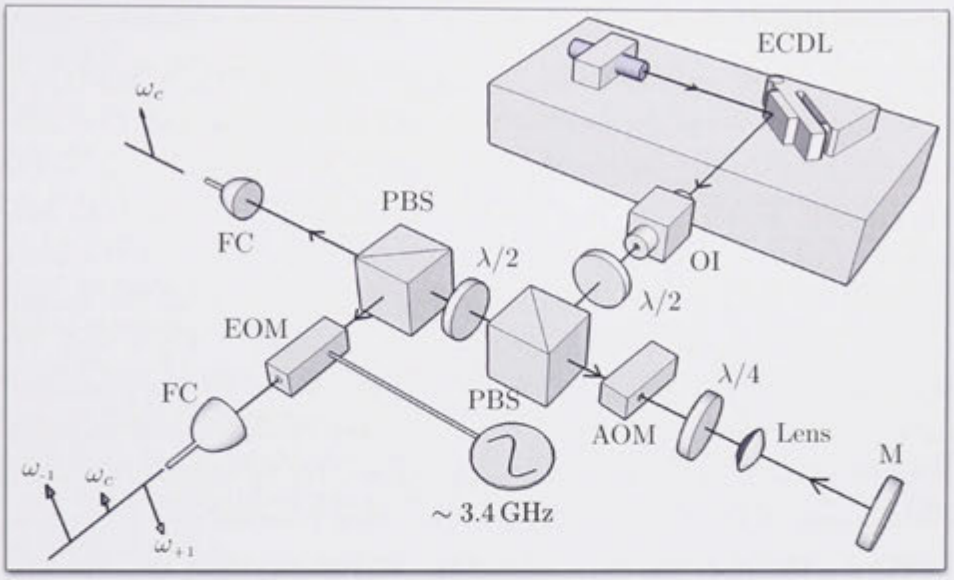

Figure 6.4: Laser-system setup for the production of two Raman laser beams for atom-laser outcoupling, separated in frequency by $\sim 6.8\,\mathrm{GHz}$. ECDL: external cavity diode laser, OI: optical isolator, $\lambda/2$: half-wave plate, $\lambda/4$: quarter-wave plate, PBS: polarizing beamsplitter cube, AOM: acousto-optic modulator used for intensity control and fast shuttering, M: mirror, FC: fiber coupler, and EOM: electro-optic modulator driven by a $\sim 3.4\,\mathrm{GHz}$ sine wave. A phasor diagram of the frequency components in each of the two Raman beams is included after each fibre coupler. Note that higher order sidebands are present in the modulated beam, but only first order are displayed in the diagram.

off-resonant when paired with the carrier, and do not contribute to the Raman coupling. It is important to minimise power in the carrier, as this suppresses formation of a standing wave with the unmodulated beam, which can result in diffraction of the condensate as well as the outcoupled atoms. This is the primary reason for choosing $\omega_m = \omega_0/2$, as the microwave frequency-generator has a limited power output, and the EOM half-wave voltage generally increases with ω_m. At this stage, one could couple both beams into a single fibre to ensure identical spatial modes. However we find this step unnecessary for atom-laser outcoupling as both beams originate from identical single-mode optical fibres, connected to identical fibre collimators. The laser-system results in two collimated beams with ~ 1 mm diameter, and approximately 4 and 8 mW for the modulated and unmodulated beams respectively.

6.2.2 Outcoupler Geometry

To test and characterise the outcoupler, we prepare BECs of ^{87}Rb in the $|1,-1\rangle$ state of typically 2.5×10^5 atoms with no discernible thermal fraction. Our Ioffe-Pritchard magnetic trap has trapping frequencies of $\omega_y = 12\,\text{Hz}$ and $\omega_x, \omega_z = 128$ Hz, a field gradient of 200 G/cm, and a stable bias field of 2 G at the trap minimum allowing highly reproducible atom laser production. Raman outcoupling is applied using the three-level coupling scheme of figure 6.5(a) with the Raman beams directed onto the condensate using the geometry shown in Fig. 6.5(b). We focus each beam using 10 cm and 50 cm focal length lenses for the horizontal and vertical beam respectively,[6] which ensures a high intensity, and therefore a high Rabi frequency. This configuration was chosen for its simplicity regarding characterisation of the coupler. It allows the beam polarisation to be set to (ideally) pure σ^+ for the modulated beam, which propagates along the magnetic trap bias field direction and (ideally) pure π polarisation for the unmodulated beam, which propagates orthogonal to bias field direction. This ensures that only the transition in figure 6.5 is possible, i.e. a photon is absorbed from the ω_{+2} sideband in the horizontal beam via a σ^+ coupling, and emitted into the

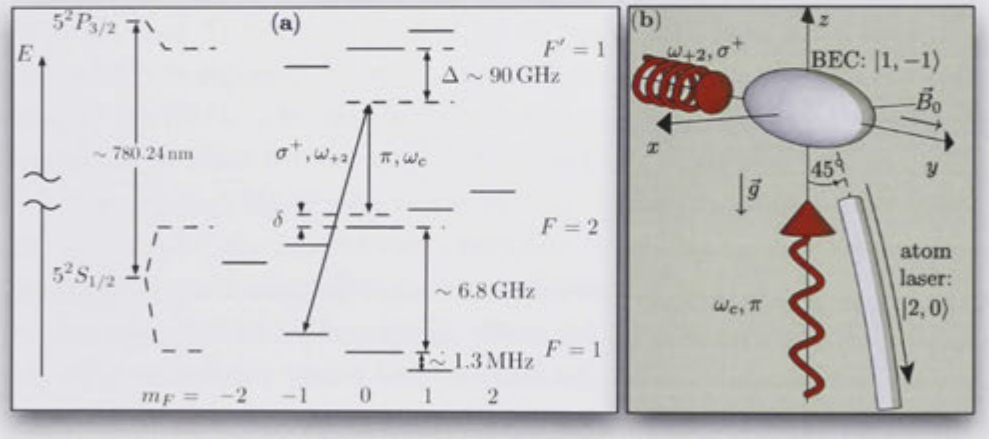

Figure 6.5: (a) Energy level scheme for outcoupling, and (b) Raman beam geometry. Only the $F' = 1$ manifold of the $5^2P_{3/2}$ excited state of ^{87}Rb is shown. δ is the two-photon detuning. The bias field, $\mathbf{B_0}$, is directed along the long axis of the condensate. We direct the modulated Raman beam along this direction, with circular polarisation to drive absorption of a σ^+ photon from the ω_{+2} sideband. The unmodulated Raman beam propagates upwards and is linearly polarised along $\mathbf{B_0}$ to drive emission of a π photon. The two-photon transition gives the outcoupled atoms a net momentum kick of $\sqrt{2}\hbar k$ producing a beam in the continuous regime.

[6] These focal lengths are chosen simply due to space limitation in the experimental setup.

unmodulated carrier beam via a π coupling. This results in a momentum transfer of $\sqrt{2}\hbar k$ at 45° relative to the vertical beam, shown by the diagrammatic atom-laser in figure 6.5(b). For other beam orientations, for example one which outcouples atoms with a downward momentum transfer, each beam may contain a combination of σ^+, σ^-, and π polarised light. The presence of a σ^- component in the modulated beam, for example, drives the same Raman transition with an opposite momentum kick due to absorption from the carrier and emission into the lower sideband, producing a second atom-laser beam. A downward coupled atom laser may be more practical for certain applications, and one remedy to the issue of multiple resonances is injection locking of a slave laser-diode to a particular sideband of the modulated field, which effectively selects just one frequency from the phase-modulated beam. We now routinely implement injection locking in our laboratories.

6.2.3 Polarisation Modulation

We now highlight an intriguing observation: that this particular configuration of the two Raman beams results in a modulation of the plane of polarisation of the electric field at the resonance frequency. The simplest way to see this is to write the electric field for the horizontal and vertical beams as:

$$\mathbf{E}_h(t) = E_h \left[\cos[(\omega_c + 2\omega_m)t]\,,\, \sin[(\omega_c + 2\omega_m)t]\,,\, 0\right] \tag{6.9}$$

$$\mathbf{E}_v(t) = E_v \left[0\,,\, 0\,,\, \cos(\omega_c t + \theta)\right] \tag{6.10}$$

where θ is some general phase difference between the two beams, and $2\omega_m = \omega_0$. If we consider the total electric field, $\mathbf{E}_t(t) = \mathbf{E}_h(t) + \mathbf{E}_v(t)$ and time-average over a single optical period, we find a constant amplitude in time. On the other hand, consider the area which is swept out by $\mathbf{E}_t(t)$ over a single period. This is represented by the blue circles in figure 6.6, and defines the plane of polarisation at time t. If we advance t, and monitor the orientation of this plane, we see it oscillates in two dimensions – precessing about the z-axis in the figure (z represents the direction of propagation for the horizontal beam). This motion is akin to a "wobbling plate" thrown into the air.[7] The precession is represented using the black vector, which is normal to the blue plane. The red circle, which should be visualised as centred on the z-axis in the yz-plane, shows the trajectory of the

[7] There is an interesting story told by Feynman about how he observed the wobble of a plate thrown into the air at a cafeteria, whose motion he then proceeded to analyse [156]. "Feynman's wobbling plate" has even received attention in the literature, with an analysis of the motion given in [157].

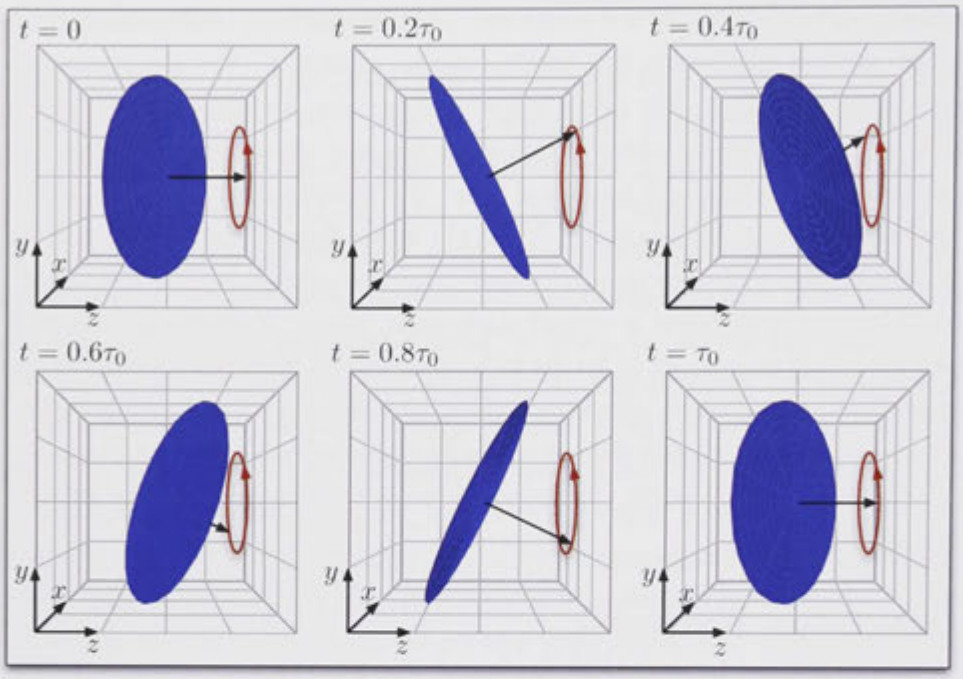

Figure 6.6: Schematic representation of polarisation-modulation, resulting from the superposition of two orthogonal electromagnetic waves with slightly different frequencies. The blue circle represents the plane of polarisation at time t. The black vector is normal to this plane in all figures, and is used to help guide the eye. This vector, and therefore the polarisation plane, precesses around the z-axis, completing one full cycle in a time $\tau_0 = 2\pi/\omega_0$. The trajectory of the normal vector is represented by the red circle, which is centred on the z-axis. Thus, the plane of polarisation is modulated at the hyperfine-resonance frequency ω_0.

normal vector in time, to help guide the eye. The figure plots six orientations of the polarisation plane, at values of t ranging from $t = 0$ to $t = \tau_0$, where $\tau_0 = 2\pi/\omega_0$ – the period of the microwave frequency corresponding to resonance. We see that at $t = \tau_0$, the plane of polarisation has completed one full oscillation, and is thus modulated at the hyperfine resonance frequency. This observation will be contrasted to the presence of amplitude-modulation, when we discuss operation of the Raman coupler as an atomic beamsplitter in section 6.3.

6.2.4 Outcoupler Characterisation

To characterise the outcoupler, we apply the Raman beams with a given pulse shape, directly after evaporation to BEC. The magnetic trap is then suddenly switched off, allowing all atom clouds to expand for 15 ms. The atoms are then illuminated by a 100 μs pulse of resonant light, and imaged onto a CCD camera.

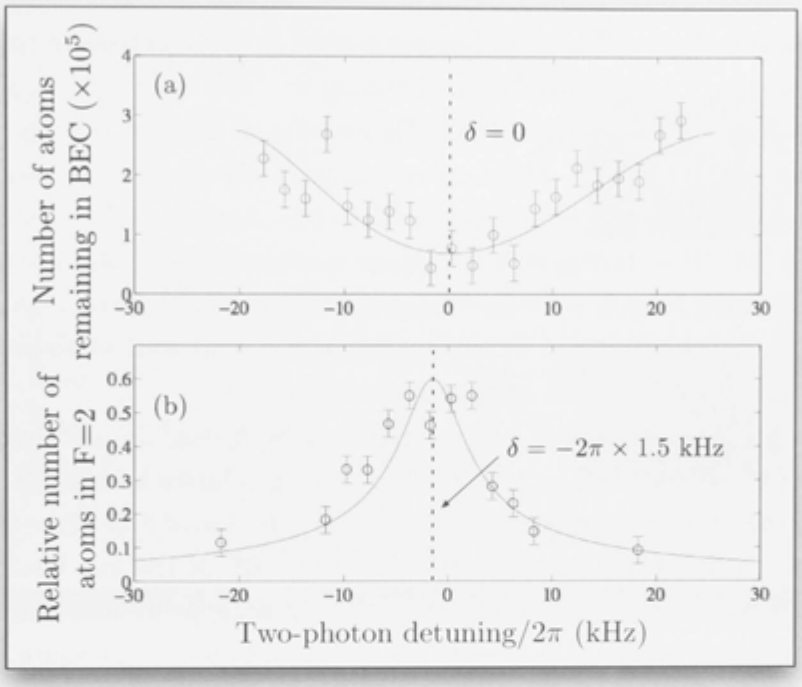

Figure 6.7: Resonance curves for the (a) weak- and (b) strong-coupling regimes, showing the lineshape of the resonance and the effect of the AC Stark shift. In (a), we use a 100 ms outcoupling pulse and plot the number of atoms remaining in the condensate as a function of two-photon detuning. The solid line is a fit to the experimental data using a Thomas-Fermi approximation, and integrating over a resonant slice of the wavefunction. In (b), the relative number of atoms transferred to the $F = 2$ ground state is plotted as a function of two-photon detuning. A envelope function of equation (2.27) is fitted to the data (solid line) to determine the centre of the resonance. In both data sets, zero detuning corresponds to the centre of the Raman resonance for weak coupling, and error bars represent one standard deviation in the total atom number.

Outcoupled atoms are displaced to the side, and away from the BEC for this expansion time, due to the momentum transfer from the Raman transition (see figures 6.8 and 6.9).

Based on our experimental parameters, we estimate the maximum intensity at the condensate to be on the order of $10\,\mathrm{W/cm^2}$ leading to a maximum calculated Rabi frequency of $\Omega_e = 2\pi \times 20\,\mathrm{kHz}$. Our setup can be operated in the continuous weak-coupling regime, or in the pulsed strong-coupling regime.

To define the microwave frequency operating points, we measure resonance curves for both weakly- and strongly-coupled systems.[8] In the weakly-coupled

[8] 'Weak' and 'strong' here can simply be understood to mean continuous atom-laser and pulsed atom-laser respectively. A formal definition can be found in chapter 7.

system, we use a Rabi frequency of $\Omega_e \simeq 2\pi \times 200\,\mathrm{Hz}$, and a long Raman pulse of 100 ms, plotting the number of atoms remaining in the condensate in figure 6.7(a) as a function of the two-photon detuning δ. The solid line is a theoretical fit based on an integration of the Thomas-Fermi density, $|\psi(x,y,z)|^2 = \frac{1}{U}\left[\mu - \frac{m}{2}\left(\omega_y^2 y^2 + \omega_r^2\left[x^2+z^2\right]\right)\right]$ over a energy width of $\hbar\Omega_e$ centred on resonance. Flux is then modelled as directly proportional to this number multiplied by Ω_e, as was done in [54]. $U = 4\pi\hbar^2 a/m$ is the effective atomic interaction strength, a the s-wave scattering length, $\mu = (15NU\omega_y\omega_r^2/8\pi)^{2/5}(m/2)^{3/5}$ the chemical potential, with N the total number of condensate atoms, and m the atomic mass of ^{87}Rb. We take $\delta = 0$ to be the minimum of this curve.

In the strongly-coupled regime, a 60 μs Raman pulse is used for our maximum measured Rabi frequency of $\Omega_e \simeq 2\pi \times 10\,\mathrm{kHz}$, and the relative number of atoms transferred to the $|2,0\rangle$ ground state is plotted as a function of δ in figure 6.7(b). The solid line is a fit to the data, based on the envelope of the two-level atom model [see equation (2.27)], used to extract the operating point from the data. This maximum point occurs at $\delta = -2\pi \times 1.5\,\mathrm{kHz}$, and gives a measure of the maximum relative AC Stark shift in this system.

Although we have estimated an upper bound on the maximum Rabi frequency of our outcoupler, accurate knowledge of the light intensity at the condensate is difficult to obtain. It is therefore important to calibrate the Rabi frequency for any given setup. This is accomplished by comparing experimental data with a 3D mean-field calculation. The Raman lasers are applied to the condensate for a fixed pulse length of 135 μs, and the power in the beams varied. This outcouples a pulse of atoms in the $|2,0\rangle$ state, whose relative number depends on Ω_e, and is plotted in figure 6.8(a) as a function of the total power in the two beams. The calibration is then extracted by fitting the experimental data to a 3D simulation of the GPE based on measured parameters of our system. Our maximum attainable Rabi frequency is on the order of $2\pi \times 10$ kHz.

In figure. 6.8(b), we demonstrate coherent Rabi oscillations at the maximum Rabi frequency for this setup. The solid line again represents a 3D simulation of the GPE for our experimental parameters. For complete Rabi oscillations to occur, it is necessary for the spatial wavefunctions of each state to remain well overlapped over the duration of a Rabi cycle. As the $|2,0\rangle$ state receives an initial momentum kick in addition to experiencing acceleration due to gravity, complete transfer was not observed, with a maximum transfer of $\sim 75\%$ in the first oscillation. Over time, and successive oscillations, the overlap continues to decrease and a decay in the Rabi oscillations is observed. This behaviour is

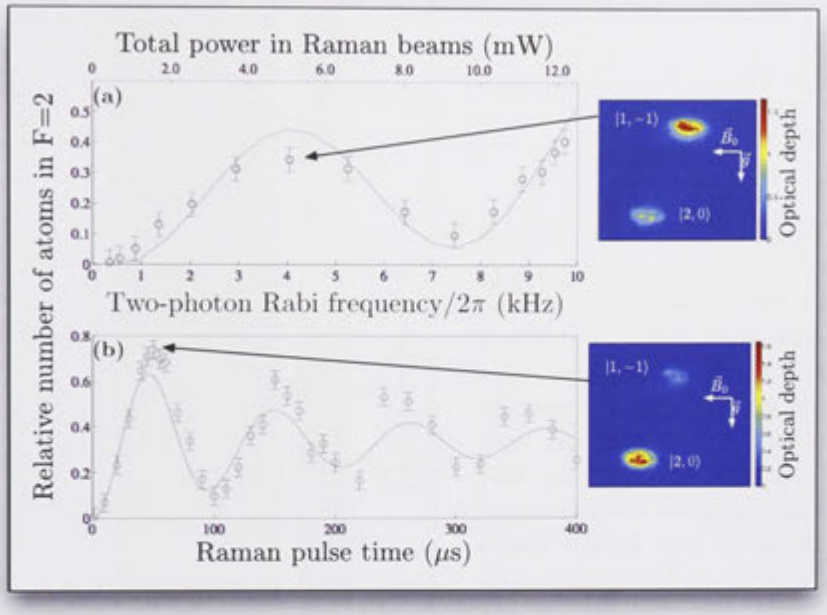

Figure 6.8: (a) Calibration of the two-photon Rabi frequency. The circles represent the relative number of atoms in the $|2,0\rangle$ state as a function of total power in the Raman beams. (b) Rabi oscillations between the $|1,-1\rangle$ and $|2,0\rangle$ hyperfine ground states of ^{87}Rb. The relative number of atoms in the $F = 2$ ground state is plotted as a function of pulse time, with a oscillation frequency of ~ 10 kHz. Incomplete and decaying oscillations are observed due to an imperfect and decreasing overlap of the wavefunctions for the two coupled states in time. In both data sets, the error bars represent one standard deviation in total atom number and the solid line is a simulation of the GPE for our experimental parameters, which allows calibration of the Rabi frequency in (a).

qualitatively captured by the numerics. One possible reason for the quantitative discrepancy is that the simulation assumes a uniform Rabi frequency across the condensate, whereas in the experiment we focus the beams to maximise the intensity. This could result in a intensity gradient across the cloud. In future applications, we could use larger beams with a relatively flat intensity profile to mitigate this effect.

Figure 6.9, shows an absorption image of a atom-laser produced by the Raman outcoupler for 9 ms of outcoupling. The condensate is released at the end of this 9 ms, and the atoms are allowed to expand for a further 15 ms before an absorption image is taken. The beam is displaced horizontally from the BEC due to the horizontal component of the momentum transfer by the Raman transition. It is also displaced vertically because of the vertical component of the transferred momentum. It should also be noted that it represents the last 9 ms of a 24 ms

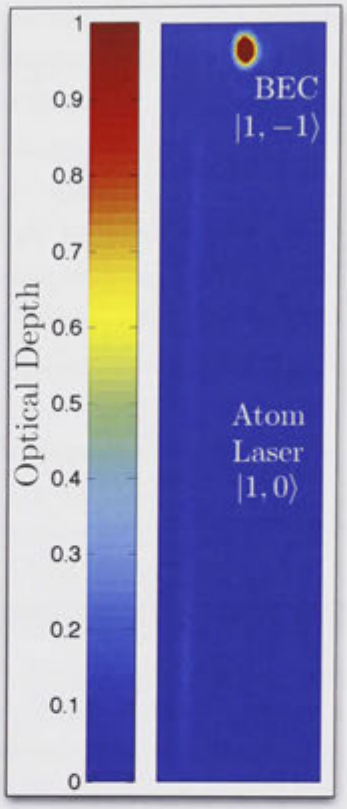

Figure 6.9: Absorption image of a typical atom-laser, outcoupled for 9 ms using the hyperfine-Raman outcoupler. The Raman coupler readily produces these low divergence, clean atom laser beams. A horizontal and vertical displacement from the BEC its the result of the momentum transfer of the Raman transition at 45° to (downward) vertical. The atomic trajectory corresponds to the last 9 ms of a parabolic trajectory, evolving for a total of 24 ms, due to 15 ms of free expansion before the absorption image is taken.

parabolic trajectory, and as such looks relatively vertical. In chapter 7, a detailed comparison between this hyperfine-Raman outcoupler, a Zeeman-Raman outcoupler, and an RF outcoupler will be presented.

6.3 The Raman-Laser System as an Atomic Beamsplitter

We now turn to using the EOM based Raman laser-system as an atomic beamsplitter. In general, this could be used to build either a Mach-Zehnder, or Ramsey interferometer. However, for the work in this thesis, we apply it to a free-space Ramsey interferometer, which utilises a low-density, freely-falling, $|1,0\rangle$ atom-laser pulse as the atomic source. Using the EOM with a novel modification to the system so far presented, allowed passive phase-stabilisation, enabling operation of an atomic shot-noise limited Ramsey interferometer, as presented by D. Döring *et al.* in [105].

In addition to requiring a highly-stable relative phase, a Ramsey interferometer uses a co-propagating Raman transition, with negligible momentum transfer and spatial separation between states (see section 3.3). Furthermore, it is typical

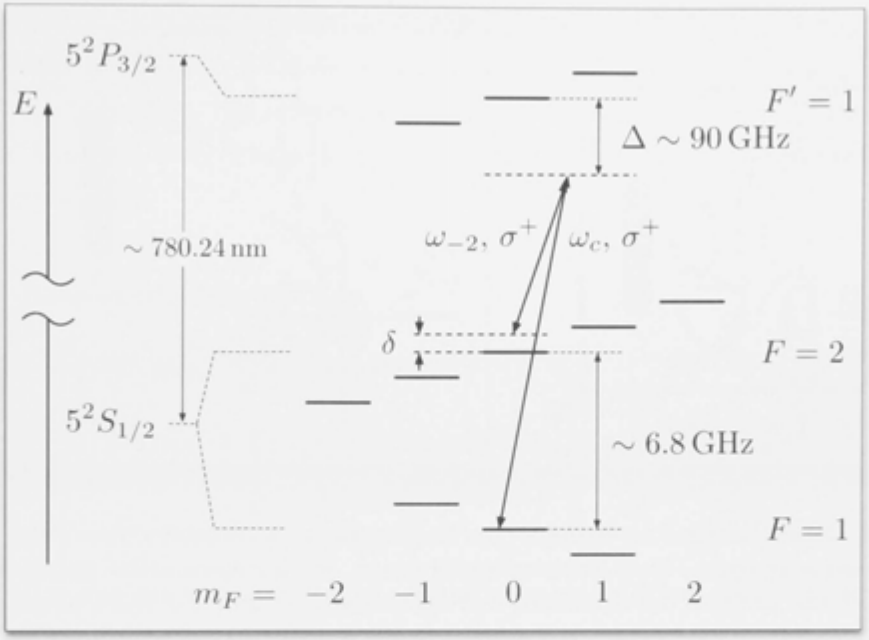

Figure 6.10: Energy level diagram for the Raman transition between the ^{87}Rb clock states used for our free-space Ramsey interferometer

to couple the first-order magnetically insensitive ^{87}Rb clock states, $|1,0\rangle \leftrightarrow |2,0\rangle$. The required Raman-transition is shown in figure 6.10. We again need to modify the phase-modulated light in order to couple this Raman transition, and in this case we superimpose a phase-shifted carrier beam with the EOM output. To do this, the EOM is placed into one arm of an optical interferometer. As we will see, this to produces a partly amplitude-modulated beam. Figure 6.11 shows two interferometer configurations including the EOM; a Mach-Zehnder in (a) and a Sagnac in (b).

To see how these configurations can drive Raman transitions, consider the electric field at the output beamsplitter, given by:

$$\mathbf{E}(t) = \mathbf{E}_0 \left(A e^{i(\omega_c t + \theta)} + B \sum_{n=-\infty}^{\infty} i^n J_n(\phi/2) e^{i[(\omega_c + n\omega_m)t]} \right) \tag{6.11}$$

where θ is a general phase-shift between the carrier in the unmodulated and modulated beams. If we assume $\mathbf{E}_0$ is the electric field entering the interferometer, then in general $A^2 + B^2 \leq 1$. Equality corresponds to a lossless system with $A^2 = B^2 = 1/2$ for a 50:50 beamsplitter. Of course, the EOM and other optical components have associated losses, and $A^2, B^2 < 1/2$ in general. Using the three-

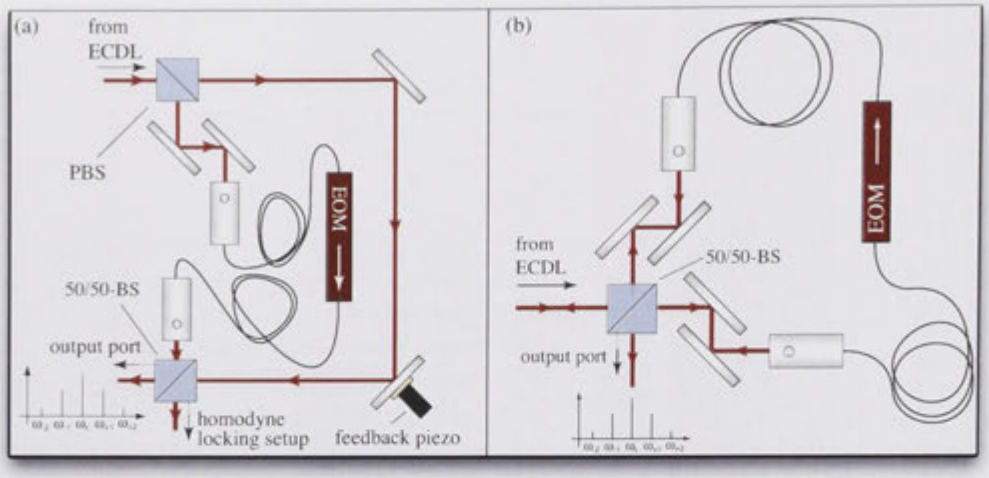

Figure 6.11: Raman laser-system setups for our Ramsey atom interferometer, from [105]. (a) EOM placed inside an optical Mach-Zehnder interferometer, which requires active stabilisation to lock the relative phase of the modulated and unmodulated beams. (b) EOM used in an optical Sagnac interferometer, which has a high passive stability, as phase fluctuations are common to both paths.

level atom formalism from chapter 4, it can be shown that:

$$\Omega_1 = A\Omega_0 e^{i\theta} + B\Omega_0 \sum_{n=-\infty}^{\infty} i^n J_n(\phi/2) e^{in\omega_m t} \tag{6.12}$$

$$\Omega_2 = A\Omega_0 e^{i(k\omega_m t+\theta)} + B\Omega_0 \sum_{n=-\infty}^{\infty} i^n J_n(\phi/2) e^{i(n+k)\omega_m t} \tag{6.13}$$

where, as for equations (6.4) and (6.5), ω_c and ω_{-k} have been used to define the rotating frame, and the rotating wave approximation has been applied. The effective Rabi frequency is then:

$$\Omega_e = -\frac{\Omega_1 \Omega_2^*}{2\Delta} = -i^k AB J_k(\phi/2) \frac{\Omega_0^2}{2\Delta} \left[(-1)^k e^{i\theta} + e^{-i\theta}\right]$$

$$= \left\{ \begin{array}{ll} -i^k AB J_k(\phi/2) \frac{\Omega_0^2}{\Delta} \cos(\theta), & \text{even } k \\ \\ i^{k+1} AB J_k(\phi/2) \frac{\Omega_0^2}{\Delta} \sin(\theta), & \text{odd } k \end{array} \right\} \tag{6.14}$$

where we again neglect off-resonant terms, assuming $\omega_m \gg \frac{\Omega_0^2}{\Delta}$. We see that for even k, $\delta = j\pi$ gives the maximum magnitude for Ω_e, with j an integer. Whereas

for odd k, $\delta = (j + 1/2)\pi$ gives the maximum magnitude for Ω_e. Although not immediately obvious, this result is equivalent to the output field having a non-zero intensity-beat at the resonance frequency – an amplitude modulation. To help see this, we now briefly discuss amplitude-modulation and compare it to phase-modulation.

6.3.1 Amplitude Modulation

Consider an amplitude modulated field, which can be written as:

$$\begin{aligned}\mathbf{E}_{AM}(t) &= \mathbf{E}_0[1 + M\cos(\omega_m t)]e^{i\omega_c t} \\ &= \mathbf{E}_0\left(e^{i\omega_c t} + \frac{M}{2}e^{i(\omega_c+\omega_m)t} + \frac{M}{2}e^{i(\omega_c-\omega_m)t}\right)\end{aligned} \tag{6.15}$$

where M is the modulation depth. Amplitude-modulation also produces sidebands, although in this case there are just two at $\omega_c \pm \omega_m$. The intensity of this field is proportional to:

$$|\mathbf{E}_{AM}(t)|^2 = |\mathbf{E}_0|^2\left[1 + \frac{M^2}{2} + 2M\cos(\omega_m t) + \frac{M^2}{2}\cos(2\omega_m t)\right] \tag{6.16}$$

which has two beat frequencies, one at ω_m resulting from the beat between each sideband and the carrier, and one at $2\omega_m$ resulting from a beat between the sidebands themselves. Often in practice, $M < 1$ and the $2\omega_m$ component is smaller than the ω_m component by a factor of M.

In figure 6.12, we compare amplitude-modulation in (a) to phase-modulation in (b) using a phasor diagram like that of figure 6.3. In particular, note the different phase relationship between the carrier and the 1^{st} order sidebands for amplitude-modulation and phase-modulation, which is represented by the angle between the sidebands and the carrier. For phase-modulation, they are orthogonal, whereas for amplitude-modulation they are parallel. In general, odd sidebands are orthogonal to the carrier, and even sidebands parallel to the carrier in a phase-modulated beam. It is this particular phase relationship which results on a cancelation of all beats in the case of pure phase-modulation, leading to a constant intensity in time. If however this phase-relationship is modified, for example by shifting the carrier-phase (corresponding to a rotation about the frequency axis), then this cancellation no longer occurs, as the carrier now has components parallel to the odd sidebands, and a reduced amplitude with respect to the even sidebands.

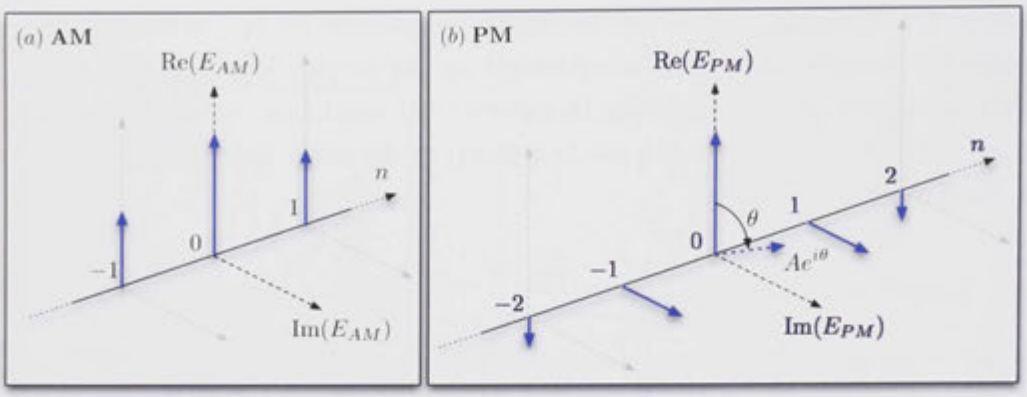

Figure 6.12: Comparing phasor diagrams for (a) an amplitude-modulated electric field, and (b) a phase-modulated electric field. (b) Is identical to figure 6.3. In both cases, phasors are drawn at $t = 0$. Notice that for amplitude-modulation, the sidebands are parallel to the carrier, whereas for phase-modulation, only the even sidebands are parallel to the carrier. Although not shown, every eventh order sideband is out of phase with the adjacent eventh order.

In the case of the Raman coupler we superimpose a second carrier beam [the dashed phasor in figure 6.12(b)] onto the phase-modulated beam. This second carrier can then be amplitude-modulated by the sidebands in the phase-modulated beam by the previous reasoning. Comparing (a) and (b), if the additional carrier has $\theta = 0$, then it has an amplitude-modulation-like phase relationship with even sidebands, whereas if $\theta = \pi/2$, it has this relationship with the odd sidebands. Thus there will be an intensity beat at even and odd multiples of the modulation frequency for each respective case. For a general phase, the even and odd beats will be proportional in magnitude to $\cos(\theta)$ and $\sin(\theta)$ respectively. With respect to driving a Raman transitions, it is the k^{th} sideband which satisfies two-photon resonance with the additional carrier, and thus the result of equation (6.14) is equivalent to the presence of an intensity beat at $k\omega_m = \omega_0$; the hyperfine-resonance frequency.

It is worth pausing at this point to highlight an interesting classical picture. We have seen that it is necessary to have either a polarisation-modulation, or amplitude-modulation at the resonance frequency, in order to effectively drive a Raman transition. Both of these cases correspond to a modulation of a the electric field at the resonance frequency – either a modulation in its direction, or its magnitude. If we model our atomic resonance as a classical dipole – charges connected by a spring, with resonant frequency ω_0 – then both polarisation- and amplitude-modulation generates a driving force at the spring's resonance frequency.

6.3.2 Atomic Beamsplitter Characterisation

A consequence of equation (6.14) is that θ should be stable in time. Any instabilities will lead to fluctuations in the Rabi frequency and thus the efficacy of the Raman beamsplitter. What this implies for the case of the Mach-Zehnder design in figure 6.11(a), is that the optical interferometer must be actively stabilised in order to stabilise θ. This is done by using a homodyne detection at one of the interferometer output ports, and using this to feedback to one of the interferometer mirrors attached to a piezo, as shown in figure 6.11(a). Thus, the bandwidth of this lock will directly impact the stability atomic beamsplitter. One could just as well build a suitable optical cavity, and correspondingly demanding lock, which filters the EOM output.

A far more attractive option is to use the EOM in an optical Sagnac interferometer, as shown in figure 6.11(b). This design relies on a useful byproduct of the principle of operation of the fibre-coupled EOM. Namely, that it is a directional device with effective phase-modulation occurring in one propagation direction, as specified by the arrow in figure 6.11. Thus, one optical path around the Sagnac is effectively modulated, while the opposing path is not; giving us the desired result at the output of the beamsplitter. Both the modulated and unmodulated beams travel around a common optical path, allowing for a strong passive rejection of relative phase-noise, such as that induced though mechanical vibrations of the optical elements, and temperature drifts of the fibre.

In the Sagnac configuration, the phase difference between each path around the interferometer is $\theta = \pi$ due to the beamsplitter (one path has an external and internal reflection, the other has two transmissions). Thus, from equations (6.14), we see that choosing an even k will maximise the Rabi frequency. Equivalently, there should be a maximum amplitude-modulation at even multiples of ω_m, resulting in a beat signal at these frequencies. In figure 6.13, we measure the amplitude of a beat signal at 1, 2, and 3 GHz, for $\omega_m = 1\,\text{GHz}$, as a function of the EOM drive voltage. Blue triangles, red circles, and black squares correspond to beat signals at 1, 2, and 3 GHz ($k = 1, 2, 3$) respectively. There is a clear suppression at odd multiples of ω_m, and the residual signal at these frequencies is likely the result of imperfect alignment of the polarisation to the EOM modulation axis. Higher order sideband beats are not measured due to the rapidly diminishing amplitude of these sidebands, as seen in figure 6.2.

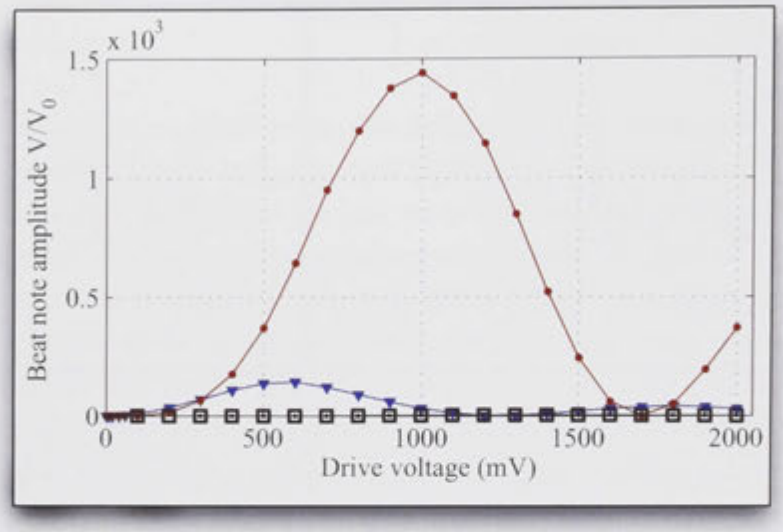

Figure 6.13: Beat signal from an optical Sagnac with an EOM in the interferometer arms, as a function of the EOM drive voltage, from [105]. V_0 is an arbitrary reference voltage. The EOM is driven at $\omega_m = 1\,\text{GHz}$. For a Sagnac interferometer, $\delta = \pi$, and thus we expect the signal at odd multiples of the modulation frequency to be suppressed. Blue triangles, red circles, and black squares correspond to beat signals at 1, 2, and 3 GHz ($k = 1, 2, 3$) respectively. Figure courtesy of D. Döring.

6.3.3 Resultant Ramsey Fringes

We now present atom interferometry results, in order to highlight the effectiveness of the Raman coupler as a beamsplitter, which is able to produce an atomic projection-noise limited Ramsey interferometer [105]. This work was conducted in collaboration with D. Döring *et al.*, and is not the focus of this thesis. It is, however, an important product of the Raman coupler. Specifically, we present the results of two free-space Ramsey interferometers, one using the Mach-Zehnder configuration [151], and the other using the Sagnac configuration [105].

We only briefly describe the general experiment here. A more detailed account can be found in [105, 151]. In particular, measurement at the atomic shot-noise limit required not only a sufficiently quiet beamsplitter, but also suitable absorption imaging and number counting/calibration. Details of the detection system can also be found in [105], and in the theses of G. D. McDonald [143], and D. Döring [158].

After producing a BEC, as described earlier, we outcouple a pulsed atom-laser in the $|1,0\rangle$ state using RF outcoupling. This pulse typically contains on the order of 10^4 ^{87}Rb atoms. It evolves freely under gravity, falling through two

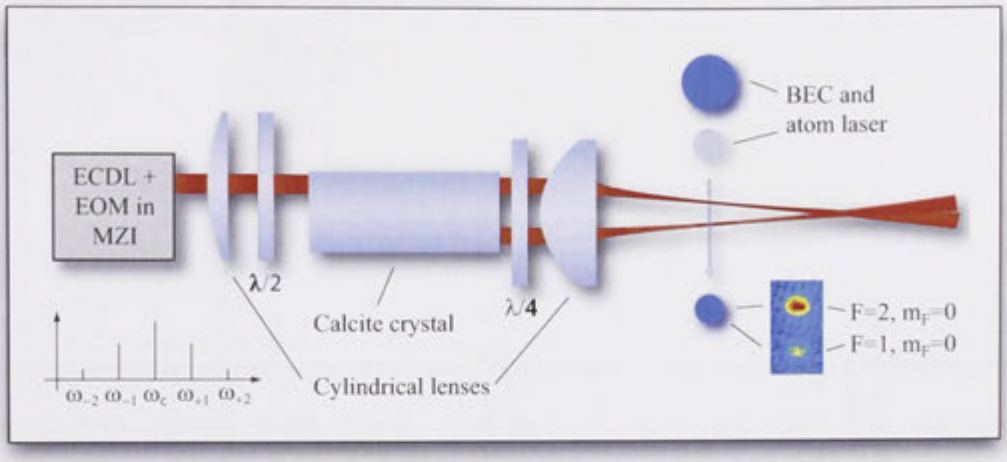

Figure 6.14: Optical setup for generating the two Ramsey interaction zones, from [151].

Raman interaction zones situated on the order of 100 μm below the magnetic trap minimum. The interaction zones are two parallel light-sheets sourced from either the Mach-Zehnder or Sagnac configuration Raman coupler, and separated vertically by $\sim 300\,\mu$m. The intensity of each light-sheet is adjusted to compensate for the difference in the speed of the cloud at each sheet, as well as any difference in the sheet thickness. This ensures both interaction zones correspond to a $\pi/2$ pulse. Figure 6.14 summarises this optical setup. The two light sheets are generated using a birefringent calcite crystal, resulting in two emergent beams with orthogonal polarisation. The power in each beam is controlled by rotating the input (linear) polarisation with respect to the crystal axis using a half-wave plate. Two cylindrical lenses, one before and one after the calcite, produce the light sheets, ensuring that the focal point of each is well separated from the point at which they cross (as drawn in the figure). A quarter-wave plate is used to produce circularly polarised light for driving σ transitions.

After falling through the Ramsey interaction zones, the two clock states are spatially separated using the Stern-Gerlach effect, which separates different magnetic states using a magnetic field gradient. In this case, we are utilising the second order Zeeman shift, which also depends on the total atomic angular momentum F. The field gradient is generated by pulsing the magnetic trap coils. Each state to is then simultaneously absorption imaged on the $F = 2 \rightarrow F' = 3$ transition, after repumping atoms from $F = 1$ to $F = 2$ using a short repumping pulse (100 μs). This allows us to calculate the probability of measuring atoms in $|2, 0\rangle$ as $p = \frac{N_1}{N_1+N_2}$, where N_i is the number of atoms in the i^{th} state.

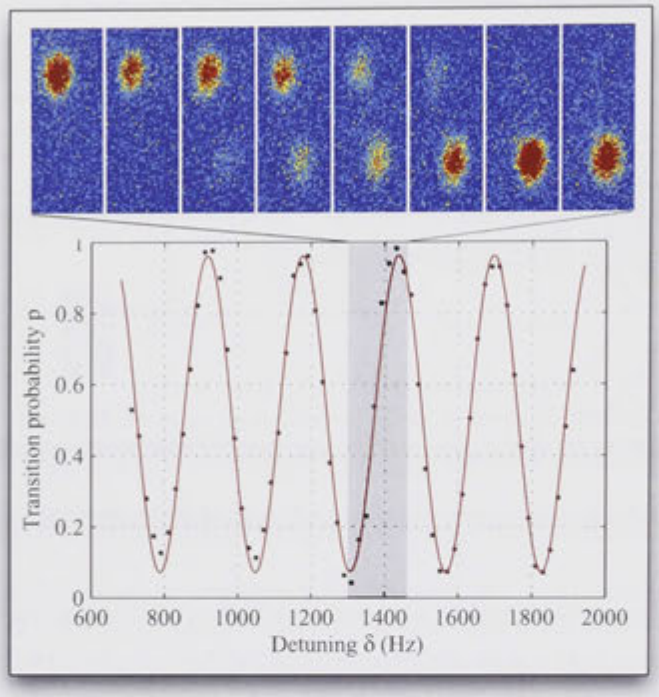

Figure 6.15: Typical interference fringes from an atom-laser based Ramsey interferometer, from [105].

Figure 6.15 shows a typical set of ramsey fringes, and corresponding absorption images, from a Ramsey interferometer driven using the Sagnac configuration Raman coupler. The fringes are scanned by varying the detuning [see equation (3.8)], which amounts to varying the microwave frequency that drives the EOM. We observe a high fringe visibility, with a fringe period of 259.5(5) Hz corresponding to $T = 3.853(8)$ ms, extracted from a sinusoidal fit (red line).

In figure 6.16, we compare fringes obtained using (a) the Mach-Zender configuration (from [151]) to those obtained using (b) the Sagnac configuration (from [105]). In both cases, each data point represents the average of 5 experimental runs, with the error bars giving one standard deviation. There is a clear improvement in the signal-to-noise ratio (SNR) for the Sagnac configuration. The Mach-Zehnder configuration gives a phase-uncertainty of ~ 240 mrad over 5 experimental runs, whereas the Sagnac configuration gives ~ 5 mrad. This demonstrates the high level of passive stability for the Sagnac configuration, and that the Mach-Zehnder configuration was limited primarily by the stability of the optical Mach-Zehder interferometer, and its active lock system.

The Sagnac configuration is in fact stable enough to produce a Ramsey inter-

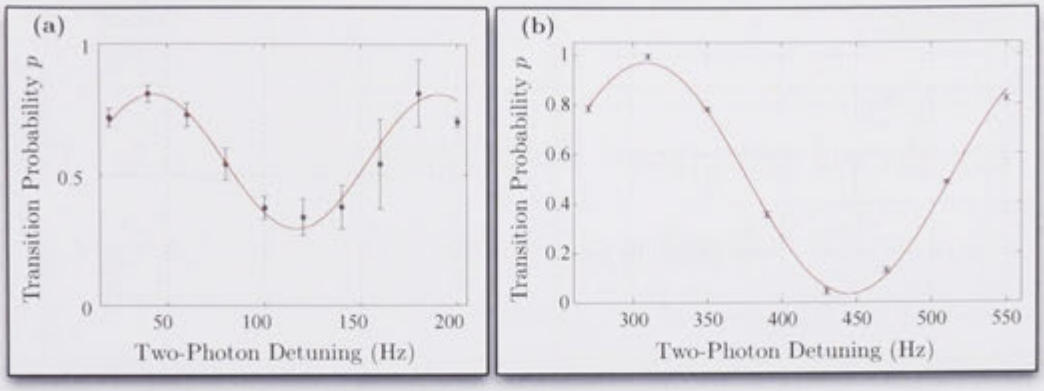

Figure 6.16: Ramsey fringes obtained using the hyperfine-Raman coupler in (a) the Mach-Zehnder configuration, and (b) the Sagnac configuration

ferometer, limited primarily by atomic projection noise. Projection noise is most simply understood from binomial statistics. At the output of the interferometer, each of N atoms is in a superposition of two internal states, with a probability p for being in state $|2,0\rangle$. Upon measurement, the atom is projected into one of these states, and a sample with N atoms represents N trials of this proverbial 'coin flip' experiment. In any given experimental run, we measure p by measuring the number of atoms in each state, and binomial statistics then predicts that the variance in p is given by:

$$\sigma_p^2 = \frac{1}{N} p(1-p) \tag{6.17}$$

$$\therefore \ \sigma_p = \frac{1}{\sqrt{N}} \sqrt{p(1-p)} \tag{6.18}$$

Typically, an interferometer is operated at mid-fringe ($p = 0.5$) to maximise the change in p for a given phase shift, and thus $\sigma_p = \frac{1}{2\sqrt{N}}$ is the atomic projection-noise contribution. Additionally, there will be a contribution from photon shot-noise in the absorption imaging process. The details of this are beyond the scope of this thesis, other than to state that the photon shot-noise contribution scales as $\sigma_{p,\gamma} \propto \frac{1}{N}$ (see [143, 158] for details). Thus, for sufficiently large atoms numbers, atomic projection-noise will be dominant.

Figure 6.17 shows the measured variance in p as a function of total atom number for (a) a single beamsplitter operation, and (b) the full Ramsey interferometer cycle. The long-dashed lines represent the theoretical atomic projection-noise, and the short-dashed lines represent the photon shot-noise. The solid lines are their sum. Data points represent the experimentally measured standard

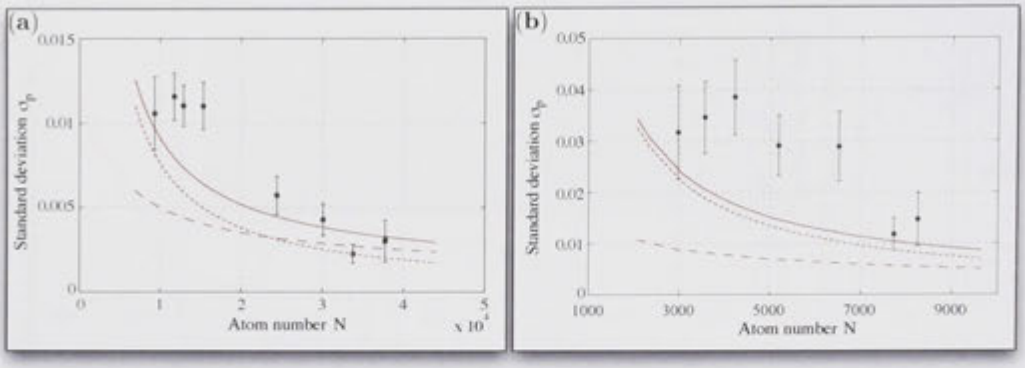

Figure 6.17: Atomic projection noise in (a) an atomic beamsplitter, and (b) a Ramsey interferometer.

deviation for 5-10 samples, with error bars giving the confidence in the measurement due to the finite sample number. It is evident that quantum noise (atomic and photonic) are the fundamental noise sources in both cases, particularly for the higher atoms numbers; demonstrating the excellent passive stability of the Sagnac configuration for the Raman coupler.

6.4 Conclusions

In this chapter, we have demonstrated a Raman laser-system that is a versatile and effective tool for coherently manipulating atomic ensembles at the level required for atom interferometry. Operating via a pure two-state coupling, it produces atom lasers in a single atomic state and has the potential to transfer correlation statistics from a quadrature squeezed optical beam, making it a promising tool for investigating quadrature squeezing of atom lasers and entanglement in atomic beams. The same basic system, operated as an atomic beamsplitter between the hyperfine ground states of ^{87}Rb, was used to build a quantum projection-noise limited Ramsey interferometry, with a freely-falling atom-laser pulse as the atomic source. Although we have demonstrated operation of this system using ^{87}Rb, the optical setup is relatively straightforward compared with other Raman laser-systems, such as OPLLs, and can easily be transferred to other atom species such as sodium, lithium, or caesium; as well as to other applications of Raman transitions. Chapter 7 will present a detailed comparison of the Raman laser-system to other typical atom-laser outcoupling systems.

Chapter 7

An Experimental Comparison of Atom-Laser Outcouplers

Work in this chapter has been peer-reviewed and published in:

J. E. Debs, D. Döring, P. A. Altin, C. Figl, J. Dugué, M. Jeppesen, J. T. Schultz, N. P. Robins, and J. D. Close. Experimental comparison of Raman and rf outcouplers for high-flux atom lasers. Phys. Rev. A 81, 013618 (2010). [159]

In the previous chapters, we have shown that Bose-condensed sources offer attractive properties as atomic sources for atom interferometry-based inertial sensors. In particular, atom-lasers were shown to have a substantially narrower momentum width than any other atomic source. In addition to a low divergence and simple spatial mode, a high flux is desirable for maximising the SNR, especially when comparing devices at the shot-noise limit. The flux of Bose-condensed sources is currently limited by the repetition rate of a given BEC machine. This in turn limits the flux of the atom-laser, which can only be continuous over times less than the machine cycle-time. Such continuous sources will also be beneficial for combating the "Dick effect," which is the downsampling of high frequency noise in pulsed devices [160], such as the majority of current atom interferometers.

In producing a continuous Bose-condensed source, there is the question of pumping for an atom-laser: the ability to coherently pump atoms into a "lasing" BEC, which is being used as the source for an atom-laser outcoupler. Pumping has been extensively investigated by N. P. Robins *et al.*, who demonstrated continuous pumping of a lasing BEC from a source BEC. Details, which are beyond

the scope of this thesis, can be found in [161, 162], as well as the theses of M. Jeppesen [132] and D. Döring [158]. See also the related work on superradiance by S. Inouye *et al.* [163]. Demonstration of pumping was a pivotal step along the path to a truly continuous atom-laser, however, how to replenish the source condensate remains an open but likely solvable problem.

In the event that a truly continuous atom-laser is developed, there is the question of which outcoupler is the best choice. As will be shown in this chapter, the continuous operation of an outcoupler shuts down for a strongly coupled system due to dressed bound states [164]. This in turns provides a limit to the atom-laser flux that can be extracted from a magnetically confined BEC. In what follows, we compare the flux-limit of a (multi-level) RF outcoupler, a (multi-level) Zeeman-Raman outcoupler, and the (two-level) hyperfine-Raman outcoupler from chapter 6. Combined with the results of previous work on the divergence of atom-lasers, we conclude that our hyperfine-Raman outcoupler is the preferred choice for outcoupling the brightest atom-lasers from magnetically trapped BEC; verifying predictions by Robins *et al.* [54] and Duguè *et al.* [131]. In addition, we include preliminary results of an atom laser sourced from an optically trapped BEC; results which strongly suggest a Heisenberg-limited divergence, and are yet to be fully explored.

7.1 Shutdown of an Atom Laser

The physics of atom laser shutdown is described well by the formation of dressed states and their associated potentials – a well known phenomenon of electromagnetically coupled atomic systems (see equation (2.17) and reference [165]). We use a two-level model in one spatial dimension to highlight the key feature of atom-laser shutdown; based largely on concepts developed in chapters 2 and 5. For simplicity, we also ignore mean-field effects. A rigorous treatment of BECs in dressed potentials can be found in [166], and such potentials have been studied experimentally in the context of forming rf-induced trapping potentials [167, 168, 169, 170].

Consider a two-level atom in a harmonic magnetic field, with bare trapped and untrapped atomic states, $|t\rangle$ and $|u\rangle$. These represent any trapped and untrapped states that can be coupled, however, we assume they are the $|1,-1\rangle$ and $|1,0\rangle$ states of ^{87}Rb respectively in what follows.[1] Their energy levels are thus given by equations (5.24) and (5.25) respectively. As the gravitational potential is common

[1] All subscripts $\{t\}$ and $\{u\}$ are thus equivalent to $\{1,1\}$ and $\{1,0\}$ respectively.

to both states, it does not affect the resonance condition as a function of z, which is equation (5.26) and is restated here for convenience: $\hbar\omega_r(z) = 1/2m\omega_z^2 z^2 + \hbar\omega_b$. Thus, we may neglect the gravitational terms when considering the energy-level diagram for coupling these states with radiation of frequency ω, which is given as the inset of figure 7.1. Assuming ω is resonant with the centre of the condensate, we define a spatially dependent detuning:

$$\begin{aligned}\hbar\Delta(z) &= \omega_r(z) - \omega_r(z_s) \\ &= \frac{1}{2}m\omega_z^2 z^2 + \hbar\Delta_g \end{aligned} \tag{7.1}$$

where $\Delta_g = \omega_b - \omega_r(z_s) = -mg^2/2\hbar\omega_z^2$. Thus Δ_g is a measure of the gravitational sag for ω on resonance with the centre of the condensate.

We consider now the position-space wave functions of the two states, $\psi_t(z,t) = \langle z|t\rangle$ and $\psi_u(z,t) = \langle z|u\rangle$. The equations governing the evolution of these states in the frame rotating at ω are then (from the Schrödinger equation):

$$i\hbar\dot{\psi}_t = \left(-\frac{\hbar^2}{2m}\frac{\partial^2}{\partial z^2} + \hbar\Delta(z) + mgz\right)\psi_t + \hbar\Omega\psi_u \tag{7.2}$$

$$i\hbar\dot{\psi}_u = \left(-\frac{\hbar^2}{2m}\frac{\partial^2}{\partial z^2} + mgz\right)\psi_u + \hbar\Omega\psi_t \tag{7.3}$$

The Hamiltonian can therefore be written as:

$$\hat{H} = \underbrace{-\hat{I}\frac{\hbar^2}{2m}\frac{\partial^2}{\partial z^2}}_{\text{kinetic}} + \underbrace{\frac{\hbar}{2}\begin{pmatrix}\Delta(z) & \Omega \\ \Omega & -\Delta(z)\end{pmatrix}}_{\text{coupling}} + \underbrace{\left(\frac{\hbar\Delta(z)}{2} + mgz\right)\hat{I}}_{\text{offset}} \tag{7.4}$$

where $\hat{I}$ is a 2×2 identity matrix and Ω is the angular Rabi frequency as defined in chapters 2 and 4. For example, in the case of RF coupling, $\hbar\Omega = \langle t|\boldsymbol{\mu}_M \cdot \mathbf{B}_{\mathrm{rf}}|u\rangle$ is the energy of the magnetic dipole coupling, where $|\mathbf{B}_{\mathrm{rf}}|$ is the amplitude of the coupling field and $\boldsymbol{\mu}_M$ is the magnetic dipole moment. In the case of Raman coupling, it is the effective Rabi frequency. In the absence of the kinetic term, this Hamiltonian differs from the two-level Hamiltonian in chapter 2 by only a point-wise energy offset. Thus, utilising the unitary matrix, equation (2.21), we diagonalise the potential and coupling terms to give the equations of motion for

the dressed state wave functions:

$$i\hbar\dot{\psi}_+ = \left(-\frac{\hbar^2}{2m}\frac{\partial^2}{\partial z^2} + V_+(z) + V_{kin}(z)\right)\psi_+ + V_c(z)\psi_- \tag{7.5}$$

$$i\hbar\dot{\psi}_- = \left(-\frac{\hbar^2}{2m}\frac{\partial^2}{\partial z^2} + V_-(z) + V_{kin}(z)\right)\psi_- - V_c(z)\psi_+ \tag{7.6}$$

where $V_\pm(z) = \hbar/2\left(\Delta(z) \pm [\Delta(z)^2 + \Omega^2]^{1/2}\right) + mgz$ are the adiabatic potentials for the dressed states $|\lambda_\pm\rangle$; plotted in figure 7.1. In the absence of V_{kin} and V_c, these equations are identical to the results of chapter 2 [equation (2.22)], and the dressed states are stationary. Their presence stems from the kinetic term of the Hamiltonian and the position-dependent detuning; in particular, V_c induces a coupling *between* the dressed states. V_{kin} and V_c are given by:

$$V_{kin}(z) = \frac{\hbar^2\Delta'(z)^2}{8m\Omega^2\left(1 + \frac{\Delta(z)^2}{\Omega^2}\right)} \tag{7.7}$$

and

$$V_c(z) = \frac{\hbar^2}{2m\Omega\left(1 + \frac{\Delta(z)^2}{\Omega^2}\right)}\left[\frac{\Delta'(z)^2\Delta(z)}{\Omega^2\left(1 + \frac{\Delta(z)^2}{\Omega^2}\right)} - 2\Delta''(z) - \Delta'(z)\frac{d}{dz}\right] \tag{7.8}$$

By considering the magnitude of these terms, we may define regimes for strong and weak outcoupling.

7.1.1 Strong Outcoupling and the Atom-Laser Bound State

By inspecting V_{kin} and V_c, it is apparent that as Ω increases these terms will become vanishingly small. Converting equations (7.7) and (7.8) into dimensionless form using the harmonic oscillator length, time, and energy scales, it can be shown that this occurs when:

$$\Omega \gg g\sqrt{\frac{m}{\hbar\omega_z}} \tag{7.9}$$

where we have used the value of $\Delta'(z)$ at the trap minimum.[2] This is the condition for which the dressed states are stationary states of the adiabatic potentials.

[2] This assumes that $\Delta'(z)$ varies little across the cloud compared with its value at the centre; equivalent to $a_{ho} < z_s$. Additionally the Δ'' term vanishes for $\Omega \gg \omega_z$, which is also satisfied if inequality (7.9) holds. In the absence of gravity, this would be the only condition for the strong coupling regime.

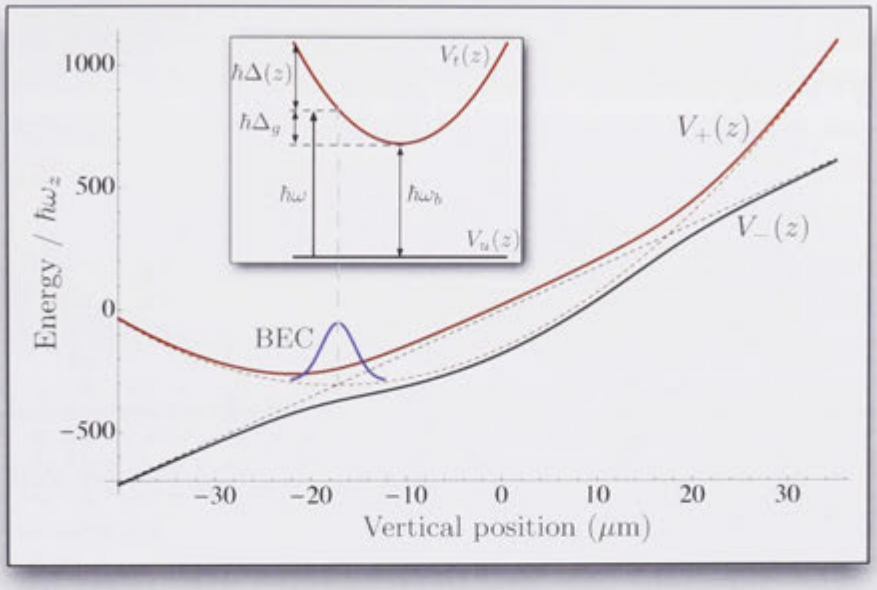

Figure 7.1: Adiabatic potentials (solid lines) formed by coupling $|t\rangle$ and $|i\rangle$ with radiation of frequency ω. The inset shows the level coupling diagram as a function of the vertical position in the trap. The dashed lines represent the potentials when the coupling is switched off, showing two crossings. The crossing at $z \sim -17\,\mu m$ represents the centre-of-mass position of the condensate, with the blue curve representing spatial extent of the BEC in the potentials. Note that the height of blue curve is *not* indicative of the chemical potential.

Figure 7.1 plots the adiabatic potentials as a function of z. The dashed lines represent the bare atomic potentials in the rotating frame, which cross at the point of resonance. Clearly V_+ admits bound states, and atoms in $|\lambda_+\rangle$ remain bound in the limit of very strong coupling.

For a typical sequence used to produce an atom laser, outcoupling is switched on non-adiabatically, projecting the atoms onto the dressed basis. For a two-state system this expansion is given by $|t\rangle = \frac{1}{\sqrt{2}}(|\lambda_+\rangle - |\lambda_-\rangle)$ at $\Delta(z) = 0$ [see equations (2.17)], and is valid even beyond the extent of the cloud in the strong coupling limit. The wavefunction is therefore distributed evenly between a bound and unbound component leading to approximately half the atoms remaining trapped in the V_+ potential, while the other half leave the trapping region in the V_- potential. When the outcoupling is switched off, the clouds are projected back onto the bare states, producing a second burst of atoms which may leave the trap region; however, a significant fraction of the atoms remain trapped. Hence a beam is not produced, and the bound dressed state prevents production of an atom-laser for strong outcoupling.

Figure 7.2(b) clearly demonstrates these features of atom laser shutdown for a Raman outcoupler operating between the Zeeman levels of the $F = 1$ ground state of ^{87}Rb [see figure 7.3(a)]. This figure collates absorption images taken for continuous outcoupling over 14ms as the coupling strength is increased. The absorption image of each individual run of the experiment has been integrated in the direction perpendicular to the atom-laser beam, giving the vertical linear atom density. Each of these integrated profiles is one pixel-column in the figure, and each column corresponds to a different value of coupling strength. The coupling strength is characterised by ν_0, which is the oscillation frequency of the untrapped state population for a semiclassical Rabi-flopping model. For a two-level system, $\nu_0 = \Omega/2\pi$. However, for a multi-state outcoupler this is not so. For example, $\nu_0 = 2^{3/2}\Omega/2\pi$ for a three-level outcoupler operating between Zeeman states of the $F = 1$ ground state.

A continuous atom laser beam can be seen at low frequencies, with the onset of complex outcoupling dynamics, and shutdown, as the coupling strength is increased. Figure 7.2(a) is a selection of data used to calibrate the Rabi frequency using the technique described in section 6.2.4, figure 6.8.

7.1.2 The Weak Coupling Limit

The previous section shows that production of an atom-laser beam requires operation outside the strong coupling regime. Although the two-level model is suitable in the strong coupling limit, in the case of weak coupling, atoms are coupled to a continuum of energy states given by the gravitational potential, and the dressed-state model is not particularly useful.

The weak coupling regime has been successfully modelled by Gerbier *et al.* [171], who applied Fermi's golden rule [94] for coupling a single initial state to a continuum of final states; treating the coupling field as perturbative. The outcoupling (or transition) rate is then:

$$R_{t\to u} = \frac{2\pi}{\hbar}|\langle u|\hat{V}_I|t\rangle|^2\rho(E_z) \tag{7.10}$$

$$\propto \Omega^2 \tag{7.11}$$

where $\hat{V}_I$ is the perturbative interaction Hamiltonian, and $\rho(E_z)$ is the density of final states $|u\rangle$ at energy E_z. $|u\rangle$ in this case represents the continuous spectrum of gravitational potential modes, which are Airy functions [171]. Note that the transition rate is proportional to the Rabi frequency squared.

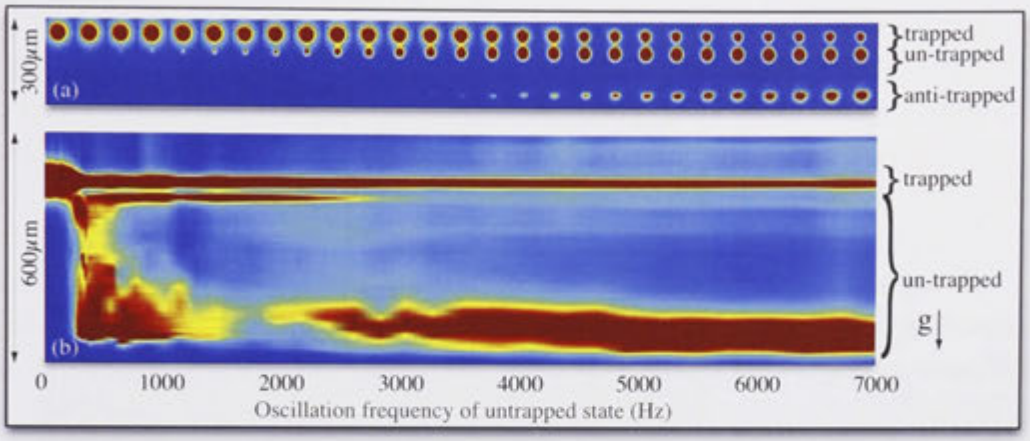

Figure 7.2: Absorption image data for a Raman outcoupler operating between Zeeman states of the $F = 1$ ground state of ^{87}Rb. Red (blue) represents a high (low) atom density, and the vertical scales give the vertical extent in space. (a) Raw absorption images displayed for a $100\,\mu$s pulse of outcoupling. Images from left to right correspond to increasing coupling strength. These images were used to calibrate the Rabi frequency for our setup, as described in Section III. (b) These data represent absorption images taken for 14 ms of outcoupling, and different coupling strengths. Each column of pixels corresponds to a single absorption image that has been integrated (summed) in the direction perpendicular to propagation of the atom laser beam. Hence, each column represents the linear atomic density in the vertical direction for a different coupling strength. In the left most columns, a smooth continuous beam is visible for low coupling strengths. As coupling strength is increased, atom laser shutdown can be seen in the form of complex density profiles at intermediate coupling strength, and then the clear effect of the dressed states at the highest coupling strengths (right most columns).

A useful intuitive picture of weak outcoupling is an irreversible process caused by the gravitational force removing atoms from the resonant region within the trapped cloud. Strong coupling, on the other hand, is reversible and well described by a two-level model. The boundary between these two limits corresponds to the onset of complex outcoupling dynamics and atom laser shutdown. The intermediate coupling strength has been estimated using a simple model in [54] by comparing the timescale associated with the Rabi-flopping frequency ν_0 to that associated with the fall time τ_{fall} through the coupling region due to gravity.

As the coupling strength and hence ν_0 is increased, the time required for an oscillation of the untrapped state population becomes comparable to or less than the fall time τ_{fall}, and one can no longer consider the effect of gravity to be irreversible. Atoms are coupled back into the trapped state and remain localised within the coupling region. It is by this reasoning that ν_0, and not Ω has been used as the parameter for comparison of RF and Raman based outcouplers. Any momentum imparted by a Raman transition will reduce τ_{fall}, enabling a stronger

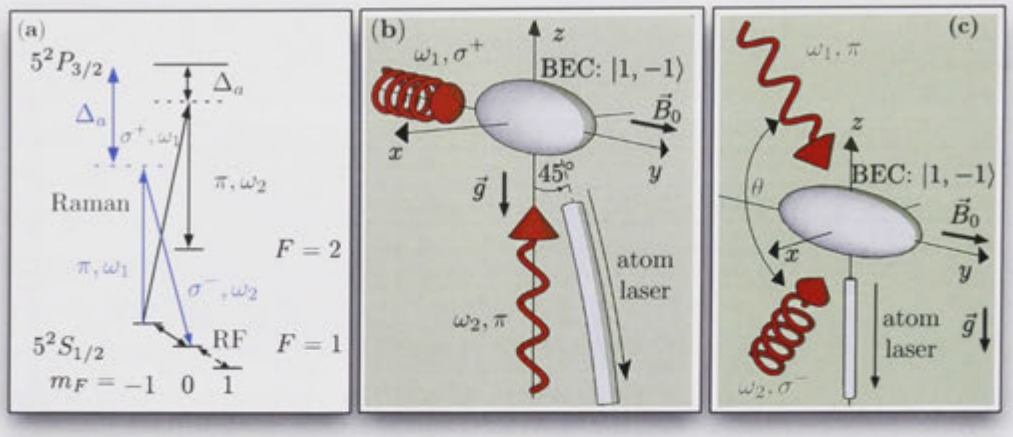

Figure 7.3: (a) Simplified level diagram of ^{87}Rb for the different outcoupling schemes. (b) Orientation of the Raman beams with respect to our magnetic trap for the two-state hyperfine outcoupler. (c) Orientation of the Raman beams with respect to our magnetic trap for three-state Zeeman coupling. An rf antenna (not shown) drives transitions between Zeeman states in the $F = 1$ ground state. Optical Raman beams drive a two-photon transition between hyperfine (black) or Zeeman (blue) ground states of ^{87}Rb.

coupling to be used before reaching the boundary between the strong and weak outcoupling regimes; hence a Raman outcoupler will result in a larger flux than an RF outcoupler, while still remaining in the weak outcoupling regime. In addition, Dugué *et al.* predicted that a two-level system will result in a higher flux than a multi-level system for the same value of ν_0 [131].

7.2 The Comparison of Raman and RF Outcouplers

Our production of BEC is described in section 5.4.2. Specifically, condensates of approximately 2×10^5 atoms of ^{87}Rb are prepared in the $|1, -1\rangle$ state in the QUIC trap, with $(\omega_\rho, \omega_y) = 2\pi \times (130, 13)$ Hz. Radio frequency outcoupling is performed using an RF loop antenna driven directly by a signal generator at ~ 1.34 MHz, which couples the three Zeeman states in the $F = 1$ manifold. We compare this to two Raman outcouplers, one of which operates between the Zeeman states of $F = 1$ and the other between the $F = 1$ and $F = 2$ hyperfine ground states. The former is described in detail in reference [172]. Briefly, we drive the two-photon transition between $|1, -1\rangle$ and $|1, 0\rangle$ using two phase locked optical beams separated in frequency by ~ 1.34 MHz, and detuned from the $5^2P_{3/2}$ resonance by $\Delta_a \simeq 300$ GHz. The Raman beams are produced by

sourcing two beams from a single ECDL, and sending each of these through an acousto-optic modulator (AOM) in a double-pass configuration. Each modulator is driven by phase-locked signal generators, separated in frequency by approximately 0.67 MHz. The beams are directed onto the condensate as shown in figure 7.3(c). They are co-planar with gravity and the magnetic trap bias field, separated by $\theta = 140°$ and given appropriate polarisation to optimise the $\Delta m_F = 1$ transition. This results in a momentum kick of $2\hbar k \sin\theta/2 \simeq 1.8\hbar k$ parallel to gravity. For Zeeman-outcoupling, atoms coupled to $m_F = 0$ can also be coupled to $m_F = 1$ due to the negligible second-order Zeeman shift for our trap bias field.

The hyperfine Raman coupler was described in section 6.2, with the beam configuration given again in figure 7.3(b) for convenience. All three outcouplers are operated on resonance, as depicted in figure 7.3(a), and the Rabi frequency for each of our systems is calibrated using the method described in section 6.2.4, figure 6.8.

7.2.1 The Zeeman-Raman Outcoupler

The data used to demonstrate the atom laser shutdown [figure 7.2(b)] were taken using the following outcoupling scheme. Raman coupling between Zeeman levels is switched on suddenly (< 200 ns) projecting the condensate onto the dressed basis. The coupling field remains on for 14 ms and is then suddenly switched off projecting back onto the bare atomic basis. The system is left to evolve for 5 ms before the trap is switched off, and for a further 2 ms before standard absorption imaging along the weak trapping direction [y in figure 7.3(b)]. The relative number of atoms transferred to the untrapped (atom laser) state is measured and plotted as a function of ν_0 in figure 7.4. These data show the dramatic effect of atom laser shutdown. For low ν_0, a continuous and clean beam is extracted. At $\nu_0 = 500$ Hz the effect of the bound dressed state manifests, causing an increasing number of atoms to remain trapped. As the coupling strength is further increased, the fraction of untrapped atoms saturates at around 0.35, dictated by the projection onto and from the dressed basis.

7.2.2 The Hyperfine-Raman and the RF Outcouplers

We now present a comparison of the RF and (two-level) hyperfine-Raman outcouplers. For these data, several changes are made to the outcoupling sequence given in section 7.2. Firstly, the coupling field remains on for only 3 ms in order to allow imaging of all atoms (trapped, untrapped, and anti-trapped). For the rf

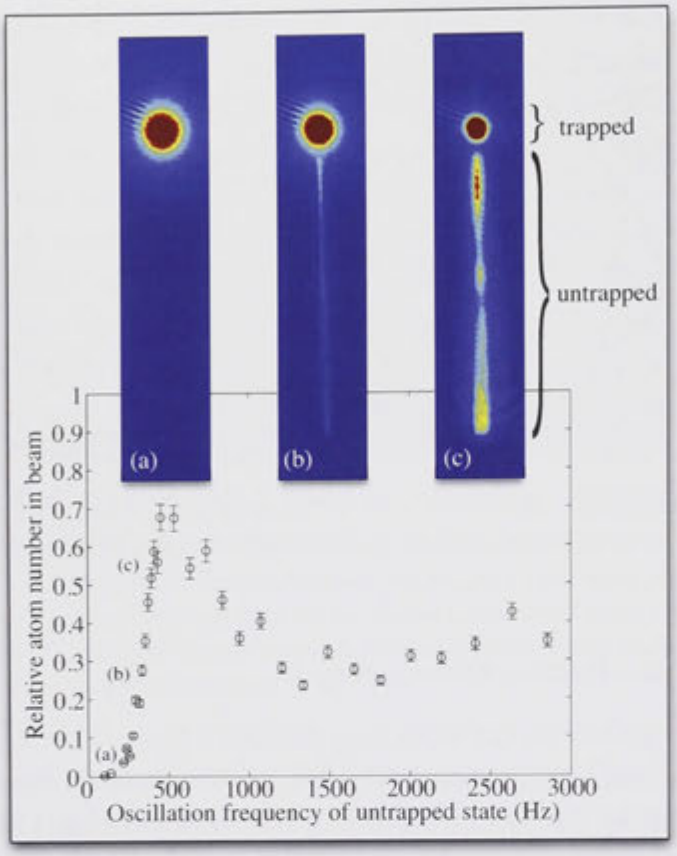

Figure 7.4: Relative number of atoms in the atom laser beam for Zeeman-Raman outcoupling as a function of ν_0. At $\nu_0 = 500\,\text{Hz}$ the number of atoms in the atom laser begins to decrease showing a clear effect of the bound dressed state shutting down the operation of the outcoupler. Absorption images are shown for each of the specified data points, and correspond to 14 ms of outcoupling. Error bars represent statistical uncertainty in the total number of atoms.

outcoupler, the system is left to evolve for $800\,\mu\text{s}$ after the coupling is switched off. This evolution time was maximised in order to separate the three magnetic sub-states as much as possible, while still imaging all atoms onto the CCD camera. For the Raman outcoupler, the system can be evolved for 3.5 ms after the coupling is switched off due to the absence of an anti-trapped state. The clouds are left to expand for 4.5 ms after the trap is switched off, and a standard absorption image is taken along the radial trapping direction [x in figure 7.3(c)]. The sequence is repeated for different coupling strengths and the relative number of atoms transferred to the untrapped state is plotted as a function of ν_0 in figure 7.5 for RF (black circles) and Raman (blue diamonds) outcoupling.

Three examples of the absorption images used to extract the atom number

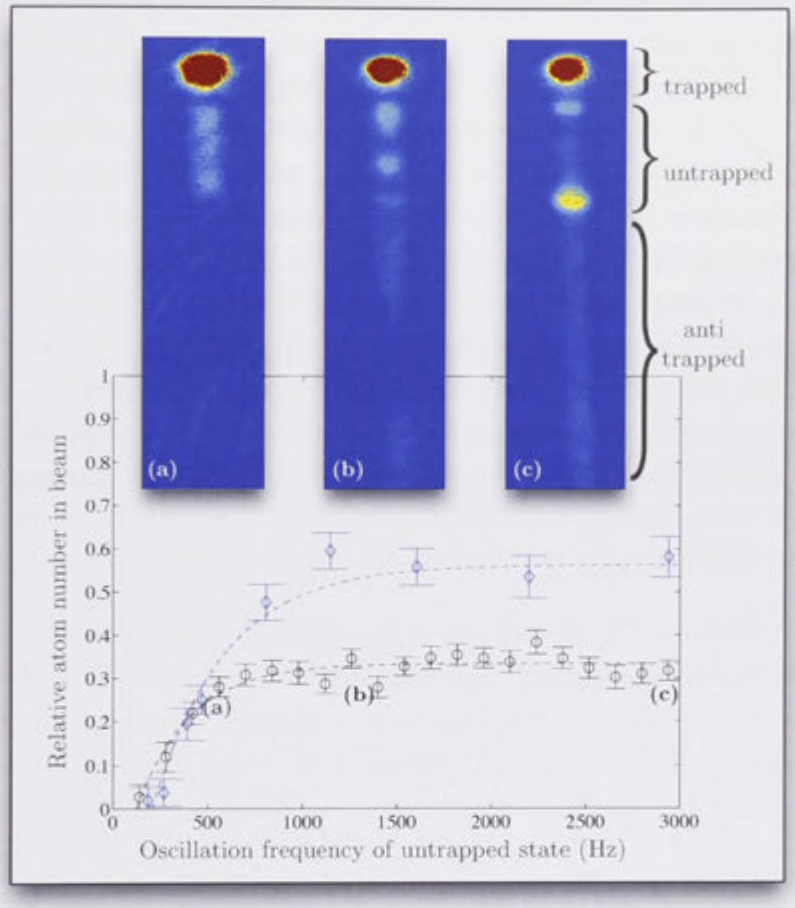

Figure 7.5: Relative atom number in the atom laser beam as a function of ν_0. Black circles correspond to rf data, and blue diamonds to the Raman data. The dashed lines are fits to the data of the form $y = A(1 - e^{-(x-x_0)/r})$, and allow a comparison of the bound state onset for each data set via the free parameter, r. Absorption images are shown for each of the specified points in the rf data. Error bars represent uncertainty in the fitted atom number for each image.

for RF data are shown in figure 7.5, as well as regions of interest corresponding to trapped, untrapped, and anti-trapped atoms. Atom numbers are extracted by integrating a Gaussian fitted to each row of an image and summing over all rows for a given region. To a good approximation, the 'trapped,' 'untrapped,' and 'anti-trapped' regions correspond to $m_F = -1, 0,$ and 1 respectively, and the expected features are visible in all three images. For weak coupling [point (a)], a reasonably clean beam is seen, 3 ms in length. This defines the region in which untrapped atoms will lie for all images. There are no discernible anti-trapped atoms. At the other extreme [point (c)], the strong coupling image shows

a burst of atoms at the bottom of the 'untrapped' region, corresponding to the initial projection, as well as a second burst at the top of the 'untrapped' region corresponding to the final projection. A cloud of accelerated atoms defines the 'anti-trapped' region, corresponding to atoms coupled to the anti-trapped state. Finally, as was the case in figure 7.2(b), for intermediate coupling strength [point (b)], complex dynamics are seen in the form of spatial oscillations in the atomic density. It should be noted that as $m_F = 0$ atoms evolve freely under gravity (neglecting second order Zeeman effects), it is likely that upon projecting back to the atomic basis for the strongly coupled system, some of them will mix in with other states in our defined regions (e.g. in the anti-trapped region). However, our fundamental interest is in the onset of the bound state and atom laser shutdown, thus the finer details of the strong coupling regime have not been investigated in this work.

In the graph of figure 7.5, the behaviour theoretically predicted in section 7.1 is observed. For weak outcoupling ($\nu_0 < 500\,\mathrm{Hz}$), both data sets coincide. More importantly, as coupling strength is increased, a plateau is seen in the number of atoms transferred to the untrapped state for both rf and Raman outcoupling. This plateau occurs at a lower value of ν_0 for rf outcoupling, and also saturates at a smaller fraction of atoms outcoupled. The dashed lines are fits to the data of the form $y = A(1 - e^{-(x-x_0)/r})$, and the parameter r is used to compare the maximum ν_0 for the two systems. We find ν_0 is larger by a factor of 1.45 for Raman outcoupling, translating to an increase in flux of approximately 2.1. By utilising a full $2\hbar k$ momentum kick, this could be improved to an overall increase in flux by a factor of 5 for (two-state) Raman outcoupling over rf outcoupling. It is worth noting that when considering the two-state Raman outcoupler, the model in section 7.1 predicts a maximum ν_0 of $\sim 1\,\mathrm{kHz}$, which is in reasonable agreement with the experimental data.

A final important result is that the three-level Raman outcoupler data in figure 7.4 plateaus at a higher relative number than the RF outcoupler, but at a lower relative number than the two-state Raman coupler. This provides experimental evidence that a two-level outcoupler will achieve a higher maximum flux than a three-level outcoupler, as predicted in [131]. Thus, by combining figure 7.4 and 7.5, we find that a two-state Raman outcoupler can produce the highest continuous atom laser flux of any outcoupler for magnetically confined samples.

7.3 Conclusions for RF vs. Raman Outcouplers

When momentum is imparted to atoms outcoupled from a BEC to form an atom laser beam, a higher continuous flux is achievable compared with zero momentum transfer systems. We have experimentally verified that a two-state Raman outcoupler can achieve higher continuous flux than any RF-based or multi-level system. Coupled with the previous work on divergence and the spatial mode of Raman outcoupled beams [126], it is now clear that a two-level Raman outcoupler produces the highest-brightness atom laser beam of any outcoupler to date for magnetically confined samples. With rapidly developing technology for producing larger condensates with shorter machine duty cycles, the recent work on pumping [161, 162] and development of an atom laser Ramsey interferometer [151], as well as the potential of utilizing squeezing, the atom laser is becoming a strong contender as a beam source for applications in atom interferometry.

7.4 Outcoupling an Atom-Laser from an Optical Trap

In close collaboration with P. Altin, we have recently produced atom-lasers from optically confined ^{87}Rb condensates in our dual-species machine (section 5.4.3). Our preliminary results are evidence of a beam with a transverse momentum width limited by Heisenberg uncertainty. This results from the details of all-optical outcoupling, which we motivate with a simple model below. Cennini *et al.* first demonstrated outcoupling from an optical trap in [53], however, no evidence was presented that suggested a Heisenberg-limited beam.

The principle of outcoupling from an optical trap is outlined in figure 7.6. As evaporation in an optical trap is induced by decreasing the trap depth, allowing the most energetic atoms to 'spill' out, the final trap depth is comparable to the chemical potential of the BEC. In other words, the BEC fills the entire trapping volume. An atom-laser can therefore be extracted by slowly reducing the trap depth further, allowing atoms to leave the condensate due to gravity. This is illustrated in figure 7.6(a). The blue curve represents the total potential due to gravity, a Gaussian optical potential, and the mean-field energy, which mirrors the trap profile. The dashed line is the potential without the mean-field for reference. Note that atoms with the cloud see a flat potential. We use this feature to motivate a Heisenberg-limited divergence.

The total potential is drawn in two dimensions in (b). As the trap depth is lowered, gravity extracts atoms, which have classical trajectories represented by

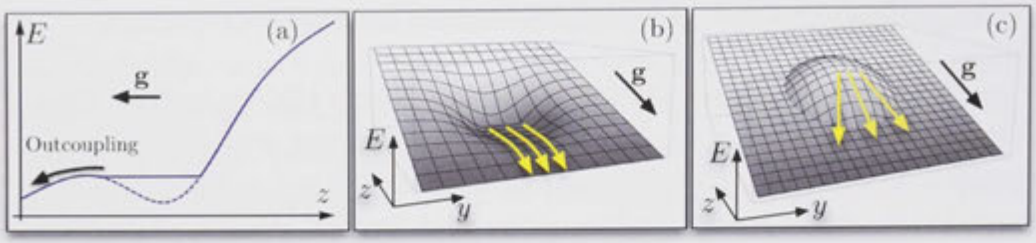

Figure 7.6: Schematic representation of atom-laser outcoupling from an optical trap. (a) The total traping potential in the vertical direction, which is the sum of the gravitational potential, a Gaussian optical potential, and the mean-field energy. As the trap depth is lowered, atoms are extracted from the trap by the gravitational force. Note that atoms with the cloud see a flat potential. (b) The same potential drawn in two-dimensions, with classical trajectories given by the yellow arrows. As atoms are still influenced by the optical potential, and thus are not repelled transversely by the mean-field. (c) Surface potential of an magnetically outcoupled atom-laser for comparison. In this case, the atoms are insensitive to the trapping potential, and diverge due to mean-field as discussed in section 5.3.1.

the yellow arrows. Notice that as atoms leave the trap, they are still influenced by the (attractive) optical potential, which perfectly balances the mean-field repulsion, and are thus not repelled by the mean-field. This should be compared with the case of outcoupling from a magnetic trap, in which outcoupled atoms are no longer sensitive to the magnetic field, and only evolve under the gravitational and mean-field potential. The potential surface is shown in (c), along with classical trajectories, and was used to estimate the atom-laser momentum width in 5.3.1.

Figure 7.7 gives a tantalising set of data for a typical optical atom-laser produced in our system. (a) is an absorption image, taken after $\sim 20\,\mathrm{ms}$ of expansion after switching off the dipole trap, and the beam length corresponds to $\sim 11\,\mathrm{ms}$ propogation from the bottom of the BEC to the bottom of the image. We measure the divergence of the beam by fitting transverse line profiles to the integrated Thomas-Fermi distribution $\rho_z(y) = \rho_0(1 - y^2/R^2)^{3/2}$ where R is the beam radius and ρ_0 the peak column density. Two examples of these fits are given at position I and II. The fitted radius is plotted as a function of the vertical position z in (c). Although in principle $R \propto y^{1/2}$, a linear fit is sufficient for our data, particularly after 20 ms of expansion. From the linear fit, we extract a divergence angle $\theta = (0.05 \pm 0.12)\,\mathrm{mrad}$.

Although our measured divergence is not discernible with the current measurement uncertainty, the expected Heisenberg limit for our experimental parameters ($\omega_y = 2\pi \times 28\,\mathrm{Hz}$, $N \sim 10^6$ atoms) is on the order of 0.1 mrad; consistent with

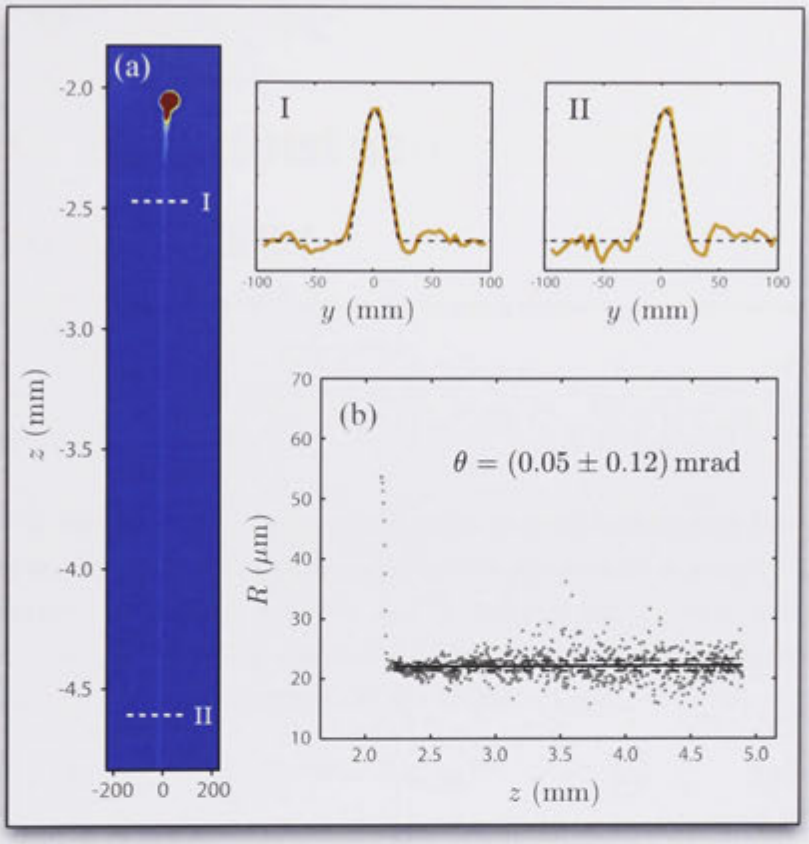

Figure 7.7: (a) Absorption image of a typical atom-laser outcoupled from an optical trap by lowering the trap depth. (b) Beam radius as a function of the vertical position in the beam. The Radius is given by fitting a Thomas-Fermi profiles fit to horizontal slices of the beam, with two examples given in I and II. Figure courtesy of P. Altin.

the measurement uncertainty. This is strongly suggestive of a Heisenberg-limited atom-laser beam divergence. These preliminary results are being investigated further, and will be improved by increasing our absorption imaging resolution, in addition to theoretical modelling of the outcoupling process.

In any case, freely propagating atom-laser beams such as that of figure 7.7 are rarely, if ever, found in the literature; such a clean, narrow momentum-width source holds great promise as an atomic source for future inertial sensors.

Chapter 8

Large Momentum Transfer Beamsplitters

In chapter 3, we derived the phase shift of an atomic interference based inertial measurement. In general, it was found that the phase-shift is linearly dependent on the effective space-time area ($\propto k_e T^2$) enclosed by the two interferometer paths. For example, recalling equation (3.18) for uniform gravitational acceleration in a Mach-Zehnder configuration, we have:

$$\Phi = -\mathbf{k}_e \cdot \mathbf{g} T^2 \tag{8.1}$$

with a projection-noise limited sensitivity of:

$$\Delta g_{||} = \frac{1}{2k_e T^2 \sqrt{N}} \tag{8.2}$$

where $g_{||}$ is the component of acceleration parallel to $\mathbf{k}_e$. There are therefore three parameters available for increasing the sensitivity: the interrogation time T, the effective wave vector $\mathbf{k}_e$, (which as will be motivated below, is proportional to the momentum transferred in the beam splitting process), and the number of atoms N (or flux for a given measurement time).[1] Flux is currently limited by atomic source technology to around 10^{11} atoms/s for thermal beams [14], 10^7 atoms/s for laser cooled sources [10], and 10^6 atoms/s for Bose-condensed sources [77].[2] Furthermore, the dependence on N is weakest of all available parameters.

Although the sensitivity scales most strongly with interrogation time, increas-

[1] It is important to note, that although equation (8.2) is derived from the projection-noise limit, a signal will always increase with $\sqrt{N}$ for N independent measurements. This follows from the central-limit theorem. As N atoms in the majority of interferometers can be treated as N independent measurements of phase, then the sensitivity will improve with $\sqrt{N}$ for a random-noise limited system.

[2] These numbers for total flux are not the number of atoms participating in the interferometer, which is usually a larger fraction of the total for a narrower momentum width source.

ing it becomes a practical consideration regarding apparatus size and application. For example, $T = 1\,\mathrm{s}$ corresponds to at least a 5 m drop (or a 2.5 m launch) in a free-fall gravimeter. Similar apparatus sizes result when considering a gyroscope, for both thermal beam and ultra-cold sources. To date, the highest reported value for the interrogation time is for a gravimeter with $T = 0.4\,\mathrm{s}$ and an apparatus height $\sim 1\,\mathrm{m}$ [10]. Such long times may be considered unsuitable, particularly for portable devices.

LMT beamsplitting therefore currently offers the most promising avenue for increasing the sensitivity. This is particularly so due to the modest *useful* momentum transfer demonstrated to date [85], and as current state-of-the-art devices for both rotation and acceleration operate using the minimum transfer of just two photon recoils ($2\hbar k$). Dimopoulos *et al.* have, for example, suggested a gravitational wave detector which requires 1000 photon recoils [28]. In general, optical lattices have been used to produce LMT atom-optical elements. These either utilise Bragg diffraction [85], or Bloch oscillations [173], both of which can be described by the exchange of $2n$-photons between the counter-propagating beams forming the lattice, leading to an increase in the phase shift by a factor of n.

We focus on the use of Bragg diffraction, and this chapter describes the theory of Bragg diffraction and its use for LMT beamsplitting. We outline the details of our LMT beamsplitter laser-system, including recent improvements to the noise characteristics, which is used for gravimetry with a BEC in chapter 9.

8.1 Bragg Diffraction

8.1.1 Bragg Scattering

In 1912, Sir William Lawrence Bragg discovered the law of X-ray diffraction from crystals; now known as "Bragg's Law" [174]. This won his father, Sir William Henry Bragg, and him the Nobel Prize in Physics in 1915, and enabled the study of crystal structure by analysing the X-ray diffraction patterns. In contrast to normal diffraction from a thin gratting, Bragg diffraction occurs when a wave of wavelength λ, incident at an angle θ scatters weakly from multiple periodic planes such as those in a crystal lattice. Only at particular scattering angles 2θ do these scattered waves add in phase, favouring a strongly enhanced diffraction order, n. This process is illustrated in figure 8.1 using scattering from just two adjacent crystal planes. The red section of one scattered wave represents the

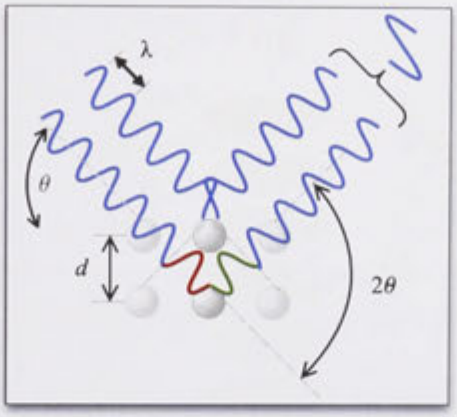

Figure 8.1: Schematic representation of Bragg diffraction in crystals [176].

optical path difference (OPD), equal to $2d\sin\theta$, where d is the spacing between planes as shown. When the OPD is equal to a whole number of wavelengths $n\lambda$ as shown, the waves constructively interfere and this condition is known as Bragg's Law:

$$n\lambda = 2d\sin\theta_n \tag{8.3}$$

It is important to note that this simple derivation assumes the wave are *refleted* from individual planes, implicitly assuming that many scattering centres and crystal planes are sampled in a highly symmetric system - essentially a "thick" reflection grating and the signature of strict Bragg diffraction. This point will be important when we consider diffraction of atoms the quasi-Bragg regime [175] in chapter 10.

8.1.2 Bragg Diffraction of Atoms

Given the wave nature of matter, Kapitza and Dirac theorised in 1933 that an electron beam could be diffracted by an optical standing wave [177]. It was not until the availability of the optical laser that this was observed in 1965 by Bartell *et al.* [178]. We can equivalently consider Bragg diffraction of atoms by a periodic potential generated with an off-resonant optical standing wave. In the case of atoms, the process is resonantly enhanced due to their internal level structure [179]. The description is essentially identical, with the role of light and matter reversed, and λ replaced by the de Broglie wavelength λ_{dB}. This was first demonstrated with sodium and published in 1988 [80]. In this case, the analogy is explicit; a collimated beam of sodium atoms was scattered from an optical standing wave at a variable angle of incidence, leading to the observation of

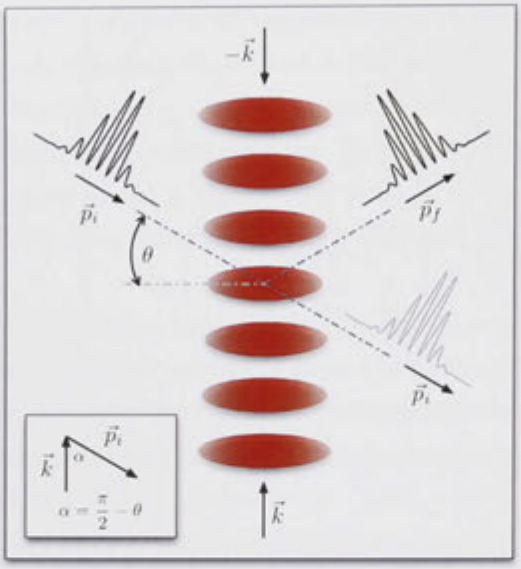

Figure 8.2: Schematic representation of Bragg diffraction of atoms from a one-dimensional optical lattice. Red ellipses represent antinodes of the standing wave, and wave packets represent an atom. The grey transmitted wave packet represents an atom that is only partially diffracted, for example, in the case of a beam splitter.

diffraction orders. Bragg diffraction, often thought of as the 'thick-grating' regime in reference to the optical analogy, should be distinguished from the Raman-Nath or "thin-grating" regime [114]. Raman-Nath diffraction is analogous to normal diffraction in optics resulting in multiple diffraction orders. Normal diffraction of atoms has been used for atom interferometry [111], however it leads to inefficient population of high-momentum states and is therefore not well suited for LMT beamsplitting.

In figure 8.2, we illustrate diffraction in the lab frame for atoms incident at an angle of θ, and momentum $\mathbf{p}_i$. Notice the similarity with figure 8.1. The optical standing wave, represented by the red ellipses, is composed of two counter-propagating laser beams of wavevector $\mathbf{k}$. As $\theta \neq 0$, there is a component of velocity along $\mathbf{k}$. The Bragg condition on the incidence angle can then be restated as a condition on this component of the atomic velocity:

$$n\lambda_{\mathrm{dB}} = 2d\sin(\theta_n) \tag{8.4}$$

$$n\frac{h}{m} = 2dv_i\sin(\theta_n) \tag{8.5}$$

$$n\frac{h}{2dm} = v_n \tag{8.6}$$

$$\therefore v_n = n\frac{\hbar k}{m} \tag{8.7}$$

where v_n is the resonant atomic velocity along the lattice for nth order diffraction, and we have used the de Broglie relation $\lambda_{\mathrm{dB}} = h/mv_i$. The spacing between nodes of the optical lattice is $d = \lambda/2 = \pi/k$. It is important to note that Bragg diffraction 'reflects' this component of velocity, and the change in momentum along the lattice is therefore $2mv_n = 2n\hbar k$. We see here the first suggestion of a quantised description of Bragg diffraction, namely that $2n$ photon momenta are imparted to the atom.

We may gain further insight by considering figure 8.2 in the frame of the atom. In this frame $\lambda_{\mathrm{dB}} \to \infty$. However, the optical lattice now travels at a velocity $-v_n$ for nth-order diffraction. This is equivalent to a detuning of the counter-propagating beams due to the Doppler shift, given by:

$$\Delta\omega_n = 2kv_n = \frac{4n\hbar k^2}{2m} = 4n\omega_r \tag{8.8}$$

Furthermore, the atoms experience the optical lattice as a pulse in time. Hence, Bragg diffraction can be described as a $2n$-photon Raman transition between momentum states separated by $2n\hbar k$. It is therefore possible to diffract stationary atoms by producing a traveling lattice in the lab frame, with equation (8.8) defining the resonance condition for the frequency-difference of the counter-propagating beams. This was first demonstrated with a BEC by Kozuma *et al.* in 1999. The process is illustrated in figure 8.3, which shows the dispersion curve for the ground state of the atom. The excited state is omitted for simplicity, and it is assumed that the single-photon detuning is such that spontaneous emission is negligible. Photons at ω_1 are absorbed from one lattice beam, and photons at ω_2 are stimulated to emit into the counter-propagating beam. Each absorption-emission event transfers two photon momenta and adds the relative phase of the lasers onto the atomic phase. Therefore, after n such events, the state $|p = 0\rangle$ is coupled to $e^{-in\phi}|p = 2n\hbar k\rangle$.[3] Thus the interferometer phase shift for uniform acceleration becomes:

$$\Phi = n(\phi_1 - 2\phi_2 + \phi_3) = 2n\mathbf{k} \cdot \mathbf{g}T^2 \tag{8.9}$$

showing the enhanced sensitivity when using an LMT beamsplitter. This is equivalent to increasing the effective wave vector of a Raman transition by a

[3] It is assumed that $k_{1,2} = \omega_{1,2}/c \approx k$. For example, k_1 and k_2 differ by $10^{-10}k_1$ for $n = 10$.

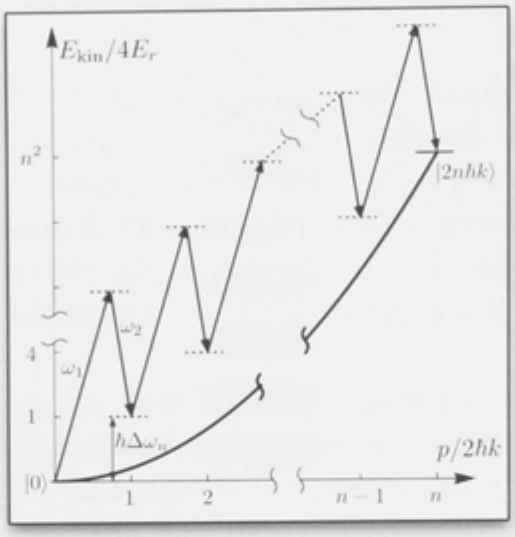

Figure 8.3: Bragg diffraction as a multi-photon transition between momentum states $|p\rangle$, in the frame of an atom. The excited atomic state is omitted for simplicity. For nth order diffraction, n photons at ω_1 are absorbed and stimulated to emit at ω_2, leading to a transfer of $2n\hbar k$ momentum, and an energy of $nh\Delta\omega_n$

factor of n.

8.2 The Bragg Laser-System

In designing a Bragg-based LMT laser system, identical features are required as those discussed for the Raman laser-system in section 6.1. Repeating the list here, we require:

1. Two lasers fields, with a tuneable frequency difference to address a particular Bragg resonance or drive Bloch oscillations.
2. An ultra-stable relative phase between the two lasers.
3. Intensity control and timing for pulse shaping.
4. Clean and simple spatial modes (e.g. Gaussian), ideally identical for each laser beam.

Whereas for the Raman coupler we required phase-locked lasers with a frequency difference of $\sim 6.34\,\mathrm{GHz}$, the frequency difference for driving Bragg transitions is only on the order of hundreds of kHz, as $4\omega_r \simeq 15\,\mathrm{kHz}$ [see equation (8.8)]. This means that the same AOMs used to satisfy point 3. can be used to control the

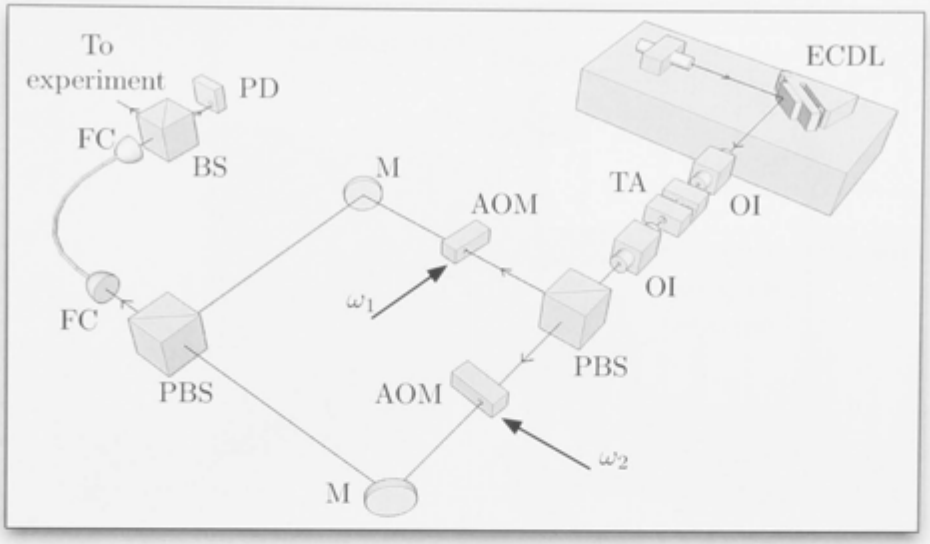

Figure 8.4: Simplified representation of the LMT laser system. TA: tapered amplifier, OI: optical isolator, M: mirror, BS: beamsplitter, FC: fibre coupler, PD: photo detector.

frequency difference by driving them at slightly different RF frequencies. Point 2. is again satisfied by using a single ECDL.

8.2.1 Optical Setup

A simplified diagram of our LMT laser system is given in figure 8.4. Light is sourced from a single ECDL which is detuned by $\sim 90\,\mathrm{GHz}$ from one-photon resonance to greatly suppress spontaneous emission. This is then amplified by a high power tapered amplifier [142] giving 1.3 W of power. The light is evenly split using a polarising beamsplitter (PBS) and directed through two 80 MHz AOMs each driven at slightly different frequencies by a single direct digital synthesiser (DDS) (PulseBlasterDDS-II-300 [180]), which allows for the arbitrary pulse shapes and coherent relative-frequency sweeps required for our experiments. The DDS is controlled via a custom optimisation software written by R. P. Anderson. The first-order of each AOM is then recombined on a second PBS, before being coupled into a single-mode polarisation-maintaining optical fibre, to be sent to the experiment.

Figure 8.5 shows the optical configuration of the LMT laser for producing the counter-propagating beams required to drive Bragg transitions. The co-propagating frequencies from the fibre have a total power of 150 mW and are collimated to 3mm $1/e^2$ diameter. They are directed into the science cell of our

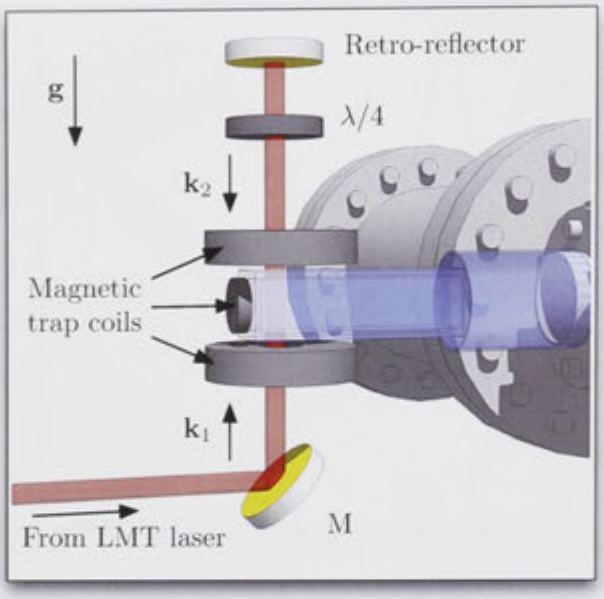

Figure 8.5: Optical setup of the LMT beamsplitter at the science cell of our dual-species BEC machine. The incoming beam contains both (phase-locked) laser frequencies co-propagating and orthogonally polarised, travels vertically through the cell and is retro-reflected to produce counter-propagating frequencies. The quarter-wave plate ($\lambda/4$) is necessary to produce the optical standing-wave that diffracts the atoms. The magnetic-trap coils are shown for reference; to be compared with figure 5.9.

dual-species BEC machine from below, ideally parallel to gravity. As $\mathbf{k}_1$ and $\mathbf{k}_2$ are orthogonally polarised, the light propagates through a quarter-wave plate after emerging from the cell, before being retro-reflected by a mirror. This results in a 90° rotation of the polarisation for the downward propagating beams, which results in two (generally travelling) optical lattices with opposite $\mathbf{k}_e$. As the atoms are in free fall during the interferometer sequence, only one of these lattices is kept on resonance when compensating the Doppler shift by sweeping the laser frequency difference. Alternatively, one of the frequencies can be rejected using a PBS just before the retro-reflector, and a second quarter-wave plate below the glass cell.

8.2.2 Phase-Noise Analysis

Although the two beams are sourced from a single ECDL, which ensures a common phase, the counter-propagating frequencies reaching the atoms have travelled slightly different paths via the two AOMs and then the retro-reflector for $\mathbf{k}_2$. Thus the relative phase of the two beams will be compromised by mirror

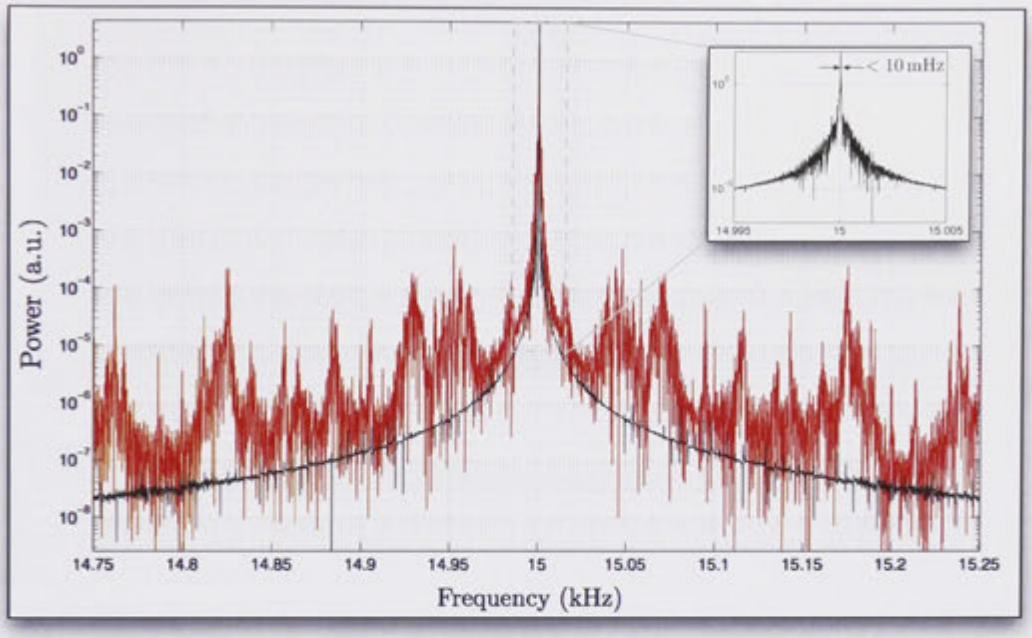

Figure 8.6: Power spectral density of the Bragg laser-system optical-beat signal for our original setup used in reference [63] (red), and our recently improved setup, housed in an acoustically isolated laboratory (black). The inset zooms into a 10 Hz span of the black trace, shown as the grey-dashed rectangular region.

vibrations, air currents, as well as slow drifts in the birefringent optical fibre. To ensure a locked phase after the fibre, we have the option of phase-locking the two frequencies using an OPLL operating in the hundreds of kHz band, relatively simple compared with an OPLL operating at GHz frequencies. In principle, the photodetector signal could also be used to stabilise the intensity of the light, ensuring the stability of the effective Rabi frequency, although this has not been necessary for our work so far.

Our initial setup, used for the work in reference [63] and part of chapter 9, was built on a sorbothane isolated optical bench to help reduce vibrations. The normalised power spectral density (PSD) of the beat signal, centred at 15 kHz, is the red trace in figure 8.6. The -3dB width of the peak is ~ 0.2 Hz, with clear noise sidebands shown over a 500 Hz span.

This first incarnation of our Bragg laser-system was located in a standard physics laboratory full of typically (acoustically) noisy equipment such as power supplies. In particular, we found that acoustic noise readily coupled into our system, and to this effect, have recently moved the experiment and Bragg system into a purpose-designed low noise environment. The laboratory has been refur-

Figure 8.7: Photographs of our new acoustically isolated laboratory, showing the two air-floated optical tables (left image), and the secondary isolation enclosure around one of the tables (right image).

bished with acoustic isolation on all walls and the ceiling. This room houses a second acoustically isolated enclosure, within which we place our air-floated optical table (see figure 8.7). All power supplies, and nearly all electronic equipment is located outside the laboratory in our control room.

The Bragg laser-system is now housed directly on the air-floated table, and the black trace of figure 8.6 shows an equivalent beat signal measurement for the system in the new environment. In this case, the -3 dB width is < 10 mHz, limited by the Fourier resolution (see inset) and more than an order of magnitude narrower than in the noisier lab environment. There is also a clear *passive* reduction in noise by as much as 4 orders of magnitude, with essentially no discernible noise features beyond 5 Hz over the full 100 kHz bandwidth of the measurement (not shown). The phase noise is -107 dBc/Hz at 85 kHz from the carrier for the unstabilised setup. For comparison, a state-of-the-art *active* phase-lock between two titanium sapphire lasers achieves -138 dBc/Hz at 1 MHz from the carrier [155].

To investigate the relative-phase stability further, we have simultaneously measured the beat signal from the photo-detector and the reference signals from the DDS on a deep-memory digital sampling oscilloscope (DSO) (LeCroy WaveRunner 44Xi-A [181]). The electronic setup for this measurement is given in figure 8.8. The two DDS channels are driven at 80.0 MHz and 79.9 MHz respectively, and their outputs split evenly with a power-splitter (Mini-Circuits ZSC-2-1). One frequency pair is sent to the AOMs of the Bragg laser-system, and the pair other mixed down (Mini-Circuits ZAD-6) producing sum and dif-

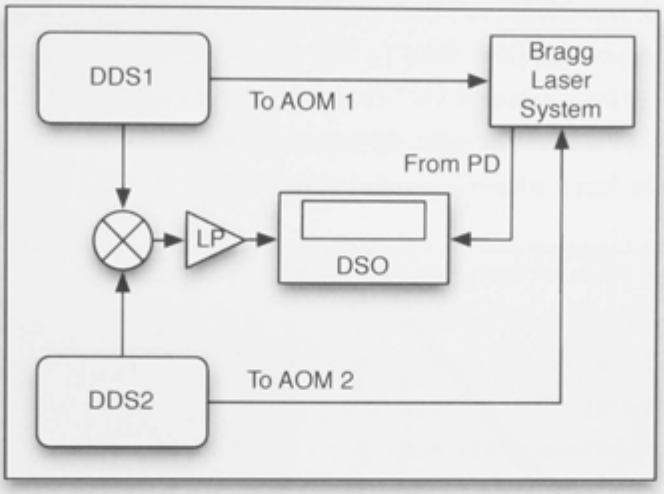

Figure 8.8: Electronic setup for measuring the relative-phase fluctuations of the Bragg laser-system. LP: 15 MHz low-pass filter, ⊗: mixer, PD: photodetector.

ference frequencies at the mixer output. A 15 MHz low-pass filter (Mini-Circuits BLP-15) removes the sum frequency, giving a reference at 100 kHz. The photodetector in the Bragg-system measures the beat signal at 100 kHz, including any phase drift between the reference's phase, and the beat's phase caused by e.g. mirror vibrations or air temperature and pressure variation in the optical path of the laser beams.

Using the DSO, we acquire time traces of both signals for up to 5 second with a sampling rate of at least 2.5 MHz. We then post-process the data by fitting sinusoids to each period of the traces, determining the beat and reference phase as a function of time. A more standard method, which yields a higher bandwidth in principle, is to mix down the reference and beat signal, which after a low-pass filter, is proportional to the sine of the phase difference. However, extracting the relative-phase from from this signal involves a small angle approximation, which is equivalent to assuming the reference and beat signals are approximately $\pi/2$ out of phase with relatively small fluctuations. This is not the case for our unlocked setup, and is better suited to the case of a closed OPLL [155].

Figure 8.9 presents the results of the relative-phase measurement for an unlocked system. In (a), we plot the relative phase between the reference and beat signals for a 2 second trace (red line). We observe a slow drift in the phase as a function of time, over a range $\lesssim 1$ rad. This is likely the result of changes in the refractive index of the air between two uncommon paths of the laser setup [see figure 8.4]. For example, a differential refractive index change of 1 part in 10^7

corresponds to a relative-phase shift of 1 rad/m. In our setup, the lasers propagate around 20 cm from the first PBS to the second PBS. In reference [182], a variation of the refractive index of 10^{-6}/K is measured at standard temperature and pressure. Thus, relatively modest in variations the ambient environment can explain the relatively large phase drift in figure 8.9.

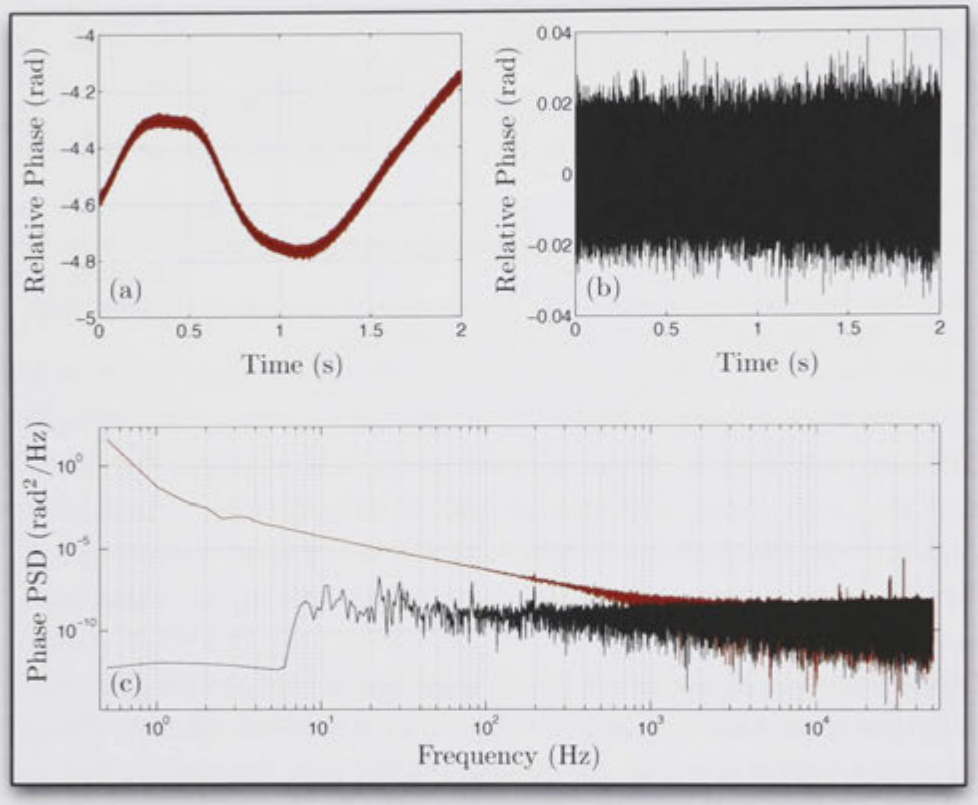

Figure 8.9: Relative-phase noise analysis for the Bragg laser-system. (a) Is the relative phase plotted as a function of time (red), including a polynomial fit to the trace (black). The same data is plotted in (b) with the polynomial fit from (a) subtracted. The phase PSD is calculated and shown in (c) for (a) and (b) respectively.

We estimate the result that would be obtained by locking out these slow drifts with a modest bandwidth OPLL by fitting and subtracting a polynomial from the data in (a). The fit is shown in black, with the subtracted result presented in (b). The phase-PSD of the data in (a) and (b) is colour-coded and shown in (c). The measured spectrum is unremarkable, with mild features around 2-3 Hz; representative of the slow drift in (a). The estimated PSD for locking out the slow drifts indicates a suppression of noise below 1 kHz; more so at lower frequencies. The residual phase-noise, integrated across the entire spectrum is 3.4×10^{-2} rad^2

for the measured data, and an estimated $6.2 \times 10^{-5}\,\mathrm{rad}^2$ for a modest bandwidth OPLL. We expect a higher bandwidth OPLL would improve even further on this estimate, and are currently in the process of incorporating an OPLL, which will feed back to the RF drive of one of the AOMs. For comparison, the state-of-the-art system in [155] achieves $\sim 10^{-6}\,\mathrm{rad}^2$ integrated over 1 Hz - 100 kHz, using a 9 MHz bandwidth OPLL.

It should finally be noted that implementation of an OPLL will only lock the relative phase at the photodetector. Once the two frequencies propagate to the atoms, k_1 further propagates to the retro-reflector and back (see figure 8.5), introducing another uncommon path length. Vibrations of this mirror, as well as drifts in the refractive index will therefore re-introduce relative-phase noise. It is for this reason that the retro-reflector in atomic gravimeters is usually well vibrationally isolated, which is often done actively [8]. In some cases, the retro-reflector is fixed to a seismometer, which produces a signal that is used to post-correct the interferometer data [9]. In any case, the phase analysis of figure 8.9 is suggestive of what we expect for our retro-reflector in the absence of any active stabilisation on our current optics table.

8.3 Bragg Beamsplitters and Mirrors

In figure 8.10, we give several examples of Bragg diffraction using our laser system. All images are absorption images of Bose-condensed samples, after applying Gaussian Bragg pulses with pulse durations on the order of $100\,\mu\mathrm{s}$. Pulses are applied 12 ms after the cloud has been released from the trap. The left image is a π-pulse, and therefore a mirror, for first-order diffraction. 93% of the atoms are diffracted from the initial state. The cloud has a momentum width $\lesssim 0.1\hbar k$. At this momentum width, the diffraction efficiency is close at the fundamental limit, as we will discuss in chapter 10. The central image shows an LMT beamsplitter for fourth-order diffraction. The splitting ratio is is close to 50/50. Notice the low population of intermediate momentum states, which occurs due to off-resonant transitions related to Raman-Nath-like diffraction (see section 10.1.2.)

We are currently limited by laser power and one-photon detuning considerations to fifth-order mirrors of around 60% efficiency, with no discernible population of the intermediate momentum states. When insufficient power is available to target yet higher orders, one option to increase the momentum transfer is to use cascaded Bragg pulses, which consecutively diffract the atoms in stages [183]. For example, $0\hbar k \rightarrow 2\hbar k \rightarrow 4\hbar k$, etc. Selective diffraction is possible

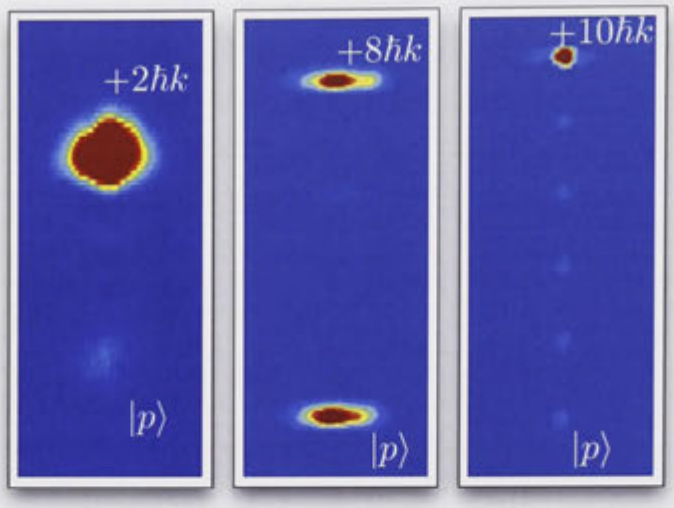

Figure 8.10: Examples of Bragg diffraction with our Bragg laser-system. Left: a $2\hbar k$ Bragg mirror of BEC with an efficiency of 93%. Centre: an $8\hbar k$ Bragg beamsplitter of a BEC. Right: five consecutive $2\hbar k$ Bragg mirrors of 90% efficiency each, giving a total efficiency of 70% for the effective $10\hbar k$ mirror. The BEC has a momentum width of $\lesssim 0.1\hbar k$ in all images, and red represents a higher atom density.

as each pulse targets a Bragg resonance with a different initial momentum (in the laboratory frame). The image on the right of figure 8.10 gives an example of such a mirror, showing five consecutive first-order Bragg pulses. Each step is $\sim 90\%$ efficient, giving an overall efficiency of 70% for a $10\hbar k$ mirror. Because of our power limitation, this is more efficient than what is possible for a single fifth-order diffraction pulse. The draw back is that the effective pulse-time for the Bragg mirror is increased. Furthermore, if higher laser power was available, then the fundamental diffraction limit is only set by the atomic cloud's momentum width (see chapter 10 and [78]), and multiple-pulse schemes will always result in a lower efficiency.

In very recent work, we have developed a frequency doubled, narrow linewidth, 780 nm fibre-laser system with over 11 W of power available for the Bragg beamsplitter [184]. Assuming a $1/e^2$ radius of 7.5 mm, this gives a peak intensity of $\sim 10\,\mathrm{W/cm^2}$. A one-photon detuning of 20 GHz would then result in a spontaneous emission-induced atom loss of 1% for a $20\,\mu$s pulse, giving a two-photon Rabi frequency of $\sim 600\omega_r$. Based on our theoretical work (again, see chapter 10 and [78]), we expect to be able to achieve at least an $n = 21$ (i.e. $42\hbar k$ LMT) Bragg mirror for a BEC, with an efficiency of $\sim 90\%$ for a single Bragg pulse.

8.4 Summary and the Advantages of Bragg Diffraction

We have developed a LMT beamsplitter for atom interferometers, based on the Bragg diffraction of atoms using a relatively simple laser system. Our system has achieved beamsplitter and mirror pulses transferring up to 10 photon momenta, with a mirror efficiency of up to 93%. By relocating the system to an acoustically isolated environment, we are able to passively improve the noise characteristics of the system by as much as 4 orders of magnitude in particular frequency bands. With a relatively modest bandwidth OPLL, we expect to be able to reach state-of-the-art relative-phase stability, on the path to a high precision atomic gravimeter.

Finally, it is worth highlighting several advantages of Bragg-based beamsplitting compared with (hyperfine) Raman transitions. In general, because Bragg transitions involve the coupling of external degrees of freedom, atoms remain in a single internal state, largely negating several state-dependent systematic effects.

Firstly, the differential AC Stark shift [see equation (4.17)] introduces an intensity-dependent shift on the Raman transition frequency, due to the (generally) different matrix elements between the two ground states and the excited states. Any intensity fluctuations will therefore introduce spurious phase shifts into the interferometer. Similarly, the second order Zeeman shift effects each hyperfine ground state differently (see the Breit-Rabi formula [128]), leading again to a systematic shift on the resonance. In the case of magnetic field gradients, there will be a path dependent shift on the resonance, which could in general also be time dependent.

In both the above examples, these systematic effect are avoided when using Bragg diffraction, as atoms remain in the same hyperfine state, and any state-dependent shift is common to both arms of the interferometer.

Furthermore, it is often assumed that after phase-locking the two lasers required for an atomic beamsplitter, any fluctuations along the co-propagating path are common to both frequencies and therefore cancels in the relative-phase. This is only strictly true if $k_1 = k_2$, as the relative phase fluctuation will be $(k_1 - k_2)\Delta x$, where Δx is a small displacement, say due to a mirror vibration. For the case of Bragg diffraction, $(k_1 - k_2)$ is on the order of 0.02 rad/m for ^{87}Rb and a frequency difference of 1 MHz. A Raman transition on the other hand, is around 150 rad/m. Thus common mode rejection for a Bragg-based beamsplitter will be almost 4 orders of magnitude better than for a Raman transition; essentially negligible for typical $\Delta x \sim$ a few microns.

Part III

Inertial Sensing with Bose-Condensed Sources

Chapter 9

Gravimetry with a Bose-Einstein Condensate

Work in this chapter has been peer-reviewed and published in:

J. E. Debs, P. A. Altin, T. H. Barter, D. Döring, G. R. Dennis, G. McDonald, R. P Anderson, J. D. Close, and N. P. Robins. Cold-atom gravimetry with a Bose-Einstein condensate. Phys. Rev. A 84, 033610 (2011). [63]

This chapter presents results on the first Mach-Zehnder atomic gravimeter based on the interference of a BEC. With one of the most promising avenues for increasing sensitivity being LMT beamsplitting [79, 85, 185, 186], we use Bragg-based LMT to increase our sensitivity to gravity, while maintaining a good fringe visibility. Although not described in chapter 8, our Bragg laser-system can also drive Bloch oscillations as an LMT technique [33, 79, 173, 186, 187]. We briefly describe Bloch oscillations and present results with a high fringe visibility. Furthermore, the use of BEC has been largely neglected by the precision measurement community due to a major concern that the comparatively high atom density will lead to interaction-induced phase diffusion, and a limitation on precision [61, 187]. We use a simple model to demonstrate that phase diffusion in an expanded BEC will not limit the precision of inertial measurements, consistent with observations at our current best precision of 10^{-5}.

9.1 Experimental Background and Methods

The basic operating principles of an atomic gravimeter were discussed in chapter 3 and have also been described in detail elsewhere [7, 8]. Briefly, we use

nth-order Bragg transitions [81, 83, 85] as our atom-optic beamsplitters ($\pi/2$ pulses) and mirrors (π pulses) in the Mach-Zehnder ($\pi/2 - \pi - \pi/2$) configuration. These couple vertical momentum states separated by $2n\hbar k$, where $k = |\mathbf{k}|$ is the wavenumber of the Bragg laser and n an integer. For uniform acceleration the atomic phase evolution of each arm is identical, and the only interferometric phase contribution is from the atom-light interaction [8]. Restating equation (8.9) for acceleration due to gravity, the interferometer phase is:

$$\Phi = n(\phi_1 - 2\phi_2 + \phi_3) = 2n\,\mathbf{k}\cdot\mathbf{g}T^2 \tag{9.1}$$

where ϕ_i is the optical phase of the ith Bragg pulse, and T is the time between pulses. Scanning Φ results in fringes $P = \frac{1}{2}(A + \mathcal{C}\cos\Phi)$ in the relative population in state $|p_0 + 2n\hbar k\rangle$, where $\mathcal{C}$ is the contrast[1] and A the fringe offset.

Our production of BEC was described in section 5.4.3. As a reminder, we produce pure ^{87}Rb $|1,-1\rangle$ condensates with up to 2×10^6 atoms in a crossed optical-dipole trap with $\omega_{x,y,z} = 2\pi\times(50, 57, 28)$ Hz. This gives a momentum width of $\sim 0.14\hbar k$ after 12 ms of ballistic expansion from the trap [see figure 9.3(c)]. We can transfer the atoms to the first-order magnetically insensitive state using a Landau-Zener RF sweep after the BEC is formed; however, we presently find this step unnecessary as we observe no effect on fringe visibility, SNR or our measurement of g at our current maximum sensitivity.

Our Bragg laser system was described in section 8.2. To operate in the Bragg regime and address the entire cloud, we use Gaussian-shaped pulse envelopes [78, 175] and choose our pulse length τ to satisfy $\frac{\Delta p}{m}\cdot\mathbf{k} < \tau^{-1} < \omega_r$, ensuring minimal loss to adjacent momentum states for a given n. For $n = 1$, we are able to maximise our π-pulse efficiency to 95% in this way. However, we find that a 300 μs velocity selection pulse is required in order to achieve 93% efficiency for $n = 3$. This narrowing of the transition momentum selectivity for finite is discussed in chapter 10. Due to the size of our science cell, we are limited to an interrogation time of $T = 5$ ms. After several milliseconds of further separation following the final $\pi/2$ beamsplitter, an absorption image is taken to measure the momentum distribution of the atoms.

As described in chapter 3, the freely-falling atoms experience a time dependent Doppler shift $\delta_d(t) = 2\pi\alpha_0 t$ where $\alpha_0 = \frac{1}{\pi}\mathbf{k}\cdot\mathbf{g}$ is a frequency chirp. This modifies the Bragg resonance condition in the laboratory frame to $\Delta\omega_n(t) = 4n\omega_r + 2\mathbf{k}\cdot\mathbf{g}t$.

[1] Note that visibility can be defined through the ability to fit a sine curve to a given data set. Contrast is indicative of coherence and it is possible to have contrast with no visibility, as is discussed in [85, 188].

We compensate this by sweeping $\Delta\omega$ at a rate $\alpha \simeq 25.1\,\mathrm{MHz/s}$, determined by local $\mathbf{g}$ near our lab in Canberra, Australia [189]. The interferometer phase then becomes $\Phi = 2n(\mathbf{k}\cdot\mathbf{g} - \pi\alpha)T^2$, as was described in chapter 3. By scanning the sweep rate α, we record interference fringes with a period of $1/nT^2$. Fitting a sinusoid to these fringes allows us to determine the central fringe and thus α_0 without varying T. This is because the fringe spacing for our modest interrogation time of a few ms corresponds a irrationally large shift in the calculated value of g.

9.2 Gravimetry with a BEC

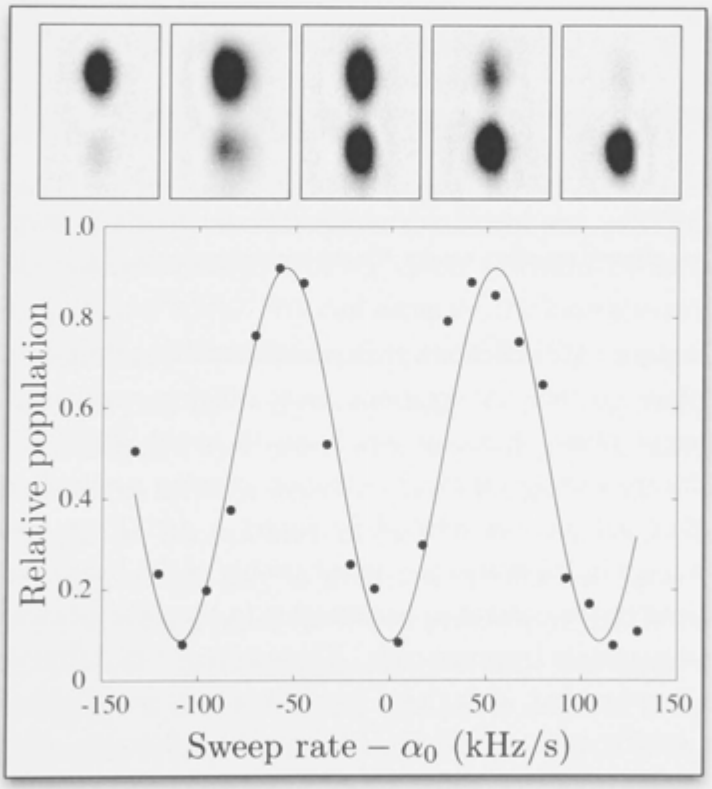

Figure 9.1: Interference fringes from a BEC-based gravimeter with $n = 1$, $T = 3\,\mathrm{ms}$. We observe a visibility of $(83 \pm 6)\%$. The solid line is a least-squares sinusoidal fit to the data, allowing us to determine α_0 (as in all fringe sets in this chapter). Above: absorption images from the interferometer showing an oscillation between the two output ports.

Figure 9.1 shows gravimeter fringes for $n = 1$, $T = 3\,\mathrm{ms}$. We observe a high visibility of $(83 \pm 6)\%$. Increasing T generally reduces the visibility, and

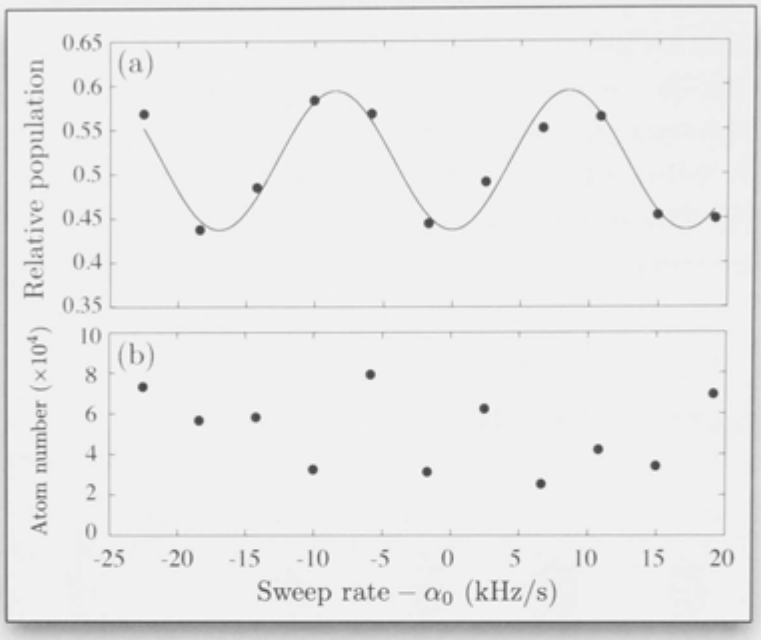

Figure 9.2: LMT fringes from our BEC gravimeter. (a) Fringes for our highest precision configuration of $n = 3$, $T = 4\,\mathrm{ms}$. (b) Atom number in each run of (a). Despite a 300% variation in density, we observe no effect on our fringes or measurement of g.

more rapidly for larger n. We speculate that wavefront aberrations in the Bragg laser beams contribute to this. Aberrations cause different atomic trajectories to experience different phase shifts, as has been discussed in [88, 89]. These different phase shifts are averaged through detection, causing a reduction in fringe visibility. This effect will be exacerbated for larger n and T, as each atomic trajectory samples more of the transverse phase profile of the beam. We suspect significant aberrations in the current apparatus due to the close proximity of the Bragg beams to our magnetic trapping coils. This can result in diffraction due to the coil edge. We suspect that with closer to ideal optical wavefronts, visibility would scale more weakly with n and T. Chapter 10 elaborates on this effect further, and includes a simple model.

Even with the reduction in visibility, we are able to improve our sensitivity by a factor of 5 from the $n = 1$ interferometer by using third-order Bragg LMT beamsplitters. We achieve a mid-fringe sensitivity of $\Delta\Phi/\Phi = 5 \times 10^{-4}\mathrm{Hz}^{-1/2}$ in this way. The corresponding fringes are given in figure 9.2(a). These data represent 16 minutes of acquisition time. We can determine gravity from α_0 to be $g = 9.7859(2)\,\mathrm{ms}^{-2}$, where the uncertainty of the fitted value for α_0 determines

the uncertainty in g. In [189], g is measured to be $9.795499189(29)\,\mathrm{ms}^{-2}$, approximately 11 km from our lab and 150 m higher in elevation. Our value disagrees at the 10^{-2} level. This low accuracy is almost certainly due to the alignment of our Bragg beam along $\mathbf{g}$, as when calculating g from α_0, we have assumed $\mathbf{k}\cdot\mathbf{g} = kg$. We estimate an alignment uncertainty of 3° in the current apparatus, which leads to a systematic error in g of up to $0.026\,\mathrm{ms}^{-2}$. Other sources of systematics, such as gravitational and magnetic field gradients, rotation of the Earth, and tidal forces, are all at least 3 orders of magnitude smaller than the alignment error (see the thesis of T. Barter [190]). Such systematics will be readily dealt with in our next generation system currently under development.

9.3 The Effect of Atomic Interactions

Figure 9.2(b) shows the atom number for each corresponding point for the fringes in (a). Despite a variation of 300% in density, we observe no detrimental effect of phase diffusion on the SNR, or our measured value of g at our limit of precision. After 12 ms, the momentum width of the cloud is within 1% of its asymptotic value, as shown in figure 9.3(a). We can estimate the interaction-induced phase uncertainty for our or a similar device using the following simple model.

First, we highlight that the many-body state of a BEC following a beamsplitter operation is distributed over states with different relative number [61]. This is the case whether the BEC is described by a Fock state or a coherent state before the beamsplitter. Because each of the different relative number states has a different interaction energy, they acquire phase at different rates; leading to the phase diffusion phenomenon often cited as a problem for BEC. For an expanding condensate, however, the density decreases in time leading to a reduction in the interaction energy. It is worth noting this phase diffusion is utilised in some methods for producing squeezed states [69, 72, 73].

To estimate the effect of residual mean-field during ballistic expansion we therefore proceed as follows with the assumption that the reader is familiar with chapter 5. The average interaction energy per particle is given by:

$$E_{int} = \frac{U}{2}\langle n \rangle \tag{9.2}$$

where $\langle n \rangle = N^{-1}\int n^2(\mathbf{r})d^3\mathbf{r}$ is the average density. In the Thomas-Fermi limit

this gives:

$$E_{int} = \frac{15UN}{28\pi} \prod_i \frac{1}{r_i} \tag{9.3}$$

After release from the trap, the Thomas-Fermi radii are scaled according to the scaling parameters $b_i(t)$ [see equation (5.12)]. Recalling equation (5.13):

$$\frac{d^2 b_i}{dt^2} = \frac{\omega_i^2}{b_i} \prod_j \frac{1}{b_j} \tag{9.4}$$

For a 50/50 beamsplitter, E_{int} is identical for both interferometer states and therefore no systematic phase-shift will occur. However the variance in the number difference for the two output modes is $\sim N/4$ from binomial statistics, giving a variance in the density of each mode. As a result the uncertainty in the interaction energy is given by:[2]

$$\Delta E_{int}(t) = \frac{15U\sqrt{N}}{112\pi} \prod_i \frac{1}{b_i(t) r_i(0)} \tag{9.5}$$

The relative-phase therefore diffuses at a rate given by $d(\Delta\Phi_{int})/dt = \Delta E_{int}/\hbar$, giving the overall phase uncertainty at the output of the interferometer:

$$\Delta\Phi_{int} = \frac{15U\sqrt{N}}{112\pi\hbar \prod_i r_i(0)} \int_{t_0}^{t_0+2T} \prod_i \frac{1}{b_i(t)} dt \tag{9.6}$$

By numerically solving equations (9.4) and calculating result (9.6) we find that for our highest sensitivity configuration, interaction-induced phase diffusion would limit precision to 10^{-8} per shot; well below our current sensitivity. Figure 9.3(b) projects this estimate towards state-of-the-art device parameters, plotting the phase diffusion-limited sensitivity as a function of T, for 10^6 condensed atoms/s and our trap parameters. The shaded region represents the phase diffusion-limited sensitivity for expansion times ranging from $t_{\mathrm{exp}} = 10 - 40\,\mathrm{ms}$ from the upper to lower boundaries respectively. The solid curve is the shot-noise limited sensitivity, and the solid circle is the value of the current state-of-the-art sensitivity for an atomic gravimeter with $T = 0.4\,\mathrm{s}$ and $n = 1$ [10]. We find that with an appropriate choice of trap parameters and expansion time, interaction-induced phase diffusion can be made negligible compared with the shot noise limit. This is demonstrated by the inset, which plots the phase diffusion limited

[2] As the density is halved in each state, note an additional factor of 2 between equation (9.3) and equation (9.5).

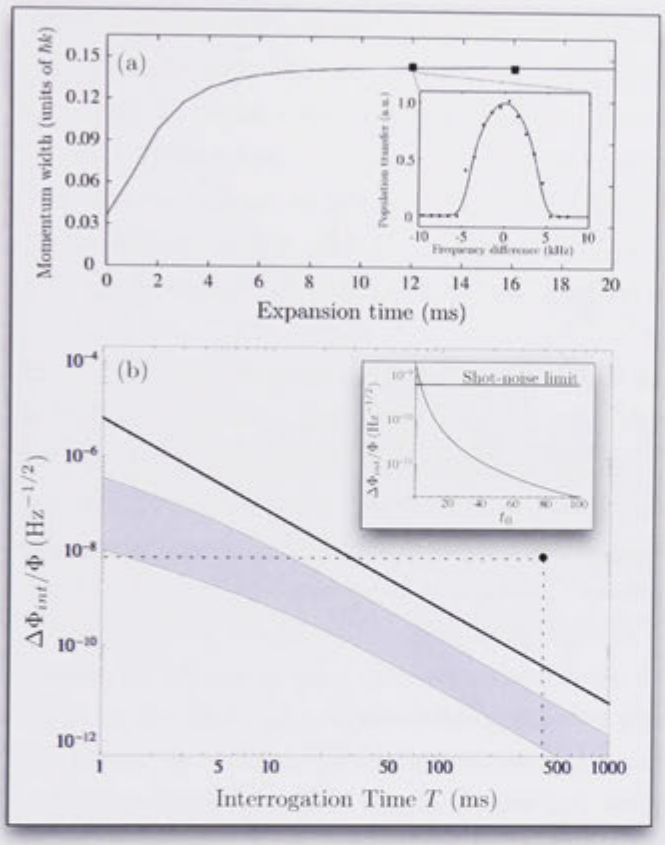

Figure 9.3: (a) Momentum width of an expanding condensate along **k** as a function of expansion time. Solid line is a GPE simulation for our experimental parameters. Black squares are measured using Bragg spectroscopy. (b) Estimated phase diffusion limited sensitivity as a function of interrogation time. The shaded region represents values for a range of expansion times $t_{\mathrm{exp}} = 10 - 40\,\mathrm{ms}$ from the upper to lower boundaries respectively. The solid line is the shot-noise limit for 10^6 atoms. The solid circle is indicative of the current state-of-the-art for an atomic gravimeter with $n = 1$. Inset: phase diffusion limited sensitivity for $T = 100\,\mathrm{ms}$ as a function of the expansion time.

sensitivity for $T = 100\,\mathrm{ms}$ as a function of the expansion time. Importantly, as T increases phase diffusion quickly becomes negligible compared with the current state-of-the-art precision due to the rapid decrease in density. It should also be noted that the above result is an upper bound, as it assumes the spatial overlap of the interferometer states is essentially zero for the entire interferometer sequence. While they are well overlapped, the phase diffusion rate is significantly lower.

Very recent work by Jamison *et al.* has comprehensively investigated the effects of atom interactions in free-space BEC interferometers, and also concludes the atomic interactions are "not a roadblock" for high precision measurement with BEC inteferometry [64].

9.4 Bloch Oscillation-Based LMT

The phenomenon of Bloch oscillations describes the oscillation in both the momentum and the position of a particle accelerating in a periodic potential. It

was first described by Felix Bloch in 1929 for electrons in solids exposed to an external electric field [191], and further discussed by Clarence Zener in 1934 [192]. They were not observed until 1992 [193, 194] due to the difficulty of measuring electron momentum distributions in a crystal. On the other hand, the momentum distribution of atomic ensembles are readily measured, and with the advent of laser-cooling and Bose-condensation, atoms travelling in optical lattices presented an ideal analog for the solid-state system. In fact, Bloch oscillations in atomic systems were first measured, and described in detail by Peik *et al.* in 1997 [173].

Use of Bloch oscillations as an LMT beamsplitter has been described in detail in [79, 185, 186, 195], and we only give a brief review here. A simple picture of the process is as follows. Atoms are adiabatically loaded into an optical lattice formed by a standing wave. The atoms are effectively pinned to the potential wells of the lattice such that if the lattice is accelerated slowly, they adiabatically follow and their momentum increases. If the acceleration is too fast, the atoms cannot follow the potential and remain stationary. The appeal of Bloch-based LMT is that it does not require a quadratic increase in laser power for increasing momentum transfer, as is the case for Bragg diffraction.

We can describe the Bloch beamsplitter using Bloch states $|n, q\rangle$, which are (periodic) solutions of the Hamiltonian (10.6), where n is now the band index and q the quasimomentum defined modulo $2\hbar k$. This range of quasimomenta is known as the 1st Brillouin zone. Figure 9.4 shows the energy-band structure of the Bloch states. Stationary atoms are loaded into the 1st band at (or near) zero quasimomentum, represented by the blue circle at $q = 0$. The lattice is accelerated by introducing a frequency-difference chirp between the counter-propagating lattice beams. This corresponds to an increase in the quasimomentum, as shown. When the quasimomentum reaches $\hbar k$, this corresponds to a Bragg resonance, hence the avoided crossing at this point. Provided the acceleration is slow enough to be adiabatic, atoms follow the ground state, staying in the first band. In other words, they remain relatively stationary in the lattice frame undergoing oscillations in momentum and position space – Bloch oscillations. In the laboratory frame, this means the atoms acquire the same final velocity as the lattice.[3] The adiabatic criterion can be computed from the Landau-Zener transition probability [185]:

$$a_L \ll \frac{\pi \mathcal{V}_n^2}{4n\hbar^2 k} \tag{9.7}$$

[3]To within an integer multiple of $2\hbar k$, as the change in momentum is quantised by the exchange of lattice photons.

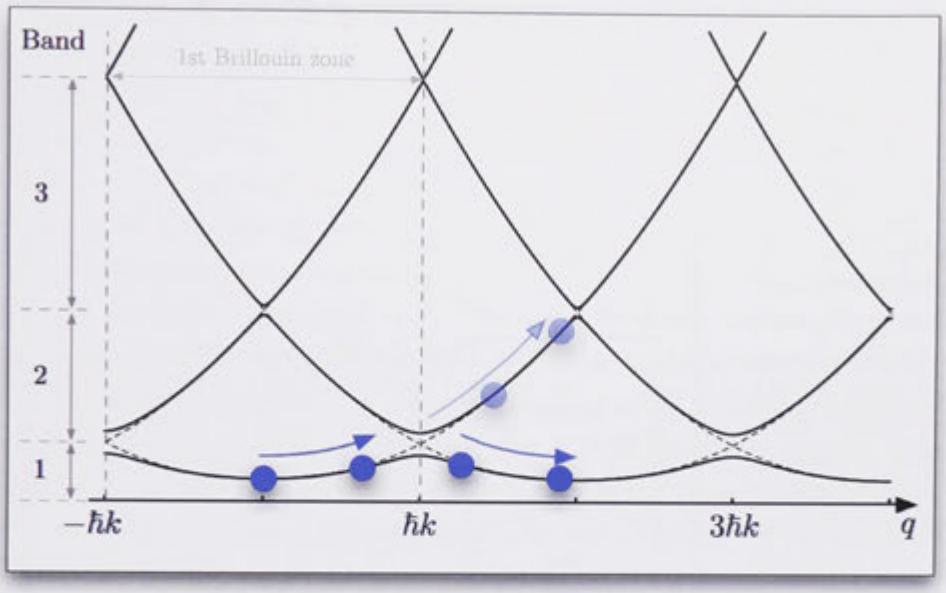

Figure 9.4: Bloch oscillations in the band structure of an optical lattice. After Cladé [186].

where $\mathcal{V}_n$ is the band-gap energy at the avoided crossing in the nth band, and a_L the lattice acceleration. If this condition is not met, atoms can undergo diabatic transitions to higher bands, increasing their energy in the lattice frame or equivalently remaining stationary in the laboratory frame. It is this feature which enables operation of a beamsplitter as follows.

A Bragg beamsplitter pulse is first applied, splitting the cloud into two momentum components. The Bloch lattice is then adiabatically ramped on such that one of these components has approximately zero quasimomentum. The other state is therefore loaded into a higher band. Because the avoided-crossings at higher bands correspond to higher-order Bragg resonances, the band-gap energy is smaller due to a weaker coupling for a given laser power (i.e. lattice depth). Thus it can be made the case that criterion (9.7) is well satisfied for only the stationary component, allowing selective acceleration of just that component. This increases the relative momentum between the two states, resulting in LMT beamsplitting. We have found that a $4\hbar k$ initial Bragg beamsplitter is sufficient to accelerate just one of the momentum states. In this way, atoms can be accelerated and decelerated in order to close the atom interferometer.

We have achieved a fringe visibility of $(24 \pm 4)\%$ in a Bloch-based LMT interferometer; the highest yet observed to the best of our knowledge. The full pulse sequence is highlighted in figure 9.5(a), as well as the space-time diagram. After

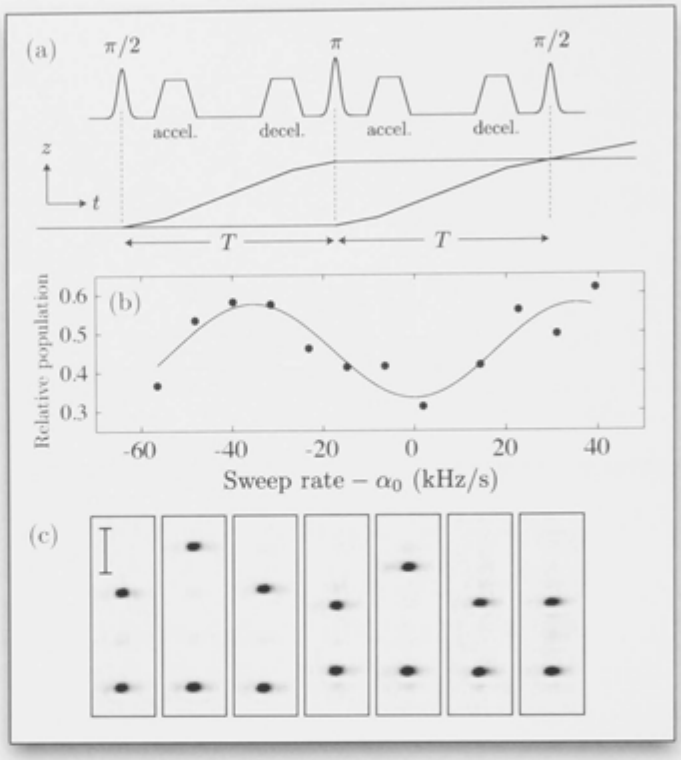

Figure 9.5: Bloch oscillations-based LMT gravimeter. (a) The intensity of the pulse sequence used for this interferometer, and the resulting space-time diagram. Using only the Gaussian pulses results in a standard Mach-Zehnder interferometer. (b) Fringes from a LMT gravimeter using Bloch beamsplitters. A visibility of 24% is observed for $T = 2.5\,\mathrm{ms}$, and effective order $n = 2.42$ calculated from the space-time area. This is in agreement with the fitted fringe period of $(70 \pm 5)\,\mathrm{kHz/s}$. (c) Absorption images showing the two arms of the interferometer after each pulse. The scale bar in (c) represents $300\,\mu\mathrm{m}$.

an initial $4\hbar k$ Bragg beamsplitter, we adiabatically load atoms into a lattice of depth $\sim 10\hbar\omega_r$ in $100\,\mu\mathrm{s}$. We then chirp $\Delta\omega$ over $200\,\mu\mathrm{s}$, sweeping q through one Brillouin zone. The momentum of one arm is thus increased by $2\hbar k$ in the lab frame. This process is reversed to decelerate this arm before a π Bragg-pulse, after which the other arm is subjected to the same procedure. We use $T = 2.5\,\mathrm{ms}$, and our pulse sequence gives the interferometer a space-time area with an effective order of $n = 2.42$, calculated from a diagram such as that in (a). The resulting fringes are shown in (b), and the fitted fringe period of $(70 \pm 5)\,\mathrm{kHz/s}$ is in agreement with the effective order.

We find that if either the lattice depth is increased beyond $10\hbar\omega_r$, or our acceleration time is increased to impart a larger momentum, the interferometer output converges to $P = 0.5$. In fact, even if we adiabatically load and unload the lattice without acceleration, we observe this effect. This is suggestive that the cause is related to the AC-stark shift, as the accelerated atoms experience a different shift to the unaccelerated atoms. Ideally this would be common to both

interferometer arms, as each spends an equal time in each lattice band. However, the inhomogeneous intensity of the laser beam leads to spatial phase shifts, which do not cancel in each half of the interferometer due to the expansion of the cloud. The result is a reduction in the contrast during detection [195]. Indeed, in work by Clade *et al.* [186] and Müller *et al.* [79], it was necessary to use symmetric acceleration of each arm in opposite directions in order to observe interference. Although we have observed significant interference without using symmetric acceleration, our space-time area is limited. We therefore expect that contrast could be increased by using larger laser beams at higher power, or a narrower momentum width source such as an atom-laser, or a BEC whose interactions are switched to zero upon release from the trap [125]. Finally, temporal intensity fluctuations can lead to randomised phase noise in the fringes, again due to the Stark shift, but should not reduce fringe contrast. This could be alleviated by intensity stabilising the laser, which we plan to do in the future.

9.5 Chapter Conclusions

We have presented results from the first BEC-based Mach-Zehnder gravimeter. We observe interference fringes with a high visibility, and are able to increase our sensitivity to gravity by imparting larger momentum to the atoms in the beamsplitting process. We have also investigated the use of Bloch oscillations as an LMT technique with BECs, again observing a comparatively high fringe visibility. Using a mean-field model, we demonstrated that interaction induced phase diffusion is negligible in an interferometric measurement with freely-falling, coherent atomic samples. In the next chapter, we discuss the effects of momentum width in inertial sensors, and demonstrate that the very narrow momentum width of a BEC, combined with LMT beamsplitters, should lead to sensitivity beyond current state-of-the-art.

Chapter 10

The Effects of Momentum Width in Inertial Sensors

Work in this chapter has been peer-reviewed and published in:

S. S. Szigeti, J. E. Debs, J. J. Hope, N. P. Robins, and J. D. Close. Why momentum width matters for atom interferometry with Bragg pulses. New J. Phys. 14, 023009 (2012). [78]

In the introduction, and several times throughout this thesis, the importance of momentum width has been highlighted. In this chapter, we give a detailed discussion of the effects of momentum width in atom interferometer-based inertial sensors. It is in this sense that Bose-condensed sources appear most promising. The discussion is divided into two sections: momentum width along the beamsplitter laser, and momentum width transverse to the beamsplitter laser. With Bragg diffraction being an attractive option for LMT beamsplitting, we begin by highlighting results from our recent and comprehensive study on the effects of momentum width in Bragg atom interferometers. We then turn to the question of transverse momentum width, and present experimental results on the comparison of a thermal atomic source and a BEC source in our gravimeter; finding that the BEC produces fringes with superior contrast. Using straightforward arguments, we conclude that wavefront errors of the Bragg laser are the most likely cause of the reduced contrast for a thermal source. Finally, we discuss in some detail the systematic effects of the Coriolis force, which can also benefit from narrower momentum width sources.

10.1 The Effect of Momentum Width Along k in Bragg Interferometers

Work in this section was done in close collaboration with S. Szigeti. The initial theoretical analysis and calculations were perform by the author, who also provided ongoing input to the detailed numerical calculations performed by S. Szigeti. A comprehensive article has been published in New Journal of Physics [78]. Here, we give a brief description of the work and highlight some key results.

10.1.1 Theoretical Description of Bragg Diffraction

As experimentalists, we have exquisite control of our laser frequencies and it is useful to describe Bragg diffraction in the atom frame, using figure 8.3. However, for a robust theoretical description which accounts for the momentum width of the atomic source, it is far more convenient to work in the lattice frame. Note that although the lattice and lab frames were equivalent in the first experiment(s) on Bragg diffraction using standing waves, this is not necessarily the case in general. In any case, equation (8.7) defines the resonance condition for Bragg diffraction in the lattice frame, as a condition on the initial momentum of the atom along the lattice. As a reminder, $p_n = n\hbar k$ for nth order diffraction. We now develop the theoretical framework that is used for investigating the effect of momentum width on Bragg diffraction.

In what follows, it is assumed the reader is familiar with concepts in chapter 2 of this thesis. Consider a two-level atom, with ground and excited electronic states $|g\rangle$ and $|e\rangle$ respectively, moving in a one-dimensional optical standing wave given by $2\mathbf{E}_0 \cos(kz)\cos(\omega t)$. This field is detuned from atomic resonance at ω_0 by $\Delta = \omega - \omega_0$. We can describe the state of the system by the Hamiltonian written in a frame rotating at the laser frequency:

$$\hat{H} = \frac{\hat{p}_z^2}{2m} - \hbar\Delta|e\rangle\langle e| + \hbar\Omega\cos(k\hat{z})(|e\rangle\langle g| + |g\rangle\langle e|) \tag{10.1}$$

Working in the position basis,[1] we can describe this system by the state vector:

$$|\psi(z,t)\rangle = g(z,t)|g\rangle + e(z,t)|e\rangle \tag{10.2}$$

where $g(z,t)$ and $e(z,t)$ are the ground and excited state centre-of-mass position

[1] In this way, the centre-of-mass momentum dependence of the system is built into the ground and and excited state wavefunctions.

wavefunctions respectively. Feeding this into the Schrödinger equation gives the coupled differential equations for the centre-of-mass wavefunctions:

$$i\hbar\frac{\partial g(z,t)}{\partial t} = -\frac{\hbar^2}{2m}\frac{\partial^2 g(z,t)}{\partial z^2} + \hbar\Omega\cos(kz)e(z,t) \tag{10.3}$$

$$i\hbar\frac{\partial e(z,t)}{\partial t} = -\frac{\hbar^2}{2m}\frac{\partial^2 e(z,t)}{\partial z^2} - \hbar\Delta e(z,t) + \hbar\Omega\cos(kz)g(z,t) \tag{10.4}$$

We operate in the regime that spontaneous emission is negligible, such that we may adiabatically eliminate the excited state using $\dot{e}(z,t) \approx 0$. Combined with the initial condition $g(z,0) = 1$, this implies $e(z,t) \approx 0$ and therefore $\frac{\partial^2 e(z,t)}{\partial z^2} = 0$. This gives the equation of motion for $g(z,t)$:

$$\begin{aligned} i\hbar\frac{\partial g(z,t)}{\partial t} &= -\frac{\hbar^2}{2m}\frac{\partial^2 g(z,t)}{\partial z^2} + 2\hbar\Omega_e f(t)\cos^2(kz)g(z,t) \\ &= -\frac{\hbar^2}{2m}\frac{\partial^2 g(z,t)}{\partial z^2} + \hbar\Omega_e f(t)[1+\cos(2kz)]g(z,t) \end{aligned} \tag{10.5}$$

where as a reminder $\Omega_e = \frac{\Omega^2}{2\Delta}$ is the two-photon Rabi frequency, and $0 \leq f(t) \leq 1$ has been included to allow for a time-dependent coupling. The 1 in the square brackets gives a term that represents the mean AC Stark shift. It is possible to subtract this term even for non-constant $f(t)$. This is done by choosing the unitary transformation $g(z,t) \to g(z,t)e^{-i\Omega_e\int f(t)dt}$ and substituting this into equation (10.5). We then achieve the desired result:

$$i\hbar\frac{\partial g(z,t)}{\partial t} = -\frac{\hbar^2}{2m}\frac{\partial^2 g(z,t)}{\partial z^2} + \frac{\hbar\Omega_e}{2}f(t)(e^{i2kz}+e^{-i2kz})g(z,t) \tag{10.6}$$

As the Hamiltonian is periodic, we expand the wavefunction as a Fourier series of plane waves:[2]

$$g(z,t) = \sum_{n=-\infty}^{\infty} c_n(t)e^{-i(nk+\kappa)z} \tag{10.7}$$

where we introduce a momentum offset κ, the utility of which be discussed shortly.

[2]Technically we use Bloch's theorem and expand in plane waves with a the lattice periodicity of $2k$. Then when considering both odd and even initial conditions for n, the result is the set of equations (10.9). We therefore take the shortcut of expanding in plane waves of periodicity k.

Substituting this expansion into (10.7) and omitting the argument of c_n gives:

$$\begin{aligned} i\hbar \sum_{n=-\infty}^{\infty} \dot{c}_n e^{-i(nk+\kappa)z} &= -\frac{\hbar^2}{2m} \sum_{n=-\infty}^{\infty} (nk+\kappa)^2 c_n e^{-i(nk+\kappa)z} \\ &\quad + \frac{\hbar\Omega_e}{2} f(t) \sum_{n=-\infty}^{\infty} c_n \left(e^{-i[(n+2)k+\kappa]z} + e^{-i[(n-2)k+\kappa]z} \right) \\ &= \sum_{n=-\infty}^{\infty} \left[-\frac{\hbar^2}{2m}(nk+\kappa)^2 c_n + \frac{\hbar\Omega_e}{2} f(t)(c_{n+2} + c_{n-2}) \right] e^{-i(nk+\kappa)z} \end{aligned} \tag{10.8}$$

This equality must hold for each term in the sum, giving a set of ODEs for the plane wave component amplitudes:

$$\dot{c}_n = -i \left[-\omega_r (n+\bar{\kappa})^2 c_n + \frac{\Omega_e}{2} f(t)(c_{n+2} + c_{n-2}) \right] \tag{10.9}$$

where $\bar{\kappa} = \kappa/k$. At this point, it would be possible to consider Raman-Nath diffraction (multiple orders populated – see figure 10.1), defined as the regime where the kinetic term can be neglected such that $\Omega_e/2 \gg n^2\omega_r$ (this assumes that κ is small compared to nk) [114]. This is equivalently a statement of the energy-time uncertainty relation for the interaction time. Similarly, the Bragg regime can be defined as a small coupling energy compared with the closest momentum resonance for a given diffraction order n:[3]

$$\Omega_e/2 \ll 4(n-1)\omega_r. \tag{10.10}$$

It is possible to solve the ODEs of (10.9) analytically, for constant $f(t)$ (or more precisely, a step function), by truncating the plane wave expansion in equation (10.7) at $\pm n$, provided we satisfy condition (10.10). Solutions for nth order diffraction are then obtained by adiabatically eliminating the intermediate momentum states between $-n$ and n. This has been done in [175] for $\kappa = 0$, and was extended by Szigeti *et al.* to $\kappa \neq 0$ in [78]. The solutions are:

$$|c_n(t)|^2 = \frac{\Omega_n^2}{\tilde{\Omega}_n^2} \sin^2\left(\frac{\tilde{\Omega}_n}{2} t\right) \tag{10.11}$$

[3]For $n = 1$ this is slightly modified, with $(n-1)$ replaced by $(n+1)$. This is because the closest adjacent state is $n+2$, not $n-2$.

and

$$|c_{-n}(t)|^2 = 1 - \frac{\Omega_n^2}{\tilde{\Omega}_n^2} \sin^2\left(\frac{\tilde{\Omega}_n}{2}t\right) \tag{10.12}$$

where $\tilde{\Omega}_n = \sqrt{\Omega_n^2 + 16n^2\bar{\kappa}^2\omega_r^2}$, and we have introduced the nth-order Rabi frequency:

$$\Omega_n = \frac{\Omega_e^n}{(8\omega_r)^{(n-1)}[(n-1)!]^2} \tag{10.13}$$

where it is assumed that $\kappa \ll \hbar k$. This result is identical to that derived in chapter 2 for the two-level atom, with the effective detuning given by $\Delta_e = 4n\bar{\kappa}\omega_r$. Indeed, in the Bragg regime, the system behaves as a two-level system with an effective wave vector $\mathbf{k}_e = 2n\mathbf{k}$; again demonstrating the factor of n enhanced phase-shift in an inertial sensor. Notice also that κ behaves like a detuning from the resonant momentum in the lattice frame. This is not surprising as in the atom's frame κ is equivalent to a Doppler shift of the lattice laser frequencies off resonance. Hence, one can think of κ as a parameter that can be used to track the width of the Bragg resonance in momentum space. Furthermore, the width is also n dependent with a FWHM given by $\Delta\bar{\kappa} = 2\Omega_n/4n\omega_r$. Thus, for a given Ω_n the Bragg resonance width decreases with n. This suggests that a narrower momentum width is preferable, at least in the case of a bound two-photon Rabi frequency.

10.1.2 The quasi-Bragg Regime

Equation (10.10) equivalently places an upper limit on the nth-order Rabi frequency:

$$\Omega_n \ll \frac{8(n-1)^n}{[(n-1)!]^2}\omega_r \implies \Omega_n \ll 18\omega_r\ ,\ n \geq 2 \tag{10.14}$$

Although Ω_n has experimentally reasonable values for $n \leq 8$, the right-hand-side of (10.14) drops rapidly for $n > 8$ due to the factorial in the denominator. This implies unrealistically long π-pulse times for the strict Bragg regime. For example, $\Omega_{10} \ll 0.2\omega_r$ gives $\tau_\pi \gg 1$ ms. In previous work, Müller *et al.* showed that one can minimise losses to undesired momentum states by using Gaussian pulse envelopes [175], i.e. $f(t) = \exp(-t^2/2\tau^2)$. This enables diffraction in the quasi-Bragg regime, which does not satisfy the strict limits imposed by equation (10.10), but allows the use of shorter pulse times.

Figure 10.1 show examples of experimental absorption images for Raman-Nath diffraction on the left, low loss Bragg diffraction in the centre ($n = 4$),

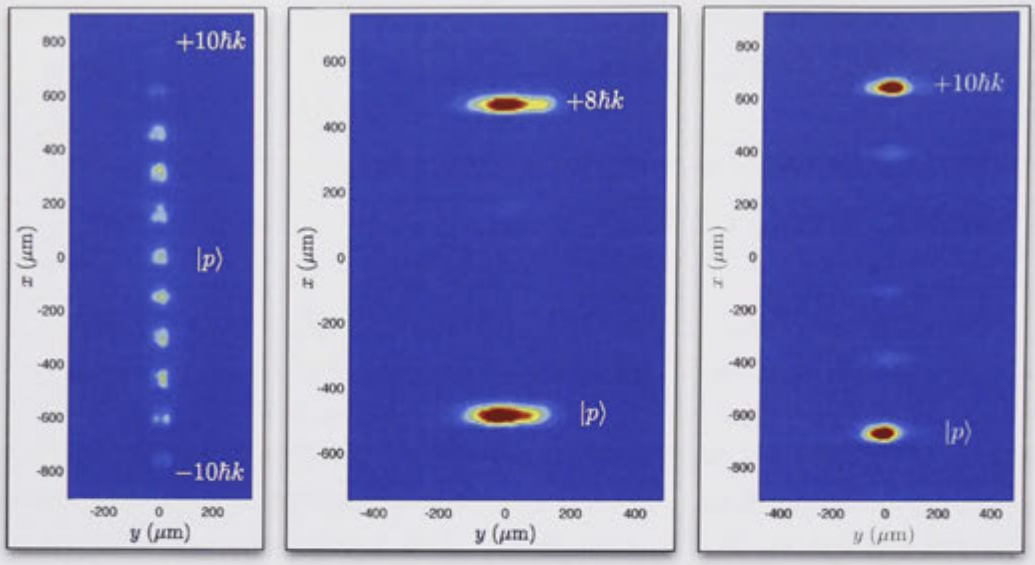

Figure 10.1: Raman-Nath diffraction vs. Bragg diffraction. Left: Raman-Nath diffraction using a (short) $10\,\mu$s pulse with relatively high intensity. Centre: 4th order diffraction using a Gaussian pulse with $\tau = 100\,\mu$s. Right: 5th order diffraction using a Gaussian pulse with $\tau = 100\,\mu$s, which is substantially more lossy. The Bragg pulses are $\pi/2$ pulses.

and lossy Bragg diffraction on the right ($n = 5$). Our goal is to investigate the effect of momentum width on the efficiency of Bragg diffraction. Notice that for $10\hbar k$ diffraction, the loss is more significant. As we shall see, this is the result of insufficient laser intensity.

10.1.3 Fidelity of a π Pulse

Assuming that the initial cloud has a momentum distribution $|\psi(\kappa)|^2$ centred at the nth order momentum resonance $p = -n\hbar k$, its state can be written as:

$$|\psi_i\rangle = \int \psi(\kappa)|(-n + \bar{\kappa})\hbar k\rangle d\bar{\kappa} \tag{10.15}$$

where $\psi(\kappa)$ is assumed to be real and is normalised to 1. Ideally, nth order diffraction would result in the entire distribution centred at $p = -n\hbar k$ to be mapped onto the same distribution centred at $p = +n\hbar k$; i.e. the ideal state is:

$$|\psi_{ideal}\rangle = \int \psi(\kappa)|(n + \bar{\kappa})\hbar k\rangle d\bar{\kappa} \tag{10.16}$$

However, there will in general be population of other momentum states, and thus the final state will have the form:

$$|\psi\rangle = \sum_m \int c_m(\bar{\kappa}, t_f)|(m + \bar{\kappa})\hbar k\rangle d\bar{\kappa} \tag{10.17}$$

where t_f is a time well after the Bragg pulse has been extinguished, and $c_m(\kappa, t)$ are the expansion coefficients in (10.7) determined by solving the set of ODEs at different values of $\bar{\kappa}$. The above expression is valid by virtue of the result at the end of chapter 2 where it was concluded that solutions for individual momentum eigenstates can be determined, and *then* summed over the momentum distribution.

We may characterise the efficiency of a π pulse through the fidelity:

$$F_\pi = |\langle\psi|\psi_{ideal}\rangle|^2 \tag{10.18}$$

which measures the projection of the state we *get* onto the state we *want*. Taking the momentum distribution to be a normalised Gaussian of momentum width σ, it can be shown that the fidelity for *nth* order diffraction is given by [78]:

$$F_\pi(\Omega_e, \tau) \leq \int \frac{1}{\sqrt{2\pi\sigma^2}} e^{-\kappa^2/2\sigma^2} |c_n(\bar{\kappa}, \tau)|^2 d\bar{\kappa} \tag{10.19}$$

where τ is the 1-sigma width of a Gaussian coupling pulse, and the upper bound occurs if the relative phase between different momentum components is zero. In what follows we assume equality for the above expression. F_π therefore represents the total efficiency of atoms transferred to a momentum distribution centred around $p = n\hbar k$, and therefore is our "mirror efficiency."

10.1.4 Results for a Bragg Mirror

Unbound Two-Photon Rabi Frequency

By performing a numerical optimisation of F_π over Ω_e and τ, we can determine the optimised fidelities for a given n and σ. Details of the numerical optimisation can be found in our paper [78]. The results are presented in figure 10.2 for n in the range $(1 - 25)$ and σ in the range $(0.01 - 1)\hbar k$. The first feature of these data is that as the momentum width increases for a given n, the mirror efficiency monotonically decreases. This can be understood by realising that a broader momentum distribution has more atoms at a larger detuning from resonance (for

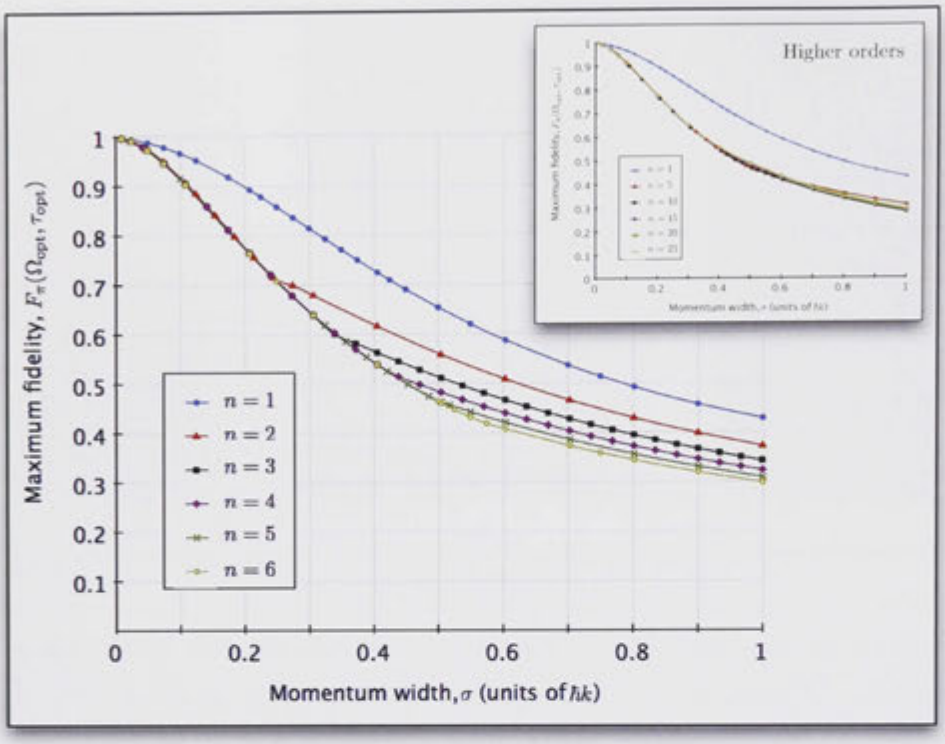

Figure 10.2: Optimised fidelity for a Bragg mirror pulse as a function of the momentum width for different n. Inset: Curves for larger values of n. Points represent numerically simulated results, joined by lines to guide the eye. From [78].

fixed atom number). Although in the limit of a two-level system, this could be compensated for by increasing the effective Rabi frequency to broaden the transition, optimised diffraction in the quasi-Bragg regime inherently involves multiple levels, and increasing the Rabi frequency further reduces the fidelity due to loss to other momentum states.

Perhaps more interestingly, for a given momentum width the maximum fidelity varies little with n for $n \geq 2$.[4] However, in order to reach the optimum fidelities our simulations show that the required two-photon Rabi frequency scales as $\Omega_e \propto n^2$, as given in figure 10.3. This also agrees with the scaling of equation (10.13) in the limit of large n, and essentially highlights that the optimum occurs for a constant nth-order Rabi frequency. Furthermore, it highlights that the quasi-Bragg regime occurs when the potential energy term ($\propto \Omega_e$) is on the order of the kinetic energy term ($\propto n^2$) in the Hamiltonian.

[4] 1st order diffraction is subtly different from all other orders in that there are no momentum states between the initial and final momentum states.

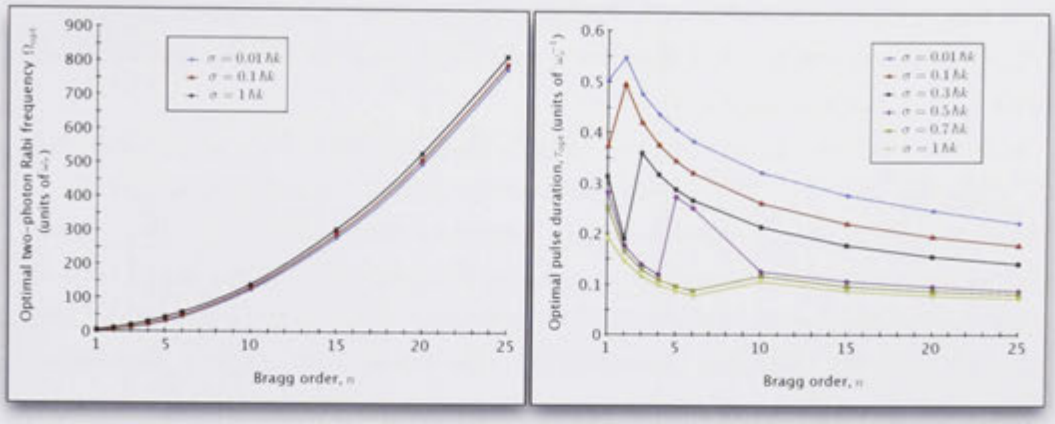

Figure 10.3: Optimised Rabi frequency (left) and Gaussian pulse duration (right) as a function of order for a Bragg mirror pulse. Points represent numerically simulated results, joined by lines to guide the eye. From [78].

The analytic solution (10.11) can give insight into this result; namely that although the transition width decreases with n, this can be compensated for by an increase in the nth order Rabi frequency, which broadens the transition. This may at first seem to contradict the earlier statement that one cannot increase the Rabi frequency indefinitely due to loss to other momentum states. While this remains true, higher order diffraction can tolerate a large Rabi frequency, as the adjacent momentum states are energetically further separated for larger n due to the quadratic dispersion relation. This is also highlighted by condition (10.10).

Thus, assuming that we have ample laser power available, the best mirror efficiency is barely affected by increasing n. As a final point of comment, the clear points of deviation from the general trend of the curve in figure 10.2 correspond to momentum widths where the system begins to optimise in a slightly different regime which involves more Raman-Nath-like diffraction. This is because the cloud's momentum width becomes large enough that off-resonant transitions can actually lead to a higher population in the target state than more Bragg-like transitions. We have verified this picture by observing the occupation in other momentum states, which undergoes a distinct rise around these points. It is also apparent in the optimised pulse times given in figure 10.3, where for a given n (e.g. $n = 2$) there is a sudden drop in the pulse time with increasing momentum width.

We have compared these theoretical results to several state-of-the-art systems in the literature. In work by Müller *et al.* [85], mirror efficiencies between 85–90% were reported for Bragg diffraction with $n \leq 9$. Their source momentum

width was velocity selected to $\sigma \simeq 0.13\hbar k$. This is consistent with our prediction of $F_\pi \sim 90\%$, suggesting that they were operating close to the fundament limit imposed by our semi-classical theory.

In recent work by Chiow *et al.*, $n = 3$ reflections of a BEC were performed with 94% efficiency [87]. From [196], we estimate the momentum width of their BEC to be $\sigma \simeq 0.05\hbar k$, which gives an upper bound on their fidelity of 95%. Again they appear to be operating close to the fundamental limit. This conclusion is in contrast to statements made by the authors that their efficiency could be improved by reducing technical uncertainties. The result is particularly important in this context, as Choiw *et al.* have used 17 successive Bragg pulses in order to produce a $102\hbar k$ beamsplitter. This of course causes a large loss in atom number of $1 - (0.94)^{17} = 75\%$. As our results imply that any improvements to the mirror efficiency would only be possible by using a narrower momentum width source, it would seem that Bose-condensed source are the only viable option for such techniques; particularly with proposals demanding $1000\hbar k$ beamsplitters [28].

Bound Two-Photon Rabi Frequency

The above results assume the two-photon Rabi frequency is unbounded. In practice this is of course not so. The laser intensity is limited via power and beam size considerations, while the one-photon detuning is limited by our chosen tolerance for spontaneous emission. In other words, once a tolerance to spontaneous emission is chosen, this limits the two-photon Rabi frequency for a given laser intensity. Figure 10.4(a) plots the atom loss due to spontaneous emission as a function of laser intensity for the optimised pulse parameters and $\sigma = 0.1\hbar k$, over a range of orders. A loss of over 100% implies the atoms each spontaneously scatter more than 1 photon on average. The blue box gives an example of how to use the figure; it highlights the orders over which the optimised fidelity can be theoretically obtained. In this case, we assume a loss of up to 1% can be tolerated, and that the maximum Bragg-laser intensity is $1\,\mathrm{W/cm^2}$. This intensity is representative of a state-of-the-art Titanium-Sapphire laser used in reference [85]. By inspection, optimised efficiency can be obtained for up to $n \simeq 7$ in this example, although we did not explicitly calculate the curve for this order. If we were to tolerate slightly more loss, say 3%, then $n = 10$ could be optimised at this intensity.

Bounding the Rabi frequency therefore has strong implications for achieving optimum mirror fidelities. In figure 10.4(b), we plot the calculated fidelities as a

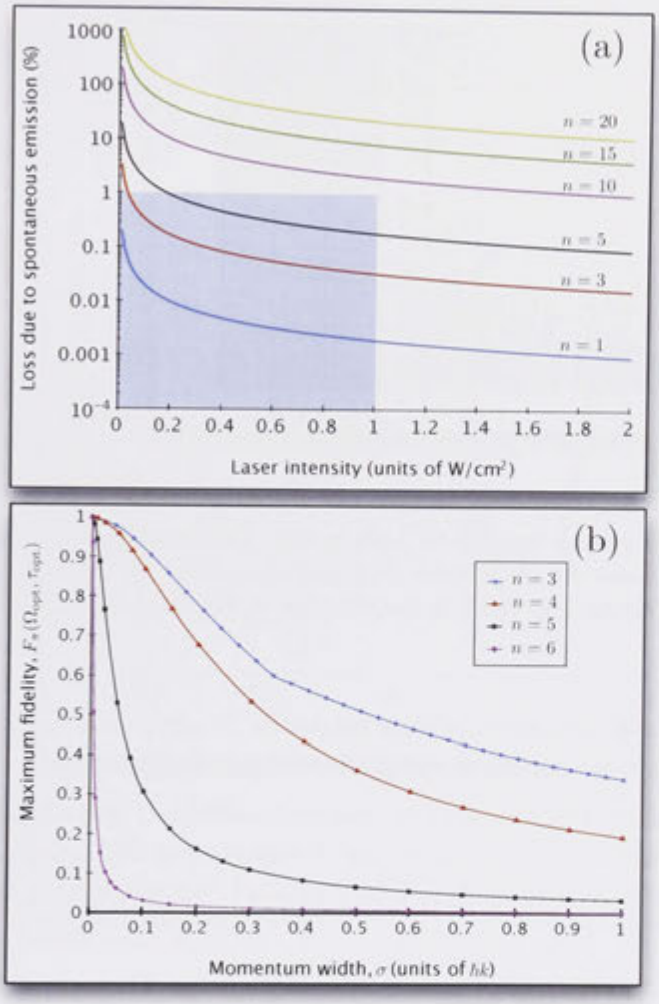

Figure 10.4: Bragg mirror efficiency for a bound Rabi frequency. In (a) we plot the loss due to spontaneous emission as a function of Bragg-laser intensity, and for $\sigma = 0.1\hbar k$, based on optimised values of the Rabi frequency and pulse duration. There is little change for other momentum widths $< 1\,\hbar k$. The blue rectangles show what Bragg orders can reach the optimised efficiency assuming that we tolerate a 1% loss, and have a maximum intensity of $1\,\mathrm{W/cm^2}$. In (b) we plot the maximum fidelities calculated assuming the Rabi frequency is bounded at $\Omega_e \leq 20\omega_r$. Optimum values are only obtained for $n \leq 4$. Points are numerically simulated values, with joining lines to guide the eye. From [78].

function of momentum width (as in figure 10.2), now assuming that $\Omega_e \leq 20\omega_r$. Although this is a relatively modest Rabi frequency, we use it for illustrative purposes as the simulations are much simpler in this case. We find that for $n < 4$, the optimised fidelities from figure 10.2 are achieved as optimum Rabi frequency is always less that $20\omega_r$. For $n \geq 4$, the optimum fidelity cannot be reached, and falls off sharply with n for a given momentum width. Decreasing the momentum width in this regime improves the fidelity for a given n, again suggestive that Bose-condensed sources could be advantageous when considering the effects of finite laser power and minimising spontaneous emission. This result is also captured by the effective two-level model discussed earlier [see equations (10.11) and (10.12)].

In figure 10.5, we present experimental data which qualitatively verifies the

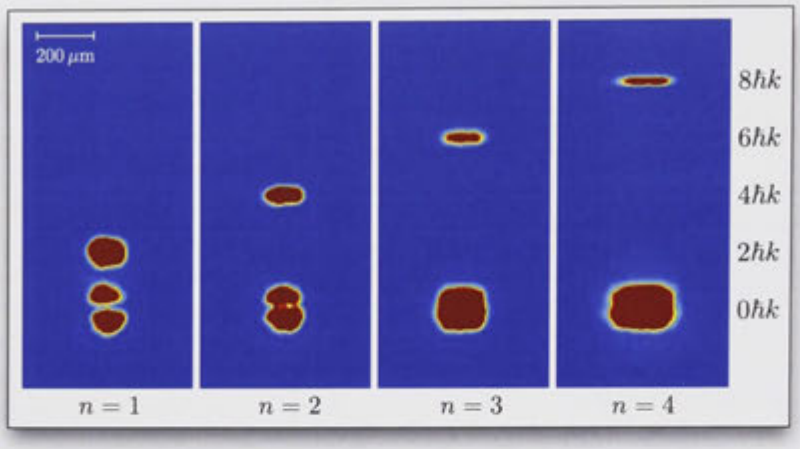

Figure 10.5: Bragg diffraction for increasing order with a near constant nth order Rabi frequency. A 100 μs Gaussian Bragg pulse is applied for each order. The intensity of the Bragg laser is increased in order to maximise the number of diffracted atoms. We see that the diffracted cloud has a decreasing momentum width in the direction of the Bragg beam for increasing order.

effect of a bound two-photon Rabi frequency. 100 μs Gaussian Bragg pulses are applied to a BEC after allowing for ballistic expansion ($\sim$ 12 ms). Absorption images are taken for Bragg orders ranging over $n = 1 - 4$. We increase the laser intensity for increasing order, in order to maximise the number of diffracted atoms. In the sense limit of two-level system, this is equivalent to maintaining a constant nth order Rabi frequency. Note that there is no discernible population of other momentum states, indication highly Bragg-like diffraction. There is a clear reduction in the momentum width (along the Bragg laser beam) of the diffracted cloud, as well as the number of diffracted atoms, for increasing order, in qualitative agreement with the theoretical results.

10.1.5 Mach-Zehnder Interferometer: Comparison to Experiment

In the paper by Szigeti *et al.*, we also investigate the effects of momentum width for a full Mach-Zehnder $\pi/2 - \pi - \pi/2$ pulse sequence. Specifically, we used the SNR of the interferometer (assuming a shot-noise limit) as a figure of merit, and looked again in the regimes of bound, and unbounded Rabi frequency. The optimised mirror pulse values were used for the mirror in the pulse-sequence, and the optimisation was performed over the beamsplitter pulse parameters. The results generally reflect those for the mirror analysis, and we therefore will not go into detail here. The interested reader should see the article [78].

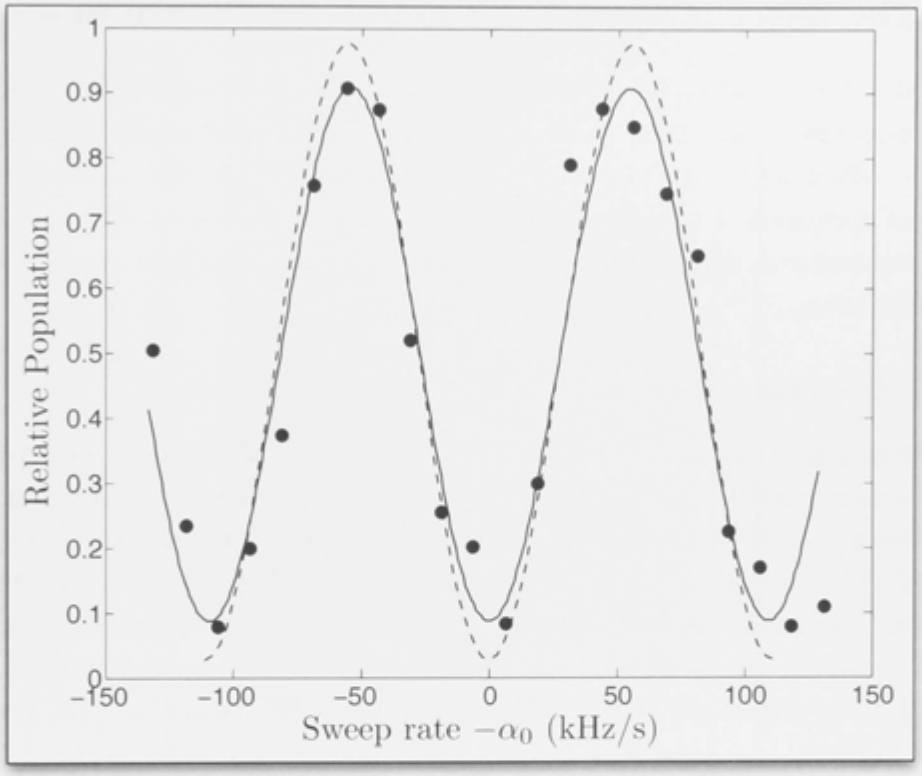

Figure 10.6: Comparison of Bragg-theory and experimental gravimeter fringes. The experimental set is identical to that of figure 9.1 with $n = 1$, $T = 3\,\text{ms}$. The solid line is a sinusoidal fit to the experimental data. The dashed line shows theoretical fringes calculated from a fully optimised Mach-Zehnder pulse sequence, for a momentum width of $\sigma = 0.14\hbar k$.

There is however another comparison we can make with experiment, not included in the published article. We performed an optimisation routine on parameters for our experimental gravimeter fringes in figure 9.1. As a reminder these data correspond to $n = 1$, $T = 3\,\text{ms}$, and the momentum width of our BEC was $\sigma = 0.14\hbar k$. Theoretical fringes were calculated for the optimised pulse sequence, and overlaid on experimental data in figure 10.6 as the dashed trace. The figure is otherwise identical to figure 9.1. Our experimental contrast was $(83 \pm 6)\%$. The theoretical contrast is 94%. Thus we find that our experiment results are consistent with our Bragg-theory, and within the predicted fundamental limit by as little as 5%. Note that the experimental data was taken long before our theoretical analysis of Bragg interferometers, and our pulses were not optimised according to the theory. Small wavefront errors could also account for the discrepancy. In the next section, we will discuss wavefront errors in more detail.

10.2 The Effect of Momentum Width Transverse to k

Mentioned in the introduction, and alluded to several times throughout this thesis, the transverse momentum width of an atomic source has implications for systematic effects and fringe contrast in an inertial sensor. In this section, we give a brief discussion of two sources of uncertainty in a gravimeter which scale with the transverse momentum width of the atomic source: wavefront errors and the Coriolis force.

10.2.1 Wavefront Errors

In the discussion of light-pulse beamsplitters throughout this thesis, we have assumed the beamsplitter laser is an ideal plane wave. In practice this is not so. Firstly, a laser beam is well described by Gaussian optics, and thus the wavefronts are curved with a radius of curvature that is a function of the distance from the beam waist. Secondly, there will always be some level of wavefront distortion such as aberrations due to e.g. dust particles in the beam and imperfect optics. These will affect the shape of the wavefronts in non-trivial ways, in both the near- and far-field.

Because any atomic source will have some transverse momentum width, the atoms in (say) a gravimeter will not only fall downward under gravity, but will also have a range of transverse velocities. There will therefore be a range of atomic trajectories through the beam, as shown schematically in figure 10.7. The black lines represent atomic trajectories with different horizontal velocities, originating at the source cloud (shown in blue). The red-dashed curves represent distorted wavefronts, and the dotted grey lines the vertical location of the ith interferometer pulse.[5] As atoms travel transversely (as well as downward) in the beam, the sampled phase at each interferometer pulse will differ from the ideal plane wave phase of $k_e z$ in a trajectory-dependent way. Thus, in addition to the usual phase shift due to gravity, there will be a trajectory-dependent phase shift of:

$$\Phi_{ab}(\mathbf{x}(t)) = \phi_{ab}(x_1) - 2\phi_{ab}(x_2) + \phi_{ab}(x_3) \tag{10.20}$$

where x_i is the horizontal position of an atom at the ith pulse and ϕ_{ab} the laser phase as a function of x. Therefore, at the output of the interferometer, there will be a non-trivial spread in phase-shift across the atomic ensemble. Because

[5] Although the three wavefronts appear to be identical in the vertical direction, this is done for simplicity. In general this is not the case as propagation of aberrations will also result in a changing wavefront profile.

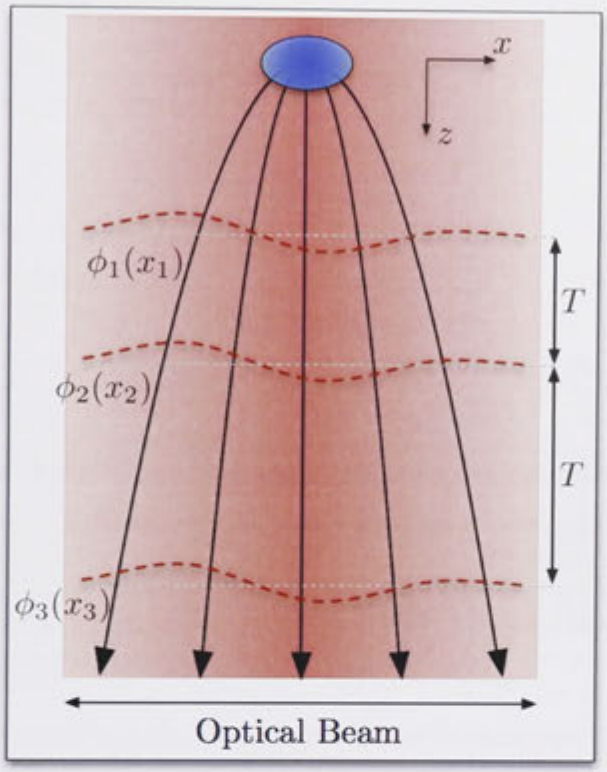

Figure 10.7: Schematic representation of the effects of wavefront distortion. Black lines represent atomic trajectories through the laser beam with different horizontal velocity components. Red-dashed lines are distorted wavefronts of the beamsplitter laser beam. As a result of different horizontal velocities, each trajectory samples a different phase at each light-pulse (represented by the dotted horizontal lines). Note the figure is not to scale.

one typically averages spatially over the ensemble during detection of the atoms, this phase information is averaged over, leading to a reduction in the observed fringe contrast, as well as a possible systematic phase shift in the fringes. The systematic phase shift has been discussed at length in several articles [9, 88, 89].

A Thermal vs. a Bose-Condensed Source

We have performed a direct experimental comparison of an ultra-cold thermal cloud and a BEC in our atomic gravimeter. To produce the thermal cloud, we cease evaporation in our optical trap just above the critical temperature for condensation. In this way, we produce an ensemble at a temperature of $\sim 100\,nK$. Figure 10.8 gives a comparison of fringes for the BEC and thermal source where we make every effort to ensure that the system is otherwise identical. In particular, we use an identical velocity-selection pulse for each sequence. The fringe

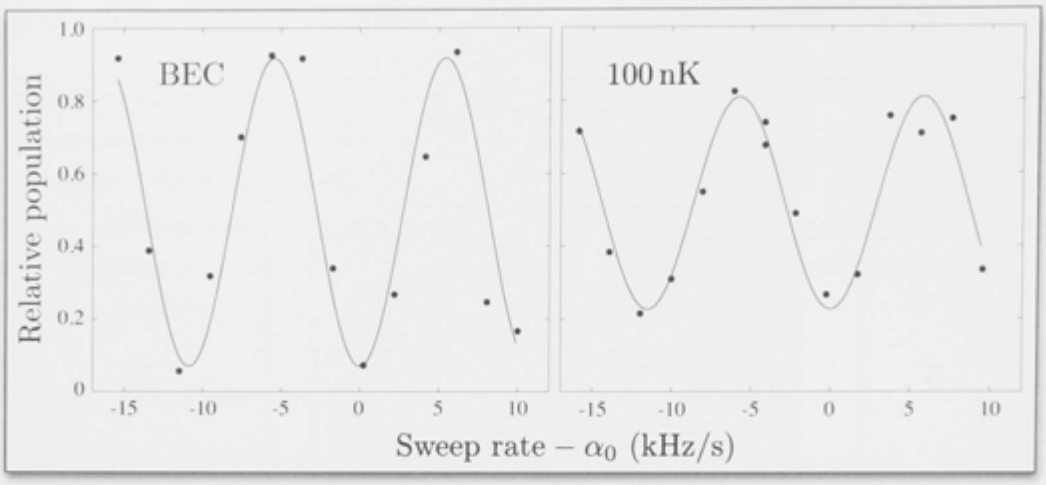

Figure 10.8: Experimental comparison of thermal and Bose-condensed atomic sources. We use $n = 1$, $T = 3$ ms gravimeter parameters. Both have an identical vertical momentum width, but differ in their transverse momentum width. A significant improvement in contrast from to $(58 \pm 4)\%$ to $(85 \pm 11)\%$ is seen for the BEC, with all other experimental parameters kept constant.

data sets were taken consecutively. The condensed source shows an improved contrast compared to the thermal souce, with an increase from $(58 \pm 4)\%$ to $(85 \pm 11)\%$. Note that this contrast agrees with the fundamental limit within experimental uncertainty. At 100 nK the thermal cloud has a factor of 3 larger transverse momentum width than the condensate.

Following [89], we can estimate the effect of local wavefront errors by Taylor expanding the wavefront curvature to second order; i.e. we estimate the the local wavefront curvature as parabolic:

$$\phi_{ab}(x) = Kx^2 \tag{10.21}$$

where K characterises the phase curvature. Assuming a Gaussian momentum distribution with a velocity variance of σ_v^2, then:

$$\phi_{ab}(\sigma_v t) = \frac{k_e}{2R}\sigma_v^2 t^2 \tag{10.22}$$

and therefore, substitution into equation (10.20) gives:

$$\Phi_{ab} = \frac{k_e}{R}\left(\frac{\sigma_p}{m}T\right)^2 \tag{10.23}$$

for the full pulse sequence, where R is the radius of curvature for a parabola. The

observed reduction in contrast to 55% requires a phase variation across the atomic ensemble on the order of $\pi/3$. For our 100 nK sample (for which $\sigma_p = 0.52\hbar k$) with $n = 1$ and $T = 3\,\text{ms}$ this gives $R \simeq 1.3\,\text{mm}$. Such aberrations could potentially be caused by imperfections in the glass cell wall, situated only 10 mm away from the atomic ensemble. The Bose-condensed source has over a factor of 3 narrower momentum width, which reduces the phase variation by more than a factor of 10. This has a negligible effect on the contrast, in agreement with the measured value of $(85 \pm 11)\%$. Thus once again we see that the narrow momentum width of Bose-condensed sources present a practical advantage for inertial sensors.

10.2.2 Coriolis Effects

In chapter 3 we highlighted that the phase-shift of a Mach-Zehnder interferometer is sensitive to rotations if the atomic source has a velocity component perpendicular to $\mathbf{k}$. As a reminder, the phase shift due to uniform rotation $\boldsymbol{\Omega}$ (or equivalently the Coriolis force) is to leading order:

$$\Phi_R = 2\mathbf{k}_e \cdot (\boldsymbol{\Omega} \times \mathbf{v}_a)T^2 \tag{10.24}$$

where $\mathbf{v}_a$ is the atomic velocity. Thus in a gravimeter, an atomic source with transverse momentum width and/or transverse centre-of-mass momentum will also have parasitic rotation induced phase-shifts. These can be divided into three classes which are summarised below, and all of which can benefit from the use of a Bose-condensed source.

Systematic Rotational Phase Shift

When atoms are released from their trap, be it a magnetic trap, optical trap, or a MOT/molasses, any uncertainty in their initial velocity can result in a Sagnac phase shift due to a centre-of-mass horizontal velocity component. The size of this effect will depend on the uncertainty in initial velocity. For example in [90], the authors estimate a 1 cm/s uncertainty in their horizontal launch velocity for an atomic fountain. This results in an uncertainty in g of $\Delta g = 6 \times 10^{-8} g$, which is a dominant contribution to the accuracy. The authors state that using a BEC does not reduce this systematic shift. Although this true in the fundamental sense, i.e. there is no benefit from its narrow momentum width, in practice the initial velocity of a condensate is typically far better controlled than for an atomic fountain, which uses an optical molassas to launch the atoms. In particular,

condensates dropped from an optical trap have a negligible initial velocity due to the symmetric reduction in the trap intensity. Therefore, use of a BEC will help reduce this systematic effect.

Distribution-Dependant Rotational Phase Shift

Assuming that the initial centre-of-mass velocity of an atomic source is negligible, there is still the possibility of a systematic rotational phase shift due to the transverse velocity *distribution*. This is again related to there being a range of horizontal velocity components, each of which encloses a different area and contributes a rotational phase shift. However, because these trajectories are averaged over in detection, the total contribution may be reduced. Consider the two horizontal velocity distributions in figure 10.9, along with the rotational phase shift equation (10.24). Notice that the phase shift reverses sign with the velocity vector. The distribution in (a) is a symmetric Gaussian distribution. In other words, the range of atomic trajectories with negative velocities is equal to the range with positive velocities. Therefore, the phase contribution from the left half of the distribution will exactly cancel that of the right half of the distribution, which is represented by the two areas under the curve. The distribution in (b) however is asymmetric, and the left and right areas do not cancel.

BEC momentum distributions are highly symmetric; often defined by the symmetry of the trap. Thermal distributions from a MOT or molasses, such as those from an atomic fountain, are typically less so. Thus, we once again expect a BEC to be advantageous.

Wavepacket Overlap

Initially, the counter-propagating beams forming the beamsplitter in a gravimeter are (ideally) aligned with the local gravity vector. Once the atoms are released and enter free-fall, however, the Earth continues to rotate taking the beamsplitter laser with it. There will therefore be a small change in the angle between $\mathbf{k}$ and $\mathbf{g}$ at successive beamsplitter/mirror pulses. The result is that the atomic trajectories do not perfectly overlap at the final beamsplitter due to momentum being transferred at slightly different directions for each pulse. This is analogous to an error in overlapping spatial modes at the final beamsplitter in an optical interferometer, and therefore causes a reduction in fringe contrast. The extent to which the contrast is reduced depend on the degree of mismatch, as well as the spatial extent of the wave-packet; equivalent to its coherence length. Interferometers

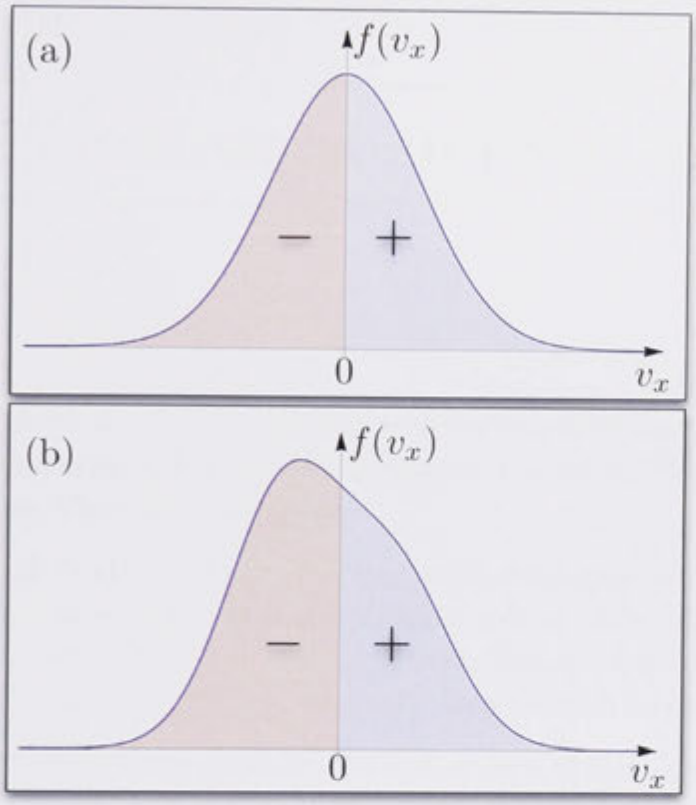

Figure 10.9: Distribution dependent Coriolis phase shift. (a) Represents a symmetric distribution in the horizontal velocity, and (b) an asymmetric distribution. The red area corresponds to a negative rotational phase-shift, and the blue area a positive phase-shift. Therefore, when averaging over the distributions the phase shifts cancel for (a), but not for (b).

with larger T are therefore more susceptible in general.

For thermal interferometers, it is often stated that 'each atom interferes with itself,' much like a Young's double slit experiment performed with single photons. Each atomic wave-packet is characterised by its thermal de Broglie wavelength, which is proportional to $1/T^{1/2}$. Thus hotter thermal sources will have smaller coherence lengths and will suffer more from this effect. A BEC on the other hand, with all atoms indistinguishable and in a single mode, has a much larger coherence length determined only by its physical size. Therefore a BEC will be less susceptible to this effect.

Very recent work by Lan *et al.* has experimentally investigated this effect in detail, and they have used an active tip-tilt mirror to compensate for rotation of the Earth; improving their contrast by 350% [90]. Their work clearly demonstrates that a BEC will be less susceptible to this effect than a thermal source, possibly even eliminating the need for a tip-tilt mirror.

Chapter 11

Conclusions and the Future

This thesis has presented experimental and theoretical research investigating the application of Bose-condensed sources to atom interferometer-based inertial sensors. Three key findings are:

- Contrary to the often held view, atom-atom interactions do not limit the applicability of Bose-condensed sources to *free-space* atom interferometers. Our analysis in chapter 9 shows that atom-atom interaction can be made negligible for very reasonable experimental parameters.

- LMT beamsplitters offer a clear path to higher sensitivity, next generation sensors, and Bragg diffraction is a particularly attractive LMT technique. Our theoretical work in chapter 10 shows that the momentum width of the atomic source sets a *fundamental* limit on the Bragg beamsplitter efficiency: the narrower the momentum width, the higher the efficiency. This becomes especially important for very large momentum transfer beamsplitters, and Bose-condensed sources are the obvious choice in this regime.

- By comparing an ultra-cold thermal cloud and a BEC in a gravimeter in chapter 10, we experimentally show how the transverse momentum width of a source has a negative impact on the interferometer signal. Combined with several other well known systematic effects due to the Coriolis force, the narrow momentum width of a BEC is again highly desirable.

The next generation of inertial sensors propose very aggressive sensitivities of up to 1 part in 10^{17} [27], and have extremely demanding technological requirements. The properties of the atomic source used will play a critical role in achieving these goals. Some proposals require beamsplitters which transfer up to $1000\hbar k$ of momentum, and long interrogations times. For example, the group of M. Kasevich is currently setting up a drop-tower for 10 m of free-fall, with the goal of testing the equivalence principle. Current devices such as that of reference [20]

are already significantly impacted by the momentum width of the atomic source. In future devices, the effect of momentum width will clearly play an even more crucial role, and Bose-condensation is the natural progression in attempting to produce narrower and brighter sources.

It is perhaps no longer a question of *"will they be useful?"* But rather, *"when will they be useful, and what is the best way forward?"* It is in this context that the work of chapters 6 and 7 is significant. Our hyperfine-Raman outcoupler produces the highest brightness atom-laser of all possible outcoupling techniques for magnetically confined BECs. Outcoupling from an optical trap results in a near Heisenberg-limited beam. Given that atom-lasers naturally have narrower (transverse) momentum widths than a BEC, pushing the boundaries of atom-laser technology seems a logical path forward. BECs are still limited in flux, and this is an obvious place for improvement. There is no reason which suggests that there is a fundamental limit to the flux of condensed sources, and we are certainly still pursuing the goal of a truly continuous atom-laser following our work on pumping mechanisms [161, 162]. Because most atom interferometers are pulsed devices, this causes a down-sampling of high frequency noise, an effect known as the "Dick effect" [160]. Continuous sources would not only have a desirable momentum width, but would also combat the Dick effect.

Investigations into the application of Bose-condensed sources in inertial sensors should continue, and key areas to focus on in the coming years include:

The production of short duty cycle, large atom number BEC machines. It should be remembered that the SNR only scales with $\sqrt{N}$, so these gains will need to be significant. Very recent work in our group [184] has indicated that a 100 fold improvement in laser power is available by moving to frequency-doubled fibre sources instead of diode-laser-based systems. These incredibly high power photon sources will not only allow the collection and cooling boost needed to achieve a high flux, but will also enable very large momentum transfer based on our theoretical analysis presented in chapter 10 and reference [78]

A significant amount of time should be invested in understanding how to build BEC- and atom-laser-based rotation sensors. It is not yet clear what kind of experimental solution is required to achieve this goal, although it is likely that atom-lasers will be more suited to the gyroscope Mach-Zehnder configuration.

In the case of differential measurements such as gravity gradiometry, equivalence principle tests, and determination of the fine-structure constant, shot-noise limited systems are on the horizon. Intriguing possibilities lie in pursuing

squeezed states in a BEC for these next generation sensors.

An obvious next step is to produce a state-of-the-art gravimeter using a BEC, with a long interrogation time and LMT beamsplitting, and again compare the BEC source to a thermal source in the same system. For example, combining the results of this thesis, we can envision a 10^6 atom/s condensed source being used in a $20\hbar k$ LMT interferometer using our recent 11 W Bragg laser system [184]. With a momentum width of $0.1\,\hbar k$ (see chapter 5), such a source could achieve a fringe contrast of up to 80% (see chapter 10). With demonstrated interrogation times of up to $T = 250\,\mathrm{ms}$ [90], such a system could achieve a shot-noise limited sensitivity of up to $\Delta g/g \sim 10^{-11}/\sqrt{\mathrm{Hz}}$. We are making rapid advances on such a purpose designed BEC-based gravimeter, which is currently at a 1 part in 10^7 sensitivity. Such a system has the potential to open up a new field of precision sensing using laser-like atomic sources.

Appendix A

Piezo-Locking a Diode Laser with Saturated Absorption Spectroscopy

This following article is based on work conducted in 2008 at the Australian National University as part of this thesis. Due to its technical nature, its was omitted from the main text for reasons of continuity.

Piezo-locking a diode laser with saturated absorption spectroscopy

J. E. Debs,[1,*] N. P. Robins,[1] A. Lance,[1] M. B. Kruger,[2] and J. D. Close[1]

[1]Australian Centre of Excellence for Quantum Atom Optics, Department of Physics, The Australian National University, Canberra, 0200, Australia

[2]Department of Physics, University of Missouri-Kansas City, Kansas City, Missouri 64110, USA

*Corresponding author: john.debs@anu.edu.au

Received 18 March 2008; revised 17 August 2008; accepted 22 August 2008; posted 27 August 2008 (Doc. ID 94016); published 25 September 2008

We demonstrate modulation-based frequency locking of an external cavity diode laser, utilizing a piezoelectrically actuated mirror, external to the laser cavity, to create an error signal from saturated absorption spectroscopy. With this method, a laser stabilized to a rubidium hyperfine transition has a FWHM of 130 kHz over seconds, making the locked laser suitable for experiments in atomic physics, such as creating and manipulating Bose–Einstein condensates. This technique combines the advantages of low-amplitude modulation, simplicity, performance, and price, factors that are usually considered to be mutually exclusive.

OCIS codes: 020.1335, 020.1475, 020.3320.

1. Introduction

Saturated absorption spectroscopy is a ubiquitous method of frequency stabilizing laser systems in many areas of atomic physics, such as spectroscopy, atomic clocks, laser cooling, and Bose–Einstein condensation [1]. Several methods for obtaining an error signal from an atomic transition are in use. These generally rely on modulation of either the laser frequency, by varying the laser current or modulation with an acousto-optic modulator (AOM), or by modulating an atomic reference source, and subsequent electronic demodulation to produce the error signal required for locking [2]. Each of the techniques in use has strengths and weaknesses. For example, modulating the laser frequency by directly modulating the current, while simple and inexpensive, suffers because the applied dither is on all of the light [3]: the light used for the experiment, as well as the light used for locking. One can circumvent this weakness by splitting off a portion of the light and sending it through an AOM. Modulating the AOM will cause a frequency modulation only on the portion of the light that is used for locking. While effective, the cost of an AOM and its driving electronics must be included in every laser that is locked directly to an atomic transition, and inherent amplitude modulation also creates an offset on the error signal. Recently, modulation-free differencing techniques have come into use [4–10], whereby an error signal is produced by subtracting two frequency or phase shifted signals generated from the same atomic reference source. Modulation-free schemes have the potential advantage, over more traditional methods, to do away with the need for lock-in electronics and the various modulation apparatus, such as AOMs and magnetic coils. However, modulation-free schemes can be very sensitive to alignment and vibration.

While all of the above-mentioned locking techniques work, producing an error signal which allows a laser to be locked, AOM modulation is one of the most common methods in use, and any alternative scheme for locking a laser can be compared with it. Through phase modulating a laser beam using an external mirror mounted on a piezo-electric transducer (PZT) [11–14], we have made a robust system

0003-6935/08/285163-04$15.00/0

for producing the modulation required for locking; an approach that results in true zero crossing error signals, is simpler to implement than AOM locking and costs at least an order of magnitude less than AOM locking.

2. Phase Modulation

It is well known that light can be phase modulated by reflecting it off a moving mirror [11–14]. For monochromatic radiation phase modulation is equivalent to frequency modulation. This can be seen by considering monochromatic light with an electric field given by $E = E_0 \cos(\omega t)$, where E_0 is the amplitude and ω the frequency of the unmodulated electric field, which is normally reflected off a mirror oscillating with an amplitude A and frequency ω_m. This will result in phase modulation, $(2\pi A/\lambda)\cos(\omega_m t)$. If we let $\delta = 2\pi A/\lambda$, then the resulting phase modulated electric field is

$$E = E_0 \cos(\omega t + \delta \cos \omega_m t). \quad (1)$$

In the limit of small phase modulations the above expression reduces to

$$E \approx E_0 \left[\cos \omega t - \frac{\delta}{2}[\sin(\omega + \omega_m)t + \sin(\omega - \omega_m)t\right], \quad (2)$$

which is the original, unmodulated wave plus two small sidebands $\pm\omega_m$ away from the unmodulated beam and is the same result as obtained by weak frequency modulation.

If phase modulated light passes through an atomic vapor and is then incident upon a photodetector, the resulting signal will be due to the mixing of the three frequencies, the carrier and the two sidebands $(\omega, \omega + \omega_m, \omega - \omega_m)$. The detector signal will be a superposition of the three beat signals, one between the carrier and the upper sideband, one between the carrier and the lower sideband, and one between the two sidebands. When the detector signal is demodulated at the PZT modulation frequency, it is the combination of the beats between the carrier and the sidebands that results in an error signal (other beat frequencies are filtered by the lock-in amplifier). If the carrier is on resonance, for modulation frequencies much less than the natural atomic line width, these beats are of equal strength and cancel, producing no signal at the modulation frequency, while if the carrier moves off resonance, the resulting error signal is due to a difference in the strength of the sidebands after passing through the atomic vapor. The result is an error signal after phase sensitive detection at the modulation frequency. The zero crossing of this signal, in principle, requires no additional electronic offset and is immune to intensity variations in the laser or the optical depth of the medium and, hence, is a true zero crossing error signal.

3. Technique

For frequency stabilizing an external cavity diode laser (ECDL) to an atomic transition, we have used the configuration of Fig. 1. A small portion of the laser light is split off from the main beam going to our experiment. This is phase modulated by a mirror that is attached to a PZT (M1), and then the light is sent to a standard saturated absorption spectrometer. The PZT-mounted mirror can be placed almost anywhere in the setup; however, we recommend positioning it with normal incidence to the light to minimize pointing errors, which can produce some degree of amplitude modulation as a result of the moving mirror. We emphasize that the grating PZT is not involved in phase modulation and that the technique is not specific to ECDLs as shown in our case. After photodetection, the modulated saturated absorption signal is converted to an error signal by using a commercial lock-in amplifier (SRS-510) [15], which demodulates the photodiode signal at the PZT drive frequency to produce the error signal. Typical data are shown in Fig. 2.

For the work that is reported here, the PZTs used are high-voltage (1,000 V) PZTs from Piezomechanik

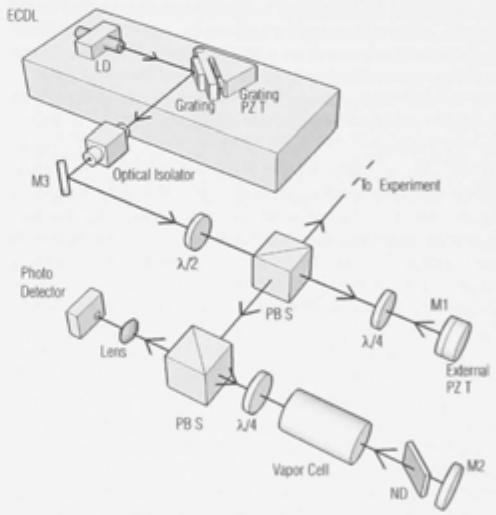

Fig. 1. (Color online) Schematic diagram of one setup used for creating externally phase modulated light for saturated absorption spectroscopy. PBS, polarizing beam splitter; $\lambda/4$, quarter-wave plate; $\lambda/2$, half-wave plate; ND, neutral-density filter; LD, laser diode; M1, M2, and M3, mirrors. For the version shown, both the probe and the pump beams are modulated. Removing the top of the system ($\lambda/4$ and M1) and modulating just the probe beam (placing the external PZT on M2) yields error signals similar to those produced by the above configuration and minimizes the amount of optics devoted to locking. We have included a schematic of the ECDL to emphasize that the grating PZT, shown behind the grating mount cantilever, is not used to produce phase modulated light.

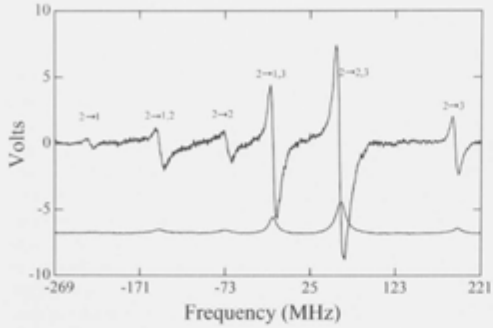

Fig. 2. (Color online) Saturated absorption of the $5^2S_{1/2}F = 2 \rightarrow 5^2P_{3/2}$ transition for ^{87}Rb (lower trace) and the corresponding error signal. The transitions are labeled, $F \rightarrow F'$, and the frequency axis is relative to the D2 transition frequency equivalent to 780.24 nm. For clarity, the saturated absorption signal's Doppler background has been subtracted; it has been offset from zero and multiplied by 20.

[16], ring shaped, with an outer diameter of 2.5 cm to match the diameter of the mirrors. The PZT is attached to a brass mount, and the mirror is attached to the PZT. A thin layer of cyanoacrylate glue is used for bonding the mount, PZT, and mirror together. The brass mount is designed to fit into a standard mirror mount, where it is held in place by a set screw. More secure methods, such as putting threads on the brass and the mirror mount, may be used.

It is well documented that piezoelectric materials display resonant responses when driven at particular frequencies [11–14]. These resonances correspond to a maximum conversion of electrical energy to mechanical energy, and there has been a significant amount of work on characterizing the mechanical and piezoelectric properties, including resonant behavior, of PZT–mount systems by directly measuring PZT displacement as a function of drive frequency by using optical interferometry [11–14]. Two identically mounted PZT–mirrors were tested, and we found that when the PZT is driven by a standard function generator with a sine wave of 8 V peak to peak, there is sufficient modulation, only at particular drive frequencies, to create a useful error signal from the saturated absorption system. We estimate that for sufficient phase modulation to result in a useful error signal the absolute minimum PZT amplitude necessary is of the order of 1–10 Å for a typical rubidium setup, depending on the feedback bandwidth required [17]. Reported mirror displacements are of the order of 1–10 Å or greater [11–13], which is more than sufficient based on our estimate. We therefore infer that these frequencies are the resonant frequencies of our mount–PZT–mirror system, with both identically mounted systems having strong resonances near 30 kHz.

Two ECDLs, one Toptica DL 100 [18] and one built in house, are locked by mirror modulation (at 30 kHz) using this setup. The error signals are symmetric about zero (see Fig. 2), needing no electronic offset to achieve this, and are stable over many hours. At this point, we wish to clarify our use of the term "true zero crossing." The source of an unwanted offset is residual amplitude modulation (AM), and although this is common in most modulation-based techniques, the major source of AM when PZT locking is used comes from possible tilting modes of the piezo crystal (assuming a well-aligned, normally incident laser beam on the modulated mirror). This results in a translation of the focused spot at the photodetector, and we estimate an upper limit of this effect to be of the order of a few micrometers [19]. This value is significantly less than both the photodetector and the focused spot size, and hence any AM due to tilt is negligible, in agreement with our experimental observations. Using the PZT-locking technique, lasers typically remain locked for long periods, as evidenced by the DL 100 readily maintaining a rubidium magneto-optic trap for the production of Bose–Einstein condensates throughout a full day of experiments [20].

Although this simple system is sufficient for low-bandwidth locking, higher modulation frequencies are advantageous for actively narrowing the laser linewidth. Mechanical resonances of a mount–PZT–mirror system of the order of 100 kHz have been previously measured by using interferometry and were attributed to bonding within the mount–PZT system [11,13,14]. Furthermore, commercially available PZTs have rated resonance frequencies for unloaded samples of the order of 100 kHz [16,21].

We have investigated higher resonant frequencies of our mount–PZT–mirror system by mounting the PZT onto a 5 kg stainless steel cylinder bolted directly to our optics table. This ensures maximum displacement of the mirror. The cylinder is 16.5 cm high with a diameter of 7.5 cm. A vertical plane is cut into the side of the cylinder to accommodate the PZT and mirror, which are glued to the mount as before. We find that the PZT mounted in this way is responsive enough to produce an error signal with the same qualities as discussed for Fig. 2 when driven directly by our SRS-510 lock-in amplifier at 100 kHz. We measure a self-beat signal of our locked home-built laser by using a self-heterodyne measurement [22], and we calculate the linewidth assuming a convolution of two Gaussian line shapes. The beat data are shown in Fig. 3. The ECDL is found to have a linewidth of 126.6 kHz for a 20 ms sweep over 100 averages. The data thus represent approximately a 2 s total integration time. In principle, one can construct a system with much higher resonant frequencies, for example, by increasing the effective spring constant with a thinner layer of mounting glue, or by using a glue that has a larger Young's modulus [11,13]. There is then room for exploration into excitation of higher-order resonances if one requires ultrahigh modulation frequencies.

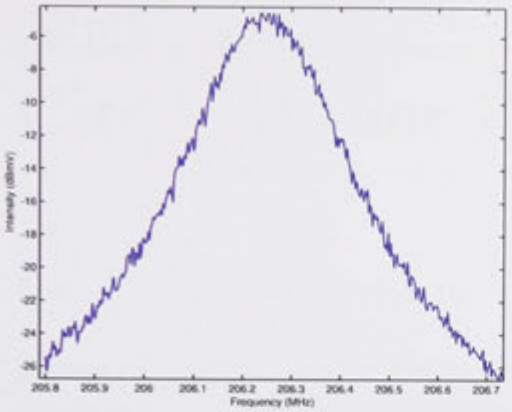

Fig. 3. (Color online) Self-heterodyne beat signal obtained for an ECDL locked to the $5^2S_{1/2}F = 2 \rightarrow 5^2P_{3/2}F = 3$ transition using an error signal produced by a 100 kHz external PZT drive frequency. The beat signal is measured on an RF spectrum analyzer using a 20 ms sweep time averaged over 100 sweeps, and thus represents a 2 s integration time. The linewidth for this integration time is calculated from the beat signal to be 126.6 kHz. A video bandwidth and resolution bandwidth of 10 kHz are used.

4. Conclusion

Phase modulation produced by a PZT-modulated mirror has been demonstrated to be a practical method for locking a diode laser to an atomic transition. It results in a laser with linewidth and stability desirable for experiments in atomic physics (e.g., for maintaining magneto-optic traps and probing Bose–Einstein condensates). Being relatively inexpensive, easy to implement, and robust, it yields true zero crossing error signals, allowing lasers to be locked for many hours at a time. Although demonstrated for an external cavity diode laser here, PZT locking via saturated absorption can be applied to other laser systems as well as other atomic species.

References and Notes

1. W. Demtroder, *Laser Spectroscopy* (Springer-Verlag, 1998).
2. W. Lu, D. Milic, M. D. Hoogerland, M. Jacka, K. G. H. Baldwin, and S. J. Buckman, "A practical direct current discharge helium absorption cell for laser frequency locking at 1083 nm," Rev. Sci. Instrum. **67**, 3003–3004 (1996).
3. We find that even for small modulation depth, the linewidth of an inherently narrow ECDL is broadened by using this technique.
4. K. L. Corwin, Z.-T. Lu, C. F. Hand, R. J. Epstein, and C. E. Wieman, "Frequency-stabilized diode laser with the zeeman shift in an atomic vapor," Appl. Opt. **37**, 3295–3298 (1998).
5. C. I. Sukenik, H. C. Busch, and M. Shiddiq, "Laser frequency stabilization and detuning," Opt. Commun. **203**, 133–137 (2002).
6. S. E. Park, H. S. Lee, T. Y. Kwon, and H. Cho, "Dispersion-like signals in velocity-selective saturated-absorption spectroscopy," Opt. Commun. **192**, 49–55 (2001).
7. N. P. Robins, B. J. J. Slagmolen, D. A. Shaddock, J. D. Close, and M. B. Gray, "Interferometric, modulation-free laser stabilization," Opt. Lett. **27**, 1905–1907 (2002).
8. P. V. der Straten, E. D. V. Ooijen, and G. Katgert, "Laser frequency stabilization using Doppler-free bichromatic spectroscopy," Appl. Phys. B **79**, 57–59 (2004).
9. C. P. Pearman, C. S. Adams, S. G. Cox, P. F. Griffin, D. A. Smith, and I. G. Hughes, "Polarization spectroscopy of a closed atomic transition: applications to laser frequency locking," J. Phys. B **35**, 5141–5151 (2002).
10. Y. Yoshikawa, T. Umeki, T. Mukae, Y. Torii, and T. Kuga, "Frequency stabilization of a laser diode with use of light-induced birefringence in an atomic vapor," Appl. Opt. **42**, 6645–6649 (2003).
11. Q. M. Zhang, W. Y. Pan, and L. E. Cross, "Laser interferometer for the study of piezo electric and electrostrictive strains," J. Appl. Phys. **63**, 2492–2496 (1988).
12. W. Y. Pan and L. E. Cross, "A sensitive double beam laser interferometer for studying high-frequency piezoelectric and electrostrictive strains," Rev. Sci. Instrum. **60**, 2701–2705 (1989).
13. J.-F. Li, P. Moses, and D. Viehland, "Simple, high-resolution interferometer for the measurement of frequency dependent complex piezoelectric responses in ferroelectric ceramics," Rev. Sci. Instrum. **66**, 215–221 (1995).
14. R. Yimnirun, P. J. Moses, R. J. Meyer, Jr., and R. E. Newnham, "A single-beam interferometer with sub-ångström displacement resolution for electrostriction measurements," Meas. Sci. Technol. **14**, 766–772 (2003).
15. See Stanford Research Systems, http://www.thinksrs.com/products/SR510530.htm.
16. See Piezomechanik GmbH, http://piezomechanik.com/f/core/frontend/http/http.php?dl=50-file-1.
17. This estimate is calculated based on a typical saturated absorption signal with 300 μW of power focused onto the photodetector. We assume a Lorenzian absorption profile and use Beer's law with Eq. (2) to calculate a theoretical error signal for a modulation frequency of 100 kHz. The absolute lower limit of 1 Å is based on a feedback bandwidth of 200 Hz, a value that is typical for two of our three BEC lasers, whereas a value of 10 Å is the lower limit required for a feedback bandwidth of 20 kHz. Both of these values result in a signal-to-noise ratio of approximately 5 relative to the shot noise, leading to theoretical stability in the lock point of 200 kHz in the laser output frequency.
18. Diode laser purchased from TOPTICA Photonics AG, Model DL 100; see http://www.toptica.com/page/scientific_lasers.php.
19. This value is based on a 50 mm focal length for the lens in Fig. 1and a tilt angle of 50 μrad, calculated assuming a 200 nm arclength due to the tilt. We feel this estimate of arclength is a more than generous number, given the previously measured piezo displacements referenced in the paper.
20. N. P. Robins, C. Figl, M. Jeppesen, G. R. Dennis, and J. D. Close., "A pumped atom laser," Nat. Phys. **4**, 731–736 (2008).
21. See Noliac, http://www.noliac.com/Ring_actuators_-56.aspx.
22. The self-heterodyne beat measurement uses an AOM to scatter a portion of the laser beam into the first order, producing a frequency-shifted beam (~200 MHz for our AOM). The unscattered zeroth order is then launched into a single-mode optical fiber before being mixed with the first order on a beam splitter. The length of the fiber should be significantly longer than the coherence length of the laser, rendering the zeroth-order beam incoherent relative to the first order. Upon mixing the two beams, a beat signal is obtained at the AOM drive frequency, and as long as the two beams are sufficiently incoherent, this results in a reliable measurement of the laser linewidth without the need for locking two identical lasers. Note that a laser with a 100 kHz linewidth has a coherence length of about 2 km, which is significantly shorter than the 3 km of fiber used in our setup.

Cited Author Index

List of cited authors and their respective citation numbers in the bibliography.

Bibliography

[1] Stuckeley, W. *Memoirs of Sir Isaac Newton's Life* (The Royal Society, 1752). URL http://royalsociety.org/library/moments/newton-apple/. Cited on page 1.

[2] The LIGO Scientific Collaboration & The Virgo Collaboration. All-sky search for periodic gravitational waves in the full S5 LIGO data. *Phys. Rev. D* **85**, 022001 (2012). URL http://link.aps.org/doi/10.1103/PhysRevD.85.022001. Cited on page 1.

[3] Le Système international d'unités. Tech. Rep., Bureau international des poids et mesures (2006). URL http://www.bipm.org/utils/common/pdf/si_brochure_8_fr.pdf. Cited on pages 2 and 25.

[4] Heavner, T. P., Jefferts, S. R., Donley, E. A., Shirley, J. H. & Parker, T. E. NIST-F1: recent improvements and accuracy evaluations. *Metrologia* **42**, 411 (2005). URL http://stacks.iop.org/0026-1394/42/i=5/a=012. Cited on page 2.

[5] Bize, S. *et al.* Cold atom clocks and applications. *Journal of Physics B: Atomic, Molecular and Optical Physics* **38**, S449 (2005). URL http://stacks.iop.org/0953-4075/38/i=9/a=002. Cited on page 2.

[6] Kasevich, M. A. & Chu, S. Atomic interferometry using stimulated Raman transitions. *Phys. Rev. Lett.* **67**, 181–184 (1991). Cited on pages 2 and 77.

[7] Kasevich, M. A. & Chu, S. Measurement of the gravitational acceleration of an atom with a light-pulse atom interferometer. *Applied Physics B: Lasers and Optics* **54**, 321–332 (1992). URL http://dx.doi.org/10.1007/BF00325375. 10.1007/BF00325375. Cited on pages 2, 77, and 137.

[8] Peters, A., Chung, K.-Y. & Chu, S. High-precision gravity measurements using atom interferometry. *Metrologia* **38**, 25 (2001). URL http://stacks.iop.org/0026-1394/38/i=1/a=4. Cited on pages 2, 8, 131, 137, and 138.

[9] Le Gouët, J. *et al.* Limits to the sensitivity of a low noise compact atomic gravimeter. *Applied Physics B: Lasers and Optics* **92**, 133–144 (2008). URL http://dx.doi.org/10.1007/s00340-008-3088-1. Cited on pages 2, 6, 131, and 163.

[10] Müller, H., Chiow, S. W., Herrmann, S., Chu, S. & Chung, K.-Y. Atom-Interferometry Tests of the Isotropy of Post-Newtonian Gravity. *Phys. Rev. Lett.* **100**, 031101 (2008). URL http://dx.doi.org/10.1103/PhysRevLett.100.031101. Cited on pages 2, 6, 38, 61, 68, 69, 119, 120, and 142.

[11] Bodart, Q. *et al.* A cold atom pyramidal gravimeter with a single laser beam. *Applied Physics Letters* **96**, 134101 (2010). URL http://link.aip.org/link/?APL/96/134101/1. Cited on page 2.

[12] McGuirk, J. M., Foster, G. T., Fixler, J. B., Snadden, M. J. & Kasevich, M. A. Sensitive absolute-gravity gradiometry using atom interferometry. *Phys. Rev. A* **65**, 033608 (2002). URL http://dx.doi.org/10.1103/PhysRevA.65.033608. Cited on page 2.

[13] Lamporesi, G., Bertoldi, A., Cacciapuoti, L., Prevedelli, M. & Tino, G. M. Determination of the Newtonian Gravitational Constant Using Atom Interferometry. *Phys. Rev. Lett.* **100**, 050801 (2008). URL http://link.aps.org/abstract/PRL/v100/e050801. Cited on page 2.

[14] Gustavson, T. L., Landragin, A. & Kasevich, M. A. Rotation sensing with a dual atom-interferometer Sagnac gyroscope. *Classical and Quantum Gravity* **17**, 2385–2398 (2000). URL http://stacks.iop.org/0264-9381/17/2385. Cited on pages 2, 38, and 119.

[15] Canuel, B. *et al.* Six-Axis Inertial Sensor Using Cold-Atom Interferometry. *Phys. Rev. Lett.* **97**, 010402 (2006). URL http://link.aps.org/abstract/PRL/v97/e010402. Cited on pages 2 and 38.

[16] Müller, T. *et al.* A compact dual atom interferometer gyroscope based on laser-cooled rubidium. *Eur. Phys. J. D* **53**, 273–281 (2009). URL http://dx.doi.org/10.1140/epjd/e2009-00139-0. Cited on pages 2 and 38.

[17] Stockton, J. K., Takase, K. & Kasevich, M. A. Absolute Geodetic Rotation Measurement Using Atom Interferometry. *Phys. Rev. Lett.* **107**,

133001 (2011). URL http://link.aps.org/doi/10.1103/PhysRevLett.107.133001. Cited on pages 2 and 38.

[18] Weiss, D. S., Young, B. C. & Chu, S. Precision measurement of $\hbar/m_{Cs}$ based on photon recoil using laser-cooled atoms and atomic interferometry. *Applied Physics B: Lasers and Optics* **59**, 217–256 (1994). URL http://dx.doi.org/10.1007/BF01081393. 10.1007/BF01081393. Cited on pages 2 and 40.

[19] Müller, H., Chiow, S. W., Long, Q., Vo, C. & Chu, S. A new photon recoil experiment: towards a determination of the fine structure constant. *Applied Physics B: Lasers and Optics* **84**, 633–642 (2006). URL http://dx.doi.org/10.1007/s00340-006-2279-x. Cited on pages 2 and 40.

[20] Bouchendira, R., Cladé, P., Guellati-Khélifa, S., Nez, F. & Biraben, F. New Determination of the Fine Structure Constant and Test of the Quantum Electrodynamics. *Phys. Rev. Lett.* **106**, 080801 (2011). URL http://link.aps.org/doi/10.1103/PhysRevLett.106.080801. Cited on pages 2, 7, 8, 40, and 169.

[21] Fixler, J. B., Foster, G. T., McGuirk, J. M. & Kasevich, M. A. Atom Interferometer Measurement of the Newtonian Constant of Gravity. *Science* **315**, 74–77 (2007/1/5). URL http://www.sciencemag.org/cgi/content/abstract/315/5808/74. Cited on page 2.

[22] Hanneke, D., Fogwell, S. & Gabrielse, G. New Measurement of the Electron Magnetic Moment and the Fine Structure Constant. *Phys. Rev. Lett.* **100**, 120801 (2008). URL http://link.aps.org/doi/10.1103/PhysRevLett.100.120801. Cited on page 2.

[23] Leblanc, M. J., Tregoning, P., Ramillien, G., Tweed, S. O. & Fakes, A. Basin-scale, integrated observations of the early 21st century multiyear drought in southeast Australia. *Water Resour. Res.* **45** (2009). URL http://dx.doi.org/10.1029/2008WR007333. Cited on page 2.

[24] Damour, T. Testing the equivalence principle: why and how? *Classical and Quantum Gravity* **13**, A33 (1996). URL http://stacks.iop.org/0264-9381/13/i=11A/a=005. Cited on page 3.

[25] Su, Y. *et al.* New tests of the universality of free fall. *Phys. Rev. D* **50**,

3614–3636 (1994). URL http://link.aps.org/doi/10.1103/PhysRevD.50.3614. Cited on page 3.

[26] Dickey, J. O. *et al.* Lunar Laser Ranging: A Continuing Legacy of the Apollo Program. *Science* **265**, 482–490 (1994). URL http://www.sciencemag.org/content/265/5171/482.abstract. http://www.sciencemag.org/content/265/5171/482.full.pdf. Cited on page 3.

[27] Dimopoulos, S., Graham, P. W., Hogan, J. M. & Kasevich, M. A. Testing General Relativity with Atom Interferometry. *Phys. Rev. Lett.* **98**, 111102 (2007). URL http://link.aps.org/doi/10.1103/PhysRevLett.98.111102. Cited on pages 3 and 169.

[28] Dimopoulos, S., Graham, P. W., Hogan, J. M., Kasevich, M. A. & Rajendran, S. Atomic gravitational wave interferometric sensor. *Phys. Rev. D* **78**, 122002 (2008). URL http://link.aps.org/abstract/PRD/v78/e122002. Cited on pages 3, 7, 120, and 158.

[29] Hogan, J. M. *et al.* An atomic gravitational wave interferometric sensor in low earth orbit (AGIS-LEO). *General Relativity and Gravitation* **43**, 1953–2009 (2011). URL http://dx.doi.org/10.1007/s10714-011-1182-x. Cited on page 3.

[30] Müller, H., Peters, A. & Chu, S. A precision measurement of the gravitational redshift by the interference of matter waves. *Nature* **463**, 926–929 (2010). URL http://dx.doi.org/10.1038/nature08776. Cited on page 3.

[31] Hohensee, M. A., Chu, S., Peters, A. & Müller, H. Equivalence Principle and Gravitational Redshift. *Phys. Rev. Lett.* **106**, 151102 (2011). URL http://link.aps.org/doi/10.1103/PhysRevLett.106.151102. Cited on page 3.

[32] Hohensee, M. A. *et al.* Gravitational redshift, equivalence principle, and matter waves. *Journal of Physics: Conference Series* **264**, 012009 (2011). URL http://stacks.iop.org/1742-6596/264/i=1/a=012009. Cited on page 3.

[33] Poli, N. *et al.* Precision Measurement of Gravity with Cold Atoms in an Optical Lattice and Comparison with a Classical Gravimeter. *Phys.*

Rev. Lett. **106**, 038501 (2011). URL http://link.aps.org/doi/10.1103/PhysRevLett.106.038501. Cited on pages 3 and 137.

[34] Wolf, P. *et al.* Does an atom interferometer test the gravitational redshift at the Compton frequency? *Classical and Quantum Gravity* **28**, 145017 (2011). URL http://stacks.iop.org/0264-9381/28/i=14/a=145017. Cited on page 3.

[35] Müller, H., Peters, A. & Chu, S. Muller, Peters & Chu reply. *Nature* **467**, E2–E2 (2010). URL http://dx.doi.org/10.1038/nature09341. Cited on page 3.

[36] Wolf, P. *et al.* Atom gravimeters and gravitational redshift. *Nature* **467**, E1–E1 (2010). URL http://dx.doi.org/10.1038/nature09340. Cited on page 3.

[37] Hohensee, M. A., Chu, S., Peters, A. & Müller, H. Comment on: "Does an atom interferometer test the gravitational redshift at the Compton frequency?". *ArXiv e-prints* (2011). URL http://arxiv.org/abs/1112.6039. 1112.6039. Cited on page 3.

[38] Wolf, P. *et al.* Reply to the comment on: "Does an atom interferometer test the gravitational redshift at the Compton frequency?". *ArXiv e-prints* (2012). URL http://arxiv.org/abs/1201.1778. 1201.1778. Cited on page 3.

[39] Geneves, G. *et al.* The BNM Watt balance project. *Instrumentation and Measurement, IEEE Transactions on* **54**, 850 – 853 (2005). URL http://dx.doi.org/10.1109/TIM.2005.843576. Cited on page 3.

[40] Geneves, G. *et al.* The e-Mass euramet joint research project: The watt balance route towards a new definition of the kilogram. In *Precision Electromagnetic Measurements (CPEM), 2010 Conference on*, 520 –521 (2010). URL http://dx.doi.org/10.1109/CPEM.2010.5543654. Cited on page 3.

[41] Chu, S. Nobel Lecture: The manipulation of neutral particles. *Rev. Mod. Phys.* **70**, 685–706 (1998). URL http://link.aps.org/doi/10.1103/RevModPhys.70.685. Cited on pages 5 and 70.

[42] Cohen-Tannoudji, C. Nobel Lecture: Manipulating atoms with photons. *Rev. Mod. Phys.* **70**, 707–719 (1998). URL http://link.aps.org/doi/10.1103/RevModPhys.70.707. Cited on pages 5 and 70.

[43] Phillips, W. D. Nobel Lecture: Laser cooling and trapping of neutral atoms. *Rev. Mod. Phys.* **70**, 721–741 (1998). URL http://link.aps.org/doi/10.1103/RevModPhys.70.721. Cited on pages 5 and 70.

[44] Anderson, M. H., Ensher, J. R., Matthews, M. R., Wieman, C. E. & Cornell, E. A. Observation of Bose-Einstein Condensation in a Dilute Atomic Vapor. *Science* **269**, 198–201 (1995). URL http://www.sciencemag.org/content/269/5221/198.abstract. Cited on pages 5 and 53.

[45] Davis, K. B. *et al.* Bose-Einstein Condensation in a Gas of Sodium Atoms. *Phys. Rev. Lett.* **75**, 3969–3973 (1995). URL http://dx.doi.org/10.1103/PhysRevLett.75.3969. Cited on pages 5 and 53.

[46] Bose, S. N. Plancks Gesetz und Lichtquantenhypothese. *Z. Phys.* **26**, 178–181 (1924). URL http://dx.doi.org/10.1007/BF01327326. 10.1007/BF01327326. Cited on pages 5 and 54.

[47] Einstein, A. *Sitzber. Kgl. Preuss. Akad. Wiss.* 261 (1924). Cited on pages 5 and 54.

[48] Einstein, A. Quantentheorie des einatomigen idealen Gases. *Sitzber. Kgl. Preuss. Akad. Wiss.* 3 (1925). Cited on pages 5 and 54.

[49] Mewes, M.-O. *et al.* Output Coupler for Bose-Einstein Condensed Atoms. *Phys. Rev. Lett.* **78**, 582–585 (1997). URL http://dx.doi.org/10.1103/PhysRevLett.78.582. Cited on pages 5, 62, and 63.

[50] Hagley, E. W. *et al.* A Well-Collimated Quasi-Continuous Atom Laser. *Science* **283**, 1706–1709 (1999). URL http://www.sciencemag.org/cgi/content/abstract/283/5408/1706. http://www.sciencemag.org/cgi/reprint/283/5408/1706.pdf. Cited on pages 5 and 63.

[51] Bloch, I., Hänsch, T. W. & Esslinger, T. Atom Laser with a cw Output Coupler. *Phys. Rev. Lett.* **82**, 3008–3011 (1999). URL http://dx.doi.org/10.1103/PhysRevLett.82.3008. Cited on pages 5 and 62.

[52] Le Coq, Y. *et al.* Atom Laser Divergence. *Phys. Rev. Lett.* **87**, 170403 (2001). URL http://prl.aps.org/abstract/PRL/v87/i17/e170403. Cited on pages 5 and 66.

[53] Cennini, G., Ritt, G., Geckeler, C. & Weitz, M. All-Optical Realization of an Atom Laser. *Phys. Rev. Lett.* **91**, 240408 (2003). URL http://link.aps.org/doi/10.1103/PhysRevLett.91.240408. Cited on pages 5 and 115.

[54] Robins, N. P. *et al.* Achieving Peak Brightness in an Atom Laser. *Phys. Rev. Lett.* **96**, 140403 (2006). URL http://link.aps.org/abstract/PRL/v96/e140403. Cited on pages 5, 66, 90, 104, and 109.

[55] Debs, J. E. *et al.* A two-state Raman coupler for coherent atom optics. *Opt. Express* **17**, 2319–2325 (2009). URL http://www.opticsexpress.org/abstract.cfm?URI=oe-17-4-2319. Cited on pages 5, 77, and 78.

[56] Öttl, A., Ritter, S., Köhl, M. & Esslinger, T. Correlations and Counting Statistics of an Atom Laser. *Phys. Rev. Lett.* **95**, 090404 (2005). URL http://link.aps.org/abstract/PRL/v95/e090404. Cited on pages 5 and 62.

[57] Stenger, J. *et al.* Bragg Spectroscopy of a Bose-Einstein Condensate. *Phys. Rev. Lett.* **82**, 4569–4573 (1999). URL http://dx.doi.org/10.1103/PhysRevLett.82.4569. Cited on pages 6, 57, and 60.

[58] Anderson, R. P. *Nonequilibrium dynamics and relative phase evolution of two-component Bose-Einstein condensates.* Ph.D. thesis, Swinburne University (2010). URL http://tiny.cc/RussellAndersonPhD. Cited on page 6.

[59] Altin, P. A. *et al.* Optically trapped atom interferometry using the clock transition of large ^{87}Rb Bose-Einstein condensates (Addendum). *New Journal of Physics* **13**, 119401 (2011). URL http://stacks.iop.org/1367-2630/13/i=11/a=119401. Cited on page 6.

[60] Egorov, M. *et al.* Long-lived periodic revivals of coherence in an interacting Bose-Einstein condensate. *Phys. Rev. A* **84**, 021605 (2011). URL http://link.aps.org/doi/10.1103/PhysRevA.84.021605. Cited on page 6.

[61] Castin, Y. & Dalibard, J. Relative phase of two Bose-Einstein condensates. *Phys. Rev. A* **55**, 4330–4337 (1997). URL http://link.aps.org/doi/10.1103/PhysRevA.55.4330. Cited on pages 6, 54, 137, and 141.

[62] Widera, A. *et al.* Quantum Spin Dynamics of Mode-Squeezed Luttinger Liquids in Two-Component Atomic Gases. *Phys. Rev. Lett.* **100**,

140401 (2008). URL http://link.aps.org/doi/10.1103/PhysRevLett.100.140401. Cited on page 6.

[63] Debs, J. E. *et al.* Cold-atom gravimetry with a Bose-Einstein condensate. *Phys. Rev. A* **84**, 033610 (2011). URL http://link.aps.org/doi/10.1103/PhysRevA.84.033610. Cited on pages 6, 7, 8, 127, and 137.

[64] Jamison, A. O., Kutz, J. N. & Gupta, S. Atomic interactions in precision interferometry using Bose-Einstein condensates. *Phys. Rev. A* **84**, 043643 (2011). URL http://link.aps.org/doi/10.1103/PhysRevA.84.043643. Cited on pages 6 and 143.

[65] Johnsson, M. T. & Haine, S. A. Generating Quadrature Squeezing in an Atom Laser through Self-Interaction. *Phys. Rev. Lett.* **99**, 010401 (2007). URL http://dx.doi.org/10.1103/PhysRevLett.99.010401. Cited on page 6.

[66] Esteve, J., Gross, C., Weller, A., Giovanazzi, S. & Oberthaler, M. Squeezing and entanglement in a Bose-Einstein condensate. *Nature* **455**, 1216–1219 (2008). URL http://dx.doi.org/10.1038/nature07332. Cited on page 6.

[67] Windpassinger, P. J. *et al.* Nondestructive Probing of Rabi Oscillations on the Cesium Clock Transition near the Standard Quantum Limit. *Phys. Rev. Lett.* **100**, 103601 (2008). URL http://link.aps.org/abstract/PRL/v100/e103601. Cited on page 6.

[68] Li, Y., Castin, Y. & Sinatra, A. Optimum Spin Squeezing in Bose-Einstein Condensates with Particle Losses. *Phys. Rev. Lett.* **100**, 210401 (2008). URL http://dx.doi.org/10.1103/PhysRevLett.100.210401. Cited on page 6.

[69] Haine, S. A. & Johnsson, M. T. Dynamic scheme for generating number squeezing in Bose-Einstein condensates through nonlinear interactions. *Phys. Rev. A* **80**, 023611 (2009). URL http://dx.doi.org/10.1103/PhysRevA.80.023611. Cited on pages 6 and 141.

[70] Bohi, P. *et al.* Coherent manipulation of Bose-Einstein condensates with state-dependent microwave potentials on an atom chip. *Nature Phys.* **5**, 592–597 (2009). URL http://dx.doi.org/10.1038/nphys1329. Cited on page 6.

[71] Louchet-Chauvet, A. *et al.* Entanglement-assisted atomic clock beyond the projection noise limit. *New Journal of Physics* **12**, 065032 (2010). URL http://stacks.iop.org/1367-2630/12/i=6/a=065032. Cited on page 6.

[72] Gross, C., Zibold, T., Nicklas, E., Esteve, J. & Oberthaler, M. Nonlinear atom interferometer surpasses classical precision limit. *Nature* **464**, 1164–1169 (2010). URL http://dx.doi.org/10.1038/nature08919. Cited on pages 6 and 141.

[73] Riedel, M. F. *et al.* Atom-chip-based generation of entanglement for quantum metrology. *Nature* **464**, 1170–1173 (2010). URL http://dx.doi.org/10.1038/nature08988. Cited on pages 6 and 141.

[74] Lücke, B. *et al.* Twin Matter Waves for Interferometry Beyond the Classical Limit. *Science* **334**, 773–776 (2011). URL http://www.sciencemag.org/content/334/6057/773.abstract. http://www.sciencemag.org/content/334/6057/773.full.pdf. Cited on page 6.

[75] Haine, S. A. & Ferris, A. J. Surpassing the standard quantum limit in an atom interferometer with four-mode entanglement produced from four-wave mixing. *Phys. Rev. A* **84**, 043624 (2011). URL http://link.aps.org/doi/10.1103/PhysRevA.84.043624. Cited on page 6.

[76] Altin, P. A. *et al.* Optically trapped atom interferometry using the clock transition of large ^{87}Rb Bose-Einstein condensates. *New J. of Phys.* **13**, 065020 (2011). URL http://stacks.iop.org/1367-2630/13/i=6/a=065020. Cited on page 6.

[77] van der Stam, K. M. R., van Ooijen, E. D., Meppelink, R., Vogels, J. M. & van der Straten, P. Large atom number Bose-Einstein condensate of sodium. *Rev. Sci. Instrum.* **78**, 013102 (2007). URL http://link.aip.org/link/?RSI/78/013102/1. Cited on pages 6, 69, and 119.

[78] Szigeti, S. S., Debs, J. E., Hope, J. J., Robins, N. P. & Close, J. D. Why momentum width matters for atom interferometry with Bragg pulses. *New Journal of Physics* **14**, 023009 (2012). URL http://stacks.iop.org/1367-2630/14/i=2/a=023009. Cited on pages 7, 61, 132, 138, 149, 150, 152, 155, 156, 157, 159, 160, and 170.

[79] Müller, H., Chiow, S. W., Herrmann, S. & Chu, S. Atom Interferometers with Scalable Enclosed Area. *Phys. Rev. Lett.* **102**, 240403 (2009). URL http://dx.doi.org/10.1103/PhysRevLett.102.240403. Cited on pages 7, 137, 144, and 147.

[80] Martin, P. J., Oldaker, B. G., Miklich, A. & Pritchard, D. E. Bragg scattering of atoms from a standing light wave. *Phys. Rev. Lett.* **60**, 515–518 (1988). URL http://dx.doi.org/10.1103/PhysRevLett.60.515. Cited on pages 7 and 121.

[81] Giltner, D. M., McGowan, R. W. & Lee, S. A. Atom Interferometer Based on Bragg Scattering from Standing Light Waves. *Phys. Rev. Lett.* **75**, 2638–2641 (1995). URL http://dx.doi.org/10.1103/PhysRevLett.75.2638. Cited on pages 7 and 138.

[82] Stenger, J. *et al.* Bragg spectroscopy and superradiant Rayleigh scattering in a Bose–Einstein condensate. *Applied Physics B: Lasers and Optics* **69**, 347–352 (1999). URL http://dx.doi.org/10.1007/s003400050818. 10.1007/s003400050818. Cited on page 7.

[83] Kozuma, M. *et al.* Coherent Splitting of Bose-Einstein Condensed Atoms with Optically Induced Bragg Diffraction. *Phys. Rev. Lett.* **82**, 871–875 (1999). URL http://dx.doi.org/10.1103/PhysRevLett.82.871. Cited on pages 7, 60, and 138.

[84] Torii, Y. *et al.* Mach-Zehnder Bragg interferometer for a Bose-Einstein condensate. *Phys. Rev. A* **61**, 041602 (2000). Cited on page 7.

[85] Müller, H., Chiow, S. W., Long, Q., Herrmann, S. & Chu, S. Atom Interferometry with up to 24-Photon-Momentum-Transfer Beam Splitters. *Phys. Rev. Lett.* **100**, 180405 (2008). URL http://link.aps.org/abstract/PRL/v100/e180405. Cited on pages 7, 40, 120, 137, 138, 157, and 158.

[86] Benton, B., Krygier, M., Heward, J., Edwards, M. & Clark, C. W. Prototyping method for Bragg-type atom interferometers. *Phys. Rev. A* **84**, 043648 (2011). URL http://link.aps.org/doi/10.1103/PhysRevA.84.043648. Cited on page 7.

[87] Chiow, S. W., Kovachy, T., Chien, H.-C. & Kasevich, M. A. $102\hbar k$ Large Area Atom Interferometers. *Phys. Rev. Lett.* **107**, 130403 (2011). URL

http://link.aps.org/doi/10.1103/PhysRevLett.107.130403. Cited on pages 7, 8, and 158.

[88] Fils, J. *et al.* Influence of optical aberrations in an atomic gyroscope. *The European Physical Journal D-Atomic, Molecular and Optical Physics* **36**, 257–260 (2005). URL http://dx.doi.org/10.1140/epjd/e2005-00255-9. Cited on pages 7, 8, 140, and 163.

[89] Louchet-Chauvet, A. *et al.* The influence of transverse motion within an atomic gravimeter. *New J. of Phys.* **13**, 065025 (2011). URL http://stacks.iop.org/1367-2630/13/i=6/a=065025. Cited on pages 7, 8, 140, 163, and 164.

[90] Lan, S.-Y., Kuan, P.-C., Estey, B., Haslinger, P. & Müller, H. Influence of the Coriolis Force in Atom Interferometry. *Phys. Rev. Lett.* **108**, 090402 (2012). URL http://link.aps.org/doi/10.1103/PhysRevLett.108.090402. Cited on pages 8, 165, 167, and 171.

[91] Cladé, P. (2011). Private communication. Cited on page 8.

[92] Griffith, W. C. *et al.* Improved Limit on the Permanent Electric Dipole Moment of ^{199}Hg. *Phys. Rev. Lett.* **102**, 101601 (2009). URL http://prl.aps.org/abstract/PRL/v102/i10/e101601. Cited on page 16.

[93] Porsev, S. G., Ginges, J. S. M. & Flambaum, V. V. Atomic electric dipole moment induced by the nuclear electric dipole moment: The magnetic moment effect. *Phys. Rev. A* **83**, 042507 (2011). URL http://pra.aps.org/abstract/PRA/v83/i4/e042507. Cited on page 16.

[94] Shankar, R. *Principles of Quantum Mechanics* (Plenum Press, New York, 1994), 2nd edn. Cited on pages 17, 22, and 108.

[95] Cohen-Tannoudji, C., Dupont-Roc, J. & Grynberg, G. *Atom-Photon Interactions: Basic Processes and Applications* (John Wiley & Sons, Inc., 1992). Cited on pages 18, 21, and 34.

[96] Foot, C. J. *Atomic Physics* (Oxford University Press, 2005). Cited on pages 19, 23, 25, 31, and 51.

[97] Grimm, R., Weidemüller, M., Ovchinnikov, Y. B., Bederson, B. & Walther, H. Optical Dipole Traps for Neutral Atoms **42**, 95–170

(2000). URL http://www.sciencedirect.com/science/article/pii/S1049250X0860186X. Cited on pages 22, 69, and 76.

[98] Rabi, I. I., Zacharias, J. R., Millman, S. & Kusch, P. A New Method of Measuring Nuclear Magnetic Moment. *Phys. Rev.* **53**, 318 (1938). URL http://dx.doi.org/10.1103/PhysRev.53.318. Cited on page 23.

[99] Loudon, R. *The Quantum Theory of Light* (Oxford Science Publications, 2000), 3rd edn. Cited on page 25.

[100] Steck, D. A. Rubidium 87 D Line Data (2010). URL http://steck.us/alkalidata/rubidium87numbers.pdf. Cited on pages 25, 41, 51, 69, and 79.

[101] Ramsey, N. F. A New Molecular Beam Resonance Method. *Phys. Rev.* **76**, 996 (1949). URL http://dx.doi.org/10.1103/PhysRev.76.996. Cited on page 28.

[102] Ramsey, N. F. A Molecular Beam Resonance Method with Separated Oscillating Fields. *Phys. Rev.* **78**, 695–699 (1950). URL http://dx.doi.org/10.1103/PhysRev.78.695. Cited on page 28.

[103] Ramsey, N. F. The Nobel Prize in Physics 1989. URL http://nobelprize.org/nobel_prizes/physics/laureates/1989/. Cited on page 28.

[104] Deutsch, C. *et al.* Spin Self-Rephasing and Very Long Coherence Times in a Trapped Atomic Ensemble. *Phys. Rev. Lett.* **105**, 020401 (2010). URL http://dx.doi.org/10.1103/PhysRevLett.105.020401. Cited on page 34.

[105] Döring, D. *et al.* Quantum-projection-noise-limited interferometry with coherent atoms in a Ramsey-type setup. *Phys. Rev. A* **81**, 043633 (2010). URL http://dx.doi.org/10.1103/PhysRevA.81.043633. Cited on pages 37, 77, 78, 92, 94, 98, and 100.

[106] Rothleitner, C., Svitlov, S., Mérimèche, H., Hu, H. & Wang, L. J. Development of new free-fall absolute gravimeters. *Metrologia* **46**, 283 (2009). URL http://stacks.iop.org/0026-1394/46/i=3/a=017. Cited on page 37.

[107] Goldstein, H. *Classical Mechanics* (Addison-Wesley Publishing Company, 1980), 2nd edn. Cited on page 38.

[108] Bongs, K., Launay, R. & Kasevich, M. A. High-order inertial phase shifts for time-domain atom interferometers. *Applied Physics B: Lasers and Optics* **84**, 599–602 (2006). URL http://dx.doi.org/10.1007/s00340-006-2397-5. 10.1007/s00340-006-2397-5. Cited on pages 38 and 40.

[109] Storey, P. & Cohen-Tannoudji, C. The Feynman path integral approach to atomic interferometry. A tutorial. *J. Phys. II France* **4**, 1999–2027 (1999). URL http://dx.doi.org/10.1051/jp2:1994103. Cited on page 39.

[110] Bordé, C. J. Atomic interferometry with internal state labelling. *Physics Letters A* **140**, 10 – 12 (1989). URL http://www.sciencedirect.com/science/article/pii/0375960189905379. Cited on page 40.

[111] Rasel, E. M., Oberthaler, M., Batelaan, H., Schmiedmayer, J. & Zeilinger, A. Atom Wave Interferometry with Diffraction Gratings of Light. *Phys. Rev. Lett.* **75**, 2633–2637 (1995). Cited on pages 40 and 122.

[112] Robert-de-Saint-Vincent, M. *et al.* A quantum trampoline for ultra-cold atoms. *EPL (Europhysics Letters)* **89**, 10002 (2010). URL http://stacks.iop.org/0295-5075/89/i=1/a=10002. Cited on page 40.

[113] Cronin, A. D., Schmiedmayer, J. & Pritchard, D. E. Optics and interferometry with atoms and molecules. *Rev. Mod. Phys.* **81**, 1051–1129 (2009). URL http://dx.doi.org/10.1103/RevModPhys.81.1051. Cited on page 40.

[114] Meystre, P. *Atom Optics* (Springer-Verlag New York, Inc., 2001). Cited on pages 45, 122, and 152.

[115] Chabé, J., Lignier, H., Szriftgiser, P. & Garreau, J. C. Improving Raman velocimetry of laser-cooled cesium atoms by spin-polarization. *Optics Communications* **274**, 254 – 259 (2007). URL http://www.sciencedirect.com/science/article/pii/S0030401807001514. Cited on page 47.

[116] Kasevich, M. A. *et al.* Atomic velocity selection using stimulated Raman transitions. *Phys. Rev. Lett.* **66**, 2297–2300 (1991). URL http://link.aps.org/doi/10.1103/PhysRevLett.66.2297. Cited on page 47.

[117] Hosseini, M., Campbell, G., Sparkes, B. M., Lam, P. K. & Buchler, B. C. Unconditional room-temperature quantum memory. *Nat Phys* **7**, 794–798

(2011). URL http://dx.doi.org/10.1038/nphys2021. Cited on page 47.

[118] Ketterle, W., Durfee, D. S. & Stamper-Kurn, D. M. Making, probing and understanding Bose-Einstein condensates. In Inguscio, M., Stringari, S. & Wieman, C. E. (eds.) *Bose-Einstein Condesates in Atomic Gases, Proceedings of the International School of Physics "Enrico Fermi"*, 67–176 (IOS Press, Amsterdam, 1999). URL http://www.citebase.org/abstract?id=oai:arXiv.org:cond-mat/9904034. Cited on pages 53 and 73.

[119] Dalfovo, F., Giorgini, S., Pitaevskii, L. P. & Stringari, S. Theory of Bose-Einstein condensation in trapped gases. *Rev. Mod. Phys.* **71**, 463–512 (1999). URL http://dx.doi.org/10.1103/RevModPhys.71.463. Cited on pages 53, 55, and 59.

[120] Pitaevskii, L. P. Vortex Lines in an Imperfect Bose Gas. *Soviet Physics JETP-USSR* **13** (1961). Cited on page 53.

[121] Gross, E. Structure of a quantized vortex in boson systems. *Il Nuovo Cimento (1955-1965)* **20**, 454–477 (1961). URL http://dx.doi.org/10.1007/BF02731494. 10.1007/BF02731494. Cited on page 53.

[122] Bogoliubov, N. N. On the Theory of Superfluidity. *J. Phys. (Moscow)* **11**, 23–32 (1947). Cited on page 55.

[123] Baym, G. & Pethick, C. J. Ground-State Properties of Magnetically Trapped Bose-Condensed Rubidium Gas. *Phys. Rev. Lett.* **76**, 6–9 (1996). URL http://link.aps.org/doi/10.1103/PhysRevLett.76.6. Cited on page 57.

[124] Claussen, N. R. *et al.* Very-high-precision bound-state spectroscopy near a ^{85}Rb Feshbach resonance. *Phys. Rev. A* **67**, 060701 (2003). URL http://link.aps.org/doi/10.1103/PhysRevA.67.060701. Cited on pages 61 and 74.

[125] Kraemer, T. *et al.* Optimized production of a cesium Bose–Einstein condensate. *Applied Physics B: Lasers and Optics* **79**, 1013–1019 (2004). URL http://dx.doi.org/10.1007/s00340-004-1657-5. 10.1007/s00340-004-1657-5. Cited on pages 61 and 147.

[126] Jeppesen, M. *et al.* Approaching the Heisenberg limit in an atom laser. *Phys. Rev. A* **77**, 063618 (2008). URL http://link.aps.org/abstract/PRA/v77/e063618. Cited on pages 61, 66, 68, and 115.

[127] Andrews, M. R. *et al.* Observation of Interference Between Two Bose Condensates. *Science* **275**, 637–641 (1997). URL http://www.sciencemag.org/cgi/content/abstract/275/5300/637. http://www.sciencemag.org/cgi/reprint/275/5300/637.pdf. Cited on page 62.

[128] Breit, G. & Rabi, I. I. Measurement of Nuclear Spin. *Phys. Rev.* **38**, 2082–2083 (1931). URL http://link.aps.org/doi/10.1103/PhysRev.38.2082.2. Cited on pages 62 and 133.

[129] Esslinger, T., Bloch, I. & Hänsch, T. W. Bose-Einstein condensation in a quadrupole-Ioffe-configuration trap. *Phys. Rev. A* **58**, R2664–R2667 (1998). URL http://dx.doi.org/10.1103/PhysRevA.58.R2664. Cited on pages 63 and 72.

[130] Dall, R. G. *et al.* Observation of transverse interference fringes on an atom laser beam. *Opt. Express* **15**, 17673–17680 (2007). URL http://www.opticsexpress.org/abstract.cfm?URI=oe-15-26-17673. Cited on page 66.

[131] Dugué, J. *et al.* Investigation and comparison of multistate and two-state atom laser-output couplers. *Phys. Rev. A* **75**, 053602 (2007). URL http://link.aps.org/abstract/PRA/v75/e053602. Cited on pages 66, 104, 110, and 114.

[132] Jeppesen, M. *Development of the Atom Laser*. Ph.D. thesis, The Australian National University (2009). URL http://atomlaser.anu.edu.au/publications/phd_masters_and_honours_the.html. Cited on pages 66, 68, and 104.

[133] Streed, E. W. *et al.* Large atom number Bose-Einstein condensate machines. *Rev. Sci. Instrum.* **77**, 023106 (2006). URL http://link.aip.org/link/?RSI/77/023106/1. Cited on page 69.

[134] Altin, P. A. *et al.* ^{85}Rb tunable-interaction Bose-Einstein condensate machine. *Rev. Sci. Instrum.* **81**, 063103 (2010). URL http://link.aip.org/link/?RSI/81/063103/1. Cited on pages 69 and 74.

[135] Dalibard, J. & Cohen-Tannoudji, C. Laser cooling below the Doppler limit by polarization gradients: simple theoretical models. *J. Opt. Soc. Am. B* **6**, 2023–2045 (1989). URL http://josab.osa.org/abstract.cfm?URI=josab-6-11-2023. Cited on pages 69 and 72.

[136] Ricci, L. *et al.* A compact grating-stabilized diode laser system for atomic physics. *Opt. Commun.* **117**, 541–549 (1995). URL http://www.sciencedirect.com/science/article/B6TVF-3XWS0SK-80/2/155d9c814d3261b70ffbd5e8c505a0eb. Cited on page 70.

[137] MogLabs Diode Lasers and Electronics. URL http://www.moglabs.com/. Cited on page 70.

[138] Drever, R. W. P. *et al.* Laser phase and frequency stabilization using an optical resonator. *Applied Physics B: Lasers and Optics* **31**, 97–105 (1983). URL http://dx.doi.org/10.1007/BF00702605. 10.1007/BF00702605. Cited on page 70.

[139] Ikegami, T., i. Ohshima, S. & Ohtsu, M. Frequency Stabilization of Laser Diodes to the Cs-D_2 Line with the Zeeman Modulation Method. *Japanese Journal of Applied Physics* **28**, L1839–L1841 (1989). URL http://jjap.jsap.jp/link?JJAP/28/L1839/. Cited on page 70.

[140] Dinneen, T. P., Wallace, C. D. & Gould, P. L. Narrow linewidth, highly stable, tunable diode laser system. *Optics Communications* **92**, 277 – 282 (1992). URL http://www.sciencedirect.com/science/article/pii/0030401892906366. Cited on page 70.

[141] Debs, J. E., Robins, N. P., Lance, A., Kruger, M. B. & Close, J. D. Piezo-locking a diode laser with saturated absorption spectroscopy. *Appl. Opt.* **47**, 5163–5166 (2008). URL http://ao.osa.org/abstract.cfm?URI=ao-47-28-5163. Cited on page 70.

[142] m2kLaser. URL http://www.m2k-laser.de/. Cited on pages 70 and 125.

[143] McDonald, G. D. Detecting Atomic Shot Noise on Ultra-Cold Atom Clouds, Honours thesis, the Australian National University (2009). URL http://atomlaser.anu.edu.au/publications/phd_masters_and_honours_the.html. Cited on pages 74, 98, and 101.

[144] Donley, E. A. *et al.* Dynamics of collapsing and exploding Bose-Einstein condensates. *Nature* **412**, 295–299 (2001). URL http://www.nature.com/nature/journal/v412/n6844/full/412295a0.html. Cited on page 74.

[145] Savage, C. M., Robins, N. P. & Hope, J. J. Bose-Einstein condensate collapse: A comparison between theory and experiment. *Phys. Rev. A* **67**, 014304 (2003). URL http://link.aps.org/doi/10.1103/PhysRevA.67.014304. Cited on page 74.

[146] Altin, P. A. *et al.* Collapse and three-body loss in a ^{85}Rb Bose-Einstein condensate. *Phys. Rev. A* **84**, 033632 (2011). URL http://link.aps.org/doi/10.1103/PhysRevA.84.033632. Cited on page 74.

[147] Landau, L. D. Zur Theorie der Energieübertragung II. *Physik. Zeits. Sowjetunion* **2** (1932). Cited on page 76.

[148] Majorana, E. Atomi orientati in campo magnetico variabile. *Il Nuovo Cimento (1924-1942)* **9**, 43–50 (1932). URL http://dx.doi.org/10.1007/BF02960953. 10.1007/BF02960953. Cited on page 76.

[149] Stückelberg, E. C. G. Theorie der unelastischen Stösse zwischen Atomen. *Helvetica Physica Acta* **5** (1932). Cited on page 76.

[150] Zener, C. Non-Adiabatic Crossing of Energy Levels. *Proceedings of the Royal Society of London. Series A* **137**, 696–702 (1932). URL http://rspa.royalsocietypublishing.org/content/137/833/696.short. Cited on page 76.

[151] Döring, D. *et al.* Ramsey interferometry with an atom laser. *Opt. Express* **17**, 20661–20668 (2009). URL http://www.opticsexpress.org/abstract.cfm?URI=oe-17-23-20661. Cited on pages 77, 78, 98, 99, 100, and 115.

[152] Morrison, A. K. Flux Limitations of Continuous Atom Lasers, Honours thesis, the Australian National Unviersity (2005). URL http://atomlaser.anu.edu.au/publications/phd_masters_and_honours_the.html. Cited on page 78.

[153] Tackmann, G. *et al.* Phase-locking of two self-seeded tapered amplifier lasers. *Opt. Express* **18**, 9258–9265 (2010). URL http://www.opticsexpress.org/abstract.cfm?URI=oe-18-9-9258. Cited on page 79.

[154] Le Gouët, J. *et al.* Wide bandwidth phase-locked diode laser with an intra-cavity electro-optic modulator. *Optics Communications* **282**, 977 – 980 (2009). URL http://www.sciencedirect.com/science/article/B6TVF-4V412CT-5/2/5f349472dd1a51f432ea2c041cc023ad. Cited on page 79.

[155] Müller, H., Chiow, S. W., Long, Q. & Chu, S. Phase-locked, low-noise, frequency agile titanium:sapphire lasers for simultaneous atom interferometers. *Opt. Lett.* **31**, 202–204 (2006). URL http://ol.osa.org/abstract.cfm?URI=ol-31-2-202. Cited on pages 80, 128, 129, and 131.

[156] Feynman, R. P. *Surely you're Joking Mr. Feynman!: Adventures of a Curious Character* (W. W. Norton, 1985). Cited on page 87.

[157] Tuleja, S., Gazovic, B., Tomori, A. & Hanc, J. Feynman's wobbling plate. *American Journal of Physics* **75**, 240–244 (2007). URL http://link.aip.org/link/?AJP/75/240/1. Cited on page 87.

[158] Döring, D. *Interferometry and precision measurements with Bose-condensed atoms.* Ph.D. thesis, The Australian National University (2011). URL http://atomlaser.anu.edu.au/publications/phd_masters_and_honours_the.html. Cited on pages 98, 101, and 104.

[159] Debs, J. E. *et al.* Experimental comparison of Raman and rf outcouplers for high-flux atom lasers. *Phys. Rev. A* **81**, 013618 (2010). URL http://dx.doi.org/10.1103/PhysRevA.81.013618. Cited on page 103.

[160] Dick, G. J. Local oscillator induced instabilities in trapped ion frequency standards. In *19th Annual PTTI Systems and Applications Meeting*, vol. 19, 133 (1987). Cited on pages 103 and 170.

[161] Robins, N. P., Figl, C., Jeppesen, M., Dennis, G. R. & Close, J. D. A pumped atom laser. *Nature Phys.* **4**, 731–736 (2008). URL http://dx.doi.org/10.1038/nphys1027. Cited on pages 104, 115, and 170.

[162] Döring, D. *et al.* Pulsed pumping of a Bose-Einstein condensate. *Phys. Rev. A* **79**, 063630 (2009). URL http://link.aps.org/abstract/PRA/v79/e063630. Cited on pages 104, 115, and 170.

[163] Inouye, S. *et al.* Superradiant Rayleigh Scattering from a Bose-Einstein Condensate. *Science* **285**, 571–574 (1999). URL http://www.sciencemag.

org/cgi/content/abstract/285/5427/571. http://www.sciencemag.org/cgi/reprint/285/5427/571.pdf. Cited on page 104.

[164] Robins, N. P., Morrison, A. K., Hope, J. J. & Close, J. D. Limits to the flux of a continuous atom laser. *Phys. Rev. A* **72**, 031606 (2005). URL http://link.aps.org/abstract/PRA/v72/e031606. Cited on page 104.

[165] Cohen-Tannoudji, C., Diu, B. & Laloë, F. *Quantum Mechanics* (Wiley, New York, 1977). Cited on page 104.

[166] Zobay, O. & Garraway, B. M. Atom trapping and two-dimensional Bose-Einstein condensates in field-induced adiabatic potentials. *Phys. Rev. A* **69**, 023605 (2004). URL http://dx.doi.org/10.1103/PhysRevA.69.023605. Cited on page 104.

[167] Colombe, Y. *et al.* Ultracold atoms confined in rf-induced two-dimensional trapping potentials. *EPL (Europhysics Letters)* **67**, 593–599 (2004). URL http://stacks.iop.org/0295-5075/67/593. Cited on page 104.

[168] White, M., Gao, H., Pasienski, M. & DeMarco, B. Bose-Einstein condensates in rf-dressed adiabatic potentials. *Phys. Rev. A* **74**, 023616 (2006). URL http://link.aps.org/abstract/PRA/v74/e023616. Cited on page 104.

[169] Lesanovsky, I. *et al.* Adiabatic radio-frequency potentials for the coherent manipulation of matter waves. *Phys. Rev. A* **73**, 033619 (2006). URL http://link.aps.org/abstract/PRA/v73/e033619. Cited on page 104.

[170] Hofferberth, S., Lesanovsky, I., Fischer, B., Verdu, J. & Schmiedmayer, J. Radiofrequency-dressed-state potentials for neutral atoms. *Nature Phys.* **2**, 710–716 (2006). URL http://dx.doi.org/10.1038/nphys420. Cited on page 104.

[171] Gerbier, F., Bouyer, P. & Aspect, A. Quasicontinuous Atom Laser in the Presence of Gravity. *Phys. Rev. Lett.* **86**, 4729–4732 (2001). URL http://link.aps.org/doi/10.1103/PhysRevLett.86.4729. Cited on page 108.

[172] Dugué, J. *et al.* Multibeam atom laser: Coherent atom beam splitting from a single far-detuned laser. *Phys. Rev. A* **77**, 031603 (2008). URL http://link.aps.org/abstract/PRA/v77/e031603. Cited on page 110.

[173] Peik, E., Dahan, M. B., Bouchoule, I., Castin, Y. & Salomon, C. Bloch oscillations of atoms, adiabatic rapid passage, and monokinetic atomic beams. *Phys. Rev. A* **55**, 2989–3001 (1997). URL http://dx.doi.org/10.1103/PhysRevA.55.2989. Cited on pages 120, 137, and 144.

[174] Bragg, W. L. The diffraction of X-rays by crystals. *Nobel Lecture* (1915). URL http://www.nobelprize.org/nobel_prizes/physics/laureates/1915/wl-bragg-lecture.pdf. Cited on page 120.

[175] Müller, H., Chiow, S. W. & Chu, S. Atom-wave diffraction between the Raman-Nath and the Bragg regime: Effective Rabi frequency, losses, and phase shifts. *Phys. Rev. A* **77**, 023609 (2008). URL http://dx.doi.org/10.1103/PhysRevA.77.023609. Cited on pages 121, 138, 152, and 153.

[176] Adapted from work by Christophe Dang Ngoc Chan under the Creative Commons Attribution-Share Alike 3.0 Unported licence. Cited on page 121.

[177] Kapitza, P. L. & Dirac, P. A. M. The reflection of electrons from standing light waves. *Mathematical Proceedings of the Cambridge Philosophical Society* **29**, 297–300 (1933). URL http://dx.doi.org/10.1017/S0305004100011105. http://journals.cambridge.org/article_S0305004100011105. Cited on page 121.

[178] Bartell, L. S., Thompson, H. B. & Roskos, R. R. Observation of Stimulated Compton Scattering of Electrons by Laser Beam. *Phys. Rev. Lett.* **14**, 851–852 (1965). URL http://dx.doi.org/10.1103/PhysRevLett.14.851. Cited on page 121.

[179] Altshuler, S., Frantz, L. M. & Braunstein, R. Reflection of Atoms from Standing Light Waves. *Phys. Rev. Lett.* **17**, 231–232 (1966). URL http://dx.doi.org/10.1103/PhysRevLett.17.231. Cited on page 121.

[180] SpinCore Technologies. URL http://www.spincore.com/products/PulseBlasterDDS-II-300/PulseBlasterDDS-II-300.shtml. Cited on page 125.

[181] LeCroy High Resolution Oscilloscopes. URL http://www.lecroy.com/oscilloscope/oscilloscopemodel.aspx?modelid=1943. Cited on page 128.

[182] Birch, K. P. & Downs, M. J. An Updated Edlén Equation for the Refractive Index of Air. *Metrologia* **30**, 155 (1993). URL http://stacks.iop.org/0026-1394/30/i=3/a=004. Cited on page 130.

[183] McGuirk, J. M., Snadden, M. J. & Kasevich, M. A. Large Area Light-Pulse Atom Interferometry. *Phys. Rev. Lett.* **85**, 4498–4501 (2000). Cited on page 131.

[184] Sané, S. S. *et al.* 11 W narrow linewidth laser source at 780nm for laser cooling and manipulation of Rubidium. *Opt. Express* **20**, 8915–8919 (2012). URL http://www.opticsexpress.org/abstract.cfm?URI=oe-20-8-8915. Cited on pages 132, 170, and 171.

[185] Denschlag, J. *et al.* A Bose-Einstein condensate in an optical lattice. *Journal of Physics B: Atomic, Molecular and Optical Physics* **35**, 3095–3110 (2002). URL http://stacks.iop.org/0953-4075/35/3095. Cited on pages 137 and 144.

[186] Cladé, P., Guellati-Khélifa, S., Nez, F. & Biraben, F. Large Momentum Beam Splitter Using Bloch Oscillations. *Phys. Rev. Lett.* **102**, 240402 (2009). URL http://dx.doi.org/10.1103/PhysRevLett.102.240402. Cited on pages 137, 144, 145, and 147.

[187] Fattori, M. *et al.* Atom Interferometry with a Weakly Interacting Bose-Einstein Condensate. *Phys. Rev. Lett.* **100**, 080405 (2008). URL http://link.aps.org/abstract/PRL/v100/e080405. Cited on page 137.

[188] Chiow, S. W., Herrmann, S., Chu, S. & Müller, H. Noise-Immune Conjugate Large-Area Atom Interferometers. *Phys. Rev. Lett.* **103**, 050402 (2009). URL http://dx.doi.org/10.1103/PhysRevLett.103.050402. Cited on page 138.

[189] Amalvict, M., McQueen, H. & Ramesh, G. Absolute gravity measurements and calibration of SG-CT031 at Canberra, 1999-2000. *J. Geodet. Soc. Jpn.* **47**, 410 (2001). URL http://www.journalarchive.jst.go.jp/japanese/jnlabstract_ja.php?cdjournal=sokuchi1954&cdvol=47&noissue=1&startpage=410. Cited on pages 139 and 141.

[190] Barter, T. H. Measuring Gravity with a Bose-Einstein Condensate, Honours Thesis, The Australian National University (2010). Cited on page 141.

[191] Bloch, F. Über die Quantenmechanik der Elektronen in Kristallgittern. *Zeitschrift für Physik A Hadrons and Nuclei* **52**, 555–600 (1929). URL http://dx.doi.org/10.1007/BF01339455. 10.1007/BF01339455. Cited on page 144.

[192] Zener, C. A Theory of the Electrical Breakdown of Solid Dielectrics. *Proceedings of the Royal Society of London. Series A* **145**, 523–529 (1934). URL http://rspa.royalsocietypublishing.org/content/145/855/523.short. http://rspa.royalsocietypublishing.org/content/145/855/523.full.pdf+html. Cited on page 144.

[193] Leo, K., Bolivar, P. H., Brüggemann, F., Schwedler, R. & Köhler, K. Observation of Bloch oscillations in a semiconductor superlattice. *Solid State Communications* **84**, 943 – 946 (1992). URL http://www.sciencedirect.com/science/article/pii/003810989290798E. Cited on page 144.

[194] Feldmann, J. *et al.* Optical investigation of Bloch oscillations in a semiconductor superlattice. *Phys. Rev. B* **46**, 7252–7255 (1992). URL http://link.aps.org/doi/10.1103/PhysRevB.46.7252. Cited on page 144.

[195] Cladé, P., Plisson, T., Guellati-Khélifa, S., Nez, F. & Biraben, F. Theoretical analysis of a large momentum beamsplitter using Bloch oscillations. *The European Physical Journal D - Atomic, Molecular, Optical and Plasma Physics* **59**, 349–360 (2010). URL http://dx.doi.org/10.1140/epjd/e2010-00198-0. 10.1140/epjd/e2010-00198-0. Cited on pages 144 and 147.

[196] Anderson, B. P. & Kasevich, M. A. Spatial observation of Bose-Einstein condensation of ^{87}Rb in a confining potential. *Phys. Rev. A* **59**, R938–R941 (1999). URL http://link.aps.org/doi/10.1103/PhysRevA.59.R938. Cited on page 158.